technische universität
dortmund

**Dissertation**
**zur Erlangung des akademischen Grades**
**Dr. rer. nat. im Fach Physik**

# Exploiting the phenomenology of flavourful $Z'$ models


Rigo Bause

geboren in Dortmund

Lehrstuhl für Theoretische Physik IV
Fakultät Physik
Technische Universität Dortmund


Juni 2022

| | |
|---|---|
| Erstgutachter: | Prof. Dr. Gudrun Hiller |
| Zweitgutachter: | Jun.-Prof. Dr. Emmanuel Stamou |
| Abgabedatum: | 02. 06. 2022 |

| | |
|---|---|
| Datum der mündlichen Promotionsprüfung: | 25. 10. 2022 |
| Vorsitzender der Prüfungskommission: | Prof. Dr. Markus Betz |

# Contents

# Abstract

This thesis comprises recent studies on extensions of the standard model (SM) involving a heavy $Z'$ boson. In the SM, flavour-changing neutral current (FCNC) quark transitions only appear at loop level and are highly suppressed. This puts forward flavourful $Z'$ models, where the new gauge boson couples non-universally to the known quarks and leptons at tree level. The models are able address the persistent deviations of the SM seen in observables of rare $B$-meson decays referred to as the $B$-anomalies. By supplementing the particle content of the SM with new scalars and vector-like fermions, the occurrence of putative Landau poles present in general $Z'$ scenarios can be averted. We discuss dedicated models in the context of the $B$-anomalies that allow for a stable and predictive theory up to the Planck scale. Moreover, flavour rotations also enable FCNC transitions in the charm sector, where the resonance pollution in branching ratios of semileptonic decays demands null test observables sensitive to physics beyond the SM. We investigate effects in such decays and present unique correlations to $CP$-violating observables in hadronic decays, accessible with future measurements by the LHCb and Belle II experiments. Recent studies involving dineutrino modes are discussed as well. We exploit an interplay between neutrino and charged lepton couplings within the SM effective field theory approach that connects decays of opposite flavour sectors. In doing so, we derive limits on diverse sets of dineutrino branching ratios and find novel tests of lepton universality using data from global fits of the $B$-anomalies.

# Kurzfassung

Die vorliegende Dissertation umfasst Studien zur Erweiterung des Standardmodells durch ein schweres $Z'$-Boson. *Flavour*-verändernde neutrale Ströme (FCNCs) von Quarkübergängen treten im Standardmodell in höheren Ordnungen auf und sind stark unterdrückt. Die Implementation von $Z'$-Modellen ermöglicht solche Übergänge auf Baumgraphen-Niveau, induziert durch nicht-universelle Kopplungen an die bekannten Quarks und Leptonen. Dies liefert eine mögliche Erklärung der Diskrepanzen zwischen theoretischer Vorhersage und Messung in Observablen von seltenen $B$-Meson-Zerfällen, den sogenannten *$B$-Anomalien*. Das Auftreten von Landau-Polen in eben solchen Theorien kann durch das Hinzufügen von neuen Teilchen zum Standardmodell-Spektrum abgewendet werden. In dieser Arbeit untersuchen wir ausgewählte Modelle, die eine direkte Erklärung der $B$-Anomalien liefern und zusätzlich eine stabile Vorhersagekraft durch Abwesenheit von Polen und Instabilitäten bis zur Planck-Skala innehaben. Auch in seltenen *charm* Zerfällen können erhebliche Beträge zu FCNCs durch das $Z'$-Boson generiert werden. In diesem Sektor spielt das Aufstellen von *null tests* des Standardmodells, sensitiv zu Effekten neuer Physik, eine besondere Rolle, da unter anderem semi-leptonische Verzweigungsverhältnisse durch die Verunreinigung von auftretenden Resonanzen schwer zugänglich sind. Wir befassen uns deshalb außerdem mit der Erforschung von Effekten neuer Physik in diesen Zerfällen und erarbeiten eindeutige Korrelationen zwischen $CP$-verletzenden Observablen, welche mit zukünftigen Messungen von den Experimenten LHCb und Belle II überprüft werden können. Wir präsentieren außerdem neue Studien zu Teilchenzerfällen in zwei Neutrinos. Durch das Zusammenspiel zwischen Kopplungen von geladenen Leptonen und Neutrinos unter Zuhilfenahme der effektiven Feldtheorie des Standardmodells bestimmen wir obere Grenzen an eine Vielzahl von Neutrino-Verzweigungsverhältnissen, und entwickeln neue Tests der Lepton-Universalität.

# Publications

This thesis is based on the following publications by the author:

- R. Bause, M. Golz, G. Hiller, and A. Tayduganov. "The new physics reach of null tests with $D \to \pi\ell\ell$ and $D_s \to K\ell\ell$ decays." In: *Eur. Phys. J. C* 80.1 (2020). [Erratum: Eur.Phys.J.C 81, 219 (2021)], p. 65. DOI: 10.1140/epjc/s10052-020-7621-7. arXiv: 1909.11108 [hep-ph]
- R. Bause, H. Gisbert, M. Golz, and G. Hiller. "Exploiting $CP$-asymmetries in rare charm decays." In: *Phys. Rev. D* 101.11 (2020), p. 115006. DOI: 10.1103/PhysRevD.101.115006. arXiv: 2004.01206 [hep-ph]
- R. Bause, H. Gisbert, M. Golz, and G. Hiller. "Lepton universality and lepton flavor conservation tests with dineutrino modes." In: *Eur. Phys. J. C* 82.2 (2022), p. 164. DOI: 10.1140/epjc/s10052-022-10113-6. arXiv: 2007.05001 [hep-ph]
- R. Bause, H. Gisbert, M. Golz, and G. Hiller. "Rare charm $\boldsymbol{c \to u\,\nu\bar{\nu}}$ dineutrino null tests for $e^+e^-$ machines." In: *Phys. Rev. D* 103.1 (2021), p. 015033. DOI: 10.1103/PhysRevD.103.015033. arXiv: 2010.02225 [hep-ph]
- R. Bause, H. Gisbert, M. Golz, and G. Hiller. "Interplay of dineutrino modes with semileptonic rare B-decays." In: *JHEP* 12 (2021), p. 061. DOI: 10.1007/JHEP12(2021)061. arXiv: 2109.01675 [hep-ph]
- R. Bause, G. Hiller, T. Höhne, D. F. Litim, and T. Steudtner. "B-anomalies from flavorful U(1)′ extensions, safely." In: *Eur. Phys. J. C* 82.1 (2022), p. 42. DOI: 10.1140/epjc/s10052-021-09957-1. arXiv: 2109.06201 [hep-ph]

In addition, results have been presented in the following proceedings:

- R. Bause, H. Gisbert, M. Golz, and G. Hiller. "Dineutrino modes probing lepton flavor violation." In: *PoS* EPS-HEP2021 (2022), p. 563. DOI: 10.22323/1.398.0563. arXiv: 2110.08795 [hep-ph]. Speaker: Hector Gisbert

# Acknowledgements

First of all, I would like to express gratitude towards my supervisor Gudrun Hiller for giving me the opportunity to work in the field of theoretical particle physics and advising my thesis. Working at the department TIII/TIV has always been a pleasure due to the wonderful people I collaborated with over the past years. I consider myself lucky that I always had the possibility to work on a variety of challenging and interesting research topics. Owed to the pleasant and wholesome vibes of the (coffee) breaks and after-work activities, the time at the department flew by as I very much enjoyed coming to work every day (or staying at home when the Covid-pandemic called for it).

I thank Marcel Golz, whom I started studying physics with as an undergraduate back in October 2013, for our joined studies and experiences at the TU Dortmund. Moreover, I want to sincerely thank Hector Gisbert not only for the work and efforts in our projects, but also for intensively supporting and helping me during my time as a PhD student. ¡Muchísimas gracias de nuevo por las conversaciones y consejos útiles como amigo!

Next, I pay tribute to my other collaborators Tim Höhne and Tom Steudtner as well as to my fellow *admins* Nico Adolph, Tim Brune and Dominik Hellmann. It goes without saying, that I appreciated the company and discussions with former ~~members~~ legends of the department, such as Stefan Bißmann, Dominik Döring, Clara Hormigos Feliu, Kevin Moch and Dennis Loose. Moreover, I warmly thank all my former (and current) office mates, where in particular Lara Nollen and Peter Schuh have not yet been mentioned explicitly, for the nice atmosphere and helpful conversations at my workplace. But also outside the theoretical physics department I met special people during my time at the university, where I give my dearest thanks to Björn Wendland (the best lab-course partner and assistant), Felix Brauers (the second-best FIFA player) and Kevin Foryt. I thank everyone (again) who proofread my thesis and provided me with useful feedback and suggestions.

Lastly, I'm forever grateful for the steady support and care of my family and close friends.

*Chapter*

# 1

# Introduction

The description of the fundamental building blocks of nature is one of the most intensely studied topics in modern science. The question concerning the origin of matter particles and their interactions has been the impetus for dedicated research of brilliant minds, which entailed major achievements by joined efforts in the fields of physics and mathematics. With important theoretical and experimental findings over the past century, a theory was developed known as the standard model (SM) of particle physics. Its proposed particle spectrum was completed in 2012 with the discovery of the Higgs boson at the Large Hadron Collider (LHC) [1, 2].

While the SM provides the most accurate and precise description of our universe, it has several shortcomings and cannot be the end of the story. It only describes three out of the four known fundamental forces of nature, that is the electromagnetic, weak, and strong forces, whereas gravity is not included. Hence, a consistent picture of physics is lacking at the Planck scale where gravitational effects become relevant. Moreover, only five per cent of the observed mass-energy budget of the universe is accounted for by fermionic matter, whereas the rest is composed of dark matter and dark energy not included in the SM. In its original formulation, no neutrino masses are present which is contradicted by the observation of neutrino oscillations [3, 4] implying small but non-zero masses. Also, the apparent asymmetry between matter and antimatter present in the universe hints at $CP$-violating physics that cannot be accounted for by the SM alone.

Consequently, the SM is developed as an effective field theory (EFT) that needs to be replaced by a more fundamental theory at high scales. Many extensions have been put forward that incorporate new particles and interactions which need to be tested by experiments, *e.g.* at particle colliders. Thereby, the search for new physics (NP) is driven by several complementary approaches. In collider experiments, the direct production and detection of new particles are limited by the centre of mass energy realised at those facilities. However, a direct search is futile if the allocated energy is too low for such particles to be created, which then only exist virtually and escape detection. Hence, direct searches at current experiments are restricted to energies up to the TeV-scale. This encourages possible indirect detections of new particles due to quantum fluctuations that are indicated by deviations between the SM prediction and measurement. Indirect searches allow us probe very high scales otherwise inaccessible, yet require extremely high precision in both theory and experiment.

For instance, the persisting discrepancies in observables of rare $B$-decays probing lepton universality (LU) offer first hints of beyond the standard model (BSM) physics with charged leptons, and are collectively called the $B$-anomalies. Over the past decade, the first measurements by the Large Hadron Collider beauty (LHCb) experiment [5, 6] motivated intense studies and elaboration of many NP models. Recent results [7–9] with improved data and statistics remain in disagreement with the SM prediction at 2-3 $\sigma$.

Prime candidates to address these anomalies are U(1)$'$ extensions of the SM, where a new gauge

boson, the $Z'$ boson, enables a non-universal flavour structure. While constraints from theory like gauge anomaly cancellation have to be met, they offer a vast model building opportunity, with phenomenological implications for many flavour processes [10–15]. Flavourful $Z'$ models can upset established SM symmetries like LU or charged lepton flavour conservation (cLFC), and generate sizeable contributions to rare decays. The study of these models constitutes the main objective of this thesis. We present models in complementary sectors that are compatible with stringent constraints from flavour-changing processes, employing flavour mixing as an essential tool to induce the necessary effects in observables. In particular, tests of LU are studied closely in charm and $B$-physics. Yet, a model-independent look beyond the SM is provided via the standard model effective field theory (SMEFT) framework, relating physics of neutrinos and charged leptons. Moreover, $Z'$ models can support large weak phases relevant for additional $CP$ violation beyond the SM. Then again, the new U(1)$'$ symmetry with sizeable coupling strength at the electroweak scale jeopardises the predictivity of the theory at higher energies, where Landau poles manifest themselves way before the Planck scale. Therefore, we review model building approaches with an extended fermionic and scalar sector that averts such divergences up to Planckian energies, and discuss their phenomenological implications.

This thesis is based on the works in Refs. [16–21] and organised as follows. In Chap. 2, we introduce the SM of particle physics, focussing on flavour mixing of SM fermions and exploring its implications on quark and lepton transitions. Afterwards, we provide the theoretical foundation necessary to study extensions of the SM in an EFT approach in Chap. 3. We also review the persistent flavour anomalies in rare $B$-decays. They motivate a global fit of observables sensitive to NP in $b\to s$ transitions which is presented in Chap. 4. In Chap. 5, we work out a comprehensive overview of various model building aspects in $Z'$ scenarios. Due to our focus on NP-induced contributions to rare decays, we discuss flavour rotations that modify the flavour-changing neutral current (FCNC) transitions of interest. In addition, necessary theoretical prerequisites like gauge anomaly cancellation and constraints from meson mixing are presented, while we also address Landau poles in U(1)$'$ extensions. In Chap. 6, we start our investigations of $Z'$ models in rare charm decays. We present a class of models that induce sizeable contributions to semileptonic Wilson coefficients while simultaneously evading tight meson mixing bounds. Promising null tests observables are assessed focussing on $Z'$-induced effects. Chapter 7 is devoted to NP studies in hadronic charm decays. We exploit the rich $CP$ phenomenology and SU(3) sum rules that allow for pronounced NP effects, correlating different decay modes. The subsequent Chap. 8 puts forward appropriate Planck-safe $Z'$ models to explain the $B$-anomalies in a BSM theory that remains predictive and perturbative towards Planckian energies. Recent works on correlations between dineutrino and charged dilepton couplings in the SMEFT framework are compiled in Chap. 9. Therein, we present novel tests of lepton universality and implications of possible BSM scenarios. We conclude in Chap. 10.

Supplementary descriptions and details are provided in Apps. A to G. We use the LaTeX package `TikZ-Feynman` [22] for all Feynman diagrams shown throughout this thesis.

Chapter

# 2

# Flavour physics in the standard model

Following the literature [23–26], we recapitulate the standard model (SM) with a focus on its flavour sector. In Sec. 2.1, we introduce the SM particles and gauge interactions, followed by a brief review of the Higgs mechanism in Sec. 2.2. Section 2.3 deals with the flavour structure and mixing, while Sec. 2.4 discusses flavour-changing quark transitions and their parametrisation. Afterwards, we discuss symmetries of the SM in Sec. 2.5.

## 2.1 Field content and gauge symmetries of the standard model

The SM describes all known elementary particles and their interactions with the exception of gravity at the most fundamental level. It is constructed as a gauge quantum field theory (QFT) with the local gauge group

$$\mathcal{G}_{\text{SM}} = \text{U}(1)_Y \times \text{SU}(2)_L \times \text{SU}(3)_C \,, \tag{2.1}$$

where $\text{SU}(3)_C$ denotes the symmetry of quantum chromodynamics (QCD), the theory of strong interactions, while the gauge group of weak interactions is given by $\text{SU}(2)_L$. The $\text{U}(1)_Y$ force is felt by all particles with a non-zero hypercharge quantum number $Y$. The other quantum numbers of $\text{SU}(3)_C$ and $\text{SU}(2)_L$ are called colour and weak isospin, respectively. While $\text{SU}(3)_C$ remains intact, the electroweak sector, *i.e.* $\text{U}(1)_Y \times \text{SU}(2)_L$, is spontaneously broken down to $\text{U}(1)_{\text{em}}$, the gauge group of quantum electrodynamics (QED), by the Higgs mechanism. The electric charge $Q_e$ of a particle is related to its weak isospin component $T^3$ belonging to $\text{SU}(2)_L$ and hypercharge $Y$ via

$$Q_e = T^3 + Y \,. \tag{2.2}$$

This equation is the well-known Gell-Mann-Nishijima relation.

The matter content of the SM consists of two classes of fermions called quarks and leptons, where the former includes the colour-charged up- and down-type quarks, denoted by $u$ and $d$, respectively. The latter is divided into electrically neutral neutrinos $\nu$ and electrically charged leptons $e$, both carrying no colour. In addition, each fermion comes in three different copies or *generations*, which yields in total six *flavours* of both quarks and leptons. These fields are separated into $\text{SU}(2)_L$ doublets ($Q$ for quarks, $L$ for leptons) and $\text{SU}(2)_L$ singlets ($U$, $D$ for quarks, $E$ for leptons) distinguishing their chirality as left-handed (LH) and right-handed (RH), respectively. We define

the chiral fields [1]

$$Q \equiv \begin{pmatrix} u_L \\ d_L \end{pmatrix} , \quad L \equiv \begin{pmatrix} \nu_L \\ e_L \end{pmatrix} , \quad U \equiv u_R , \quad D \equiv d_R , \quad E \equiv e_R , \tag{2.3}$$

where generation and $\mathrm{SU}(3)_C$ structure are left implicit. In Tab. 2.1, we summarise the field content of the SM providing the respective transformation properties under $\mathcal{G}_{\mathrm{SM}}$. By introducing the complex scalar Higgs field $H$, fermion masses are realised which would be forbidden otherwise due to gauge invariance. Likewise, the requirement of local gauge invariance predicts the existence of massless gauge bosons for each part of the gauge group.

| Field | Flavour | $\mathrm{U}(1)_Y$ | $\mathrm{SU}(2)_L$ | $\mathrm{SU}(3)_C$ | $Q_e$ | $T^3$ |
|---|---|---|---|---|---|---|
| $Q$ | $\begin{pmatrix} u_L \\ d_L \end{pmatrix}, \begin{pmatrix} c_L \\ s_L \end{pmatrix}, \begin{pmatrix} t_L \\ b_L \end{pmatrix}$ | $\frac{1}{6}$ | 2 | 3 | $\frac{2}{3}$<br>$-\frac{1}{3}$ | $+\frac{1}{2}$<br>$-\frac{1}{2}$ |
| $U$ | $u_R,\, c_R,\, t_R$ | $\frac{2}{3}$ | 1 | 3 | $\frac{2}{3}$ | 0 |
| $D$ | $d_R,\, s_R,\, b_R$ | $-\frac{1}{3}$ | 1 | 3 | $-\frac{1}{3}$ | 0 |
| $L$ | $\begin{pmatrix} \nu_{e\,L} \\ e_L \end{pmatrix}, \begin{pmatrix} \nu_{\mu\,L} \\ \mu_L \end{pmatrix}, \begin{pmatrix} \nu_{\tau\,L} \\ \tau_L \end{pmatrix}$ | $-\frac{1}{2}$ | 2 | 1 | 0<br>$-1$ | $+\frac{1}{2}$<br>$-\frac{1}{2}$ |
| $E$ | $e_R,\, \mu_R,\, \tau_R$ | $-1$ | 1 | 1 | $-1$ | 0 |
| $H$ | $\begin{pmatrix} \varphi^+ \\ \varphi^0 \end{pmatrix}$ | $\frac{1}{2}$ | 2 | 1 | 1<br>0 | $+\frac{1}{2}$<br>$-\frac{1}{2}$ |

**Table 2.1:** Field content of the SM and transformation properties, where we show the different flavours in terms of their $\mathrm{SU}(2)_L$ components and the associated electric charge $Q_e$.

Before reviewing the mechanism responsible for generating mass terms in Sec. 2.3, we break down the most general renormalisable Lagrangian formulated within the SM that contains the aforementioned matter fields.

The SM Lagrangian can be split into four parts as

$$\mathcal{L}_{\mathrm{SM}} = \mathcal{L}_{\mathrm{fermion}} + \mathcal{L}_{\mathrm{gauge}} + \mathcal{L}_{\mathrm{Higgs}} + \mathcal{L}_{\mathrm{Yuk}} , \tag{2.4}$$

where the individual terms are given in Eqs. (2.5), (2.7), (2.10), and (2.19). We provide a short recap of all terms in the following, starting with the gauge interactions of the SM fermions. The kinetic terms and couplings to gauge bosons are embedded in

$$\mathcal{L}_{\mathrm{fermion}} = \overline{Q}\,\mathrm{i}\not{D}Q + \overline{U}\,\mathrm{i}\not{D}U + \overline{D}\,\mathrm{i}\not{D}D + \overline{L}\,\mathrm{i}\not{D}L + \overline{E}\,\mathrm{i}\not{D}E , \tag{2.5}$$

with the shorthand notation $\not{D} = D_\mu \gamma^\mu$ and summing over all generations and gauge indices

[1] We refer to App. A for the definition of chiral projectors, and details on the mathematical notation and conventions employed throughout this thesis.

implicitly. The gauge covariant derivatives $D_\mu$ for the different fermions fields are given by

$$\begin{aligned}
D_\mu Q_i &= \left(\partial_\mu - \mathrm{i}\, g_1 Y B_\mu - \mathrm{i}\, g_2 T^a W_\mu^a - \mathrm{i}\, g_3 t^b G_\mu^b\right) Q_i\,, \\
D_\mu U_i &= \left(\partial_\mu - \mathrm{i}\, g_1 Y B_\mu - \mathrm{i}\, g_3 t^b G_\mu^b\right) U_i\,, \\
D_\mu D_i &= \left(\partial_\mu - \mathrm{i}\, g_1 Y B_\mu - \mathrm{i}\, g_3 t^b G_\mu^b\right) D_i\,, \\
D_\mu L_i &= \left(\partial_\mu - \mathrm{i}\, g_1 Y B_\mu - \mathrm{i}\, g_2 T^a W_\mu^a\right) L_i\,, \\
D_\mu E_i &= \left(\partial_\mu - \mathrm{i}\, g_1 Y B_\mu\right) E_i\,,
\end{aligned} \tag{2.6}$$

universal for all generations. Here, $Y$ is the (hypercharge) generator associated with the $\mathrm{U}(1)_Y$ group. Conversely, $T^a$ and $t^b$ denote the canonically normalised generators of $\mathrm{SU}(2)_L$ and $\mathrm{SU}(3)_C$, respectively, with the number of (linear independent) generators $a = 1, 2, 3$ and $b = 1, 2, \ldots, 8$ given by dimension of the Lie algebra as $N^2 - 1$ in any $\mathrm{SU}(N)$ group. The gauge bosons of $\mathrm{U}(1)_Y$, $\mathrm{SU}(2)_L$, and $\mathrm{SU}(3)_C$ are represented by the fields $B_\mu$, $W_\mu^a$, and $G_\mu^b$, respectively, with corresponding couplings $g_1$, $g_2$, and $g_3$. Following the notation commonly employed in the literature, the gauge coupling $g_3$ is also referred to as the *strong* coupling $g_s$ throughout this thesis.

Next, we display the kinetic term of the gauge bosons,

$$\mathcal{L}_{\text{gauge}} = -\frac{1}{4} B_{\mu\nu} B^{\mu\nu} - \frac{1}{4} W_{\mu\nu}^a W^{\mu\nu,a} - \frac{1}{4} G_{\mu\nu}^b G^{\mu\nu,b}\,, \tag{2.7}$$

where the field strength tensors have the form

$$F_{\mu\nu}^a \equiv \partial_\mu A_\nu^i - \partial_\nu A_\mu^i + \kappa\, f^{ijk} A_\mu^j A_\nu^k \tag{2.8}$$

for a given gauge group with coupling $\kappa$, gauge boson $A$, and structure constants $f^{ijk}$ of the associated Lie algebra. As $f^{ijk} = 0$ for any abelian symmetry, no self-couplings emerge for $B_{\mu\nu}$, while three and four gauge boson self-couplings follow for the non-abelian $\mathrm{SU}(2)_L$ and $\mathrm{SU}(3)_C$, respectively. No explicit mass terms for both fermions and gauge bosons are allowed in the SM due to the different transformation of LH and RH fields under $\mathrm{SU}(2)_L$ and breaking gauge invariance, respectively. This puts forward the Higgs mechanism giving mass to fermions and bosons via electroweak symmetry breaking (EWSB).

## 2.2 Electroweak symmetry breaking

In the SM, the $W^\pm$, $Z^0$, and fermion masses are generated by the Higgs field through the breakdown of the electroweak to the electromagnetic gauge symmetry,

$$\mathrm{U}(1)_Y \times \mathrm{SU}(2)_L \to \mathrm{U}(1)_{\text{em}}\,. \tag{2.9}$$

The Lagrangian including the gauge and self-interactions of the Higgs reads

$$\mathcal{L}_{\text{Higgs}} = (D_\mu H)^\dagger (D^\mu H) - V(H)\,, \tag{2.10}$$

with the scalar (tree-level) potential

$$V(H) = -\mu^2 H^\dagger H + \lambda \left(H^\dagger H\right)^2\,. \tag{2.11}$$

For real, positive parameters $\mu$, $\lambda > 0$ the potential is minimised, where the neutral component of $H$ acquires a non-zero vacuum expectation value (vev) that can be chosen as

$$\langle 0|\, H\, |0\rangle = \langle H\rangle = \frac{1}{\sqrt{2}} \begin{pmatrix} 0 \\ v_h \end{pmatrix}, \quad v_h = \frac{\mu}{\sqrt{\lambda}} = 246 \text{ GeV}\,. \tag{2.12}$$

Then, $\langle H\rangle$ spontaneously breaks the electroweak symmetry down to the local gauge group $\mathrm{U}(1)_{\mathrm{em}}$, with the generator $Q_e$ and the photon as the massless gauge boson. After EWSB, the Higgs field in unitary gauge is given by

$$H = \frac{1}{\sqrt{2}} \begin{pmatrix} 0 \\ v_h + h \end{pmatrix}, \tag{2.13}$$

where $h$ denotes the physical Higgs boson. By expanding the effective potential in Eq. (2.11) with higher-order terms the extremum structure is altered and yields a metastable or unstable vacuum after renormalisation group (RG) running of the quartic (self-)coupling $\lambda$ [27–29].

To acquire massive gauge bosons, we follow *Goldstone's theorem* [30] which states that spontaneous symmetry breaking (SSB) of a global continuous symmetry yields a new scalar degree of freedom (also known as Goldstone Boson) for every broken generator. However, in the case of a broken gauge symmetry these bosons can be absorbed as extra polarisations of associated gauge bosons, and hence do not appear in the particle spectrum. Then, massive gauge bosons are acquired after inserting the Higgs vev into Eq. (2.10) and diagonalising the new mass terms. We identify $W_\mu^\pm \equiv 1/\sqrt{2}(W_\mu^1 \mp \mathrm{i} W_\mu^2)$ as electrically charged gauge bosons. Due to mixing between $B_\mu$ and $W_\mu^3$, we define an orthogonal transformation

$$\begin{pmatrix} Z_\mu \\ A_\mu \end{pmatrix} = \begin{pmatrix} \cos(\theta_{\mathrm{W}}) & -\sin(\theta_{\mathrm{W}}) \\ \sin(\theta_{\mathrm{W}}) & \cos(\theta_{\mathrm{W}}) \end{pmatrix} \begin{pmatrix} W_\mu^3 \\ B_\mu \end{pmatrix}, \tag{2.14}$$

where the Weinberg mixing angle is given by

$$\tan(\theta_{\mathrm{W}}) = \frac{g_1}{g_2}\,. \tag{2.15}$$

We identify the photon $A_\mu$ as a massless gauge boson, whereas the other one, $Z_\mu$, is massive. The gauge-invariant mass terms for the gauge bosons are extracted from the kinetic terms in Eq. (2.10), which yields in summary

$$\begin{aligned} M_W = \frac{g_2\, v_h}{2}\,, \quad M_Z = \frac{M_W}{\cos(\theta_{\mathrm{W}})} = \frac{g_Z\, v_h}{2}\,, \quad M_\gamma = 0\,, \\ g_Z = \frac{g_2}{\cos(\theta_{\mathrm{W}})} = \sqrt{(g_1)^2 + (g_2)^2}\,, \quad e = g_1\, \cos(\theta_{\mathrm{W}}) = g_2\, \sin(\theta_{\mathrm{W}})\,, \end{aligned} \tag{2.16}$$

where we have defined the electromagnetic coupling strength $e$. Utilising the relations in Eqs. (2.2) and (2.16), the covariant derivative of the electroweak part can be written as

$$D_\mu = \partial_\mu - \mathrm{i}\frac{g_2}{\sqrt{2}}\left[T^+ W_\mu^+ + T^- W_\mu^-\right] - \mathrm{i}\, e\left[\cot(\theta_{\mathrm{W}})\, T^3 - \tan(\theta_{\mathrm{W}})\, Y\right] Z_\mu - \mathrm{i}\, e\, Q_e\, A_\mu\,, \tag{2.17}$$

with the shorthand notation $T^\pm = T^1 \pm \mathrm{i}\, T^2$ for the $\mathrm{SU}(2)_L$ generators.

A useful parameter to test the SM can be constructed involving the ratio of $Z$- and $W$-boson masses. To this end, we define the $\rho$ parameter given at tree level by

$$\rho = \frac{M_W^2}{M_Z^2 \cos^2(\theta_{\rm W})} = 1\,. \tag{2.18}$$

Modifications of this parameter can be realised in extensions of the SM with additional scalar content, which we study later in this thesis. The relevance of such high-precision tests of the SM is further emphasised by, *e.g.*, the recent measurement of the $W$-boson mass by the Collider Detector at Fermilab (CDF) experiment [31], which is in significant tension with the SM expectation.

## 2.3 The flavour structure of the standard model

The last part of the SM Lagrangian is given by the Yukawa sector

$$\mathcal{L}_{\rm Yuk} = -Y_u^{ij}\,\overline{Q}_i\,\tilde{H}\,U_j - Y_d^{ij}\,\overline{Q}_i\,H\,D_j - Y_e^{ij}\,\overline{L}_i\,H\,E_j + \text{h.c.}\,, \tag{2.19}$$

which describes the interactions of the SM fermions to the Higgs. Here, $\tilde{H} \equiv \mathrm{i}\,\sigma_2\,H^*$ denotes the charged conjugated Higgs field and the Yukawa couplings $Y_{u,d,e}$ are given by $3\times 3$ matrices, which are a crucial part of the SM as they determine the flavour structure. Therefore, we explicitly show the generation indices in Eq. (2.19). Most of the free parameters of the SM are included in this sector, *i.e.* six quark masses, three charged lepton masses, three mixing angles and one phase. As neutrinos are massless in the SM, no mixing occurs in the lepton sector as we show later in this section.

As mentioned after Eq. (2.8), Dirac mass terms like $m_u\,\overline{u}_L\,u_R$ explicitly break $\mathrm{SU}(2)_L$ invariance, and hence they are forbidden. However, by incorporating the Higgs doublet each term in Eq. (2.19) is invariant under $\mathcal{G}_{\rm SM}$. After SSB and the Higgs acquiring a vev, the fermion mass terms read

$$\mathcal{L}_{\rm mass} = -\frac{v_h}{\sqrt{2}}\left[\overline{u}_L\,Y_u\,u_R + \overline{d}_L\,Y_d\,d_R + \overline{e}_L\,Y_e\,e_R\right] + \text{h.c.}\,. \tag{2.20}$$

To diagonalise the mass matrices, we define the bi-unitary transformations

$$\begin{aligned} u'_L &\equiv V_u\,u_L\,, \quad & d'_L &\equiv V_d\,d_L\,, \quad & e'_L &\equiv V_\ell\,e_L\,,\\ u'_R &\equiv U_u\,u_R\,, \quad & d'_R &\equiv U_d\,d_R\,, \quad & e'_R &\equiv U_\ell\,e_R\,, \end{aligned} \tag{2.21}$$

where primed (unprimed) fields denote flavour (mass) eigenstates. Here, $V_f$ and $U_f$ are unitary $3\times 3$ matrices, with $f = u,\,d,\,\ell$ for up-type quarks, down-type quarks, and charged leptons, respectively. Going from flavour to mass basis yields diagonal Yukawa couplings $y_f = (V_f)^\dagger\,Y_f\,U_f$ with corresponding diagonal mass matrices $M_f = v_h/\sqrt{2}\,y_f$, *e.g.* $m_c = M_u^{22} = v_h/\sqrt{2}\,y_u^{22}$. The experimentally determined fermion masses read [32] [2]

$$\begin{aligned} m_u &\simeq 2.2\text{ MeV}\,, \quad & m_c &\simeq 1.3\text{ GeV}\,, \quad & m_t &\simeq 173\text{ GeV}\,,\\ m_d &\simeq 4.7\text{ MeV}\,, \quad & m_s &\simeq 93\text{ MeV}\,, \quad & m_b &\simeq 4.2\text{ GeV}\,,\\ m_e &\simeq 0.511\text{ MeV}\,, \quad & m_\mu &\simeq 106\text{ MeV}\,, \quad & m_\tau &\simeq 1.78\text{ GeV}\,, \end{aligned} \tag{2.22}$$

[2] The quark masses are given in the $\overline{\rm MS}$ scheme, where $m_u$, $m_d$, and $m_s$ are computed at a scale $\mu \approx 2$ GeV while $m_c(\mu = m_c)$ and $m_b(\mu = m_b)$. The top-quark mass $m_t$ is determined from direct measurements [32].

and are also displayed in Fig. 2.1. One observes that the fermion masses (and hence the Yukawa couplings) follow a strong hierarchy within each species, where masses differ by up to several orders of magnitude. The fact that SM parameters obey these peculiar hierarchies is part of the SM *flavour puzzle*.

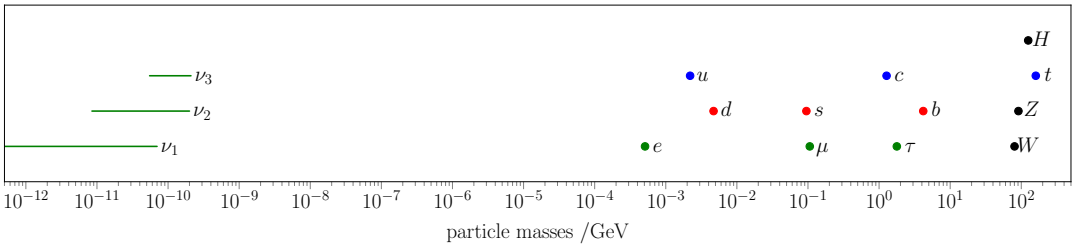


**Figure 2.1:** Schematic visualisation of the mass hierarchies in the flavour sector. Numerical values of fermion and boson masses are provided in Tab. B.2. The ranges for the neutrino masses are based on the known squared mass differences from neutrino oscillations [32] and the constraint on the sum of neutrino masses from cosmological data [33], where the lightest neutrino could be massless. *Figure adapted from Ref.* [34].

The kinetic terms in Eq. (2.5) are also modified by this basis change. In the flavour basis (also referred to as gauge basis), the gauge boson interactions do not mix different generations. In the mass basis, this remains true for the neutral currents, *e.g.*

$$\overline{u}'_L \, u'_L = \overline{u}_L \, (V_u)^\dagger \, V_u \, u_L = \overline{u}_L u_L \,, \tag{2.23}$$

which are not affected by the rotations as the $Z$-boson and photon couplings are flavour universal. However, a mismatch is generated for charged-current interactions altering the $W^\pm$ couplings. We take a look at couplings to quarks first. In the mass basis, the relevant terms read

$$\mathcal{L}_{\text{fermion}} \supset \frac{g_2}{\sqrt{2}} \left( \overline{u}_L \, \gamma^\mu \, V_{\text{CKM}} \, d_L \, W^+_\mu + \overline{d}_L \, \gamma^\mu \, (V_{\text{CKM}})^\dagger \, u_L \, W^-_\mu \right) , \tag{2.24}$$

where the fields include the mass eigenstates *up (u)*, *charm (c)*, *top (t)* and *down (d)*, *strange (s)*, and *bottom (b)* of the up- and down-type quarks, respectively. In Eq. (2.24), we have established the Cabibbo-Kobayashi-Maskawa (CKM) matrix [26, 35, 36]

$$V_{\text{CKM}} \equiv (V_u)^\dagger \, V_d = \begin{pmatrix} V_{ud} & V_{us} & V_{ub} \\ V_{cd} & V_{cs} & V_{cb} \\ V_{td} & V_{ts} & V_{tb} \end{pmatrix} , \tag{2.25}$$

which is responsible for flavour transitions in the SM. Known as the Glashow-Iliopoulos-Maiani (GIM) mechanism [37], it prevents FCNC transitions at tree level in the SM due to the unitarity of the CKM matrix. Yet, the GIM mechanism is present in many loop processes, where FCNCs emerge in so-called penguin diagrams at loop level depicted in Fig. 2.2 for $c \to u$ and $b \to s$ transitions.

Before taking a closer look at the hierarchy of the CKM matrix, we conclude this section by reviewing possible flavour mixing in the lepton sector, where the situation is different due to the fact that neutrinos are massless and RH neutrino fields are not present in the SM. Again, writing

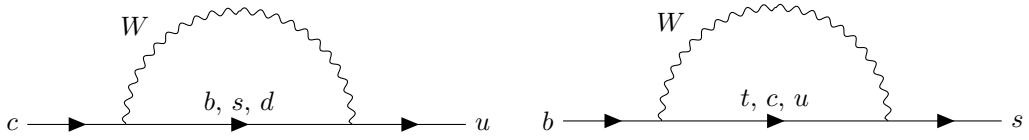


**Figure 2.2:** Loop-level Feynman diagrams of FCNC transitions $c \to u$ (left-hand side diagram) and $b \to s$ (right-hand side diagram) in the SM.

the relevant kinetic terms in the mass basis we find

$$\mathcal{L}_{\text{fermion}} \supset \frac{g_2}{\sqrt{2}} \left( \overline{e}_L \, \gamma^\mu \, U_{\text{PMNS}} \, \nu_L \, W_\mu^- + \overline{\nu}_L \, \gamma^\mu \, (U_{\text{PMNS}})^\dagger \, e_L \, W_\mu^+ \right) , \tag{2.26}$$

with the Pontecorvo-Maki-Nakagawa-Sakata (PMNS) matrix parametrised as

$$U_{\text{PMNS}} \equiv (V_\ell)^\dagger \, V_\nu \, , \tag{2.27}$$

and the rotation to the mass eigenstates is then given by

$$\begin{pmatrix} \nu_e \\ \nu_\mu \\ \nu_\tau \end{pmatrix} = \begin{pmatrix} U_{e1} & U_{e2} & U_{e3} \\ U_{\mu 1} & U_{\mu 2} & U_{\mu 3} \\ U_{\tau 1} & U_{\tau 2} & U_{\tau 3} \end{pmatrix} \begin{pmatrix} \nu_1 \\ \nu_2 \\ \nu_3 \end{pmatrix} . \tag{2.28}$$

Here, we have introduced the (unitary) rotation matrix $V_\nu$ for the neutrinos where flavour and mass eigenstates are denoted by $\nu_\ell$ with $\ell = e, \, \mu, \, \tau$ and $\nu_i$ with $i = 1, \, 2, \, 3$, respectively. However, as no Yukawa matrix for neutrinos is realised we are free to choose $V_\nu$ arbitrarily. Consequently, in the (original) formulation of the SM it is $U_{\text{PMNS}} = \mathbb{1}$ conserving lepton flavour.

Due to the observation of neutrino oscillations, we know that neutrinos must possess small masses, where cosmological data provides an upper bound $\sum m_\nu \lesssim 0.4$ eV on the total neutrino mass [32, 33]. As its scale is tiny compared to the other mass scales (even compared to the electron, the lightest SM particle), neutrino contributions to FCNCs in the charged lepton sector are negligible by means of the GIM mechanism. Hence, (almost) no charged lepton flavour violation (cLFV) is present in SM processes.

As the presence of non-zero neutrino masses already requires BSM physics, one can think of adding a RH neutrino field to the SM, which transforms as a SM-singlet $\nu_R \sim (0, 1, 1)$. Then, the Yukawa Lagrangian in Eq. (2.19) is topped up with terms [26]

$$\mathcal{L}_{\text{Yuk}} \supset -Y_\nu^{ij} \overline{L}_i \tilde{H} \, \nu_{R,j} - \frac{1}{2} \, \overline{\nu}_{R,i}^c \, M_N^{ij} \, \nu_{R,j} + \text{h.c.} \, , \tag{2.29}$$

where $Y_\nu$ and $M_N$ denote the neutrino Yukawa and Majorana mass matrices, respectively. The generation of neutrino masses via $Y_\nu$ assumes that neutrinos are Dirac particles, and thus masses are generated similarly as in the quark sector. However, the expected tiny neutrino masses may suggest a different mechanism for mass generation involving RH neutrinos. By assuming that the neutrino is its own antiparticle, we are able to write down the Majorana mass term in Eq. (2.29). Since this mass term is not protected by any symmetry, the mass matrix $M_N$ can be chosen arbitrarily and may be much larger than the electroweak scale. This is the main idea of the *seesaw* mechanism, where a high Majorana mass scale induces the light neutrino masses observed in nature [38].

## 2.4 Hierarchies of the CKM matrix

The CKM matrix can be parametrised by three mixing angles $\theta_{ij}$ and one complex phase $\delta$. The standard parametrisation of the fermion mixing matrix reads [32, 39]

$$V_{\text{CKM}} = \begin{pmatrix} \mathrm{c}_{12}\,\mathrm{c}_{13} & \mathrm{c}_{13}\,\mathrm{s}_{12} & \mathrm{s}_{13}\,e^{-\mathrm{i}\delta} \\ -\mathrm{c}_{23}\,\mathrm{s}_{12} - \mathrm{c}_{12}\,\mathrm{s}_{13}\,\mathrm{s}_{23}\,e^{\mathrm{i}\delta} & -\mathrm{c}_{13}\,\mathrm{c}_{23} - \mathrm{s}_{12}\,\mathrm{s}_{13}\,\mathrm{s}_{23}\,e^{\mathrm{i}\delta} & \mathrm{c}_{13}\,\mathrm{s}_{23} \\ -\mathrm{s}_{12}\,\mathrm{s}_{23} - \mathrm{c}_{12}\,\mathrm{c}_{23}\,\mathrm{s}_{13}\,e^{\mathrm{i}\delta} & -\mathrm{c}_{12}\,\mathrm{s}_{23} - \mathrm{c}_{23}\,\mathrm{s}_{12}\,\mathrm{s}_{13}\,e^{\mathrm{i}\delta} & \mathrm{c}_{13}\,\mathrm{c}_{23} \end{pmatrix}, \tag{2.30}$$

where $\mathrm{c}_{ij} = \cos(\theta_{ij})$, $\mathrm{s}_{ij} = \sin(\theta_{ij})$ and $i\,, j$ denote common generation indices.

Experimentally it holds $\mathrm{s}_{13} \ll \mathrm{s}_{23} \ll \mathrm{s}_{12} \ll 1$ [32], which motivates the Wolfenstein expansion [40], that features the three mixing parameters $\lambda$, $A$, $\rho$ and one source of $CP$ violation $\eta$,

$$\begin{gathered} \mathrm{s}_{12} \equiv \lambda = \frac{|V_{us}|}{\sqrt{|V_{ud}|^2 + |V_{us}|^2}}\,, \quad \mathrm{s}_{23} \equiv A\,\lambda^2 = \frac{|V_{cb}|}{\sqrt{|V_{ud}|^2 + |V_{us}|^2}}\,, \\ \mathrm{s}_{13} e^{\mathrm{i}\delta} \equiv A\,\lambda^3\,(\rho + \mathrm{i}\eta) = V_{ub}^*\,. \end{gathered} \tag{2.31}$$

For the last two CKM parameters an alternative, phase convention-independent convention exists in the literature given by [32, 41]

$$\rho + \mathrm{i}\eta = \frac{V_{ud}^*}{V_{us}\,V_{cb}^*} = \left(1 + \frac{1}{2}\lambda^2\right)(\bar{\rho} + \mathrm{i}\bar{\eta}) + \mathcal{O}\left(\lambda^4\right). \tag{2.32}$$

To highlight the hierarchical structure of the CKM matrix, we exploit its unitarity and expand in powers of the small parameter $\lambda = \mathrm{s}_{12} \simeq 0.2$. This yields

$$V_{\text{CKM}}^{(3)} = \begin{pmatrix} 1 - \frac{1}{2}\lambda^2 & \lambda & A\,\lambda^3\,(\rho - \mathrm{i}\,\eta) \\ -\lambda & 1 - \frac{1}{2}\lambda^2 & A\,\lambda^2 \\ A\,\lambda^3\,[1 - (\rho + \mathrm{i}\,\eta)] & -A\,\lambda^2 & 1 \end{pmatrix} + \mathcal{O}\left(\lambda^4\right), \tag{2.33}$$

given in the *traditional* way, where the superscript indicates the considered order in the expansion. Then again, we can express the matrix in terms of $\bar{\kappa} \equiv \bar{\rho} + \mathrm{i}\,\bar{\eta}$, written up to higher orders as

$$V_{\text{CKM}}^{(5)} = \begin{pmatrix} 1 - \frac{1}{2}\lambda^2 - \frac{1}{8}\lambda^4 & \lambda & A\,\lambda^3\,\bar{\kappa}^* \\ -\lambda + \frac{1}{2}\,A^2\lambda^5\,(1 - 2\,\bar{\kappa}) & 1 - \frac{1}{2}\lambda^2 - \frac{1}{8}\lambda^4\left(1 + 4\,A^2\right) & A\,\lambda^2 \\ A\,\lambda^3\,(1 - \bar{\kappa}) & -A\,\lambda^2 + \frac{1}{2}A\lambda^4\,(1 - 2\,\bar{\kappa}) & 1 - \frac{1}{2}A^2\lambda^4 \end{pmatrix} + \mathcal{O}\left(\lambda^6\right). \tag{2.34}$$

The latest determined values of the Wolfenstein parameters obtained from a global fit read [32]

$$\begin{aligned} \lambda_{\text{CKM}} \equiv \lambda &= 0.22650 \pm 0.00048\,, & A &= 0.790 \pm 0.017\,, \\ \bar{\rho} &= 0.141 \pm 0.017\,, & \bar{\eta} &= 0.357 \pm 0.011\,. \end{aligned} \tag{2.35}$$

For details on the numerical input employed in our analyses see App. B, in particular Tab. B.1.

In both approximations, Eqs. (2.33) and (2.34), we readily see the dominantly diagonal structure

of the CKM matrix. Transitions of quarks of different generation and charge (flavour), referred to as flavour-changing charged currents (FCCCs), are therefore suppressed. Recent works regarding a possible substructure of the CKM matrix beyond the Wolfenstein parametrisation and novel CKM relations can be found in Refs. [42, 43].

Decays of particles, for instance $D^+ \to \pi^+\mu^+\mu^-$, can be classified in terms of powers of $\lambda_{\text{CKM}}$ that enter the decay amplitude $\mathcal{A}$. Schematically, we write

$$\mathcal{A} \propto \begin{cases} \lambda^0_{\text{CKM}}: & \text{Cabibbo-favoured (CF)}\,, \\ \lambda^1_{\text{CKM}}: & \text{singly Cabibbo-suppressed (SCS)}\,, \\ \lambda^2_{\text{CKM}}: & \text{doubly Cabibbo-suppressed (DCS)}\,, \end{cases} \tag{2.36}$$

that indicates the suppression of the amplitude in terms of the Wolfenstein parameter. The unitarity of the CKM matrix,

$$\sum_k V_{ik}\, V^*_{jk} = \delta_{ij}\,, \quad \sum_i V_{ik}\, V^*_{ij} = \delta_{kj}\,, \tag{2.37}$$

gives rise to the following useful relation

$$\lambda_d + \lambda_s + \lambda_b = 0\,, \tag{2.38}$$

with fixed $\lambda_q = V_{uq}V^*_{cq}$. Analogously, one can construct

$$\lambda_u + \lambda_c + \lambda_t = 0\,, \tag{2.39}$$

where in this case $\lambda_{q'} = V_{q's(d)}V^*_{q'b}$. To illustrate the GIM mechanism in loop processes, we consider the FCNC $b\to s$ (and $b\to d$) transitions where up-type quarks enter in the loop, *cf.* Fig. 2.2. The generic structure is given by

$$P = \lambda_u\, f_u + \lambda_c\, f_c + \lambda_t\, f_t = \lambda_c\,(f_c - f_u) + \lambda_t\,(f_t - f_u)\,, \tag{2.40}$$

where $f_q \equiv f(m_q, M_W) \sim 1/(4\pi)^2\, m_q^2/m_W^2$ denotes a loop function [44]. We observe that the GIM mechanism not only forbids tree-level FCNCs, but additionally suppresses FCNCs at loop level for observables where only light quark masses appear. Moreover, we find that for degenerate masses $m_u = m_c = m_t$ penguin contributions in Eq. (2.40) would vanish due to the unitarity of the CKM matrix. For different masses, a GIM-suppression factor $f_c - f_u \propto (m_c^2 - m_u^2)/m_W^2 \approx \mathcal{O}\left(10^{-4}\right)$ arises if only $c$- and $u$-quark contributions are relevant. For instance, a natural suppression of certain observables in the $K$-meson (kaon) system is realised to the desired level. Conversely, the GIM suppression fails whenever contributions of the top quark dominate in the loops due to $m_t > m_W \gg m_{u,c}$. In FCNC $c\to u$ transitions, the GIM mechanism implies an even stronger suppression as light down-type quarks propagate in the loop.

## 2.5 Symmetries in the standard model

The SM exhibits accidental global symmetries that arise only as a consequence of imposing renormalisability and gauge invariance. These symmetries can be either exact or approximate in the SM, and are quite useful for constraining BSM physics due to typically tight experimental constraints on a possible violation by NP. For instance, baryon-number conservation is an exact

accidental symmetry in the SM. Conversely, in BSM scenarios baryon-number violating operators can be present, though subject to stringent constraints from proton decay. Beyond that, other approximate symmetries can be realised in gauge theories. While accidental symmetries persist independent of parameter values of the theory, the emergence of approximate symmetries is only due to the smallness of specific parameters, and entails an exact global symmetry when set to zero.

### Symmetries in the flavour sector

In the SM Lagrangian, we observe the large accidental flavour symmetry

$$\mathcal{G}_F = \left[\mathrm{U}(3)_Q \times \mathrm{U}(3)_U \times \mathrm{U}(3)_D\right] \times \left[\mathrm{U}(3)_L \times \mathrm{U}(3)_E\right] . \tag{2.41}$$

It is broken down by Yukawa interactions into

$$\mathcal{G}_F \to \mathrm{U}(1)_B \times \mathrm{U}(1)_{L_e} \times \mathrm{U}(1)_{L_\mu} \times \mathrm{U}(1)_{L_\tau} , \tag{2.42}$$

which represents the conservation of baryon number $B$ and individual lepton number $L$ of each generation in the SM. In particular, we have $\mathrm{U}(3)_L \times \mathrm{U}(3)_E \to \mathrm{U}(1)^3$ that infers 15 broken generators for the lepton Yukawa. As the Yukawa matrices are in general parametrised by a $3 \times 3$ complex matrix that features 18 (free) parameters, we are left with $18 - 15 = 3$ physical parameters in this sector, whereas we count $36 - 26 = 10$ parameters in the quark sector.

In total, the SM can be described by 18 physical parameters, which we summarise given our previous review of the SM flavour structure. We have three couplings $g_1$, $g_2$ and $g_3$ embedded in the kinetic Lagrangian given in Eq. (2.5), and further the vev $v_h$ and the quartic coupling $\lambda$ in the Higgs Lagrangian, see Eq. (2.10). The 13 remaining parameters are given by three charged fermion masses, six quark masses as well as three mixing angles plus one physical phase all comprised in the Yukawa sector in Eq. (2.19). The hierarchies between the various quark and charged lepton masses shown in Fig. 2.1, together with the different structures observed in the two mixing matrices are commonly referred to as the SM flavour puzzle. For a summary of different ideas developed to address the puzzle see, *e.g.*, Ref. [34].

### The $\mathrm{SU}(3)_F$ symmetry

An approximate global symmetry of the SM is the SU(2) isospin symmetry rotating up and down quarks, which is broken due to quark masses for one thing. The isospin violation can be parametrised by the ratio $(m_u - m_d)/\Lambda_{\mathrm{QCD}}$, where $\Lambda_{\mathrm{QCD}} \approx \mathcal{O}(0.1)$ GeV [32] denotes the QCD confinement scale. Additional breaking is induced by the fine-structure constant $\alpha_e$ since the $u$ and $d$ quarks have different electric charges $Q_e$. Moreover, promoting the strange quark to this picture the $\mathrm{SU}(3)_F$ flavour symmetry is realised assuming equal masses of the $u$, $d$, and $s$ quarks. Due to the apparent larger mass splitting between the strange and the lighter two quarks, this symmetry is even more approximate. In fact, there are three SU(2) subgroups embedded in the $\mathrm{SU}(3)_F$. We identify the familiar isospin ($u \leftrightarrow d$), as well as $V$-spin ($u \leftrightarrow s$) and $U$-spin ($d \leftrightarrow s$), where the latter two, however, suffer from breaking of the order $m_s/\Lambda_{\mathrm{QCD}}$ similar to $\mathrm{SU}(3)_F$ itself [25]. In Sec. 7.3, we explore the $U$-spin and isospin breaking patterns of $\mathrm{U}(1)'$ extensions in hadronic charm decays.

*Chapter*

# 3

# Tools and directions beyond the standard model

The absence of NP particles or signals thereof close to the electroweak scale at LHC searches so far suggests a wide scale-separation of electroweak and BSM physics. To establish a theoretical framework that describes both low and high-energy physics, one has to keep in mind that the dynamics at low energies are independent of the details of the high-energy dynamics, supported by the decoupling theorem [45]. Physical processes are described in perturbation theory employing a convergent expansion of (small) theory parameters. However, this necessitates a separation of (electro)weak and QCD interactions, where only the former can be handled perturbatively. This puts forward effective field theories (EFTs) which are important tools to portray a model-independent view on physical processes at certain energy scales. These effective theories are constructed as a simplified version of an underlying theory, where processes are described considering only relevant degrees of freedom. The application of such tools allows us to parametrise BSM physics and compute predictions that can be tested by experiments.

In this chapter, we introduce the main tools of theoretical particle physics and discuss how they can be employed to test the SM while also providing predictions of BSM physics. We start by reviewing the concept of renormalisation and study the running of couplings in the SM in Sec. 3.1. Moving on, Sec. 3.2 deals with the concept of EFTs, followed by a brief overview of the SMEFT in Sec. 3.3. Afterwards, we discuss flavour anomalies present in rare $B$-decays in Sec. 3.4.

## 3.1 Renormalisation and running of couplings

In particle physics, predictions for observables are computed in perturbation theory by expanding them in powers of small parameters, *i.e.* coupling constants. While tree-level contributions serve as a first approximation, more precise results are obtained by including higher-order corrections in which loop contributions of Feynman diagrams need to be considered. However, those loop diagrams often yield ultraviolet (UV) divergences evaluating momentum integrals at high energies, which are then also preserved in Green's functions and decay amplitudes. The concept of renormalisation removes these unphysical infinities and consequently allows for the computation of finite predictions for observables as functions of *renormalised* parameters of the theory, such as coupling constants and masses that can be compared to those measured by experiments. To make the divergences explicit in calculations and to renormalise all parameters of the Lagrangian at hand, a *regularisation scheme* is utilised. As physical predictions do not depend on the chosen regulator and renormalisation condition, all explicit dependencies need to cancel when computing observables. This is encoded in the renormalisation group (RG) which is a convenient tool to improve perturbation theory

results.

Theories, where all UV divergences can be cancelled by a finite number of so-called *counterterms* to all orders in perturbation theory are called *renormalisable theories*. Conversely, theories that require an infinite number of such counterterms to remove all the divergences are called *non-renormalisable* theories. Then, generalising to individual interactions we describe operators with coupling constants of mass dimension $\Delta = 0$ as marginal, while dimensions $\Delta > 0$ and $\Delta < 0$ are termed relevant and irrelevant, respectively. That being said, non-renormalisable theories are still very predictive at low energies, where only a certain number of non-renormalisable interactions are important and can be fixed by a finite number of measurements. This puts forward the construction of *effective theories*, where the relevant degrees of freedom of a certain process are isolated. Such an effective description has only a limited range of applicability, *i.e.* the energy scale of the process, and is generally non-renormalisable. Yet, it is more predictive in that range than the corresponding overarching renormalisable theory. For instance, the effective Fermi theory of weak decays is very predictive in the low-energy regime. Alas, perturbation theory breaks down at energies $1/\sqrt{G_\mathrm{F}} \sim 300$ GeV and above, where $G_\mathrm{F}$ denotes the Fermi constant. From the vast literature concerning renormalisation, we consult Refs. [24, 26, 46] in this section.

To get an idea of how the procedure of renormalisation is applied, we consider the example of QED, where we focus on the simplest version of the theory involving a single charged fermion, *i.e.* electrons and positrons. The bare QED Lagrangian reads [1] [24]

$$\mathcal{L}_\mathrm{QED} = \bar{\psi}_0 \left(\mathrm{i}\partial\!\!\!/ - m_0\right) \psi_0 - \frac{1}{4} F_{0\mu\nu} F_0^{\mu\nu} - e_0 \, \bar{\psi}_0 \, A\!\!\!/_0 \, \psi_0 \,, \tag{3.1}$$

where $F_0^{\mu\nu} = \partial^\mu A_0^\nu - \partial^\nu A_0^\mu$ is the bare field strength tensor, while $m_0$ and $e_0$ denote the bare mass and electric charge of the electron, respectively. The subscript '0' is used to distinguish the *bare* (unrenormalised) quantities from the corresponding *physical* ones, *i.e.* the observable mass $m_e$ and electric charge $e$ of the electron. We define the renormalised quantities (without the subscript '0') by

$$A^\mu = \frac{1}{\sqrt{Z_A}} A_0^\mu \,, \quad \psi = \frac{1}{\sqrt{Z_\psi}} \psi_0 \,, \quad m_e = \frac{1}{Z_m} \, m_0 \,, \quad e = \frac{1}{Z_e} \, \mu^{(d-4)/2} \, e_0 \,. \tag{3.2}$$

Here, the renormalisation scale $\mu$ enters employing the dimensional regularisation scheme [47, 48], where the dimensionality of spacetime is analytically continued from 4 to $d < 4$. This ensures that the renormalised charge $e$ is a dimensionless parameter. The $Z_i$ are referred to as renormalisation constants and the renormalised fields are chosen such that their two-point functions (*i.e.* renormalised propagators) have finite residue at $p^2 = m_e^2$. Expressed in terms of renormalised fields and parameters, the QED Lagrangian can be written as

$$\begin{aligned}
\mathcal{L}_\mathrm{QED} &= Z_\psi \, \bar{\psi} \, \mathrm{i} \, \partial\!\!\!/ \, \psi - Z_m \, Z_\psi \, m_e \, \bar{\psi}\psi - \frac{Z_A}{4} F_{\mu\nu} F^{\mu\nu} - \mu^{(4-d)/2} \, Z_e \, Z_\psi \, \sqrt{Z_A} \, e \, \bar{\psi} \, A\!\!\!/ \, \psi \\
&= \bar{\psi} \left(\mathrm{i}\partial\!\!\!/ - m_e\right) \psi - \frac{1}{4} F_{\mu\nu} F^{\mu\nu} - \mu^{(4-d)/2} \, e \, \bar{\psi} \, A\!\!\!/ \, \psi \\
&\quad + \bar{\psi} \left[(Z_\psi - 1) \, \mathrm{i}\partial\!\!\!/ - (Z_\psi \, Z_m - 1) \, m_e\right] \psi - \frac{Z_A}{4} F_{\mu\nu} F^{\mu\nu} - \mu^{(4-d)/2} \, (Z_e \, Z_\psi \, \sqrt{Z_A} - 1) \, \bar{\psi} \, A\!\!\!/ \, \psi \,.
\end{aligned} \tag{3.3}$$

The first line of Eq. (3.3) exhibits the same structure as the original QED Lagrangian in Eq. (3.1), and therefore gives rise to the usual QED Feynman rules. Without the additional terms in second line one would still obtain UV divergences when computing the Feynman graphs. However, these

[1] For simplicity we omit gauge-fixing terms.

divergences are cancelled by counterterms $\sim Z_i$, which themselves generate additional Feynman rules. Then, finite scattering amplitudes are obtained in renormalised perturbation theory using the renormalised Lagrangian. The renormalisation constants are fixed by choosing a regularisation scheme. In dimensional regularisation, logarithmically divergent integrals are rendered UV finite if evaluated in $d = 4 - \varepsilon < 4$ spacetime dimensions, where $\varepsilon$ is an infinitesimal, positive parameter. While UV singularities appear as $1/\varepsilon^n$ pole terms in $d = 4$ dimensions, they cancel when adding the counterterms to the original Feynman diagrams, and we can take the limit $\varepsilon \to 0$ in the final result. This way, the $Z_i$ can be computed at any given order in the coupling constant, requiring that all divergences cancel at every order. To compute the counterterms it is convenient to employ the minimal subtraction (MS) scheme, *i.e.* the $\overline{\text{MS}}$ scheme [48, 49], where only divergent parts are absorbed and the rescaling $\mu^2 = \mu^2\, e^{\gamma_e}/(4\pi)$ is applied to simplify results. Here, $\gamma_e = 0.5772\ldots$ denotes the Euler-Mascheroni constant. In the $\overline{\text{MS}}$ scheme, the renormalisation constants have the structure

$$Z_i = 1 + \frac{z_1}{\varepsilon}\,\frac{e^2}{(4\pi)^2} + \left(\frac{z_{22}}{\varepsilon^2} + \frac{z_{21}}{\varepsilon}\right)\frac{e^4}{(4\pi)^4} + \ldots\,, \tag{3.4}$$

where the counterterms in $Z_i$ appear at $\mathcal{O}\left(e^2\right)$ in perturbation theory and have a perturbative expansion in powers of the renormalised coupling $e$. Next, we consider the next-to-leading order (NLO) contributions in QED to fix the renormalisation constants up to $\mathcal{O}\left(e^2\right)$. For instance, the photon field renormalisation constant $Z_A$ is computed schematically by imposing

finite = 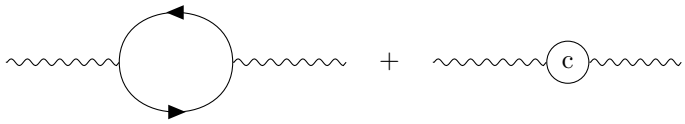 +  , (3.5)



where the first diagram corresponds to the photon propagator correction via a vacuum polarisation loop, and the second diagram is the counterterm $-1/4\,(Z_A - 1)\,F_{\mu\nu}\,F^{\mu\nu}$. Then, Eq. (3.5) is satisfied for $\varepsilon \to 0$ by [24]

$$Z_A = 1 - \frac{8}{3}\,\frac{e^2}{(4\pi)^2}\,\frac{1}{\varepsilon} + \mathcal{O}\left(e^4\right). \tag{3.6}$$

In a similar way, the constants $Z_\psi$ and $Z_m$ are extracted from

finite = 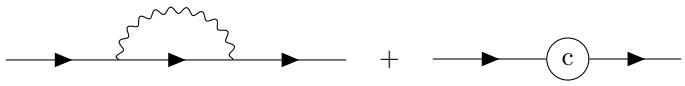 +  , (3.7)



where the first diagram denotes the electron self-energy and the second one illustrates the counterterm contributions $\bar{\psi}\left[(Z_\psi - 1)\,\mathrm{i}\,\partial\!\!\!/ - (Z_\psi\, Z_m - 1)\,m_e\right]\psi$. One derives the expressions

$$Z_\psi = 1 - 2\,\frac{e^2}{(4\pi)^2}\,\frac{1}{\varepsilon} + \mathcal{O}\left(e^4\right), \quad Z_m = 1 - 6\,\frac{e^2}{(4\pi)^2}\,\frac{1}{\varepsilon} + \mathcal{O}\left(e^4\right). \tag{3.8}$$

The remaining constant $Z_e$ is fixed by considering vertex corrections,

finite = 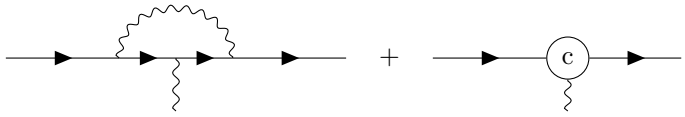 +  , (3.9)

which yields

$$Z_e = 1 + \frac{4}{3}\,\frac{e^2}{(4\pi)^2}\,\frac{1}{\varepsilon} + \mathcal{O}\left(e^4\right). \tag{3.10}$$

With these results at hand, we can express the bare coupling $e_0$ as

$$e_0 = \mu^{\varepsilon/2}\, e\, Z_e = \mu^{\varepsilon/2}\, e\, \left[1 + \frac{4}{3}\,\frac{e^2}{(4\pi)^2}\,\frac{1}{\varepsilon}\right]. \tag{3.11}$$

As the $\mu$-dependence appears only in the renormalised but not in bare Lagrangian, we must have

$$0 = \frac{\mathrm{d}e_0}{\mathrm{d}\ln(\mu)} = \mu^{\varepsilon/2}\, e\, Z_e \left[\frac{\varepsilon}{2} + \frac{1}{e}\frac{\mathrm{d}e}{\mathrm{d}\ln(\mu)} + \frac{1}{Z_e}\frac{\mathrm{d}Z_e}{\mathrm{d}\ln(\mu)}\right]. \tag{3.12}$$

This way, we obtain a differential equation called renormalisation group equation (RGE) that encodes the scale dependence of the renormalised coupling $e$. To this end, we define the $\beta$-function

$$\beta(e) \equiv \frac{\mathrm{d}e}{\mathrm{d}\ln(\mu)} = -\frac{\varepsilon}{2}\, e - e\,\frac{1}{Z_e}\,\frac{\mathrm{d}Z_e}{\mathrm{d}\ln(\mu)} = -\frac{\varepsilon}{2}\, e + \frac{e^3}{12\pi^2} + \mathcal{O}\left(e^5\right), \tag{3.13}$$

which yields a finite result for $\varepsilon \to 0$. In the last step we have inserted $1/Z_e \approx 1 - e^2/(12\pi^2\,\varepsilon)$ keeping terms to appropriate order. While the renormalisation scale can be set arbitrarily, one typically chooses $\mu \simeq s$, where $s$ denotes the centre of mass energy of the process considered, to guarantee a quick convergence of the series. The $\beta$-function is often expressed as a function of

$$\alpha_e = \frac{e^2}{4\pi}, \tag{3.14}$$

and $\beta(\alpha_e) \equiv \mathrm{d}\alpha_e/\mathrm{d}\ln(\mu)$. Then, the RGE in Eq. (3.13) can be conveniently rewritten as

$$\beta(\alpha_e) = \frac{\mathrm{d}\alpha_e}{\mathrm{d}\ln(\mu)} = -2\,\alpha_e \left(\frac{\varepsilon}{2} + \sum_{k=0}^{\infty} \beta_k^{\mathrm{QED}} \left(\frac{\alpha_e}{4\pi}\right)^{k+1}\right). \tag{3.15}$$

Solving Eq. (3.15) for $\varepsilon \to 0$ yields at leading order (LO)

$$\alpha_e(\mu) = \frac{\alpha_e(\mu_0)}{1 + \frac{\beta_0^{\mathrm{QED}}}{4\pi}\alpha_e(\mu_0)\,\ln\left(\frac{\mu^2}{\mu_0^2}\right)}, \tag{3.16}$$

with $\beta_0^{\mathrm{QED}} = -4/3$. The evolution of $\alpha_e(\mu)$ is fixed by a measurement of $\alpha_e(\mu_0)$ at a certain energy scale $\mu_0$. Since $\alpha_e$ rises with increasing energy due to $\beta_0^{\mathrm{QED}} < 0$, a divergence of the theory is entailed at a large scale $\Lambda_{\mathrm{QED}}$, referred to as a *Landau pole*. Utilising the measurement of $\alpha_e(m_e) = 1/137$ [32], we can identify this scale as $\mu_0 = \Lambda_{\mathrm{QED}} \approx 10^{286}$ eV. Hence, perturbation theory in QED breaks down at short distances.

### 3.1.1 Renormalisation group evolution in the standard model

In the following, we review the RG evolution of the SM in the unbroken phase. Here, we use the rescaled gauge couplings

$$\alpha_X = \frac{X^2}{(4\,\pi)^2} \quad \text{with} \quad X = \{g_1,\, g_2,\, g_3\}\,. \tag{3.17}$$

To avoid confusion regarding the commonly used gauge coupling of the strong interaction $\alpha_s$ which is shy of a factor of $4\pi$ compared to the definition above, we distinguish between the two notations as

$$\alpha_s = \frac{g_s^2}{4\pi}\,, \quad \alpha_3 = \frac{g_3^2}{(4\pi)^2}\,. \tag{3.18}$$

The Yukawa coupling of the $t$ quark $\alpha_t = y_t^2/(4\pi)^2$ and the Higgs quartic $\alpha_\lambda = \lambda/(4\pi)^2$ are also taken into account, see notations given in App. A.4. Due to their subleading $(y_b, y_\tau)$ or negligible effects we do not consider the remaining Yukawa couplings of the SM in this discussion. In Fig. 3.1,

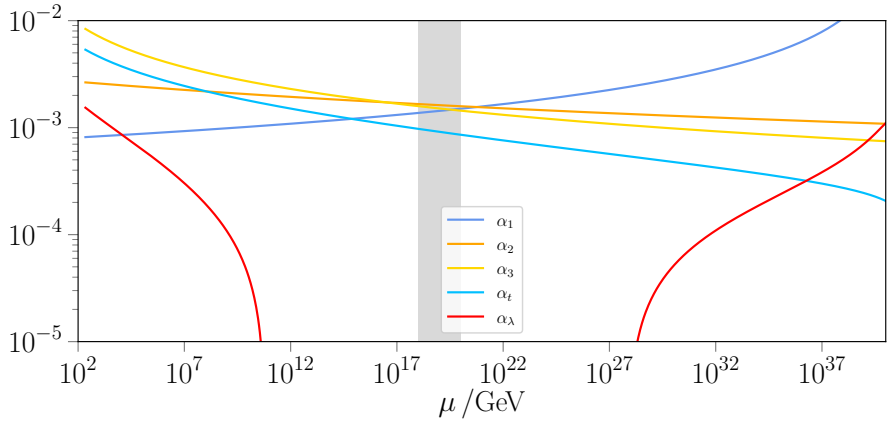


**Figure 3.1:** RG evolution of couplings in the SM. Here, $\alpha_{1-3}$ are the gauge couplings, while the $t$-quark Yukawa and Higgs quartic couplings are denoted by $\alpha_t$ and $\alpha_\lambda$, respectively. The grey area indicates the Planck scale, $\mu_{\rm Pl} \sim 10^{19}$ GeV, where quantum gravity effects are expected to become relevant. The RGEs are solved at two-loop accuracy for all couplings [21, 50].

we display the RG evolution of the SM couplings within two-loop accuracy. While not directly shown in this plot, $\alpha_\lambda$ acquires negative values at $\mu \sim 10^{10}$ GeV, which has striking implications as the vacuum configuration of the Higgs potential becomes metastable given the current Higgs and $t$-quark mass measurements [28, 51]. This is explained by the fact that not all terms in the $\beta$-function $\beta_\lambda$ are proportional to $\alpha_\lambda$ itself, which is a feature only attributed to the Higgs quartic in the SM [28].

In the following, we study the behaviour of the gauge couplings. The $\mathrm{U}(1)_Y$ gauge coupling $\alpha_1$ runs into a Landau pole in the UV regime due to its abelian nature, similar to the QED coupling $\alpha_e$.

The energy scale of this divergence, $\mu_{\rm LP}$, can be estimated by considering the LO RG running

$$\beta_i \equiv \frac{\mathrm{d}\alpha_i}{\mathrm{d}\ln(\mu)} = B_i\,\alpha_i^2\,, \tag{3.19}$$

where $B_i$ denotes the one-loop coefficient, *e.g.* $B_1 = 41/3 > 0$. Solving Eq. (3.19), we detect a Landau pole at high energies for a positive coefficient $B_i$. Integrating Eq. (3.19) and solving for $1/\alpha_i(\mu_{\rm LP}) = 0$ yields

$$\ln\left(\frac{\mu_{\rm LP}}{\mu_0}\right) = \frac{1}{B_i\,\alpha_i(\mu_0)}\,. \tag{3.20}$$

From electroweak measurements we fix $\alpha_1(\mu_0 = m_Z) = 8.1 \cdot 10^{-4}$ [32], which reveals a Landau pole at $\mu_{\rm LP} \approx 10^{41}$ GeV way beyond the Planck scale of $\mu_{\rm Pl} \sim 10^{19}$ GeV. Conversely, the coupling $\alpha_3$ features a divergence in the infrared (IR) regime $\mu \to 0$. The location of this pole $\Lambda_{\rm QCD} \approx \mathcal{O}\,(0.1)$ GeV is called the confinement scale, which depends on the number of active quarks $n_f$ at the energy scale $\mu$. The one-loop coefficient is given by $B_3 = -2\,\beta_0^{\rm QCD}$ with [2]

$$\beta_0^{\rm QCD}(n_f) = 11 - \frac{2}{3}\,n_f\,. \tag{3.21}$$

In the SM, we have $n_f = 6$ for $\mu > m_t$, and hence $B_3 = -14 < 0$ which dictates the opposite behaviour compared to $\alpha_1$, where $B_1 > 0$. The strong coupling asymptotically approaches zero at highest energies which is called *asymptotic freedom* [52].

While in the SM the $\mathrm{U}(1)_Y$ Landau pole arises at high energies beyond the validity of our theory, the divergence can be moved towards significantly lower energies (below the Planck scale) when additional BSM interactions are present in our theory. This is the case in $\mathrm{U}(1)'$ extensions which we further outline in Sec. 5.5.

## 3.2 Model-independent description with effective field theories

Describing a physical process or system often involves widely separated energy scales. To successfully distinguish and study the low-energy (long-distance) and high-energy (short-distance) contributions independently, we need to identify those parameters which are very large (small) compared to the relevant energy scale of the underlying process and put them to infinity (zero). A theoretical tool that follows these basic principles and provides an approximate low-energy description is effective field theories (EFTs), where *low* refers to energies $E$ (significantly) smaller than an associated large, fundamental energy scale $\Lambda$. In this framework, only the relevant degrees of freedom are taken into account, *i.e.* those states with $m \ll \Lambda$. Conversely, heavier excitations $M \gg \Lambda$ are integrated out from the action, but remain encoded in the couplings of the formulated low-energy Lagrangian. The approximate theory then involves an expansion in powers of $E/\Lambda$ [53]. The effective Lagrangian is derived using the operator product expansion (OPE). It allows us to replace products of operators evaluated at different points by a sum over composite (local) operators in

[2] $B_3 = -2\,\beta_0^{\rm QCD}$ holds in the convention of rescaled gauge couplings $\alpha_3 = (g_3)^2/(4\pi)^2$ . See App. A.4 for details.

the limit of approaching points, *i.e.*

$$\lim_{x\to y} A(x)\,B(y) = \sum_n \mathcal{C}_n(x-y)\,O_n(x)\,, \tag{3.22}$$

for any operators $A$ and $B$ [24]. Most eminently, the coefficients $\mathcal{C}_n$ are independent of the external states, thus the expansion holds at the operator level rendering the OPE a powerful method applied in effective theories. The coefficients can be computed to a given order in perturbation theory and then be utilised for any process. In perturbative EFTs only a finite number of operators needs to be taken into account to acquire a given precision.

In what follows, we outline the main concepts of EFTs utilising the Fermi theory [54] as an instructive example [55, 56]. Further in-depth literature on EFTs can be found in Refs. [44, 53, 55–60]. Let us revisit the only flavour-changing interactions in the SM present in the charged-current Lagrangians in Eqs. (2.24) and (2.26). After *integrating out* the heavy fields following the OPE, we obtain an effective theory that describes the weak interaction in the SM at energies $E \ll M_W$. By going from the full to the effective theory the $W$ boson is removed as an explicit, dynamical degree of freedom. This yields local four-fermion operators as illustrated in Fig. 3.2.

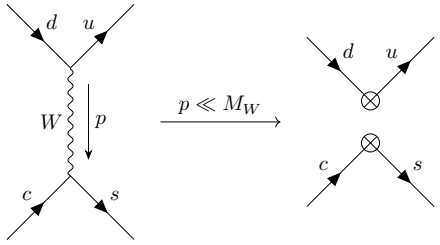


**Figure 3.2:** Example of an effective four-fermion interaction obtained by integrating out the $W$ boson in the SM. The crossed dots in the right-hand side diagram indicate a local four-fermion operator in the effective theory.

The effective Lagrangian reads

$$\mathcal{L}_{\text{eff}} = -\frac{4\,G_{\text{F}}}{\sqrt{2}}\,\mathcal{J}^-_\mu\,\mathcal{J}^{+\mu} + \mathcal{O}\left(\frac{p^2}{M_W^2}\right), \tag{3.23}$$

where $p$ denotes the momentum carried by the intermediate $W$ boson and $G_{\text{F}} \equiv \sqrt{2}\,g_2/(8\,M_W^2)$ is the Fermi constant. The charged currents are given by

$$\mathcal{J}^+_\mu = V_{ij}\,\overline{u}_{L,i}\gamma_\mu\,d_{L,j} + \overline{\nu}_{L,i}\,\gamma_\mu\,e_{L,i}\,, \quad \mathcal{J}^-_\mu = \left(\mathcal{J}^+_\mu\right)^\dagger\,, \tag{3.24}$$

where a summation over the flavour indices $i$, $j$ is understood. While the truncation of the operator series in the OPE yields a systematic approximation for low energy processes, the series is equivalent to the full theory when considering all orders in $1/M_W^2$. One observes that the coupling constant $G_{\text{F}}$ associated with the dimension-six operator $\mathcal{J}^+\mathcal{J}^-$ is suppressed by two powers of the fundamental scale, $M_W^2$, a characteristic that emerges when integrating out heavy fields from the fundamental theory at low energies. The effects of subleading terms in Eq. (3.23) are tiny due to their suppression by powers of $p^2/m_W^2$ and can be neglected for (almost) all practical purposes. However, beyond tree-level approximation the contributions from strong interactions are not accounted for in the effective description in Eq. (3.23). These challenges are met by performing a general *matching* procedure, which we outline in the following.

We write down the OPE for the effective Lagrangian describing weak decays with the generic structure

$$\mathcal{L}_{\text{eff}} = -\frac{4\,G_{\text{F}}}{\sqrt{2}} \sum_i \mathcal{C}_i(\mu)\, O_i(\mu)\,, \tag{3.25}$$

where the sum includes all possible gauge-invariant operators of a given dimension allowed by symmetries. While the local operators $O_i$ encode the dynamics at low energies, the high-energy physics involving heavy masses are parametrised by the process-independent Wilson coefficients $\mathcal{C}_i$. Hence, non-perturbative and perturbative QCD effects are separated. The values of $\mathcal{C}_i$ are extracted by matching the amplitude of the effective theory and the full theory.

Let us consider the quark transition $c \to s\,u\overline{d}$ depicted in Fig. 3.2. Neglecting strong interactions, the transition is described by the Fermi theory in Eq. (3.23). Taking into account QCD corrections, we obtain the generalisation

$$\mathcal{L}_{\text{eff}} = -\frac{4\,G_{\text{F}}}{\sqrt{2}}\, V_{cs}^* V_{ud}\, \left(\mathcal{C}_1\, O_1 + \mathcal{C}_2\, O_2\right)\,, \tag{3.26}$$

with operators

$$O_1 = (\overline{s}_\alpha\, \gamma_\mu\, P_L\, c_\alpha)\, (\overline{u}_\alpha\, \gamma_\mu\, P_L\, d_\alpha)\,, \quad O_2 = (\overline{s}_\alpha\, \gamma_\mu\, P_L\, c_\beta)\, (\overline{u}_\alpha\, \gamma_\mu\, P_L\, d_\beta)\,, \tag{3.27}$$

assuming an implicit summation over repeated colour indices $\alpha, \beta$. The Wilson coefficients are determined by comparing the Feynman diagrams in the EFT with those of the full theory. From tree-level matching we obtain $\mathcal{C}_1(m_W) = 1 + \mathcal{O}\left(\alpha_s\right)$ and $\mathcal{C}_2(m_W) = \mathcal{O}\left(\alpha_s\right)$. The one-loop matching results are given by

$$\mathcal{C}_1(\mu) = 1 + \frac{\alpha_s(\mu)}{4\pi}\left[\ln\left(\frac{m_W^2}{\mu^2}\right) - \frac{11}{6}\right] + \mathcal{O}\left(\alpha_s^2\right), \tag{3.28}$$

$$\mathcal{C}_2(\mu) = -3\,\frac{\alpha_s(\mu)}{4\pi}\left[\ln\left(\frac{m_W^2}{\mu^2}\right) - \frac{11}{6}\right] + \mathcal{O}\left(\alpha_s^2\right). \tag{3.29}$$

One notices that the expansion parameter is in fact not given by $\alpha_s/\pi \sim 0.1$, but instead reads $\alpha_s/\pi\, \ln(m_W^2/\mu^2) \sim 0.8$. A poor convergence of the expansion is a generic issue in perturbation theory whenever widely separated scales $\Lambda \gg \mu$ are present, and necessitates a resummation of logarithmic terms. For instance considering QCD effects, large logarithms appear that need to be resummed to all orders. This procedure is generally referred to as RG-improved perturbation theory, in which $\alpha_s\, \ln\left(\Lambda/\mu\right)$ is treated as an $\mathcal{O}\left(1\right)$ parameter, while $\alpha_s \ll 1$. By solving the RGEs, the large logarithms are resummed to all orders in the perturbative expansion. That is, in the $n$-th order of RG-improved perturbation theory the terms of the from $\alpha_s^n(\mu)\left(\alpha_s(\mu)\ln\left(\Lambda/\mu\right)\right)^k$ are summed to all order in $k$, with $k = 0, 1, \ldots, \infty$. The nomenclature commonly utilised in the literature is as follows. Resummation at LO ($n = 0$) incorporates all terms $(\alpha_s\, \ln(\Lambda/\mu))^k$ and yields an $\mathcal{O}\left(1\right)$ contribution to the Wilson coefficients. At NLO, one further considers terms with $n = 1$ of the form $\alpha_s(\alpha_s\, \ln(\Lambda/\mu))^k$, all of which count as $\mathcal{O}\left(\alpha_s\right)$.

To better understand and actually perform such resummations, we need to study the renormalisation of the operators contained in the effective Lagrangian. To this end, we check Eq. (3.25) recalling that physical observables are scale-independent, which translates into

$$0 = \frac{\mathrm{d}\left(\mathcal{C}_i(\mu) O_i(\mu)\right)}{\mathrm{d}\ln(\mu)} = \frac{\mathrm{d}\mathcal{C}_i(\mu)}{\mathrm{d}\ln(\mu)}\, O_i(\mu) + \frac{\mathrm{d}O_i(\mu)}{\mathrm{d}\ln(\mu)}\, \mathcal{C}_i(\mu)\,. \tag{3.30}$$

Similar to the renormalisation outlined in Eq. (3.2), we define the bare operators

$$O_i^0 = Z_{ij}(\mu)\, O_j(\mu)\,. \tag{3.31}$$

where an implicit summation over $j$ is understood. The bare operators are independent of the renormalisation scale $\mu$, and hence it follows that

$$0 = \frac{\mathrm{d}O_i^0}{\mathrm{d}\ln(\mu)} = \frac{\mathrm{d}Z_{ij}}{\mathrm{d}\ln(\mu)}\, O_j + \frac{\mathrm{d}O_j}{\mathrm{d}\ln(\mu)}\, Z_{ij}\,. \tag{3.32}$$

Rewriting this equation yields

$$0 = \frac{\mathrm{d}O_i}{\mathrm{d}\ln(\mu)} = \frac{1}{Z_{ki}} \frac{\mathrm{d}Z_{kj}}{\mathrm{d}\ln(\mu)}\, O_j = -\gamma_{ij}\, O_j\,, \tag{3.33}$$

where we have introduced the matrix $\gamma_{ij}(\alpha_s)$ called the anomalous dimension matrix (ADM). It describes the mixing of operators under scale variation, assuming that more than one operator is present. The ADM itself depends on the scale $\mu$ only through the running coupling $\alpha_s(\mu)$. Since by assumption the operators $O_i$ are linearly independent, we just insert the definition of the ADM in Eq. (3.30) and obtain

$$\frac{\mathrm{d}\mathcal{C}_i}{\mathrm{d}\ln(\mu)} = \gamma_{ji}\, \mathcal{C}_j = \left(\gamma^{\mathsf{T}}\right)_{ij} \mathcal{C}_j\,. \tag{3.34}$$

The ADM can be expressed by an expansion in $\alpha_s$ of the form

$$\gamma_{ij}(\alpha) = \sum_{l=0}^{\infty} \gamma_{ij}^{(l)} \left(\frac{\alpha}{4\pi}\right)^{l+1}\,. \tag{3.35}$$

Then, one determines the Wilson coefficients by solving the RGE in (3.34). In the case of a single operator, the LO contribution reads [56]

$$\mathcal{C}(\mu) = \left(\frac{\alpha_s(\Lambda)}{\alpha_s(\mu)}\right)^{\gamma^{(0)}/(2\,\beta_0^{\mathrm{QCD}})} \left(1 + \mathcal{O}\left(\alpha_s\right)\right)\,, \tag{3.36}$$

where the running of $\alpha_s$ is encoded in the corresponding $\beta$-function with the LO coefficient $\beta_0^{\mathrm{QCD}}$ defined in Eq. (3.21). If multiple Wilson coefficients $\mathcal{C}_i$ are present, the ADM is diagonalised before solving the RGEs in the new basis.

Coming back to our EFT in Eq. (3.26), the lowest-order contribution to the ADM reads [56, 57]

$$\gamma = \frac{\alpha_s}{4\pi} \begin{pmatrix} -2 & 6 \\ 6 & -2 \end{pmatrix}\,, \tag{3.37}$$

which induces mixing between the operators $O_{1,2}$ in the RG evolution due to its non-diagonal structure. Employing the change of basis

$$C_\pm = C_1 \pm C_2 \tag{3.38}$$

we find a diagonal ADM, where the lowest-order entries in Eq. (3.35) are given by the eigenvalues of the matrix in Eq. (3.37), *i.e.* $\gamma_\pm^{(0)} = -2 \pm 6$. Using these results, we can utilise the solution in

Eq. (3.36) and obtain

$$C_+(\mu) = \left[\frac{\alpha_s(m_W)}{\alpha_s(\mu)}\right]^{6/(33-2\,n_f)} , \quad C_-(\mu) = \left[\frac{\alpha_s(m_W)}{\alpha_s(\mu)}\right]^{-12/(33-2\,n_f)} . \tag{3.39}$$

## 3.3 The standard model effective field theory

Following the EFT approach outlined in Sec. 3.2, we introduce a generalisation of the SM which comprises all SM particles and their interactions applicable up to energies not exceeding the scale $\Lambda \sim \Lambda_{\rm NP}$. Assuming that the electroweak scale $\sim v_h \approx 246$ GeV and the NP scale are sufficiently separated, we can put forward an OPE consisting of dimension-five, dimension-six, and higher-dimensional operators. They are solely built out of SM fields and are invariant under the full SM gauge symmetry $\mathcal{G}_{\rm SM}$, *i.e.* Eq. (2.1). The corresponding EFT is called standard model effective field theory (SMEFT), where the degrees of freedom involving NP are integrated out and only SM parameters remain as dynamical degrees of freedom. Hence, the Wilson coefficients of the theory include only NP effects and can be conveniently used to test for BSM signatures. The SMEFT is reduced to the SM at low energies, provided that no undiscovered but weakly coupled light particles exist.

The SMEFT Lagrangian is given by

$$\mathcal{L}_{\rm SMEFT} = \mathcal{L}^{(4)}_{\rm SM} + \sum_{d=5}^{\infty} \mathcal{L}^{(d)} , \qquad \mathcal{L}^{(d)} = \sum_k \frac{1}{\Lambda^{d-4}} \mathcal{C}^{(d)}_k \, O^{(d)}_k , \tag{3.40}$$

where $\mathcal{L}^{(4)}_{\rm SM}$ is the usual renormalisable SM Lagrangian, while higher-dimensional operators are suppressed by powers of $\Lambda$. By taking into account all operators allowed by gauge symmetries, the Lagrangian in Eq. (3.40) can be renormalised order by order in $1/\Lambda$. As the RG evolution between the NP scale and the electroweak scale involves operator mixing, we stress that an observed pattern of deviations from SM expectations at low-energy scales can differ significantly from the pattern of Wilson coefficients present at energies where NP comes into play.

The dominant NP effects in SMEFT for phenomenological studies are induced by dimension-six operators suppressed by a factor of $1/\Lambda^2$. Depending on the operator considered, current LHC experiments are sensitive to $\Lambda$ within $\mathcal{O}\left(\text{1-10}^3 \text{ TeV}\right)$ assuming $\mathcal{C} \approx 1$. In total, there are 59 independent dimension-six operators assuming lepton- and baryon-number conservation which are given in the so-called *Warsaw* basis [61] [3]. Note that the fermion fields in these operators carry additional flavour indices, which strictly speaking yields 2499 (1350 $CP$-even and 1149 $CP$-odd) operators in full flavour generality assuming three generations of fermions. The corresponding Wilson coefficients $\mathcal{C}^{(6)}_k$ contain the information about NP at and above scales $\mathcal{O}(\Lambda)$. One readily acknowledges that, *e.g.*, a determination of all these Wilson coefficients from a comparison to SM expectations at low-energy scales in this model-independent approach seems unfeasible due to the vast number of free parameters. However, a classification of operators and studies of the RG

[3] Only a single operator exists at dimension-five, which is the lepton-number violating Weinberg operator [62] responsible for Majorana masses of LH neutrinos in the spontaneously broken theory. The small neutrino masses stipulated by neutrino oscillation experiments necessitate a very large scale of lepton-number violation $\Lambda_{\not L}$. Generally, one assumes the scale $\Lambda_{\not L}$ ($\Lambda_{\not B}$) to be much larger than $\Lambda$, which allows for a significant suppression of lepton-number violating (baryon-number violating) operators compared to the conserving dimension-six ones [63].

| $(\bar{L}L)(\bar{L}L)$ | | $(\bar{R}R)(\bar{R}R)$ | | $(\bar{L}L)(\bar{R}R)$ | |
|---|---|---|---|---|---|
| $\mathcal{C}_{ll}$ | $(\overline{L}\gamma_\mu L)(\overline{L}\gamma^\mu L)$ | $\mathcal{C}_{ee}$ | $(\overline{E}\gamma_\mu E)(\overline{E}\gamma^\mu E)$ | $\mathcal{C}_{le}$ | $(\overline{L}\gamma_\mu L)(\overline{E}\gamma^\mu E)$ |
| $\mathcal{C}_{qq}^{(1)}$ | $(\overline{Q}\gamma_\mu Q)(\overline{Q}\gamma^\mu Q)$ | $\mathcal{C}_{uu}$ | $(\overline{U}\gamma_\mu U)(\overline{U}\gamma^\mu U)$ | $\mathcal{C}_{lu}$ | $(\overline{L}\gamma_\mu L)(\overline{U}\gamma^\mu U)$ |
| $\mathcal{C}_{qq}^{(3)}$ | $(\overline{Q}\gamma_\mu\sigma^a Q)(\overline{Q}\gamma^\mu\sigma^a Q)$ | $\mathcal{C}_{dd}$ | $(\overline{D}\gamma_\mu D)(\overline{D}\gamma^\mu D)$ | $\mathcal{C}_{ld}$ | $(\overline{L}\gamma_\mu L)(\overline{D}\gamma^\mu D)$ |
| $\mathcal{C}_{lq}^{(1)}$ | $(\overline{L}\gamma_\mu L)(\overline{Q}\gamma^\mu Q)$ | $\mathcal{C}_{eu}$ | $(\overline{E}\gamma_\mu E)(\overline{U}\gamma^\mu U)$ | $\mathcal{C}_{qe}$ | $(\overline{Q}\gamma_\mu Q)(\overline{E}\gamma^\mu E)$ |
| $\mathcal{C}_{lq}^{(3)}$ | $(\overline{L}\gamma_\mu\sigma^a L)(\overline{Q}\gamma^\mu\sigma^a Q)$ | $\mathcal{C}_{ed}$ | $(\overline{E}\gamma_\mu E)(\overline{D}\gamma^\mu D)$ | $\mathcal{C}_{qu}^{(1)}$ | $(\overline{Q}\gamma_\mu Q)(\overline{U}\gamma^\mu U)$ |
| | | $\mathcal{C}_{ud}^{(1)}$ | $(\overline{U}\gamma_\mu U)(\overline{D}\gamma^\mu D)$ | $\mathcal{C}_{qu}^{(8)}$ | $(\overline{Q}\gamma_\mu t^b Q)(\overline{U}\gamma^\mu t^b U)$ |
| | | $\mathcal{C}_{ud}^{(8)}$ | $(\overline{U}\gamma_\mu t^b U)(\overline{D}\gamma^\mu t^b D)$ | $\mathcal{C}_{qd}^{(1)}$ | $(\overline{Q}\gamma_\mu Q)(\overline{D}\gamma^\mu D)$ |
| | | | | $\mathcal{C}_{qd}^{(8)}$ | $(\overline{Q}\gamma_\mu t^b Q)(\overline{D}\gamma^\mu t^b D)$ |

**Table 3.1:** Overview of selected dimension-six four-fermion operators and their corresponding Wilson coefficient in SMEFT imposing baryon-number conservation. In this table, we categorise the operators into classes $(\bar{L}L)(\bar{L}L)$, $(\bar{R}R)(\bar{R}R)$, and $(\bar{L}L)(\bar{R}R)$ indicating the chirality of the fermion fields involved while suppressing the flavour indices for brevity. The $\sigma^a$ are the Pauli matrices while $t^b$ denote the $\mathrm{SU}(3)_C$ generators. Five additional operators with $(\bar{L}R)(\bar{R}L)$ and $(\bar{L}R)(\bar{L}R)$ structure exist, but are not shown here [61].

effects proves useful in concrete models [26].

In Tab. 3.1, we display 20 four-fermion operators, which are categorised in terms of the chiralities of the fermion fields involved while suppressing flavour indices. Here, we guide the reader towards contributions of $\mathcal{C}_{lq}^{(1)}$, $\mathcal{C}_{lq}^{(3)}$, $\mathcal{C}_{lu}$, and $\mathcal{C}_{ld}$ featuring couplings of quarks to LH lepton fields. These kind of operators allow to expose correlations between charged leptons and neutrinos due to $\mathrm{SU}(2)_L$-invariance of the SMEFT, which is investigated in Chap. 9. For reviews and applications of the SMEFT, we refer to Refs. [26, 61, 63–68]. In particular, the complete set of dimension-six operators is provided in Ref. [61].

## 3.4 Hints of new physics in rare $B$-decays

In this section, we review flavour anomalies present in measurements of rare $B$-decays that show discernible deviations from their SM predictions. In doing so, we introduce the EFT description of the underlying $b\to s\,\ell^+\ell^-$ transition and review the key players of these anomalies.

The effective Hamiltonian for $b\to s\,\ell^+\ell^-$ transitions at the $b$-quark scale $\mu_b\approx m_b$ is given by [69]

$$\mathcal{H}_{\text{eff}}^{bs\ell\ell} = -\frac{4G_{\text{F}}}{\sqrt{2}}\frac{\alpha_e}{4\pi}V_{tb}\,V_{ts}^*\left[\mathcal{C}_7\,O_7+\mathcal{C}_7'\,O_7'+\sum_{\ell=e,\mu,\tau}\sum_{i=9,10,S,P}\left(\mathcal{C}_i^{\ell\ell}O_i^{\ell\ell}+\mathcal{C}_i^{\prime\ell\ell}O_i^{\prime\ell\ell}\right)\right], \tag{3.41}$$

with the semileptonic operators

$$\begin{aligned} O_9^{\ell\ell} &= (\bar{s}_L\gamma_\mu b_L)(\bar{\ell}\gamma^\mu\ell)\,, & O_9^{\prime\ell\ell} &= (\bar{s}_R\gamma_\mu b_R)(\bar{\ell}\gamma^\mu\ell)\,, \\ O_{10}^{\ell\ell} &= (\bar{s}_L\gamma_\mu b_L)(\bar{\ell}\,\gamma^\mu\gamma_5\ell)\,, & O_{10}^{\prime\ell\ell} &= (\bar{s}_R\gamma_\mu b_R)(\bar{\ell}\gamma^\mu\gamma_5\ell)\,, \\ O_S^{\ell\ell} &= m_b\,(\bar{s}_L\,b_R)(\bar{\ell}\,\ell)\,, & O_S^{\prime\ell\ell} &= m_b\,(\bar{s}_R\,b_L)(\bar{\ell}\,\ell)\,, \\ O_P^{\ell\ell} &= m_b\,(\bar{s}_L\,b_R)(\bar{\ell}\,\gamma_5\,\ell)\,, & O_P^{\prime\ell\ell} &= m_b\,(\bar{s}_R\,b_L)(\bar{\ell}\gamma_5\ell)\,. \end{aligned} \tag{3.42}$$

Here and in the following, we employ a notation where $\ell = e,\ \mu,\ \tau$ are chosen as placeholders for fields of a specific flavour and further used as flavour indices of the operators and Wilson coefficients. Additional lepton flavour violating contributions induced via Wilson coefficients $\mathcal{C}_i^{\ell\ell'}$ with $\ell \neq \ell'$ are not considered at this point, but may be included straightforwardly in Eq. (3.41). The contributions to dipole operators read

$$O_7 = \frac{m_b}{e}\,(\bar{s}_L\,\sigma_{\mu\nu}\,b_R)F^{\mu\nu}\,, \qquad O_7' = \frac{m_b}{e}\,(\bar{s}_R\,\sigma_{\mu\nu}\,b_L)F^{\mu\nu}\,, \tag{3.43}$$

where $F^{\mu\nu}$ denotes the electromagnetic field strength tensor. Contributions from primed operators are negligible in the SM. The dominant contribution arises with LH quark currents from electroweak penguin diagrams shown previously in the right-hand side diagram of Fig. 2.2, that yields lepton universal couplings $\mathcal{C}_9^{\rm SM}(m_b) \simeq -\mathcal{C}_{10}^{\rm SM}(m_b) \simeq 4.2$. In addition, it is $\mathcal{C}_7^{\rm SM}(m_b) = -0.3$ [70]. Due to our focus on BSM effects, we expose the different contributions as

$$\mathcal{C}_i^{\ell\ell} = \mathcal{C}_i^{\rm SM} + \mathcal{C}_{i,\ell}\,, \quad \mathcal{C}_i^{\prime\ell\ell} = \mathcal{C}_{i,\ell}'\,, \tag{3.44}$$

separating the SM contribution, $\mathcal{C}_i^{\rm SM}$, and the pure NP one, $\mathcal{C}_{i,\ell}$.

While (pseudo)scalar and primed operators are highly suppressed and negligible in the SM due to the small masses of leptons, they may become large in NP extensions. However, possible NP in scalar operators can be constrained by $B_s \to \mu^+\mu^-$ decays [71]. Tensor operators are not present in the SM and also not induced in $Z'$ models, and hence neglected in this thesis. See, *e.g.*, Ref. [72] for a comprehensive study of the weak effective theory (WET) framework of rare $B$-decays.

### 3.4.1 A brief review of the $B$-anomalies

In recent years, several deviations from SM predictions have been surfaced in measurements of observables in rare $B$-decays. In the SM, these decays are highly suppressed due to the underlying FCNC structure and therefore sensitive to NP. While these deviations represent a first hint of BSM physics, statistical fluctuations as well as underestimated experimental or theoretical systematic uncertainties cannot be ruled out at the moment. However, the huge set of experimental data already available and updated measurements with reduced uncertainties expected in the future elevate these *flavour* anomalies to be prime candidates for studies involving possible NP. The deviations are collectively referred to as the $B$-anomalies and can be categorised as follows [69]:

(i) Apparent suppression of various branching ratios of exclusive decays with underlying $b \to s\,\mu^+\mu^-$ transition, *e.g.* $B \to K\,\mu^+\mu^-$ and $B \to K^*\,\mu^+\mu^-$, where the main source of theoretical uncertainties comes from hadronic form factors.

(ii) Measurements of angular observables in $B \to K^*\mu^+\mu^-$ decays deviate from the SM expectation. Compared to the branching ratio measurements, such *optimised* observables feature

smaller form factor uncertainties, however significant hadronic uncertainties remain present.

(iii) Tests of lepton universality (LU) have been analysed, where the ratio of muon and electron modes in observables $R_K$ and $R_{K^*}$ exhibits significant deviations from the SM prediction of unity. In such ratios theoretical uncertainties are negligible, and their sensitivity is presently only limited by statistical uncertainties in experiment.

Furthermore, apparent deviations from LU, *i.e.* $\tau$-$\mu$ and $\tau$-$e$ universality, are observed in FCCCs $b\to c\,\ell\nu$ transitions [73–79], which appear at tree level in the SM. We do not consider them in this work as they are less sensitive to NP effects compared to the loop-induced neutral-current transitions. Our focus resides solely on observables of decays with an underlying FCNC $b\to s$ transition that can be modified by contributions involving a $Z'$ boson. For a detailed review on the full $B$-anomalies, see, *e.g.*, Refs. [80, 81].

In what follows, we introduce the tests of LU in $b\to s\,\ell^+\ell^-$ transitions. One of the key features of the SM is LU, which states that all three generations of leptons interact identically except for effects due to their different masses. In recent years, LU has been challenged by measurements of observables that probe couplings to muons and electrons in branching ratios

$$R_H = \frac{\displaystyle\int_{q^2_{\rm min}}^{q^2_{\rm max}} \frac{{\rm d}\mathcal{B}\,(B\to H\mu^+\mu^-)}{{\rm d}q^2}{\rm d}q^2}{\displaystyle\int_{q^2_{\rm min}}^{q^2_{\rm max}} \frac{{\rm d}\mathcal{B}\,(B\to He^+e^-)}{{\rm d}q^2}{\rm d}q^2}\,, \tag{3.45}$$

with $H = K,\, K^*,\,\ldots$ [82, 83]. Here, $q^2$ denotes the dilepton invariant mass squared, while $q^2_{\rm min}$ ($q^2_{\rm max}$) refers to the lower (upper) dilepton mass cut. These ratios provide a precise theoretical prediction where hadronic uncertainties largely cancel in the ratio utilising a factorisation of hadronic and leptonic parts of the branching ratios. Notably, experiments are able to measure these observables with reduced uncertainties [4]. Most prominently, the LHCb experiment has performed several such measurements in different $q^2$-bins with values below unity, which indicates a different treatment of BSM physics towards muons and electrons. For instance, the latest measurement [8]

$$R_{K^+}|_{[1.1,6.0]} = 0.846^{+0.042}_{-0.039}\,({\rm stat})\,^{+0.013}_{-0.012}\,({\rm syst}) \tag{3.46}$$

exhibits a $3.1\,\sigma$ deviation from the SM prediction, $R^{\rm SM} = 1 + \mathcal{O}\,(\%)$. Here, the respective $q^2$-bin in units of ${\rm GeV}^2$ is specified as a subscript, while the statistical (stat) and systematic (syst) uncertainties are stated as well. The measurement of the related $B$ to pseudoscalar ratio [9]

$$R_{K^0_{\rm S}}|_{[1.1,6.0]} = 0.66^{+0.20}_{-0.14}\,({\rm stat})\,^{+0.02}_{-0.04}\,({\rm syst})\,, \tag{3.47}$$

in the same $q^2$-region, reveals a similar reduction of the LU ratio with a smaller deviation about $1.5\,\sigma$ from the SM hypothesis. Moreover, measurements of ratios with a vector meson, $H = K^*$, in the final state have been performed, where [84]

$$R_{K^{*0}}|_{[0.045,1.1]} = 0.66^{+0.11}_{-0.07}\,({\rm stat})\,\pm 0.03\,({\rm syst})\,, \tag{3.48}$$

$$R_{K^{*0}}|_{[1.1,6.0]} = 0.69^{+0.11}_{-0.07}\,({\rm stat})\,\pm 0.05\,({\rm syst})\,, \tag{3.49}$$

[4] It is crucial to impose identical cuts for electron and muon modes to ensure maximal cancellation of hadronic uncertainties.

differ from the SM hypothesis by 2.2 and 2.5 standard deviations, respectively. While assumed to be affected by the same NP contributions, the measurements of $R_{K^0_S}$ (and $R_{K^{*+}}$) suffer from a reduced experimental efficiency at LHCb compared to its isospin partner due to the presence of a long-lived $K^0_S$ or $\pi^0$ meson in the final state [9].

In Tab. C.5, we give the full list of SM predictions and measurements of $R_{K^{(*)}}$ in different $q^2$-regions. Therein, we also show results obtained by the Belle collaboration which, in contrast to the ones from LHCb, are in agreement with the SM predictions due to their large uncertainties. However, the successor experiment Belle II is expected to provide improved measurements in the near future [80, 85] which may reinforce the implications of the LHCb data. In Fig. 3.3, we display selected measurements of $R_{K^{*0}}$ with corresponding SM predictions.

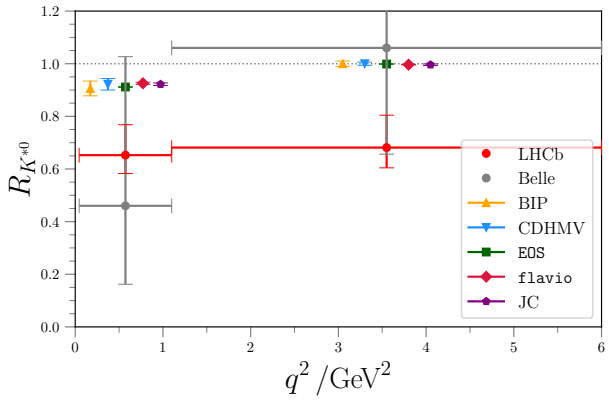


**Figure 3.3:** Comparison of LHCb [84] and Belle [86] $R_{K^{*0}}$ measurements with the SM theoretical predictions [87–92].

A way to emphasise the potential of the LU ratios is to express their theory prediction in terms of Wilson coefficients. By requiring parity and Lorentz invariance, we find that distinct combinations of LH and RH coefficients appear in the decay amplitudes of exclusive semileptonic decays, that is $\mathcal{C}_i + \mathcal{C}'_i$ and $\mathcal{C}_i - \mathcal{C}'_i$ for $B \to K\,\mu^+\mu^-$ and $B \to K^*\,\mu^+\mu^-$, respectively. Considering only linear terms in BSM coefficients, we can cleanly isolate RH currents in the double ratio

$$\frac{R_{K^*}}{R_K} \simeq 1 - 0.48\,p\,\left[\mathcal{C}'_{9,\mu} - \mathcal{C}'_{10,\mu} - \left(\mathcal{C}'_{9,e} - \mathcal{C}'_{10,e}\right)\right] , \tag{3.50}$$

where $p \simeq 0.86$ denotes the polarisation fraction of the $K^*$ meson [83].

As the dynamics of such FCNC decays are predicted within the SM with high precision, amplitudes of such suppressed decays governed by $b \to s$ transitions are perfect laboratories to look for NP. Effects of BSM physics can be sizeable with respect to the competing SM processes, where new particles can either participate in the loops or generate additional tree-level diagrams. In this thesis, our focus resides on such contributions mediated by a new $Z'$ gauge boson, see Chap. 8. The determination of the necessary contributions favoured by the $B$-anomalies motivates a fit of $b \to s$ observables in terms of NP Wilson coefficients, which we present in Chap. 4.

Chapter

4

# Global fits of $b \to s$ observables

With the EFT framework in Eq. (3.41), we can study the impact of BSM Wilson coefficients on flavour observables. This can be done in a well-defined manner through a *global fit*, where all the experimental data is fitted to the EFT framework. In doing so, we can exploit the complementarity between different observables sensitive to certain types of combinations of Wilson coefficients, which provides valuable information for the construction of NP models.

Motivated by the hints of LU violation outlined in Sec. 3.4, we perform a global fit with the tool `flavio` [91] including $b \to s\,\ell^+\ell^-$ (in particular $b \to s\,\mu^+\mu^-$) and $b \to s\,\gamma$ data. We incorporate the large set of available experimental data, *e.g.* (binned) branching ratios, angular observables such as $A_{\rm FB}$, $F_{\rm H}$ and $P_i^{(\prime)}$ as well as the $R_{K^{(*)}}$ observables. A complete list of the observables included is given in App. C.1, closely following the approach in Refs. [93, 94]. In this chapter, we outline the fit procedure in Sec. 4.1, and afterwards discuss the different fit set-ups and their results in Sec. 4.2.

## 4.1 Preliminaries for a global fit

### 4.1.1 Statistical treatment of the data

One of the most challenging tasks for a precision analysis that combines a large number of flavour observables, *i.e.* a global fit, is the proper and consistent treatment of both, experimental data from measurements and theoretical uncertainties of the observables included. In the following, we consider a set of observables $\vec{\mathcal{O}}$, where the general idea is to find its theoretical predictions $\mathcal{O}_i^{\rm th}$ that agree best with the data available on those observables $\mathcal{O}_i^{\rm exp}$. This is done by generating a likelihood from existing experimental data, and evaluating this function at the theoretical predictions. One of the main purposes of the `flavio` package [91] is to implement and execute this procedure. Schematically, the likelihood function is defined as

$$\mathcal{L}(\vec{p}) = \prod_i f_i\left(\mathcal{O}_i^{\rm exp}, \mathcal{O}_i^{\rm th}(\vec{p})\right) , \tag{4.1}$$

where the probability distribution functions (PDFs) $f_i$ computed for each individual measurement $i$ are multiplied. The theoretical predictions depend on a set of given input parameters $\vec{p}$ which comprise additional sources of uncertainty. The maximum likelihood estimator, called the best-fit point (point of highest probability), is obtained by maximising the likelihood function in Eq. (4.1). However, in practice we are only interested in a subset of these parameters, which leads to a splitting of $\vec{p}$ into *fit parameters* $\vec{\theta}$ and *nuisance parameters* $\vec{\nu}$, where the latter are integrated out.

Consequently, one obtains a function that only depends on the fit parameters. Common methods used for this splitting and the consecutive marginalisation of the nuisance parameters are the Bayesian and the frequentist approach, which are both computationally quite demanding [93].

An alternative way of constructing a likelihood in `flavio` is the *Fast-Likelihood* approach, which yields a likelihood independent of nuisance parameters reducing computation time and resources.

### 4.1.2 The Fast-Likelihood approach

Based on the Gaussian approximation of the likelihood, we write [93]

$$-2 \ln\left(\mathcal{L}(\vec{\theta})\right) \approx \chi^2 = \vec{\Delta}^{\mathsf{T}} \cdot \left(C_{\text{exp}} + C_{\text{th}}\left(\vec{\theta} = \vec{\theta}_{\text{c}}\right)\right)^{-1} \cdot \vec{\Delta}\,, \tag{4.2}$$

with $\vec{\Delta} = (\vec{\mathcal{O}}^{\text{exp}} - \vec{\mathcal{O}}^{\text{th}}(\vec{\theta}))$. Here, $\vec{\mathcal{O}}^{\text{exp}}$ denotes the central values of the observables as measured by experiments, while $\vec{\mathcal{O}}^{\text{th}}(\vec{\theta})$ comprises the central values of the theoretical predictions in terms of the nuisance parameters $\vec{\nu}$ (but dependent on the fit parameters $\vec{\theta}$). $C_{\text{exp}}$ is a covariance matrix that includes all experimental measurements, while $C_{\text{th}}$ is a covariance matrix including the theory predictions of the observables, evaluated for $\vec{\theta}$ at their central values $\vec{\theta}_{\text{c}}$. Hence, the matrix $C_{\text{th}}$ involves all theoretical uncertainties and their correlations, and is computed by randomly sampling the observables for nuisance parameters distributed according to their PDFs. Employing this approach, the nuisance parameters in $C_{\text{th}}$ are effectively integrated out and the likelihood function to be optimised solely depends on the fit parameters of interest. Conversely, $C_{\text{exp}}$ is obtained from approximating the true experimental PDFs as a (multivariate) Gaussian distribution. We emphasise that the validity of this approach relies not only on the assumption that experimental and theoretical uncertainties are approximated as Gaussian, but also on the basis that the covariances are assumed to be weakly dependent on the parameters $\vec{\theta}$. Then, we are able to study the likelihood function in the space of NP Wilson coefficients without worrying about nuisance parameters [91].

In our analysis, the covariance matrix $C_{\text{exp}}$ is estimated by sampling all experimental probability distributions (including their correlations) with a sample size of $N_{\text{exp}} = 10^5$ random values. Afterwards, we extract the mean values as well as the combined covariance matrix from those random samples. Similarly, the theoretical uncertainties and correlations are determined by randomly sampling all input parameters with $N = 10^4$ according to their probability distributions. By computing all observables for each sample, we obtain an estimate of the theoretical covariance matrix $C_{\text{th}}$, which then also includes the theoretical correlations between the observables. We have checked that the chosen sample sizes ($N_{\text{exp}} = 10^5$, $N = 10^4$) provide a sufficient trade-off between the convergence of the fit results and computation time.

### 4.1.3 Obtaining a best-fit result

After computing the approximate negative log-likelihood defined as $\chi^2$ in Eq. (4.2), we obtain the best-fit parameters of our global fit (that is the Wilson coefficients) by minimising the $\chi^2$ function. This minimisation is performed using the `MIGRAD` algorithm implemented in the Python package `iminuit` [95]. In doing so, we also extract the respective central values and $1\,\sigma$ uncertainties of the fit parameters.

The goodness of the fit can be described by the reduced chi-squared statistic [96]

$$\text{red}\chi^2 = \frac{\chi^2_{\text{bf}}}{n_{\text{dof}}} = \frac{\chi^2_{\text{bf}}}{n_{\text{obs}} - n_{\text{para}}}\,, \tag{4.3}$$

*i.e.* the $\chi^2$ value at the best-fit point divided by the number of degrees of freedom $n_{\text{dof}}$. Here, $n_{\text{obs}}$ and $n_{\text{para}}$ denote the number of observables included and number of fit parameters (also called dimension of the fit), respectively. In simple terms, a value of $\text{red}\chi^2 \sim 1$ indicates that the data is well described by the chosen parameters and their variances (*i.e.* uncertainties). Conversely, large deviations from unity suggest an inadequate description of the data by our results.

To estimate the deviation of a fit result from the SM hypothesis (all fit parameters fixed to zero), we compute the pull in Gaussian standard deviations $\text{pull}_{\text{SM}}$. This quantity is a function of $\Delta\chi^2 = \chi^2_{\text{SM}} - \chi^2_{\text{bf}}$ and $n_{\text{para}}$, already implemented in `flavio` by default [91]. For instance, $\text{pull}_{\text{SM}} = \sqrt{\Delta\chi^2}$ for a 1d fit with $n_{\text{para}} = 1$.

## 4.2 Fit scenarios and results

In what follows, we report on the fit scenarios considered in our analyses and discuss their results. We compute a likelihood function with `flavio` including different sets of observables. Subsequently, the resulting $\chi^2$ function is minimised with respect to the NP Wilson coefficients $\mathcal{C}^{(\prime)}_{(7,9,10),\mu}$ introduced in Eq. (3.41).

We study a variety of fit scenarios with different combinations of Wilson coefficients included:

- 1 dimensional fit with only $\mathcal{C}_{9,\mu}$ ,
- 1 dimensional fit with $\mathcal{C}_{9,\mu} = -\mathcal{C}_{10,\mu}$ ,
- 2 dimensional fit with $\mathcal{C}_{(9,10),\mu}$ ,
- 4 dimensional fit with $\mathcal{C}^{(\prime)}_{(9,10),\mu}$ ,
- 6 dimensional fit with $\mathcal{C}^{(\prime)}_{(7,9,10),\mu}$ .

Consider for instance the 4d fit. In this scenario, we choose $\mathcal{C}_{9,\mu}$, $\mathcal{C}_{10,\mu}$, $\mathcal{C}'_{9,\mu}$, and $\mathcal{C}'_{10,\mu}$ as fit parameters while fixing all other NP Wilson coefficients to zero. The list above includes the most interesting fit scenarios motivated by the search of NP in $b\to s$ transitions. Nevertheless, also different set-ups, *e.g.*, allowing for only RH contributions or 1d fits with only $\mathcal{C}^{(\prime)}_7$ or $\mathcal{C}^{(\prime)}_{10,\mu}$ are possible. In our fit procedure we assume real-valued Wilson coefficients.

Furthermore, when performing these fits we distinguish between two cases that feature different sets of observables: global fits including only pure $b\to s\,\mu^+\mu^-$ data (called 'no $R_{K^{(*)}}$') compiled in Tabs. C.1 to C.3, and others (called 'with $R_{K^{(*)}}$'), where we additionally include information from $b\to s\,e^+e^-$ observables such as $R_{K^{(*)}}$ and $B^0\to K^{*0}\,e^+e^-$ observables listed in Tab. C.4. In the latter case, these observables provide more stringent constraints on the Wilson coefficients $\mathcal{C}^{(\prime)}_7$ [97]. However, the assumption has been made that electron modes do not suffer from NP effects. In contrast, this assumption is not necessary in the case 'no $R_{K^{(*)}}$', with results of the corresponding fits used in Chap. 9 taking into account only pure $b\to s\,\mu^+\mu^-$ data.

The fit results for the two cases have been first published in Ref. [20]. After the publication, updated measurements have been made available which include the latest LHCb measurements [9] of $R_{K^+}$

and $R_{K^0_S}$, see Eqs. (3.46) and (3.47), respectively, as well as updated combined measurements of $B^0_{(s)} \to \mu^+\mu^-$ branching ratios [98] and additional $q^2$-bins of the differential $B_s \to \phi\,\mu^+\mu^-$ branching ratio [99]. The reader is referred to App. C for comprehensive details on those updates, as well as the remastered fit results. They are compatible with the ones established in Ref. [20].

In the following, we present the *published* results that are employed in the subsequent studies of this thesis.

### 4.2.1 Fit results using pure $b \to s\,\mu^+\mu^-$ data

In Tab. 4.1, we display the best-fit values of the Wilson coefficients as well as their $1\,\sigma$ uncertainties. The reduced $\chi^2$ and pull from the SM hypothesis are provided as well, see Eq. (4.3) and following. We observe that all fit scenarios yield $\text{red}\chi^2 \sim 1$ indicating a good fit and exhibit a significant pull from the SM hypothesis, $\text{pull}_{\text{SM}} \sim 4.5\,\sigma$. The correlations between the fit parameters are given in App. C.3, and are taken into account in the analyses presented in this thesis. In the 6d fit scenario, the values of $\mathcal{C}_7$ and $\mathcal{C}'_7$ are tiny and compatible with zero within $1\,\sigma$ uncertainties.

Global fits with pure $b \to s\,\mu^+\mu^-$ data ('no $R_{K^{(*)}}$')

| Dim. | $\mathcal{C}_{9,\mu}$ | $\mathcal{C}_{10,\mu}$ | $\mathcal{C}'_{9,\mu}$ | $\mathcal{C}'_{10,\mu}$ | $\mathcal{C}_7$ | $\mathcal{C}'_7$ | $\text{red}\chi^2$ | $\text{pull}_{\text{SM}}$ |
|---|---|---|---|---|---|---|---|---|
| 1 | $-0.91 \pm 0.18$ | - | - | - | - | - | 1.00 | $4.5\,\sigma$ |
| 1 | $-0.68 \pm 0.16$ | $-\mathcal{C}_{9,\mu}$ | - | - | - | - | 0.99 | $4.7\,\sigma$ |
| 2 | $-1.02 \pm 0.19$ | $0.46 \pm 0.18$ | - | - | - | - | 0.96 | $4.9\,\sigma$ |
| 4 | $-1.13 \pm 0.18$ | $0.31 \pm 0.21$ | $0.29 \pm 0.33$ | $-0.24 \pm 0.19$ | - | - | 0.92 | $5.0\,\sigma$ |
| 6 | $-1.15 \pm 0.18$ | $0.30 \pm 0.20$ | $0.22 \pm 0.34$ | $-0.24 \pm 0.19$ | $0.002 \pm 0.01$ | $0.02 \pm 0.02$ | 0.91 | $4.6\,\sigma$ |

**Table 4.1:** Best-fit values and $1\,\sigma$ uncertainties of the Wilson coefficients from a fit with only pure $b \to s\,\mu^+\mu^-$ data for different NP scenarios. We also state the respective value of $\text{red}\chi^2$ ($\chi^2$ value at the best-fit point divided by the number of degrees of freedom) and pull from the SM hypothesis, $\text{pull}_{\text{SM}}$. *Table taken from Ref.* [20].

### 4.2.2 Fit results including $R_{K^{(*)}}$ data

Assuming that electron modes do not suffer from NP effects, we can append the lepton flavour universality (LFU) observables compiled in Tab. C.4 to our analysis. Again, five different global fits are performed and their results are shown in Tab. 4.2. Note that the $\text{pull}_{\text{SM}}$ gets enhanced from $\sim 4.5\,\sigma$ up to $\sim 6\,\sigma$ compared to the previously shown results in Tab. 4.1. This strongly supports the $B$-anomalies while being consistent with other global fits performed by, *e.g.*, Refs. [69, 93, 94, 98, 100, 101]. In the remainder of this section, we briefly discuss dedicated fit results and their implications.

Global fits including $R_{K^{(*)}}$ data ('with $R_{K^{(*)}}$')

| Dim. | $\mathcal{C}_{9,\mu}$ | $\mathcal{C}_{10,\mu}$ | $\mathcal{C}'_{9,\mu}$ | $\mathcal{C}'_{10,\mu}$ | $\mathcal{C}_7$ | $\mathcal{C}'_7$ | $\text{red}\chi^2$ | $\text{pull}_{\text{SM}}$ |
|---|---|---|---|---|---|---|---|---|
| 1 | $-0.83 \pm 0.14$ | - | - | - | - | - | 0.98 | $6.0\,\sigma$ |
| 1 | $-0.41 \pm 0.07$ | $-\mathcal{C}_{9,\mu}$ | - | - | - | - | 0.99 | $6.0\,\sigma$ |
| 2 | $-0.71 \pm 0.17$ | $0.20 \pm 0.13$ | - | - | - | - | 0.97 | $5.9\,\sigma$ |
| 4 | $-1.07 \pm 0.17$ | $0.18 \pm 0.15$ | $0.27 \pm 0.32$ | $-0.28 \pm 0.19$ | - | - | 0.90 | $6.5\,\sigma$ |
| 6 | $-1.08 \pm 0.18$ | $0.18 \pm 0.15$ | $0.27 \pm 0.34$ | $-0.28 \pm 0.17$ | $0.0005 \pm 0.01$ | $0.005 \pm 0.006$ | 0.89 | $6.1\,\sigma$ |

**Table 4.2:** Best-fit values and $1\,\sigma$ uncertainties of the Wilson coefficients from a fit including observables listed in Tabs. C.1 to C.4 for different NP scenarios. *Table taken from Ref.* [20].

### 6d fit scenario

In Fig. 4.1, we show likelihood contours for the 6d global fit scenario in the plane of NP Wilson coefficients $\mathcal{C}_{9,\mu}$ versus $\mathcal{C}_{10,\mu}$ (left-hand side plot) and $\mathcal{C}_{9,\mu}$ versus $\mathcal{C}'_{9,\mu}$ (right-hand side plot), while the other coefficients are fixed to their central best-fit values. To illustrate the impact of the LFU observables on the fit, we also show the contours of the corresponding fit including only pure $b \to s\,\mu^+\mu^-$ data in violet. One notices that different sets of observables have a distinct impact on the allowed parameter space comparing both plots. The $R_K$ and $R_{K^*}$ contours (in green and orange) yield similar constraints in the $\mathcal{C}_{9,\mu}$-$\mathcal{C}_{10,\mu}$ plane, whereas complementary likelihood regions are given for $\mathcal{C}_{9,\mu}$ versus $\mathcal{C}'_{9,\mu}$. Together with the remaining observables, the global fit highlights the necessity of NP contributions, especially $\mathcal{C}_{9,\mu} < 0$, in the context of the $B$-anomalies. While both $\mathcal{C}_7$ and $\mathcal{C}'_7$ are consistent with the SM, we find that the preferred best-fit values hint at NP physics with $\mathcal{C}_{9,\mu} < 0$ and $\mathcal{C}_{10,\mu} \geq 0$. With the exception of $\mathcal{C}'_{10,\mu}$, the RH currents of semimuonic Wilson coefficients are also less preferred than contributions of their LH counterparts. Supplementary plots that show contours of different subsets of observables are displayed in Fig. C.1.

### 1d and 2d fit scenarios

As no $\mathcal{C}_7^{(\prime)}$ are induced by a $Z'$ boson and LH current contributions are already sufficient to explain the deviations, the results of the 1d and 2d fit scenarios are of special concern and are employed in Chap. 8, devoted to studies of flavourful $Z'$ models accounting for the $B$-anomalies.

Figure 4.2 visualises the results of the 2d fit in Tab. 4.2, where $\mathcal{C}_{9,\mu}$ and $\mathcal{C}_{10,\mu}$ are varied independently. Supplementary plots are shown in Fig. C.2. Comparing the two plots in Fig. 4.2, one again acknowledges the impact of including $R_{K^{(*)}}$ observables in the fit, similar to the 6d case. The significant deviation from the SM hypothesis of $\mathcal{C}_{9,\mu}$ is inferred from the overlap of the different individual contours. The 1d results listed in Tab. 4.2 confirm the overall picture of NP effects induced by LH (vector) couplings favoured by the $B$-anomalies.

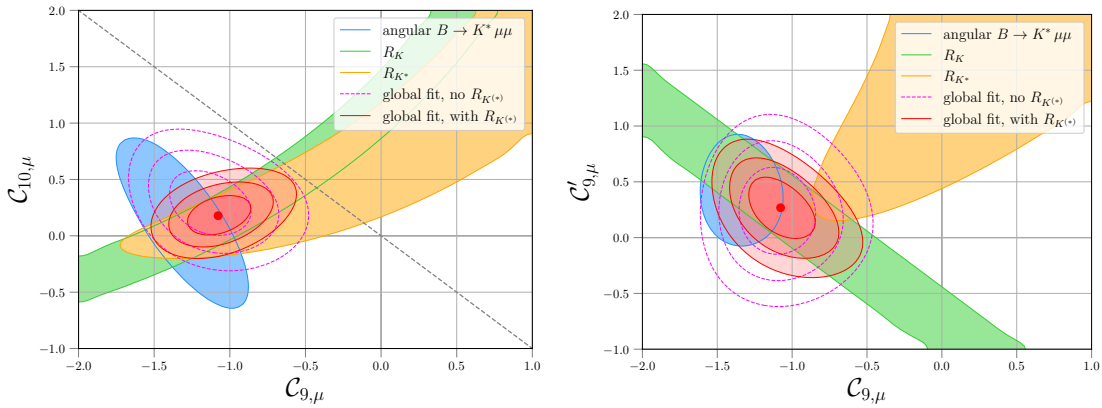


**Figure 4.1:** Global fit to rare $B$-decay data on $|\Delta b| = |\Delta s| = 1$ transitions in a 6d scenario. Depicted here are the likelihood contours using the 6d results from Tab. 4.2 in the plane of NP Wilson coefficients $\mathcal{C}_{9,\mu}$ versus $\mathcal{C}_{10,\mu}$ (left-hand side plot) and $\mathcal{C}_{9,\mu}$ versus $\mathcal{C}'_{9,\mu}$ (right-hand side plot). The red contours (at 1-3 $\sigma$) incorporate all observables used in the fit, whereas the violet contours are obtained *excluding* LU ratios and $B^0 \to K^{*0} e^+ e^-$ observables. We also show contours using only certain subsets of observables, *e.g.* only $R_K$ (green), only $R_{K^*}$ (orange) and $B \to K^* \mu^+ \mu^-$ angular observables (blue). The dashed grey line indicates $\mathcal{C}_{9,\mu} = -\mathcal{C}_{10,\mu}$. Supplementary plots showing different contours are given in Fig. C.1.

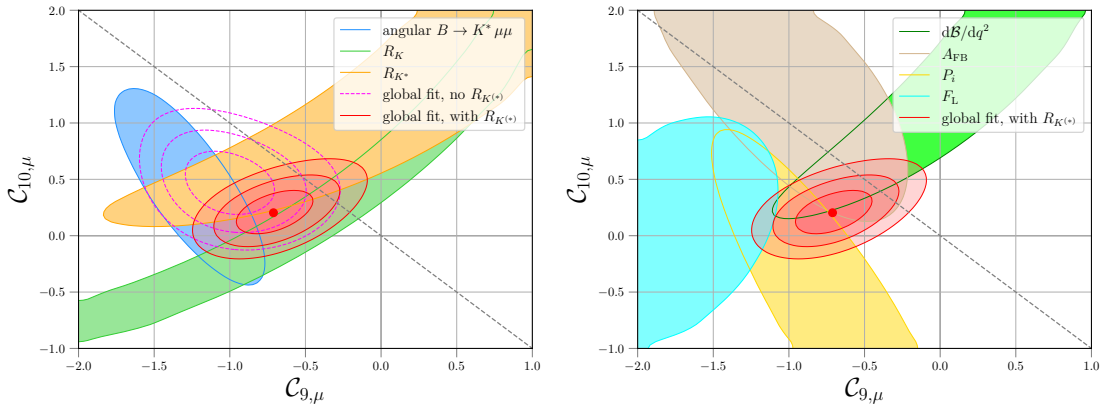


**Figure 4.2:** Global fit to rare $B$-decay data on $|\Delta b| = |\Delta s| = 1$ transitions in a 2d scenario, in the plane of NP Wilson coefficients $\mathcal{C}_{9,\mu}$ versus $\mathcal{C}_{10,\mu}$. The same colour coding for the contours as in Fig. 4.1 is applied, where we display additional subsets of observables in the right-hand side plot for comparison, *i.e.* differential branching ratios $d\mathcal{B}/dq^2$ (limegreen), lepton forward-backward asymmetries $A_{FB}$ (beige), optimised angular observables $P_i$ (gold) and fractions of the longitudinal polarisation $F_L$ (cyan). For details on the observables included see App. C, while supplementary plots can be found in Fig. C.2.

*Chapter*

# 5

# A guide for U(1)′ models

In this chapter, we provide details on the NP models of interest in this thesis, that is U(1)′ extensions. In those scenarios, the SM gauge group in Eq. (2.1) is augmented by an additional abelian symmetry U(1)′, and becomes $\mathrm{U}(1)_Y \times \mathrm{SU}(2)_L \times \mathrm{SU}(3)_C \times \mathrm{U}(1)'$. The associated gauge boson of the U(1)′ is an electrically and colourless vector boson called the $Z'$ boson.

The most general renormalisable Lagrangian for the new U(1)′ interaction is given by [102, 103]

$$\mathcal{L}_{Z'} = -\frac{1}{4} B'^{\mu\nu} B'_{\mu\nu} + \mathcal{L}_{\text{mix}} + \mathcal{L}^{\text{int}}_{Z'} \,, \tag{5.1}$$

where $B'^{\mu\nu}$ denotes the U(1)′ field strength tensor. The $\mathcal{L}_{\text{mix}}$ includes kinetic mixing interactions of the U(1)′ with the abelian $\mathrm{U}(1)_Y$ group of the SM, see Sec. 5.4. The interactions of the boson to SM fermions $f'$ in the flavour basis can be parametrised as

$$\mathcal{L}^{\text{int}}_{Z'} = g_4 \, F_f \, \overline{f}' \, \gamma^\mu \, f' \, Z'_\mu \,, \tag{5.2}$$

with the U(1)′ gauge coupling $g_4$ and generation-dependent U(1)′ charges $F_f$ of the SM fermions, where the notation $F_f = \{F_Q, F_U, F_D, F_L, F_E\}$ is understood. Additional interactions to, *e.g.*, RH neutrinos $\nu_R$ with associated charges $F_\nu$ can also be implemented in this Lagrangian. When going from flavour basis (also called *gauge* basis) to the mass basis, non-universal fermion couplings are constructed. They generally depend on the U(1)′ gauge coupling and charges of the fermions under the U(1)′. Such a generation allows for FCNC couplings to quarks at tree level, and hence constitutes an essential concept in our $Z'$ model building.

In this thesis, we confine ourselves to studies of heavy $Z'$ bosons with masses $M_{Z'}$ in the TeV-range, related to the breaking scale of the new symmetry. For studies that discuss NP interpretations with light $Z'$ bosons (with masses below or around the electroweak scale), see *e.g.* Refs. [104–108], while we suggest Refs. [103, 109–113] for additional literature on $Z'$ models and their parameter constraints.

Details on the necessary fermion mixing are discussed in Sec. 5.1. Afterwards, we study gauge anomaly cancellation which dictates theoretical constraints on the U(1)′ charges and derive phenomenological constraints on $Z'$ couplings from meson mixing in Secs. 5.2 and 5.3, respectively. Some information on gauge-kinetic mixing is given in Sec. 5.4, while we conclude this chapter in Sec. 5.5 with a review of Landau poles in U(1)′ extensions.

## 5.1 Flavour rotations in $Z'$ set-ups

In this section, we outline how FCNC couplings to the $Z'$ boson are generated via rotations from the gauge to the mass basis, mainly focussing on the quark sector.

In Sec. 2.3, we have introduced four unitary rotations that exist in the quark sector, those for up (down)-singlets $U_u(U_d)$ and up (down)-doublets $V_u(V_d)$. Those rotations are a priori unconstrained except for the product

$$(V_u)^\dagger \; V_d \equiv V_{\rm CKM} \,, \tag{5.3}$$

where $V_{\rm CKM}$ denotes the CKM matrix as defined in Eq. (2.25). Following Eq. (5.2), we write out the $Z'$ couplings to quarks

$$\mathcal{L}^{\rm int}_{Z'} \supset \; g_4 \left( \overline{u}'_L \, \mathcal{Q}' \, \gamma^\mu \, u'_L \, Z'_\mu + \overline{d}'_L \, \mathcal{Q}' \, \gamma^\mu \, d'_L \, Z'_\mu + \overline{u}'_R \, \mathcal{U}' \, \gamma^\mu \, u'_R \, Z'_\mu + \overline{d}'_R \, \mathcal{D}' \, \gamma^\mu \, d'_R \, Z'_\mu \right) , \tag{5.4}$$

with the structure of U(1)′ charges in the flavour basis parametrised by the diagonal matrices

$$\mathcal{Q}' = {\rm diag}\,(F_{Q_1},\, F_{Q_2},\, F_{Q_3}) \;, \quad \mathcal{U}' = {\rm diag}\,(F_{U_1},\, F_{U_2},\, F_{U_3}) \;, \quad \mathcal{D}' = {\rm diag}\,(F_{D_1},\, F_{D_2},\, F_{D_3}) \;. \tag{5.5}$$

To better understand how FCNC couplings, which we call $g^{ji}_{L,R}$, are generated by flavour rotations, we consider the first term in Eq. (5.4) while analogous results are obtained for the remaining terms. Inserting the field rotations defined in Eq. (2.21), we find (only looking at the *flavour* structure)

$$\overline{u}'_L \, \mathcal{Q}' \, u'_L = \overline{u}_L \; (V_u)^\dagger \; \mathcal{Q}' \, V_u \, u_L = \overline{u}_L \, \mathcal{Q}_u \, u_L \,. \tag{5.6}$$

We observe that a flavour structure $\mathcal{Q}'$ proportional to the identity matrix, *e.g.* $\mathcal{Q}' = F_Q \cdot \mathbb{1}$, prevents FCNC transitions as $\mathcal{Q}_u$ in the mass basis remains diagonal due to the unitarity of $V_u$. To obtain off-diagonal entries in $\mathcal{Q}_u$, it is therefore pivotal to assume non-universal charges, $F_{Q_i} \neq F_{Q_j}$, which yield FCNC couplings, provided that $V_u \neq \mathbb{1}$. For instance, tree-level contributions to rare charm decays via a $Z'$ boson are of the form $\overline{u}_{L,1} \, \mathcal{Q}_u^{12} \, u_{L,2} = \overline{u}_L \, \mathcal{Q}_u^{12} \, c_L$ with $\mathcal{Q}_u^{12} \sim (F_{Q_2} - F_{Q_1})$. Applying flavour rotations to the remaining terms in Eq. (5.4), we can summarise the flavour structure in the mass basis

$$\mathcal{Q}_u = (V_u)^\dagger \; \mathcal{Q}' \, V_u \,, \quad \mathcal{Q}_d = (V_d)^\dagger \; \mathcal{Q}' \, V_d \,, \quad \mathcal{U} = (U_u)^\dagger \; \mathcal{U}' \, U_u \,, \quad \mathcal{D} = (U_d)^\dagger \; \mathcal{D}' \, U_d \,. \tag{5.7}$$

Next, we study different mixing scenarios assuming distinct structures for the unitary matrices. Utilising the general set-up, we investigate flavour mixing in the up-quark and down-quark sectors with a focus on $c \to u$ and $b \to s$ transitions, respectively. While it is possible to allow for mixing effects in both sectors simultaneously using an appropriate parametrisation, see *e.g.* Ref. [114, 115], we distinctly study flavour mixing in only up- or down-quark transitions.

### 5.1.1 Flavour rotations in the right-handed quark sector

The rotations for the RH quarks are unconstrained and a general parametrisation of unitary $3 \times 3$ matrices $U_{u,d}$ can be chosen with $n^2 = 9$ real independent parameters (five angles, four phases) [116]. However, at this point we make some simplifying assumptions, since we focus mainly on mixing between first and second generation in the up-sector for charm physics (with

underlying $c \to u$ transitions), and mixing between second and third generation in the down-sector for $B$-physics (with underlying $b \to s$ transitions). These assumptions are further motivated to circumvent mixing between the first and second generation in the down-quark sector governed by strong kaon constraints [110], which we comment on in Sec. 5.3.3. Hence, it is convenient to utilise a $2 \times 2$ rotation matrix and define the two unitary matrices

$$U_u = \begin{pmatrix} \cos(\theta_u) & -e^{i\phi_R} \sin(\theta_u) & 0 \\ e^{-i\phi_R} \sin(\theta_u) & \cos(\theta_u) & 0 \\ 0 & 0 & 1 \end{pmatrix} , \tag{5.8}$$

$$U_d = \begin{pmatrix} 1 & 0 & 0 \\ 0 & \cos(\theta_d) & -e^{i\phi_R} \sin(\theta_d) \\ 0 & e^{-i\phi_R} \sin(\theta_d) & \cos(\theta_d) \end{pmatrix} , \tag{5.9}$$

where $\theta_u$ and $\theta_d$ are the $uc$- and $bs$-mixing angles for the up- and down-type quark singlets, respectively. In addition, we have introduced a $CP$-violating phase $\phi_R$. Due to the SM-like $CP$ violation in the LH quark sector, flavour mixing in the RH sector provides the opportunity to generate sizeable $CP$-violating effects. Here, we refer to Chap. 7 for a detailed study of weak phases in U(1)$'$ extensions. We emphasise that by assuming mixing only in the down-quark sector we do not generate FCNC transitions in the up-quark sector and vice versa. We also discard the possibility of large cancellations between up- and down-quark flavour rotations, corresponding to large mixing angles.

### 5.1.2 Mixing only in the up-quark sector

Assuming flavour rotations only in the up-sector, we set $V_d \approx \mathbb{1}$, $U_d \approx \mathbb{1}$. This infers $V_u \approx (V_{\rm CKM})^\dagger$ maximising effects in the up-sector. First, we study the mixing in the LH quark sector by rotating to the up mass basis via Eq. (5.7) which yields

$$\mathcal{Q}_u = V_{\rm CKM}\, \mathcal{Q}'\, (V_{\rm CKM})^\dagger \, . \tag{5.10}$$

Explicit values of the matrix elements $\mathcal{Q}_u^{ij}$ are listed in Tab. 5.1, where we also give entries in the Wolfenstein parametrisation to analyse hierarchies of the $ji$-vertices.

For instance, the $cu$-vertex can be written as

$$\mathcal{Q}_u^{12} = (F_{Q_2} - F_{Q_1})\, \lambda_s + (F_{Q_3} - F_{Q_1})\, \lambda_b \approx (F_{Q_2} - F_{Q_1})\, \lambda_{\rm CKM} \, , \tag{5.11}$$

where the approximation $\lambda_b \ll \lambda_s \approx \lambda_{\rm CKM}$ with $\lambda_q = V_{cq}^* V_{uq}$, $q = b, s$, has been performed in the last step. We find that in $Z'$ models non-universal U(1)$'$ charges are necessary to generate FCNC transitions, since flavour mixing between different generations $i, j$ is proportional to their difference of U(1)$'$ charges $F_{Q_j} - F_{Q_i}$. For charge assignments $F_{Q_j} = F_{Q_i}$, contributions can in principle emerge via mixing terms if $F_{Q_k} \neq F_{Q_i}$, however, those are highly suppressed and SM-like due to CKM suppression. For instance, contributions in $c \to u$ transitions where $F_{Q_1} = F_{Q_2}$ are given by $(F_{Q_3} - F_{Q_1})\, \lambda_b \sim \lambda_{\rm CKM}^5\, (F_{Q_3} - F_{Q_1})$.

| Mixing | Vertex $ji$ | Matrix element | $\mathcal{Q}_u^{ij}$ | $\mathcal{Q}_u^{ij}$ (Wolfenstein + $\mathcal{O}\left(\lambda_{\rm CKM}^3\right)$) |
|---|---|---|---|---|
| up-sector only | $uu$ | $(1,1)$ | $F_{Q_1} + (F_{Q_2} - F_{Q_1})\,\lvert V_{us}\rvert^2$ $+ (F_{Q_3} - F_{Q_1})\,\lvert V_{ub}\rvert^2$ | $F_{Q_1} + \lambda_{\rm CKM}^2\ (F_{Q_2} - F_{Q_1})$ |
| | $cc$ | $(2,2)$ | $F_{Q_2} + (F_{Q_1} - F_{Q_2})\,\lvert V_{cd}\rvert^2$ $+ (F_{Q_3} - F_{Q_2})\,\lvert V_{cb}\rvert^2$ | $F_{Q_2} - \lambda_{\rm CKM}^2\ (F_{Q_2} - F_{Q_1})$ |
| | $tt$ | $(3,3)$ | $F_{Q_3} + (F_{Q_2} - F_{Q_3})\,\lvert V_{ts}\rvert^2$ $+ (F_{Q_1} - F_{Q_3})\,\lvert V_{td}\rvert^2$ | $F_{Q_3}$ |
| | $cu$ | $(1,2)$ | $(F_{Q_2} - F_{Q_1})\ V_{cs}^* V_{us}$ $+(F_{Q_3} - F_{Q_1})\ V_{cb}^* V_{ub}$ | $\lambda_{\rm CKM}\ (F_{Q_2} - F_{Q_1})$ |
| | $tc$ | $(2,3)$ | $(F_{Q_3} - F_{Q_2})\ V_{tb}^* V_{cb}$ $+(F_{Q_1} - F_{Q_2})\ V_{td}^* V_{cd}$ | $\lambda_{\rm CKM}^2\, A\ (F_{Q_3} - F_{Q_2})$ |
| | $tu$ | $(1,3)$ | $(F_{Q_3} - F_{Q_1})\ V_{tb}^* V_{ub}$ $+\ (F_{Q_2} - F_{Q_1})\ V_{ts}^* V_{us}$ | $0$ |

**Table 5.1:** Overview of LH flavour rotations assuming mixing only in the up-quark sector.

Neglecting higher-order corrections $\mathcal{O}\left(\lambda_{\rm CKM}^3\right)$, the $Z'$ coupling $g_L^{cu}$ is simply given by

$$g_L^{cu} = \mathcal{Q}_u^{12}\, g_4 \approx (F_{Q_2} - F_{Q_1})\, \lambda_{\rm CKM}\, g_4\,. \tag{5.12}$$

The diagonal couplings can be readily obtained as

$$g_L^{ii} = F_{Q_i}\, g_4 + \mathcal{O}\left(\lambda_{\rm CKM}^2\right). \tag{5.13}$$

For the RH quarks, we rotate to the up mass basis as prescribed in Eq. (5.7), neglecting off-diagonal mixing of the third-generation quark singlets. In Tab. 5.2, we provide the non-trivial matrix elements $\mathcal{U}^{ij}$. The only non-vanishing FCNC $Z'$-coupling to RH quarks is given by

$$g_R^{cu} = \mathcal{U}^{12}\, g_4 = (F_{U_2} - F_{U_1})\, \cos(\theta_u)\, \sin(\theta_u)\, e^{\mathrm{i}\,\phi_R}\, g_4\,, \tag{5.14}$$

where again the non-universal charge assignment $F_{U_1} \neq F_{U_2}$ to generate FCNC contributions is evident. The generation-diagonal couplings of interest read

$$g_R^{uu} = \mathcal{U}^{11}\, g_4 = \left[F_{U_1} \cos^2(\theta_u) + F_{U_2} \sin^2(\theta_u)\right]\, g_4\,, \tag{5.15}$$

$$g_R^{cc} = \mathcal{U}^{22}\, g_4 = \left[F_{U_2} \cos^2(\theta_u) + F_{U_1} \sin^2(\theta_u)\right]\, g_4\,. \tag{5.16}$$

In the limit $\theta_u \ll 1$, the contributions from other-generation U(1)′ charges can be neglected and we obtain $g_R^{ii} \approx F_{U_i}\, g_4$. The same is obviously true assuming universal charges $F_{U_i} \approx F_{U_j}$.

### 5.1.3 Mixing only in the down-quark sector

Restricting ourselves to rotations only in the down-sector, it is $V_u \approx \mathbb{1}\,, U_u \approx \mathbb{1}$. Hence, the CKM-mixing solely resides in the down-sector, $V_d \approx V_{\rm CKM}$. Following Eq. (5.7), we rotate in the down mass basis via

$$\mathcal{Q}_d = (V_{\rm CKM})^\dagger\ \mathcal{Q}'\, V_{\rm CKM}\,. \tag{5.17}$$

| Mixing | Vertex $ji$ | Matrix element | $\mathcal{U}^{ij}$ |
|---|---|---|---|
| up-sector only | $uu$ | $(1,1)$ | $F_{U_1}\,\cos^2(\theta_u) + F_{U_2}\,\sin^2(\theta_u)$ |
| | $cc$ | $(2,2)$ | $F_{U_2}\,\cos^2(\theta_u) + F_{U_1}\,\sin^2(\theta_u)$ |
| | $tt$ | $(3,3)$ | $F_{U_3}$ |
| | $cu$ | $(1,2)$ | $\left(F_{U_2} - F_{U_1}\right)\,\cos(\theta_u)\,\sin(\theta_u)\,e^{\mathrm{i}\phi_R}$ |
| | $tc$ | $(2,3)$ | $0$ |
| | $tu$ | $(1,3)$ | $0$ |

**Table 5.2:** Overview of RH flavour rotations $\mathcal{U}^{ij}$ in the quark sector assuming rotations only in the up-sector and no mixing with the third generation, see Eq. (5.8).

A similar pattern arises as in the up-sector, where we list the corresponding entries of the matrix $\mathcal{Q}_d$ in Tab. 5.3. The mixing contribution for the $bs$-vertex is given by

$$\mathcal{Q}_d^{23} = (F_{Q_3} - F_{Q_2})\; V_{ts}^* V_{tb} + (F_{Q_1} - F_{Q_2})\; V_{us}^* V_{ub} \approx (F_{Q_3} - F_{Q_2})\; V_{ts}^* V_{tb}\,. \tag{5.18}$$

which readily reveals the $b \to s$ coupling

$$g_L^{bs} = \mathcal{Q}_d^{23}\, g_4 \approx (F_{Q_3} - F_{Q_2})\; V_{ts}^* V_{tb}\, g_4\,. \tag{5.19}$$

For the diagonal couplings we find analogous expressions as in Eq. (5.13), where $g_L^{ii} = F_{Q_i}\, g_4$ holds neglecting terms $\mathcal{O}\left(\lambda_{\mathrm{CKM}}^2\right)$.

| Mixing | Vertex $ji$ | Matrix element | $\mathcal{Q}_d^{ij}$ | $\mathcal{Q}_d^{ij}$ (Wolfenstein + $\mathcal{O}\left(\lambda_{\mathrm{CKM}}^3\right)$) |
|---|---|---|---|---|
| down-sector only | $dd$ | $(1,1)$ | $F_{Q_1} + \left(F_{Q_2} - F_{Q_1}\right)\lvert V_{cd}\rvert^2$ $+ \left(F_{Q_3} - F_{Q_1}\right)\lvert V_{td}\rvert^2$ | $F_{Q_1} + \lambda_{\mathrm{CKM}}^2\;\left(F_{Q_2} - F_{Q_1}\right)$ |
| | $ss$ | $(2,2)$ | $F_{Q_2} + \left(F_{Q_1} - F_{Q_2}\right)\lvert V_{us}\rvert^2$ $+ \left(F_{Q_3} - F_{Q_2}\right)\lvert V_{ts}\rvert^2$ | $F_{Q_2} - \lambda_{\mathrm{CKM}}^2\;\left(F_{Q_2} - F_{Q_1}\right)$ |
| | $bb$ | $(3,3)$ | $F_{Q_3} + \left(F_{Q_2} - F_{Q_3}\right)\lvert V_{cb}\rvert^2$ $+ \left(F_{Q_1} - F_{Q_3}\right)\lvert V_{ub}\rvert^2$ | $F_{Q_3}$ |
| | $sd$ | $(1,2)$ | $\left(F_{Q_2} - F_{Q_1}\right)\,V_{cd}^* V_{cs}$ $+\left(F_{Q_3} - F_{Q_1}\right)\,V_{td}^* V_{ts}$ | $-\lambda_{\mathrm{CKM}}\;\left(F_{Q_2} - F_{Q_1}\right)$ |
| | $bs$ | $(2,3)$ | $\left(F_{Q_3} - F_{Q_2}\right)\,V_{ts}^* V_{tb}$ $+\left(F_{Q_1} - F_{Q_2}\right)\,V_{us}^* V_{ub}$ | $-\lambda_{\mathrm{CKM}}^2\, A\;\left(F_{Q_3} - F_{Q_2}\right)$ |
| | $bd$ | $(1,3)$ | $\left(F_{Q_3} - F_{Q_1}\right)\,V_{td}^* V_{tb}$ $+\left(F_{Q_2} - F_{Q_1}\right)\,V_{cd}^* V_{cb}$ | $0$ |

**Table 5.3:** Overview of LH flavour rotations assuming mixing only in the down-quark sector.

For the RH quarks, we rotate to the down mass basis following Eq. (5.7), neglecting off-diagonal mixing of the first-generation quark singlets due to our focus on $b \to s$ transitions. The matrix elements $\mathcal{D}^{ij}$ are listed in Tab. 5.4. We identify

$$g_R^{bs} = \mathcal{D}^{23}\, g_4 = (F_{D_3} - F_{D_2})\sin(\theta_d)\cos(\theta_d)\; e^{\mathrm{i}\phi_R}\, g_4\,, \tag{5.20}$$

whereas $g_R^{bd} = \mathcal{D}^{13}\, g_4 = 0$ and $g_R^{sd} = \mathcal{D}^{12}\, g_4 = 0$.

| Mixing | Vertex $ji$ | Matrix element | $\mathcal{D}^{ij}$ |
|---|---|---|---|
| down-sector only | $dd$ | $(1,1)$ | $F_{D_1}$ |
| | $ss$ | $(2,2)$ | $F_{D_2}\, \cos^2(\theta_d) + F_{D_3}\, \sin^2(\theta_d)$ |
| | $bb$ | $(3,3)$ | $F_{D_3}\, \cos^2(\theta_d) + F_{D_2}\, \sin^2(\theta_d)$ |
| | $sd$ | $(1,2)$ | $0$ |
| | $bs$ | $(2,3)$ | $(F_{D_3} - F_{D_2})\, \cos(\theta_d)\, \sin(\theta_d)\, e^{\mathrm{i}\phi_R}$ |
| | $bd$ | $(1,3)$ | $0$ |

**Table 5.4:** Overview of RH flavour rotations $\mathcal{D}^{ij}$ in the quark sector assuming rotations only in the down-sector and no mixing with the first generation, see Eq. (5.9).

The generation-diagonal couplings read

$$g_R^{bb} = \mathcal{D}^{33}\, g_4 = \left[F_{D_3} \cos^2(\theta_d) + F_{D_2} \sin^2(\theta_d)\right]\, g_4\,, \tag{5.21}$$

$$g_R^{ss} = \mathcal{D}^{22}\, g_4 = \left[F_{D_2} \cos^2(\theta_d) + F_{D_3} \sin^2(\theta_d)\right]\, g_4\,, \tag{5.22}$$

which for small $bs$-mixing angles $\theta_d \ll 1$ (or $F_{D_i} \approx F_{D_j}$) simplify to $g_R^{ii} \approx F_{D_i}\, g_4$.

### 5.1.4 Flavour rotations in the lepton sector

As noted after Eq. (2.27), lepton flavour conservation in the SM is protected due to $U_{\text{PMNS}} = \mathbb{1}$. We can benefit from this SM feature as it is very sensitive to NP.

By assuming a similar misalignment between flavour and mass bases as in the quark sector, cLFV can be induced in $Z'$ scenarios with non-universal couplings to leptons $g_{L,R}^{\ell\ell'}$, $\ell \neq \ell'$. However, if the PMNS matrix is *only* constructed from rotations in the neutrino sector, $V_e = \mathbb{1}$, no left-handed cLFV is realised and it is $g_L^{\ell\ell'} = 0$. By allowing for charged lepton rotations $V_e \neq \mathbb{1}$, we can induce non-zero couplings $g_L^{\ell\ell'}$. Moreover, $g_R^{\ell\ell'} \neq 0$ is also possible via analogous rotations in the RH lepton sector if right-handed neutrinos are present and charged under the U(1)′. The most stringent bounds on these rotations are given by upper limits on the branching ratios of purely leptonic decays involving lepton flavour violation (LFV). Current limits are $\mathcal{O}\left(10^{-8}\right)$ for $\tau \to (\mu, e)\ell$, $\ell = e, \mu$, whereas $\mathcal{O}\left(10^{-12}\right)$ is achieved for $\mu \to eee$ and $\mu \to e\gamma$ [32]. These limits can be met by rotations $\theta_\ell \lesssim \sqrt{\mathcal{B}(\mu \to eee)} \cdot (M_{Z'}/g_4)^2 \cdot \mathcal{O}(10)\ \text{TeV}^{-2}$, assuming rotations only in the LH lepton sector and charges $F_{L_i} \sim \mathcal{O}(1)$ chosen such that large cancellations are avoided [111, 112]. Here, $\mathcal{B}(\mu \to eee)$ provides the most stringent limits whenever couplings to electrons are involved. We obtain the benchmark value $\theta_\ell \lesssim \mathcal{O}\left(10^{-3}\right)$ taking the upper limit $\mathcal{B}(\mu^- \to e^- e^+ e^-) < 1 \cdot 10^{-12}$ [32] as well as $M_{Z'}/g_4 = 10$ TeV. Additional remarks of LFV in $Z'$ models are given in Sec. 6.4, whereas explicit flavour structures of charged leptons and neutrinos are presented in Chap. 9.

The flavour-diagonal couplings of the $Z'$ boson to leptons are given by

$$g_L^{\ell\ell} = g_4\, F_{L_i}\,, \quad g_R^{\ell\ell} = g_4\, F_{E_i}\,, \tag{5.23}$$

where $i = 1, 2, 3$ for $\ell = e, \mu, \tau$ is understood.

## 5.2 Cancellation of gauge anomalies in U(1)′ extensions

After providing the necessary details on how non-diagonal couplings in FCNC transitions are realised in Sec. 5.1, we now study constraints on the new charges $F_f$ which enter the respective couplings. The constraints arise from imposing gauge anomaly cancellation and need to be fulfilled in every $Z'$ scenario. In doing so, we summarise the tools and equations necessary to construct anomaly-free $Z'$ models. We refer to App. D for a brief introduction of anomaly cancellation in QFTs, where we also moot the SM as an example of an anomaly-free theory. Instrumental for our U(1)′ charge assignments is the fact that only chiral fermions (whether SM or new BSM fermions) contribute to the gauge anomaly when charged non-trivially under the respective (gauge) group.

In U(1)′ extensions, gauge anomalies arise from six (potentially) non-vanishing triangle diagrams involving at least one U(1)′ gauge boson, see Fig. D.1. The cancellation of such diagrams is translated into Diophantine equations called anomaly cancellation conditions (ACCs). Taking into account SM fermions (as well as three possible RH neutrinos $\nu_R$ with charges $F_\nu$), the corresponding ACCs read as follows [11, 26],

$$[\mathrm{SU}(3)_C]^2 \times \mathrm{U}(1)' : \quad \sum_{i=1}^{3} (2\, F_{Q_i} - F_{U_i} - F_{D_i}) = 0\,, \tag{5.24a}$$

$$[\mathrm{SU}(2)_L]^2 \times \mathrm{U}(1)' : \quad \sum_{i=1}^{3} (3\, F_{Q_i} + F_{L_i}) = 0\,, \tag{5.24b}$$

$$[\mathrm{U}(1)_Y]^2 \times \mathrm{U}(1)' : \quad \sum_{i=1}^{3} (F_{Q_i} + 3\, F_{L_i} - 8\, F_{U_i} - 2\, F_{D_i} - 6\, F_{E_i}) = 0\,, \tag{5.24c}$$

$$\text{gauge-gravity:} \quad \sum_{i=1}^{3} (6\, F_{Q_i} + 2\, F_{L_i} - 3\, F_{U_i} - 3\, F_{D_i} - F_{E_i} - F_{\nu_i}) = 0\,, \tag{5.24d}$$

$$\mathrm{U}(1)_Y \times [\mathrm{U}(1)']^2 : \quad \sum_{i=1}^{3} \left(F_{Q_i}^2 - F_{L_i}^2 - 2\, F_{U_i}^2 + F_{D_i}^2 + F_{E_i}^2\right) = 0\,, \tag{5.24e}$$

$$[\mathrm{U}(1)']^3 : \quad \sum_{i=1}^{3} \left(6\, F_{Q_i}^3 + 2\, F_{L_i}^3 - 3\, F_{U_i}^3 - 3\, F_{D_i}^3 - F_{E_i}^3 - F_{\nu_i}^3\right) = 0\,. \tag{5.24f}$$

Compared to similar conditions present in the SM, which are universal for all three generations of SM fermions and fix the $\mathrm{U}(1)_Y$ charges, we now explicitly distinguish different generations. Since the RH neutrinos are singlets under the SM gauge group, the charges $F_{\nu_i}$ only appear in the gauge-gravity and $[\mathrm{U}(1)']^3$ constraints, see Eqs. (5.24d) and (5.24f), respectively. Overall, 18 charges are constrained by six ACCs. However, the system can be reduced to 15 charges when decoupling the RH neutrinos by setting $F_{\nu_i} = 0$. If any BSM fermions are considered in this thesis, we include them as SM-singlets and vector-like charged, hence their charges drop out in the ACCs. See Refs. [10, 11, 14, 117–119] for recent phenomenological applications that also include

an advanced chiral BSM sector.

In our studies, we demand anomaly cancellation together with imposing phenomenological constraints to further reduce the number of free parameters in the model building process, which we present at the appropriate place whenever relevant. They can be implemented into an advanced system of equations combining anomaly cancellation and phenomenological input. In order to extract solutions of the system, we use computational algebraic geometry and perform a *Gröbner basis* computation to deduce the most reduced version of the system [118, 120].

In what follows, we give some closing remarks on the ACCs. A set of charges $F_f$ that solves Eq. (5.24) is referred to as a *solution*. In our studies, we exploit the following features.

- Rational solutions:

  We assume that all U(1)′ charges are rational numbers $F_f \in \mathbb{Q}$.

- Rescaling invariance:

  Any solution can be rescaled by any rational number $k \in \mathbb{Q}$, which gives $F_f \to k\,F_f$, $\forall f$, which constitutes another solution. As this rescaling is equivalent to just rescaling the U(1)′ gauge coupling, these solutions are in the same equivalence class and therefore not independent from each other. Hence, we can consider only integer solutions $F_f \in \mathbb{Z}$ without loss of generality.

- Permutation invariance of fermions:

  The ACCs are invariant under the permutation of generation indices within each specific species $f$, which is also known as charge inversion symmetry. However, this degeneracy of charges for each species is lifted whenever additional (phenomenological) constraints, which link certain generations of fermions, are added to the system.

In the next part, we study constraints on $Z'$ couplings due to meson mixing which provides stringent limits on the FCNC quark couplings $g_{L,R}$. While not pivotal to every U(1)′ extension, they need to be considered when studying rare decays.

## 5.3 Meson mixing in $Z'$ models

Up to this point, we have focussed mainly on FCNC transitions $\Delta F = 1$. Here, we briefly discuss FCNCs transitions of $\Delta F = 2$, which induce strong constraints on the NP parameters elaborated so far. The transitions describe neutral meson oscillations that generate mixing between the neutral mesons and their antiparticles. Studies regarding meson mixing have already played a vital role in tests of the SM and its extensions for many years. In addition to their absent tree-level contributions in the SM, they occur within the SM to an excellent approximation only via box diagrams with internal quark and $W$-boson exchanges.

In what follows, we provide constraints from mixing observables on our $Z'$ model couplings that outline the parameter space of NP parameters. Due to our emphasis on charm and $B$-physics, we consider the corresponding $D^0$-$\overline{D}^0$ mixing and $B_s^0$-$\overline{B}_s^0$ mixing effects, with mesons that include up-type and down-type quarks, respectively. We also detail how constraints from kaon oscillations are met. Before that, we shortly review the general formalism.

The time evolution of meson mixing with, *e.g.*, $P = D^0, B_s, \ldots$ is described by the Schrödinger equation and reads [121, 122]

$$\mathrm{i}\frac{\partial}{\partial t}\begin{pmatrix}|P(t)\rangle\\ |\overline{P}(t)\rangle\end{pmatrix} = \mathcal{H}^{\text{mix}}\begin{pmatrix}|P(t)\rangle\\ |\overline{P}(t)\rangle\end{pmatrix} = \left(\tilde{M} - \frac{\mathrm{i}}{2}\tilde{\Gamma}\right)\begin{pmatrix}|P(t)\rangle\\ |\overline{P}(t)\rangle\end{pmatrix}, \tag{5.25}$$

where $\tilde{M}$ and $\tilde{\Gamma}$ denote the mass and decay matrices, respectively. The $CPT$ invariance requires that $M \equiv \tilde{M}_{11} = \tilde{M}_{22}$ and $\Gamma \equiv \tilde{\Gamma}_{11} = \tilde{\Gamma}_{22}$, while the off-diagonal elements obey $M_{12} \equiv \tilde{M}_{12} = \tilde{M}^*_{21}$ and $\Gamma_{12} \equiv \tilde{\Gamma}_{12} = \tilde{\Gamma}^*_{21}$ due to the hermiticity of $\tilde{M}$ and $\tilde{\Gamma}$, respectively. The physical eigenstates $|P_\pm\rangle$, with masses $M_\pm$ and decay rates $\Gamma_\pm$, are obtained by diagonalising the Hamiltonian in Eq. (5.25). The oscillations are parametrised by three physical quantities

$$x_{12} = \frac{2\,|M_{12}|}{\Gamma}, \quad y_{12} = \frac{|\Gamma_{12}|}{\Gamma}, \quad \phi_{12} = \arg\left(\frac{M_{12}}{\Gamma_{12}}\right). \tag{5.26}$$

While the quantities $x_{12}$ and $y_{12}$ are $CP$-conserving, the phase difference $\phi_{12}$ induces $CP$ violation in mixing. The mass and width differences between $P_+$ and $P_-$ are related to them as

$$\Delta M = M_+ - M_- = 2\,|M_{12}|, \quad \Delta\Gamma = \Gamma_+ - \Gamma_- = 2\,|\Gamma_{12}|\,\cos(\phi_{12}), \tag{5.27}$$

where $\Delta M$ is simply the oscillation frequency and $\Gamma = (\Gamma_+ + \Gamma_-)/2$ denotes the average width.

### 5.3.1 Constraints from $D^0$-$\overline{D}^0$ mixing

The $Z'$-couplings $g_L^{cu}$ and $g_R^{cu}$ are subject to constraints from $D^0$-$\overline{D}^0$ mixing, where the dominant tree-level contribution in the SM as well as the contribution via a $Z'$ boson are depicted in Fig. 5.1.

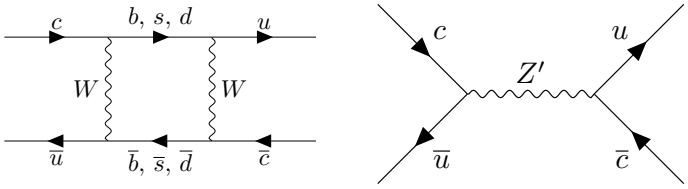


**Figure 5.1:** Dominant contribution to the $D^0$-$\overline{D}^0$ mixing amplitude in the SM via a box-diagram (left-hand side diagram) and via a $Z'$ boson at tree level (right-hand side diagram). For each diagram shown there is also a second one, obtained by a 90° rotation.

To study the impact of $Z'$ contributions to $D^0$-$\overline{D}^0$ mixing observables, we consider the latest *published* world averages of the mixing observables that are collected in Eq. (B.5), where in particular [123]

$$x_{12} \in [0.22\,,\,0.63]\,\%\,, \quad \phi_{12} \in [-2.5^\circ,\,1.8^\circ]\,. \tag{5.28}$$

A recent update of those quantities is available online [124] and provided in Eqs. (7.59) and (B.6). For the $Z'$ models we impose

$$x_{12}^{Z'} \leq x_{12}\,, \quad x_{12}^{Z'}\,\sin\left(\phi_{12}^{Z'}\right) \leq x_{12}\,\sin(\phi_{12})\,, \tag{5.29}$$

since no sufficiently controlled SM predictions of the mixing parameters are available in charm [125]. Following Eq. (5.25), the $\overline{D}^0 - D^0$ transition amplitude reads

$$\langle D^0|\,\mathcal{H}_{\text{eff}}^{\Delta c=2}\,|\overline{D}^0\rangle = \langle D^0|\sum_i c_i\,Q_i\,|\overline{D}^0\rangle = M_{12} - \frac{\mathrm{i}}{2}\,\Gamma_{12}\,. \tag{5.30}$$

The Hamiltonian in Eq. (5.30) includes eight operators generated at the scale $\mu_{\text{NP}} \approx M_{Z'}$ [126],

$$\begin{aligned} Q_1 &= (\overline{u}_L\gamma_\mu c_L)(\overline{u}_L\gamma^\mu c_L)\,, \quad & Q_5 &= (\overline{u}_R\sigma_{\mu\nu} c_L)(\overline{u}_R\sigma^{\mu\nu} c_L)\,,\\ Q_2 &= (\overline{u}_L\gamma_\mu c_L)(\overline{u}_R\gamma^\mu c_R)\,, \quad & Q_6 &= (\overline{u}_R\gamma_\mu c_R)(\overline{u}_R\gamma^\mu c_R)\,,\\ Q_3 &= (\overline{u}_L c_R)(\overline{u}_R c_L)\,, & Q_7 &= (\overline{u}_L c_R)(\overline{u}_L c_R)\,,\\ Q_4 &= (\overline{u}_R c_L)(\overline{u}_R c_L)\,, & Q_8 &= (\overline{u}_L\sigma_{\mu\nu} c_R)(\overline{u}_L\sigma^{\mu\nu} c_R)\,. \end{aligned} \tag{5.31}$$

As the hadronic matrix elements (HMEs) $\langle Q_i\rangle \equiv \langle D^0|\,Q_i\,|\overline{D}^0\rangle$ are computed at the low scale $\mu = m_c$, the RG running of these operators to the NP scale $\mu_{\text{NP}}$ provokes an operator mixing which needs to be taken into account.

In $Z'$ models, the following $\Delta c = 2$ Wilson coefficients are stipulated

$$c_1\,(\mu = M_{Z'}) = \frac{\left(g_L^{cu}\right)^2}{2\,M_{Z'}^2}\,, \quad c_2\,(\mu = M_{Z'}) = \frac{g_L^{cu}\,g_R^{cu}}{M_{Z'}^2}\,, \quad c_6\,(\mu = M_{Z'}) = \frac{\left(g_R^{cu}\right)^2}{2\,M_{Z'}^2}\,, \tag{5.32}$$

while the operator $Q_3$ is radiatively induced and needs to be taken into account as well. Assuming no interference with the SM, we can parametrise the $Z'$ contribution to $x_{12}$ as [126, 127]

$$\begin{aligned} x_{12}^{Z'} = \frac{1}{\Gamma_{D^0} m_{D^0}}\Big| & r_1\,c_1(M_{Z'})\,\langle Q_1\rangle + \sqrt{r_1}\,c_2(M_{Z'})\,\langle Q_2\rangle \\ & + \frac{2}{3}\,c_2(M_{Z'})\,(\sqrt{r_1} - r_1^{-4})\,\langle Q_3\rangle + r_1\,c_6(M_{Z'})\,\langle Q_6\rangle\Big|\,. \end{aligned} \tag{5.33}$$

The renormalisation factor is given by [127]

$$r_1 = r_1(\mu,\,M_{Z'}) = \left(\frac{\alpha_s^{(4)}(m_b)}{\alpha_s^{(4)}(\mu)}\right)^{\frac{6}{25}} \left(\frac{\alpha_s^{(5)}(m_t)}{\alpha_s^{(5)}(m_b)}\right)^{\frac{6}{23}} \left(\frac{\alpha_s^{(6)}(M_{Z'})}{\alpha_s^{(6)}(m_t)}\right)^{\frac{2}{7}}\,, \tag{5.34}$$

where the strong coupling $\alpha_s$ at LO is provided in Eq. (A.30). After inserting the Wilson coefficients in Eq. (5.32) into Eq. (5.33), we derive the formula

$$x_{12}^{Z'} = \frac{r_1\langle Q_1\rangle}{2\,\Gamma_{D^0}\,m_{D^0}}\,\frac{\left|\,\left(g_L^{cu}\right)^2 + \left(g_R^{cu}\right)^2 - X\,g_L^{cu}\,g_R^{cu}\right|}{M_{Z'}^2}\,, \tag{5.35}$$

where

$$X = -2\left(\sqrt{r_1}\,\langle Q_2\rangle + \frac{2}{3}\,(\sqrt{r_1} - r_1^{-4})\,\langle Q_3\rangle\right)\cdot\left(r_1\,\langle Q_1\rangle\right)^{-1}\,. \tag{5.36}$$

Utilising numerical values of the matrix elements given in Eq. (B.7), we obtain the benchmark values $X = 19.2,\ 24.0,\ 26.2$ for $M_{Z'} = 1, 5, 10$ TeV, respectively.

Rearranging Eq. (5.35) and imposing Eq. (5.29) yields the quadratic equation

$$\left|\,\left(g_L^{cu}\right)^2 + \left(g_R^{cu}\right)^2 - X\,g_L^{cu}\,g_R^{cu}\right| \leq \tilde{x}\,, \tag{5.37}$$

that is symmetric in terms of the couplings $g_L^{cu}$ and $g_R^{cu}$, where

$$\tilde{x} = \frac{2\, x_{12}\, \Gamma_{D^0}\, m_{D^0}\, M_{Z'}^2}{r_1 \langle Q_1 \rangle} \in [2.2\,,\, 6.4] \cdot 10^{-7} \left(\frac{M_{Z'}}{\text{TeV}}\right)^2 . \tag{5.38}$$

Here, the allowed 95 % C.L. interval is determined by the experimental limit on $x_{12}$ and the HMEs, *cf.* Eqs. (5.28) and (B.7), respectively. Note that the function $r_1$ also depends on $M_{Z'}$, and we have assumed $M_{Z'} \sim 6$ TeV in Eq. (5.38). In the maximum case of $x_{12}^{Z'} = x_{12}$, we can rewrite Eq. (5.37) as

$$\left| \left(g_L^{cu}\right)^2 + \left(g_R^{cu}\right)^2 - X\, g_L^{cu}\, g_R^{cu} \right| - \tilde{x} = 0\,. \tag{5.39}$$

Solving Eq. (5.39) for $g_{L,R} \neq 0$ yields

$$|g_{L,R}^{cu}| = |g_{R,L}^{cu}| \left( \frac{X}{2} \pm \sqrt{\left(\frac{X^2}{4} - 1\right) + \frac{\tilde{x}}{|g_{R,L}^{cu}|^2}} \right) . \tag{5.40}$$

After employing $\tilde{x} \ll |g_R^{cu}|^2$ and $4/X^2 \ll 1$, the following two cases emerge

$$g_L^{cu} = X\, g_R^{cu} \qquad \text{or} \qquad g_R^{cu} = X\, g_L^{cu} \Leftrightarrow g_L^{cu} = \frac{1}{X}\, g_R^{cu}\,, \tag{5.41}$$

at linear order neglecting terms $\mathcal{O}\,(1/X)$.

In the case of only one non-zero coupling the hierarchy in Eq. (5.41) is obviously irrelevant, and we derive the upper limit

$$|g_{L,R}^{cu}| = \sqrt{\tilde{x}} \lesssim 8.0 \cdot 10^{-4} \left(\frac{M_{Z'}}{\text{TeV}}\right) . \tag{5.42}$$

Let us summarise the main implications of this study. The effects of $Z'$-induced contributions $g_{L,R}^{uc}$ can be strongly constrained by meson mixing. However, we can evade such bounds via a cancellation whenever LH and RH couplings are present, imposing the hierarchy put forward in Eq. (5.41). Throughout this thesis, we implement two different cases, which we anticipate in the following to give the reader a clearer picture of the proposed hierarchy between the couplings.

- In Sec. 6.3, we study the hierarchical $Z'$ models in Eq. (5.41) that evade the $D^0$-$\overline{D}^0$ mixing bounds assuming real-valued couplings.

- In Chap. 7, large $CP$-violating phases and hence complex-valued couplings are of special interest. However, the relation in Eq. (5.41) imposes similar weak phases on both couplings $g_L^{cu}$ and $g_R^{cu}$, which unfortunately kills possible $CP$-violating effects as only SM-like $CP$ phases in $g_L^{cu}$ are viable. For details, we refer to the discussion in Sec. 7.1.4.

### 5.3.2 Constraints from $B^0$-$\overline{B}^0$ mixing

In our $Z'$ framework, the NP contributions with vector (colour-singlet) operators to $B_q$-mixing, $q = s,\, d$, are described by the effective Hamiltonian [128]

$$\mathcal{H}_{\text{eff}}^{\Delta B=2} \supset \frac{4\,G_{\text{F}}}{\sqrt{2}}\, v_{bq}^2 \left[ \mathcal{C}_{bq}^{LL}\, \left(\overline{q}_L \gamma^\mu b_L\right)^2 + \mathcal{C}_{bq}^{RR}\, \left(\overline{q}_R \gamma^\mu b_R\right)^2 + \mathcal{C}_{bq}^{LR}\, \left(\overline{q}_L \gamma^\mu b_L\right) \left(\overline{q}_R \gamma_\mu b_R\right) \right] + \text{h.c.}\,, \quad (5.43)$$

where $v_{bq} = V_{tb}\, V_{tq}^*$ and the Wilson coefficients are given by

$$\mathcal{C}_{bq}^{LL} = \frac{v_{bq}^{-2}}{4\sqrt{2}\, G_{\text{F}}}\, \frac{\left(g_L^{bq}\right)^2}{M_{Z'}^2}\,, \quad \mathcal{C}_{bq}^{RR} = \frac{v_{bq}^{-2}}{4\sqrt{2}\, G_{\text{F}}}\, \frac{\left(g_R^{bq}\right)^2}{M_{Z'}^2}\,, \quad \mathcal{C}_{bq}^{LR} = \frac{\sqrt{2}\, v_{bq}^{-2}}{4\, G_{\text{F}}}\, \frac{g_L^{bq}\, g_R^{bq}}{M_{Z'}^2}\,. \quad (5.44)$$

Here, we focus on transitions with $q = s$, while analogous relations are readily obtained for $B_d$-mixing. In Fig. 5.2, we show the tree-level contributions to the $B_s^0$-$\overline{B}_s^0$ mixing amplitude mediated by a $Z'$ boson.

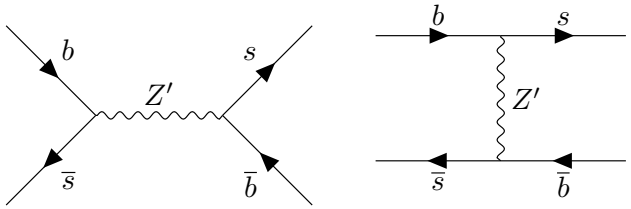


**Figure 5.2:** $B_s^0$-$\overline{B}_s^0$ mixing contributions via a $Z'$ boson at tree level. Similar diagrams for $B_d^0$-$\overline{B}_d^0$ mixing exist when swapping $s$ with $d$ quarks.

Taking the SM predictions as well as the experimental values of the mass differences of the $B$ mesons [128], collected in Eqs. (B.8) to (B.11), within their $2.5\,\sigma$ uncertainties, we obtain the total (SM+NP) contribution normalised to the SM. It reads [21]

$$\frac{\Delta M_{s(d)}^{\text{SM+NP}}}{\Delta M_{s(d)}^{\text{SM}}} \leq 1.156\,(1.154)\,, \quad (5.45)$$

where NP effects in both $B_s$- and $B_d$-mixing can be as large as 15 % compared to the SM.

In what follows, we utilise a similar idea as for $D$-mixing to parametrise NP effects. Provided the limit in Eq. (5.45), we can express the $B_s$-mixing contributions via a $Z'$ boson as [21, 128]

$$\frac{\Delta M_s^{\text{SM+NP}}}{\Delta M_s^{\text{SM}}} = \left| 1 + 200 \left( \frac{5\ \text{TeV}}{M_{Z'}} \right)^2 \cdot \left[ \left(g_L^{bs}\right)^2 + \left(g_R^{bs}\right)^2 - X_s\, g_L^{bs}\, g_R^{bs} \right] \right|, \quad (5.46)$$

with $X_s \approx 10$ for $M_{Z'} \sim 5$ TeV. Notice the similarity to the quadratic equation derived in Eq. (5.39). Applying analogous simplifications, we minimise the NP-effects in $B_s$-mixing with

$$\left(g_L^{bs}\right)^2 + \left(g_R^{bs}\right)^2 - X_s\, g_L^{bs}\, g_R^{bs} = w\,, \quad (5.47)$$

where $w \approx 0$ has to hold, allowing for very small deviations from mixing constraints. Assuming $4/X_s^2 \ll 1$ together with $w/(g_R^{bs})^2 \ll 1$, we solve Eq. (5.47) and re-encounter the hierarchical

structure

$$g_L^{bs} = X_s\, g_R^{bs} \qquad \text{or} \qquad g_L^{bs} = \frac{1}{X_s}\, g_R^{bs}\,. \tag{5.48}$$

For the case of only one non-vanishing coupling, the hierarchy collapses and we find the two equivalent expressions at 99 % C.L. [129]

$$\frac{\left|g_{L,R}^{bs}\right|^2}{M_{Z'}^2} \lesssim 1.24 \cdot 10^{-5}\ \text{TeV}^{-2}\,, \quad \left|g_{L,R}^{bs}\right| \lesssim 3.5 \cdot 10^{-3} \left(\frac{M_{Z'}}{\text{TeV}}\right)\,. \tag{5.49}$$

Constraints from $B_d$-mixing on our $Z'$ models are similar to those coming from $B_s$-mixing as both sectors provide similar room for NP-effects, *cf.* Eq. (5.45), where $Z'$-induced contributions $(g_L^{bq}) \sim v_{bq}$ follow the CKM suppression of the SM. Adapting Eq. (5.46) for $B_d$-mixing [128], we obtain the bound

$$\left|g_{L,R}^{bd}\right| \lesssim 1.1 \cdot 10^{-3} \left(\frac{M_{Z'}}{\text{TeV}}\right)\,, \tag{5.50}$$

assuming only one non-vanishing coupling.

### 5.3.3 Constraints from $K^0$-$\overline{K}^0$ mixing

In the down-sector, $K^0$-$\overline{K}^0$ oscillations can be subject to NP effects and set tight constraints on possible BSM couplings connected to $s \to d$ transitions. A well-suited observable to study short-distance $CP$-violating effects in these transitions is

$$\varepsilon_K = \frac{\kappa_\varepsilon\, e^{\mathrm{i}\,\phi_\varepsilon}}{\sqrt{2}}\, \frac{\text{Im}\left(M_{12}^{K^0}\right)}{\Delta M_K}\,, \tag{5.51}$$

where small corrections from long-distance contributions are encoded in $\kappa_\varepsilon = 0.92 \pm 0.02$ [130]. The phase of $\varepsilon_K$ is experimentally determined as $\phi_\varepsilon = (43.5 \pm 0.5)^\circ$, and $\Delta M_K = (3.484 \pm 0.006) \cdot 10^{-15}$ GeV [32]. The comparison of the SM prediction with the experimental value [32, 131],

$$|\varepsilon_K|_{\text{SM}} = (2.161 \pm 0.183) \cdot 10^{-3}\,, \quad |\varepsilon_K|_{\text{exp}} = (2.228 \pm 0.011) \cdot 10^{-3}\,, \tag{5.52}$$

sets strong constraints on NP contributions.

In this thesis, we avoid BSM contributions to kaon observables by imposing appropriate (universal) charge assignments to the $s$ and $d$ quarks whenever flavour rotations in the down-sector are present. Due to $g_L^{sd} = g_4\, \mathcal{Q}_d^{12} \sim F_{Q_2} - F_{Q_1}$, we set $F_{Q_2} = F_{Q_1}$ to avoid tree-level kaon FCNCs in our $Z'$ models, see Tab. 5.3. For RH quark transitions, we consider mixing only between the second and third generation, stipulated by $F_{D_2} = F_{D_1}$. Moreover, $CP$-violating effects are not induced assuming real-valued Wilson coefficients.

## 5.4 $Z$-$Z'$ kinetic mixing interlude

Additional constraints on NP parameters can be worked out considering kinetic mixing between the abelian sectors. This mixing manifests itself via the parameter $\eta$ (with $|\eta| < 1$) as

$$\mathcal{L}_{\text{mix}} = -\frac{1}{4\,(1-\eta^2)} \begin{pmatrix} B^{\mu\nu} & B'^{\mu\nu} \end{pmatrix} \begin{pmatrix} 1 & -\eta \\ -\eta & 1 \end{pmatrix} \begin{pmatrix} B^{\mu\nu} \\ B'^{\mu\nu} \end{pmatrix} , \tag{5.53}$$

where $B^{\mu\nu}$ and $B'^{\mu\nu}$ are the field strength tensors of the $\mathrm{U}(1)_Y$ and $\mathrm{U}(1)'$ interactions, respectively. As the parameter $\eta$ is not natural, it cannot be switched off by adjusting theory parameters [21]. It also violates the custodial symmetry of the Higgs potential in Eq. (2.11).

For non-trivial kinetic mixing the $\rho$ parameter is altered, $\rho_{\text{SM}} = 1$ as in Eq. (2.18), and reads

$$\rho^{-1} = 1 + \frac{\eta^2 \,\sin^2(\theta_{\text{W}})}{1-z^2} \quad \text{with} \quad z = \left(\frac{M_Z}{M_{Z'}}\right)\Bigg|_{\eta=0} . \tag{5.54}$$

Yet, a global fit of electroweak precision parameters [32],

$$\rho = 1.00039 \pm 0.00019\,, \tag{5.55}$$

suggests a NP contribution of the opposite sign. Therefore, without any cancellations from other sources, kinetic mixing is expected to be subleading at the electroweak scale, which necessitates

$$|\eta| \lesssim \mathcal{O}\left(10^{-2}\right). \tag{5.56}$$

Implications of this are studied in Chap. 8. For details on accidental symmetries and kinetic mixing involving $Z'$ bosons facing the $B$-anomalies see, *e.g.*, Ref. [13].

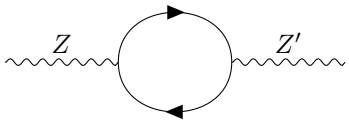


**Figure 5.3:** Kinetic mixing induced by the $\mathrm{U}(1)_Y$ and $\mathrm{U}(1)'$ gauge bosons with a fermion loop.

Another way to prevent large kinetic mixing contributions is to impose a cancellation of the one-loop diagram depicted in Fig. 5.3. This can be realised if $\sum_f Y_f\, F_f = 0$ [132], which translates into a linear equation of the $\mathrm{U}(1)'$ charges to fermions,

$$\sum_{i=1}^{3} \left(F_{Q_i} - F_{L_i} + 2\,F_{U_i} - F_{D_i} - F_{E_i}\right) = 0\,. \tag{5.57}$$

For instance, the anomaly-free $Z'$ models 1, 2, 4, 5, 9, 10, and 10$\mu$ presented in Tabs. 6.1 and 7.3 satisfy Eq. (5.57), and therefore one-loop contributions to kinetic mixing are cancelled in these models. This is due to them featuring $\sum_{i=1}^{3} F_{f_i} = 0$, where $f = \{Q, U, D, \ldots\}$, and hence all linear ACCs in Eq. (5.24) and Eq. (5.57) are fulfilled by this construction.

## 5.5 Generic Landau poles in U(1)′ extensions

We recall from Sec. 3.1 that Landau poles in the RG flow indicate the breakdown of perturbation theory. In what follows, we review bounds on arising Landau poles in U(1)′ extensions.

As outlined in Sec. 3.4, an explanation of the $B$-anomalies requires sizeable NP couplings. In our case, $\mathcal{O}(1)$ couplings induced by a tree-level mediator dictate a scale of about 40 TeV [133, 134], while generic lower bounds on the heavy $Z'$ mass yield a NP scale of $\mu_0 \simeq 5$ TeV [135]. Then, assuming a minimal model set-up to induce the $b \to s\,\mu^+\mu^-$ transition via flavour mixing, we estimate [21]

$$\alpha_4\,(\mu_0 = 5\text{ TeV}) \sim \frac{1}{(4\,\pi)^2}\,\frac{(5\text{ TeV}/40\text{ TeV})^2}{V_{tb}\,V_{ts}^*\,F_{L_2}\,F_{Q_3}} \sim \frac{1}{40\,\pi^2}\,\frac{1}{F_{L_2}\,F_{Q_3}} \tag{5.58}$$

for the U(1)′ gauge coupling $\alpha_4 = g_4^2/(4\pi)^2$. The running of the gauge coupling as in Eq. (3.19) implies a Landau pole at high energies. Interestingly, we find that the one-loop coefficient $B_4$ is bounded from below by the minimal amount of U(1)′ charges necessary to explain the $B$-anomalies while simultaneously avoiding gauge anomalies through Eq. (5.24). We derive the bound

$$B_4 \gtrsim \frac{16}{3}\left(F_{L_2}^2 + 3\,F_{Q_3}^2\right)\,, \tag{5.59}$$

which together with Eq. (5.58) yields

$$\ln\left(\frac{\mu_{\rm LP}}{\mu_0}\right) = \frac{1}{B_4\,\alpha_4(\mu_0)} = \frac{15\,\pi^2}{2}\,\frac{F_{L_2}\,F_{Q_3}}{F_{L_2}^2 + 3\,F_{Q_3}^2} \lesssim \frac{15\,\pi^2}{4\,\sqrt{3}}\,. \tag{5.60}$$

On a quantitative level, this relation can be translated into an upper bound for the scale of the Landau pole,

$$\mu_{\rm LP} \lesssim 10^{13}\text{ GeV} \ll \mu_{\rm Pl} \sim 10^{19}\text{ GeV}\,. \tag{5.61}$$

Here we make a few remarks. First, we note that by introducing additional U(1)′ couplings to SM or BSM particles the Landau pole is shifted towards (significantly) lower energies. Figure 5.4 displays the RG evolution of couplings in a benchmark model with beyond-minimal U(1)′ charge assignment that yields a putative Landau pole at roughly $\mu_{\rm LP} \approx 3 \cdot 10^7$ GeV. The scenario corresponds to a benchmark model $\text{BM}_3$ discussed in Sec. 8.3, where possible BSM fields have been explicitly decoupled. The scale of the Landau pole is further reduced if additional couplings to BSM particles are introduced. Yet, there are ways to lift or mitigate the generic bound in Eq. (5.61) provided fine-tuning assumptions. For example, larger $bs$-mixing angles in the LH quark sector can be generated by assuming strong cancellations between $V_d$ and $V_u$, which lowers $\alpha_4(\mu_0)$ in Eq. (5.58). However, we have discarded this possibility in our studies. Another way to reduce $\alpha_4(\mu_0)$ is to assume a smaller $Z'$ mass. This becomes feasible in models with first- and second-generation quarks being uncharged under the U(1)′, evading the limits from $pp$-production [135, 136]. Nonetheless, while exploring such a setting, it is still possible to find Landau poles below the Planck scale even for scenarios with $M_{Z'} \gtrsim 1.8$ TeV and decoupled BSM fields [20]. On a last note, one might consider explaining the $B$-anomalies with substantially lighter $Z'$ bosons (that is $M_{Z'} \lesssim 150$ GeV) as studied in, *e.g.*, Ref. [134]. While fine-tuned flavour mixing is still of the essence, it may be possible to push the Landau pole beyond Planckian energies. Yet, the in- or metastability of the Higgs potential remains present in these scenarios [21].

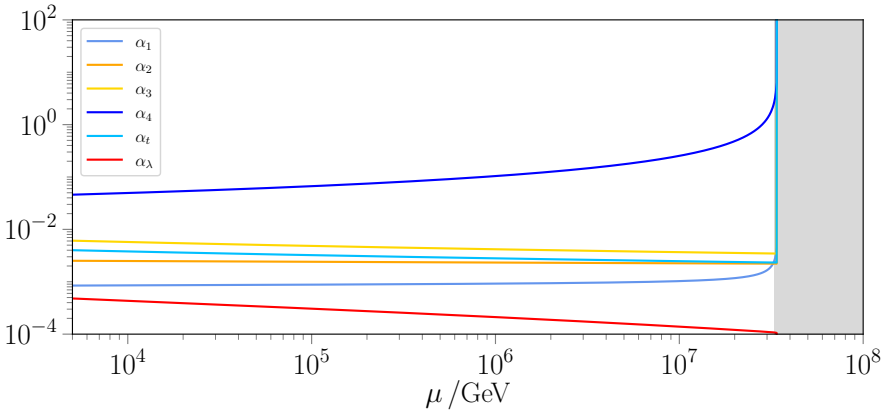


**Figure 5.4:** RG evolution of couplings in am U(1)′ extension of the SM as in the benchmark scenario $BM_3$ discussed in Sec. 8.3, *without* any BSM fields, see Chap. 8 for details. The U(1)′ gauge coupling $\alpha_4$ runs into a Landau pole at $\mu_{\rm LP} \approx 3 \cdot 10^7$ GeV. For consistency, the RGEs are solved at two-loop accuracy for all couplings [21, 50].

### 5.5.1 Planck safety essentials

A concept to both tackle the Landau pole problem as well as stabilise the scalar potential is the *Planck safety approach*. In general terms, such Planck-safe theories are characterised by the absence of Landau poles and instabilities up to Planckian energies.

One possible way of constructing Planck-safe models is described in the following. It is well established that Landau poles can be delayed or even removed by new Yukawa interactions, slowing down the growth of the gauge couplings due to counteracting contributions in the $\beta$-functions [137, 138]. These Yukawa interactions can be integrated by introducing a rich scalar and fermionic BSM particle content. Then, extensions of the SM may be realised in which Landau poles are moved towards higher energies, possibly even beyond the Planck scale where quantised gravity effects become strong. By doing so, new constraints on the BSM matter fields and their interactions are introduced. Moreover, the instabilities in the scalar Higgs sector are avoided by certain conditions complementary to phenomenological ones [139, 140].

In conclusion, Planck-safe model building can be realised given a flavourful BSM sector where both fermions and scalars are instrumental. While new Yukawa and quartic couplings play an important role in delaying putative Landau poles, the Higgs can be stabilised by, *e.g.*, portal couplings. As studied intensively over the past years, it is possible to find trajectories of the RG flow that run into fixed points at highest scales and remove the arising Landau pole altogether known as *asymptotic safety* [141–146]. In this thesis, we do not study the BSM parameter space for fixed points of the theory, but instead scan for viable coupling trajectories that remain physical and perturbative, *i.e.* $0 \leq \alpha_i \leq 1$, up to the Planck scale. For recent studies of Planck-safe model building concerning the $(g-2)_\mu$ anomalies see Ref. [139], whereas aspects of flavour via Higgs portal couplings are provided in, *e.g.*, Refs. [140, 147]. For more details, the reader is encouraged to consult the cited literature and references therein.

Chapter 8 is dedicated to studies of Planck-safe model building explaining the $B$-anomalies with flavourful $Z'$ models. Therein, we give details on the particle content and review conditions on the couplings and U(1)′ charges considered.

Chapter

6

# Flavourful U(1)′ extensions in semileptonic charm decays

After providing the most important ingredients to $Z'$ model building in the previous chapter, we begin our investigations of NP-effects in rare charm decays which have been published in Refs. [16, 17]. In this chapter, we study implications in semileptonic FCNC $c\to u\,\ell^+\ell^-$ transitions, whereas NP studies of $CP$-violating observables and $U$-spin-breaking in hadronic charm decays are discussed in the subsequent Chap. 7.

First, we introduce the EFT description of $c\to u\,\ell^+\ell^-$ transitions and discuss model-independent bounds on Wilson coefficients in Sec. 6.1. In Sec. 6.2, we work out limits on possible $Z'$ contributions. Afterwards, Sec. 6.3 deals with $Z'$ models that feature a certain hierarchical structure able to evade tight constraints from $D$-mixing entailing sizeable effects in charm observables. Due to the resonant pollution and poor convergence of the heavy quark expansion [148], SM null tests are indispensable in this sector and are discussed in Sec. 6.4. Therein, we put a special emphasis on tests that benefit from $Z'$ contributions.

## 6.1 Effective description of $c\to u\,\ell^+\ell^-$ transitions

In the SM, the FCNC $|\Delta c| = |\Delta u| = 1$ transitions appear at one-loop level as depicted in the left-hand side diagram of Fig. 2.2. Contrary to studies of kaon or $B$-physics, internal down-type quarks $(d, s, b)$ propagate in the loop of $c\to u$ transitions. The corresponding weak amplitude can be expressed as [149]

$$\mathcal{A}(c\to u) = \lambda_s\,\left(f_s - f_d + \xi_b\,[f_b - f_d]\right)\,, \quad |\xi_b| = |\lambda_b/\lambda_s| \sim 10^{-3}\,, \tag{6.1}$$

with CKM factors $\lambda_q = V_{cq}^* V_{uq}$ encoding $CP$-violating phenomena in the SM. Here, $f_q$ denotes the loop function defined after Eq. (2.40). The strong GIM suppression in these transitions is made clear evaluating the leading term in Eq. (6.1), which yields a naive estimation of $\mathcal{A}(c\to u) \sim 10^{-8}$. Moreover, $CP$ asymmetries induced by $|\xi_b|$ are suppressed as well. Due to the combination of both strong CKM and GIM suppression, the short-distance contributions in the SM are currently well below experimental reach. That being said, electroweak contributions within the SM can differ by several orders of magnitude depending on which contributions are taken into account [150], while also being shielded by resonance contributions. Therefore, a robust theoretical framework is instrumental to provide calculations beyond the naive estimation of the SM contribution.

Using the OPE, we can treat the short-distance and long-distance dynamics separately. However, the determination of non-perturbative dynamics at low energies within a robust EFT framework

proves challenging in charm due to $\Lambda_{\rm QCD} \sim m_c$, which hinders the convergence of the perturbative expansion in powers of $1/m_c$. Therefore, the computation of the HMEs with naive factorisation is not entirely reliable. The main OPE set-up is described for example in Ref. [151], where a consistent expansion of the full SM computation for rare charm transitions to $\mathcal{O}(\alpha_s)$ within RG-improved perturbation theory is available. In what follows, we outline the short- and long-distance description.

### 6.1.1 Short-distance description

The effective Hamiltonian that describes rare $c \to u\,\ell^+\ell^-$ processes is given by [72, 152]

$$\begin{aligned}\mathcal{H}_{\rm eff}^{cu\ell\ell} \supset -\frac{4G_{\rm F}}{\sqrt{2}}\frac{\alpha_e}{4\pi}\Bigg[\mathcal{C}_7\,O_7 + \mathcal{C}_7'\,O_7' + \sum_{\ell=e,\mu,\tau}\sum_{i=9,10,S,P}\left(\mathcal{C}_i^{\ell\ell}O_i^{\ell\ell} + \mathcal{C}_i'^{\ell\ell}O_i'^{\ell\ell}\right) + \sum_{i=T,T5}\mathcal{C}_i^{\ell\ell}O_i^{\ell\ell}\Bigg] \\ + \frac{4G_{\rm F}}{\sqrt{2}}\Bigg[\sum_{q=d,s}V_{cq}^*V_{uq}\sum_{i=1}^{2}\mathcal{C}_i O_i^q\Bigg]\,,\end{aligned} \tag{6.2}$$

with the dimension-six operators

$$\begin{aligned} O_7 &= \frac{m_c}{e}\,(\overline{u}_L\,\sigma_{\mu\nu}\,c_R)F^{\mu\nu}\,, \\ O_9^{\ell\ell} &= (\overline{u}_L\gamma_\mu c_L)(\overline{\ell}\gamma^\mu\ell)\,, & O_{10}^{\ell\ell} &= (\overline{u}_L\gamma_\mu c_L)(\overline{\ell}\gamma^\mu\gamma_5\ell)\,, \\ O_S^{\ell\ell} &= (\overline{u}_L c_R)(\overline{\ell}\ell)\,, & O_P^{\ell\ell} &= (\overline{u}_L c_R)(\overline{\ell}\gamma_5\ell)\,, \\ O_T^{\ell\ell} &= \frac{1}{2}(\overline{u}\,\sigma_{\mu\nu}\,c)(\overline{\ell}\,\sigma^{\mu\nu}\,\ell)\,, & O_{T5}^{\ell\ell} &= \frac{1}{2}(\overline{u}\,\sigma_{\mu\nu}\,c)(\overline{\ell}\,\sigma^{\mu\nu}\gamma_5\,\ell)\,. \end{aligned} \tag{6.3}$$

The operators $O_i'$, where $i = 7, 9, 10, S, P$, are obtained by interchanging left-handed and right-handed chiral fields. In the following, we suppress the lepton indices for both the coefficients and operators to improve readability. The Wilson coefficients in Eq. (6.3) include SM and NP contributions. However, in the SM no (pseudo)scalar and (pseudo)tensor operators are present, therefore $\mathcal{C}_{S,P,T,T5}^{\rm SM} = 0$. In addition, the SM favours LH contributions while all $\mathcal{C}_i'$ are negligible.

Most notably, as the underlying FCNC transition resides in the up-sector, the GIM mechanism removes penguin contributions to $O_{7,9,10}$ at the $W$-scale $\mu_W$, where the lights quark masses are set to zero [153]. Only the *current-current* operators

$$O_1^q = (\overline{u}_L\gamma_\mu t^a q_L)(\overline{q}_L\gamma^\mu t^a c_L)\,, \quad O_2^q = (\overline{u}_L\gamma_\mu q_L)(\overline{q}_L\gamma^\mu c_L)\,, \quad q = d,\,s\,, \tag{6.4}$$

induce effective SM contributions to $O_{7,9,10}$ through RG running down to the charm scale $\mu_c$. The four-quark operators in Eq. (6.4) also dominate pure hadronic decays, such as $D \to KK$ and $D \to \pi\pi$ with details provided in App. F.1. Following Refs. [153, 154], we can estimate

$$\mathcal{C}_7^{\rm eff}(q^2 \approx 0) \simeq -0.0011 - 0.0041\,{\rm i}\,, \tag{6.5}$$

$$\mathcal{C}_9^{\rm eff}(q^2) \simeq -0.021\,[V_{cd}^*V_{ud}\,L(q^2, m_d, \mu_c) + V_{cs}^*V_{us}\,L(q^2, m_s, \mu_c)]\,, \tag{6.6}$$

where $q^2$ denotes the dilepton invariant mass squared and the function $L(q^2, m_q, \mu_c)$ accounts for the low dynamical effects stipulated by $m_q \neq 0$. See Ref. [154] for the explicit form of $L(q^2, m_q, \mu_c)$. We find that $\mathrm{Im}(\mathcal{C}_7^{\rm eff})$ increases from $-0.004$ at $q^2 = 0$ to $-0.0014$ at high $q^2$ at next-to-next-to-leading order (NNLO), whereas $|\mathcal{C}_9^{\rm eff}| \lesssim 0.01$ for $\mu_c = m_c = 1.275$ GeV [153]. Moreover, it is

$\mathcal{C}_{10}^{\rm SM} = 0$ which delimits charm FCNC from $B$ or kaon physics, and implies that effects from the $(V-A)$-structure of the weak interaction are shut off at the charm scale. To summarise, the vanishing Wilson coefficients read

$$\mathcal{C}_i'^{\rm SM} = \mathcal{C}_S^{\rm SM} = \mathcal{C}_{T,T5}^{\rm SM} = \mathcal{C}_{10}^{\rm SM} = 0\,. \tag{6.7}$$

As displayed in Fig. 6.1, we find that in $D \to P\ell^+\ell^-$ decay rates, $P = K,\,\pi$, the short-distance SM contributions are negligible compared to the long-range resonance-induced effects, thus schematically $\mathcal{C}_9^{\rm SM} = \mathcal{C}_9^{\rm eff} + \mathcal{C}_9^{\rm R} \simeq \mathcal{C}_9^{\rm R}$. Due to our focus on NP effects, we follow our established notation put forward for rare $B$-decays in Eq. (3.44), and refer to pure BSM $c \to u\,\ell^+\ell^-$ Wilson coefficients as $\mathcal{C}_{i,\ell}^{(\prime)}$ in this chapter to enhance readability whenever possible.

### Lepton flavour violating contributions

Since lepton flavour violation is basically not present in the SM, observables sensitive to such contributions provide clear signs of BSM physics if measured by experiment.

In our EFT approach, we can add operators that induce LFV in $c \to u\,\ell^-\ell'^+$ decays as [16]

$$\mathcal{H}_{\rm eff}^{\rm LFV} = -\frac{4G_{\rm F}}{\sqrt{2}}\frac{\alpha_e}{4\pi}\sum_i \left(\mathcal{K}_i^{\ell\ell'} O_i^{\ell\ell'} + \mathcal{K}_i'^{\ell\ell'} O_i'^{\ell\ell'}\right)\,, \tag{6.8}$$

with $\ell \neq \ell'$. In this chapter, the $\mathcal{K}_i^{(\prime)}$ denote lepton flavour violating Wilson coefficients where the operators $O_i^{(\prime)}$ are constructed using the corresponding analogue of the operators in Eq. (6.2) changing the flavour in the lepton currents accordingly. In Eq. (6.8), no $O_7^{(\prime)}$ contribution exists as the photon does not couple to different lepton flavours.

## 6.1.2 Long-distance description

The lack of knowledge about the hadronic effects in a hadronic transition is parametrised by so-called form factors. The hadronisation of the operators in Eq. (6.3) yields a factorisation between the lepton and quark currents written as [149]

$$\langle h_c|\,O_i\,|F\,\ell^+\ell^-\rangle = \langle h_c|\,H^i_{\alpha_i,\ldots,\alpha_n}\,|F\rangle\;\langle 0|\,L_i^{\alpha_i,\ldots,\alpha_n}\,|\ell^+\ell^-\rangle\,, \tag{6.9}$$

where $h_c$ denotes a charged charmed hadron and $F$ is the final state. The quark and lepton currents, $H^i_{\alpha_i,\ldots,\alpha_n}$ and $L_i^{\alpha_i,\ldots,\alpha_n}$, share the Lorentz indices $\alpha_1,\ldots,\alpha_n$. While perturbation theory in QED allows for the computation of $\langle 0|\,L_i^{\alpha_i,\ldots,\alpha_n}\,|\ell^+\ell^-\rangle$, non-perturbative techniques are required to evaluate $\langle h_c|\,H^i_{\alpha_i,\ldots,\alpha_n}\,|F\rangle$, which encodes the hadronic dynamics at low energies. In the case of a $D$ meson decaying into a pseudoscalar $P$, we are able to describe the vector ($n=1$) and tensor currents ($n=2$) using $q^2$-dependent functions known as form factors. The relevant $D \to P$ form factors are denoted by $f_i(q^2)$, $i = 0, +, T$, where details and requisite input are given in App. E.3. A comprehensive overview of available form factors for various charm decays can be found in Ref. [149].

The dominant contributions to the operators $O_{9,P}$ result from $D \to P\,\gamma^*$ processes with $\gamma^* \to M \to \ell^+\ell^-$, where the different resonances $M = \rho,\,\phi,\,\eta,\,\eta'$ present in the low-$q^2$ region are annotated in Fig. 6.1.

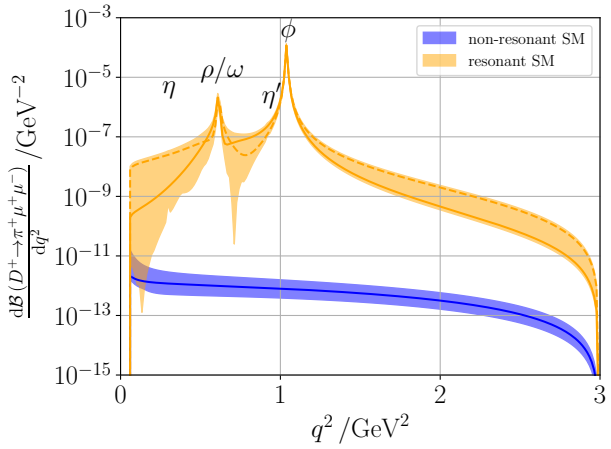


**Figure 6.1:** The differential branching ratio of the $D^+ \to \pi^+\mu^+\mu^-$ decay in the SM. The yellow (blue) bands show pure resonant (short-distance) contributions. The band widths represent theoretical uncertainties of hadronic form factors, resonance parameters and $m_c$. Darker shaded thin curves illustrate all parameters set to their central values with $\delta_\rho = 0$ and $\delta_\phi = \pi$ (solid) and $\delta_\rho = \delta_\phi = 0$ (dashed). We annotate the resonances $M = \rho,\, \phi,\, \eta,\, \eta'$ in the low-$q^2$ region. *Figure adapted from Ref.* [16].

Their phenomenological shape comprises Breit-Wigner distributions and is given by

$$\begin{aligned}
\mathcal{C}_9^{\mathrm{R}}(q^2) &= a_\rho e^{\mathrm{i}\,\delta_\rho}\left(\frac{1}{q^2 - m_\rho^2 + \mathrm{i}\, m_\rho \Gamma_\rho} - \frac{1}{3}\frac{1}{q^2 - m_\omega^2 + \mathrm{i}\, m_\omega \Gamma_\omega}\right) + \frac{a_\phi e^{\mathrm{i}\,\delta_\phi}}{q^2 - m_\phi^2 + \mathrm{i}\, m_\phi \Gamma_\phi}\,, \\
\mathcal{C}_P^{\mathrm{R}}(q^2) &= \frac{a_\eta e^{\mathrm{i}\,\delta_\eta}}{q^2 - m_\eta^2 + \mathrm{i}\, m_\phi \Gamma_\eta} + \frac{a_{\eta'}}{q^2 - m_{\eta'}^2 + \mathrm{i}\, m_{\eta'} \Gamma_{\eta'}}\,,
\end{aligned} \tag{6.10}$$

where $m_M$ and $\Gamma_M$ denote the mass and the total decay rate of the resonance $M$, respectively. As this parametrisation features various parameters, one has to employ simplifying assumptions and utilise experimental input to reduce and, subsequently, determine as many parameters as possible. In Eq. (6.10), the isospin limit $a_\omega = a_\rho/3$ has been used to reduce the input and the corresponding theoretical uncertainties. The $a_M$ parameters can be found in Tab. E.1 and have been computed from measurements of branching ratios $\mathcal{B}(D \to PM)$ and $\mathcal{B}(M \to \mu^+\mu^-)$ [155]. However, the strong phases $\delta_{\rho,\phi,\eta}$ remain undetermined and yield a large source of uncertainty illustrated by the respective (yellow) bands in Fig. 6.1, which are varied numerically within $[-\pi, \pi]$. Due to the challenging theoretical description of such resonant-dominated decays, further investigations are required. For studies on resonance effects utilising the QCD factorisation approach see, *e.g.*, Refs. [148, 156, 157]. In App. E, we provide explicit expressions of the (differential) branching ratios of semileptonic and fully leptonic $D \to \pi$ decays.

### 6.1.3 Constraints on new physics Wilson coefficients

Here, we derive model-independent bounds on Wilson coefficients in charm, which can be used to limit NP contributions in extensions of the SM such as $Z'$ models. For instance, Wilson coefficients can be constrained by the updated experimental upper limits on the $D^+ \to \pi^+\mu^+\mu^-$ branching

ratio at 90 % C.L. [158],

$$\mathcal{B}\left(D^+ \to \pi^+\mu^+\mu^-\right) < 6.7 \cdot 10^{-8}\,. \tag{6.11}$$

Using the branching ratio parametrisation in Eq. (E.1), we obtain [16, 149]

$$\begin{aligned} &1.3\,|\mathcal{C}_7|^2 + 1.3\,|\mathcal{C}_9|^2 + 1.3\,|\mathcal{C}_{10}|^2 + 2.6\,|\mathcal{C}_S|^2 + 2.7\,|\mathcal{C}_P|^2 + 0.4\,|\mathcal{C}_T|^2 + 0.4\,|\mathcal{C}_{T5}|^2 \\ &+ 0.3\,\mathrm{Re}\left(\mathcal{C}_9\,\mathcal{C}_T^*\right) + 1.1\,\mathrm{Re}\left(\mathcal{C}_{10}\,\mathcal{C}_P^*\right) + 2.6\,\mathrm{Re}\left(\mathcal{C}_7\,\mathcal{C}_9^*\right) + 0.6\,\mathrm{Re}\left(\mathcal{C}_7\,\mathcal{C}_T^*\right) \lesssim 1\,, \end{aligned} \tag{6.12}$$

where only BSM Wilson coefficients to muons are considered and RH currents are implicitly included as $\mathcal{C}_i \to \mathcal{C}_{i,\mu} + \mathcal{C}'_{i,\mu}$ to ease the notation. Analogously, the upper limit $\mathcal{B}\left(D^0 \to \mu^+\mu^-\right) < 6.2 \times 10^{-9}$ [159] inserted into Eq. (E.3) yields

$$|\mathcal{C}_S - \mathcal{C}'_S|^2 + |\mathcal{C}_P - \mathcal{C}'_P + 0.1\,\left(\mathcal{C}_{10} - \mathcal{C}'_{10}\right)|^2 \lesssim 0.007\,, \tag{6.13}$$

and provides the best constraints on NP contributions to $\mathcal{C}_{10}^{(\prime)}$ for muons. Bounds on lepton flavour violating Wilson coefficients can be extracted from the limits $\mathcal{B}\left(D^+ \to \pi^+ e^\pm \mu^\mp\right) < 210(220) \cdot 10^{-9}$ and $\mathcal{B}\left(D^0 \to e^\pm \mu^\mp\right) < 13 \cdot 10^{-9}$ at 90 % C.L. [158, 160]. With the corresponding branching ratio formulae given in Eqs. (E.4) and (E.5), we find

$$\begin{aligned} &0.4\,|\mathcal{K}_9|^2 + 0.4\,|\mathcal{K}_{10}|^2 + 0.9\,|K_S|^2 + 0.9\,|\mathcal{K}_P|^2 + 0.1\,|\mathcal{K}_T|^2 + 0.1\,\left|\mathcal{K}_{T5}\right|^2 \\ &+0.2\,\mathrm{Re}\left(\mathcal{K}_{10}\,\mathcal{K}_P^* \pm \mathcal{K}_9\,\mathcal{K}_S^*\right) + 0.1\,\mathrm{Re}\left(\mathcal{K}_9\,\mathcal{K}_T^* \pm \mathcal{K}_{10}\,\mathcal{K}_{T5}^*\right) \lesssim 1\,, \end{aligned} \tag{6.14}$$

$$|\mathcal{K}_S - \mathcal{K}'_S \pm 0.04\,\left(\mathcal{K}_9 - \mathcal{K}'_9\right)|^2 + |\mathcal{K}_P - \mathcal{K}'_P \pm 0.04\,\left(\mathcal{K}_{10} - \mathcal{K}'_{10}\right)|^2 \lesssim 0.01\,, \tag{6.15}$$

with $\mathcal{K}_i = \mathcal{K}_{i,\mu e} + \mathcal{K}'_{i,\mu e}$ and $\mathcal{K}_i = \mathcal{K}_{i,e\mu} + \mathcal{K}'_{i,e\mu}$ for $D \to P\,e^+\mu^-$ and $D \to P\,e^-\mu^+$, respectively. For a summary of constraints on a plethora of NP Wilson coefficients and future prospects in charm decays see Ref. [149].

## 6.2 New physics effects in rare charm decays

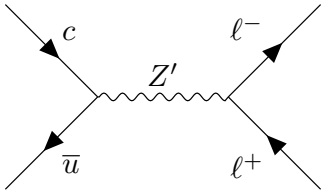


**Figure 6.2:** Tree-level diagram of a $c \to u\,\ell^+\ell^-$ transition via a $Z'$ boson.

While in the SM contributions to $c \to u\,\ell^+\ell^-$ processes are highly suppressed, NP contributions via a $Z'$ boson can be generated at tree level as depicted in Fig. 6.2. We describe the relevant effective Hamiltonian by

$$\begin{aligned} \mathcal{H}_{Z'}^{cu\ell\ell} \supset &\left(g_L^{cu}\,\bar{u}_L\gamma^\mu c_L Z'_\mu + g_R^{cu}\,\bar{u}_R\gamma^\mu c_R Z'_\mu + \text{h.c.}\right) \\ &+ g_L^{\ell\ell'}\,\bar{\ell}_L\gamma^\mu \ell'_L Z'_\mu + g_R^{\ell\ell'}\,\bar{\ell}_R\gamma^\mu \ell'_R Z'_\mu\,. \end{aligned} \tag{6.16}$$

After integrating out the $Z'$ boson and matching Eq. (6.16) with the Hamiltonian in Eq. (6.2), the

following Wilson coefficients are induced

$$\begin{aligned}\mathcal{C}_{9/10,\ell} &= -\frac{\pi}{\sqrt{2}\,G_{\rm F}\,\alpha_e}\,\frac{g_L^{cu}\left(g_R^{\ell\ell}\pm g_L^{\ell\ell}\right)}{M_{Z'}^2}\,,\\ \mathcal{C}'_{9/10,\ell} &= -\frac{\pi}{\sqrt{2}\,G_{\rm F}\,\alpha_e}\,\frac{g_R^{cu}\left(g_R^{\ell\ell}\pm g_L^{\ell\ell}\right)}{M_{Z'}^2}\,,\end{aligned} \tag{6.17}$$

where we have made the lepton index explicit to distinguish different lepton currents. One may also introduce the corresponding lepton flavour violating coefficients

$$\begin{aligned}\mathcal{K}_{9/10,\ell\ell'} &= -\frac{\pi}{\sqrt{2}\,G_{\rm F}\,\alpha_e}\,\frac{g_L^{cu}\left(g_R^{\ell\ell'}\pm g_L^{\ell\ell'}\right)}{M_{Z'}^2}\,,\\ \mathcal{K}'_{9/10,\ell\ell'} &= -\frac{\pi}{\sqrt{2}\,G_{\rm F}\,\alpha_e}\,\frac{g_R^{cu}\left(g_R^{\ell\ell'}\pm g_L^{\ell\ell'}\right)}{M_{Z'}^2}\,,\end{aligned} \tag{6.18}$$

where $\ell'\neq\ell$ is understood and we recover $\mathcal{C}_{i,\ell}=\mathcal{K}_{i,\ell\ell'}$ for $\ell'=\ell$.

The bounds in Eqs. (6.12) to (6.14) can be translated into limits on the NP couplings $g_{L,R}^{cu}$ and $g_{L,R}^{\ell\ell'}$ of our effective $Z'$ framework using Eqs. (6.17) and (6.18). At this point, we provide the limits that are given in the published version of Ref. [16], as well as updated values employing the latest experimental input available. The lepton flavour conserving bounds read

$$D^+\to\pi^+\mu^+\mu^-: \qquad \left|g_L^{cu}+g_R^{cu}\right|\sqrt{\left|g_L^{\mu\mu}\right|^2+\left|g_R^{\mu\mu}\right|^2}\lesssim 0.02\,[0.04]\left(\frac{M_{Z'}}{\rm TeV}\right)^2\,, \tag{6.19}$$

$$D^0\to\mu^+\mu^-: \qquad \left|(g_L^{cu}-g_R^{cu})(g_L^{\mu\mu}-g_R^{\mu\mu})\right|\lesssim 0.03\left(\frac{M_{Z'}}{\rm TeV}\right)^2\,, \tag{6.20}$$

where the value in brackets denotes the outdated limit from Ref. [16]. Similarly, we obtain

$$D^+\to\pi^+e^\pm\mu^\mp: \qquad \left|g_L^{cu}+g_R^{cu}\right|\sqrt{\left|g_L^{\mu e}\right|^2+\left|g_R^{\mu e}\right|^2}\lesssim 0.04\,[0.17]\left(\frac{M_{Z'}}{\rm TeV}\right)^2\,, \tag{6.21}$$

$$D^0\to e^\pm\mu^\mp: \qquad \left|g_L^{cu}-g_R^{cu}\right|\sqrt{\left|g_L^{\mu e}\right|^2+\left|g_R^{\mu e}\right|^2}\lesssim 0.07\left(\frac{M_{Z'}}{\rm TeV}\right)^2\,, \tag{6.22}$$

from the lepton flavour violating decays.

## 6.3 Hierarchical $Z'$ models

In what follows, we study $Z'$ models that generate sizeable NP effects in charm, while satisfying the limits derived in Eqs. (6.19) to (6.22). However, the tightest constraints are due to $D^0$-$\overline{D}^0$ mixing which demands $|g_{L,R}^{cu}|\lesssim 8.0\cdot 10^{-4}$ in the case of only one non-zero coupling, see Eq. (5.42). Then, assuming $\mathcal{O}(1)$ muon couplings in Eqs. (6.19) and (6.20), we find BSM Wilson coefficients

$$\mathcal{C}_{9/10,\mu}^{(\prime)}\lesssim\mathcal{O}\left(10^{-2}\right), \tag{6.23}$$

consistent with limits worked out in Refs. [161, 162].

As promoted in Sec. 5.3.1, we can evade the mixing bound by assuming so-called hierarchical couplings. In this case, it is possible to satisfy the mixing constraints for both $g_L^{cu} \neq 0$ and $g_R^{cu} \neq 0$ even with arbitrarily large values that obey the hierarchy in Eq. (5.41),

$$g_L^{cu} = X\, g_R^{cu} \qquad \text{or} \qquad g_L^{cu} = \frac{1}{X}\, g_R^{cu}\,, \tag{6.24}$$

with $X \approx 20$ assuming $M_{Z'}$ in the TeV-range. Consequently, NP effects are only bounded by the constraints from semileptonic decays in Eqs. (6.19) to (6.22).

We investigate this set-up in the context of anomaly-free $Z'$ models assuming real couplings and no weak phases $\phi_R = 0$, *i.e.* no $CP$-violating effects. In doing so, we follow the model building guidelines established in Chap. 5:

- The U(1)$'$ charges $F_f$ of the SM fermions and (possible) new fermions satisfy the ACCs listed in Eq. (5.24).
- We focus on FCNC transitions solely in the up-quark sector, and hence evade the strong constraints from rare kaon decays [32]. The FCNC $c \to u$ couplings are generated through flavour mixing as (see Eqs. (5.12) and (5.14))

$$g_L^{cu} = g_4\, \Delta F_L\, \lambda_{\text{CKM}}\,, \tag{6.25}$$
$$g_R^{cu} = g_4\, \Delta F_R\, \cos(\theta_u)\, \sin(\theta_u)\,, \tag{6.26}$$

  where

$$\Delta F_L = F_{Q_2} - F_{Q_1}\,, \quad \Delta F_R = F_{U_2} - F_{U_1}\,. \tag{6.27}$$

  We repeat the necessity of non-universal U(1)$'$ charges to the $c$ and $u$ quark, that is $\Delta F_{L,R} \neq 0$, to generate the desired FCNC transitions at tree level.

From Eqs. (6.25) and (6.26) we determine the ratio

$$\frac{g_R^{cu}}{g_L^{cu}} \simeq \frac{\Delta F_R\, \cos(\theta_u)\, \sin(\theta_u)}{\Delta F_L\, \lambda_{\text{CKM}}}\,, \tag{6.28}$$

which solely depends on the charge differences and mixing angles. We can classify

$$\frac{\Delta F_R}{\Delta F_L}\, \sin(2\theta_u) \simeq 8 \qquad \text{in the case} \quad \frac{g_R^{cu}}{g_L^{cu}} = X \approx 20 \qquad \text{(RH-dominated)}\,, \tag{6.29}$$
$$\frac{\Delta F_R}{\Delta F_L}\, \sin(\theta_u) \simeq \frac{1}{100} \qquad \text{in the case} \quad \frac{g_R^{cu}}{g_L^{cu}} = 1/X \approx 1/20 \qquad \text{(LH-dominated)}\,, \tag{6.30}$$

assuming small mixing angles $\theta_u \ll 1$. In the RH-dominated case, a mild hierarchy between $\Delta F_R$ and $\Delta F_L$ is needed, whereas we can accommodate the LH-dominated scenario with mixing alone, *i.e.* $\theta_u \sim 10^{-2}$. However, in both cases the ratio of both couplings is fixed as

$$\frac{\mathcal{C}'_{9,\ell}}{\mathcal{C}_{9,\ell}} = \frac{\mathcal{C}'_{10,\ell}}{\mathcal{C}_{10,\ell}} = \frac{g_R^{cu}}{g_L^{cu}} = \begin{cases} X & \text{(RH-dominated)} \\ 1/X & \text{(LH-dominated)} \end{cases}\,. \tag{6.31}$$

Both scenarios can be realised for a plethora of $Z'$ models. A list of sample solutions is listed in Tab. 6.1 and an overview of selected scenarios with specific assignments of relevant U(1)$'$ charges

| Model | $F_{Q_i}$ | | | $F_{U_i}$ | | | $F_{D_i}$ | | | $F_{L_i}$ | | | $F_{E_i}$ | | | $F_{\nu_i}$ | | |
|---|---|---|---|---|---|---|---|---|---|---|---|---|---|---|---|---|---|---|
| 1 | -4 | -2 | 6 | -2 | 1 | 1 | 0 | 0 | 0 | 3 | -8 | 5 | -3 | 6 | -3 | 0 | 0 | 0 |
| 2 | -6 | 3 | 3 | -8 | 4 | 4 | -10 | 10 | 0 | 1 | -6 | 5 | 0 | 0 | 0 | 0 | 0 | 0 |
| 3 | 7 | 8 | -20 | -29 | 6 | 3 | -19 | 4 | 25 | 0 | 9 | 6 | 3 | 14 | 13 | 0 | 0 | 0 |
| 4 | -1 | 2 | -1 | -1 | 2 | -1 | 0 | 0 | 0 | 0 | 1 | -1 | 0 | 2 | -2 | -2 | -1 | 3 |
| 5 | -1 | 2 | -1 | -1 | 2 | -1 | 2 | -1 | -1 | 0 | 1 | -1 | 0 | 1 | -1 | 0 | 0 | 0 |
| 6 | -10 | 6 | 2 | -13 | 2 | 3 | -11 | 2 | 13 | 3 | 9 | -6 | 2 | 6 | 4 | 0 | 0 | 0 |
| 7 | 1 | 1 | 1 | 1 | 1 | 1 | 1 | 1 | 1 | -3 | -3 | -3 | -3 | -3 | -3 | -3 | -3 | -3 |
| 8 | 6 | 7 | -15 | -14 | 4 | 2 | -25 | 9 | 20 | 11 | -24 | 19 | 1 | 8 | 3 | 0 | 0 | 0 |

**Table 6.1:** Sample solutions of an anomaly-free U(1)′ extension of the SM+3 $\nu_R$. In general, the ordering of generations is arbitrary due to permutation invariance. In this chapter, however, we explicitly use the ordering given here, that is, the $i$-th entry corresponds to the $i$-th generation, unless mentioned otherwise. *Table adapted from Ref.* [16].

| Model | $\Delta F_R$ | $\Delta F_L$ | $g_R^{cu}/g_L^{cu}$ case | $\theta_u$ |
|---|---|---|---|---|
| 1 | 3 | 2 | $1/X$ | 0.008 |
| 2 | 12 | 9 | $1/X$ | 0.009 |
| 3′ | 35 | 1 | $X$ | 0.122 |
| 3 | 35 | 1 | $1/X$ | 0.0003 |
| 4 | 3 | 3 | $1/X$ | 0.011 |
| 5 | 3 | 3 | $1/X$ | 0.011 |
| 6 | 15 | 16 | $1/X$ | 0.012 |
| 7 | 0 | 0 | - | - |
| 8′ | 18 | 1 | $X$ | 0.244 |
| 8 | 18 | 1 | $1/X$ | 0.0006 |

**Table 6.2:** Scenarios of anomaly-free $Z'$ models and the mixing angle $\theta_u$ for different charge assignments taken from Tab. 6.1. The primed solutions are RH-dominated, whereas the unprimed ones are LH-dominated. *Table taken from Ref.* [16].

is presented in Tab. 6.2. Let us briefly discuss the different solutions. While in general the charge assignments within each fermion species can be chosen freely due to the permutation invariance of charges, we explicitly use the fermion charges following the ordering in Tab. 6.1. Notably, model 7, which exhibits universal charge assignments to leptons and quarks, is unable to generate $\Delta F_{L,R} \neq 0$, and is given only for illustrative purposes. Extending the SM particle content by three RH neutrino fields $\nu_R$ with non-zero U(1)′ charges $F_\nu$ can also be realised as in model 4 (and 7).

The ratio $\Delta F_R/\Delta F_L$ ranges within $\sim$ [0.9, 35] for the models presented, while the mixing angle $\theta_u$ is tuned according to Eqs. (6.29) and (6.30) and given in Tab. 6.2. We see that models with $\Delta F_R/\Delta F_L \geq 8$ can be either RH or LH-dominated, depending on the chosen flavour rotation $\theta_u$. Having specified different $Z'$ models, we now work out parameter constraints for them. The *updated* bound on the $D^+ \to \pi^+\mu^+\mu^-$ branching ratio in Eq. (6.19) can be rewritten as

$$g_4^4 \left(\lambda_{\rm CKM}\, \Delta F_L\right)^2 \left[1 + \left(\frac{\Delta F_R \,\sin\left(2\theta_u\right)}{2\,\Delta F_L\, \lambda_{\rm CKM}}\right)\right]^2 \left(F_{L_2}^2 + F_{E_2}^2\right) \lesssim 5.6 \cdot 10^{-4} \,\left(\frac{M_{Z'}}{\rm TeV}\right)^4 , \tag{6.32}$$

where we have inserted the expressions for $g^{uc}_{L,R}$ as well as the flavour-diagonal lepton couplings in Eq. (5.23), that is $g^{\ell\ell}_L = g_4\, F_{L_i}$ and $g^{\ell\ell}_R = g_4\, F_{E_i}$. Together with the constraints from $D^0$-$\overline{D}^0$ mixing, the ratio $g_4/M_{Z'}$ is fixed for each model and two solutions emerge from Eq. (6.32). They read

$$g_4^2 \lesssim \frac{0.12}{\Delta F_L \sqrt{F_{L_2}^2 + F_{E_2}^2}} \left(\frac{M_{Z'}}{\text{TeV}}\right)^2 \cdot \begin{cases} (1+X)^{-1} & \text{(RH-dominated)} \\ \left(1+\frac{1}{X}\right)^{-1} & \text{(LH-dominated)} \end{cases} . \tag{6.33}$$

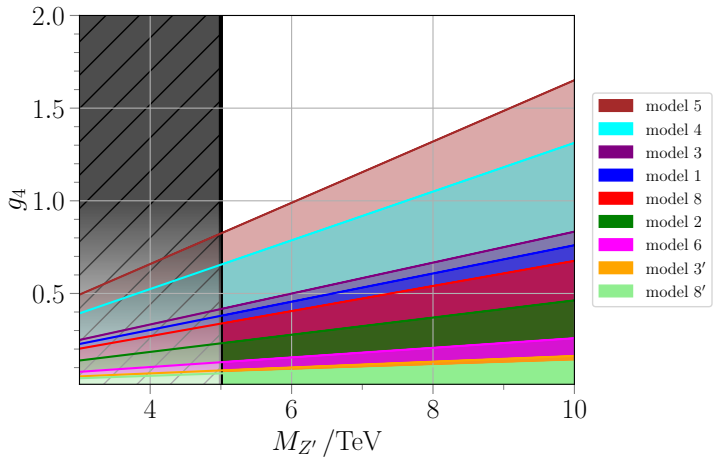


**Figure 6.3:** Upper limits on the U(1)′ gauge coupling $g_4$ as a function of the $Z'$ mass in Eq. (6.33) for selected models with $\Delta F_{L,R} \neq 0$ in Tab. 6.2. The black region is excluded by direct searches in dimuon and dielectron spectra [32]. For lower values of $g_4$, the bounds become model-dependent as indicated by the lighter colouring, see main text. *Updated figure adapted from Ref.* [16].

In Fig. 6.3, the U(1)′ gauge coupling $g_4$ is shown as a function of $M_{Z'}$ for the LH- or RH-scenarios given in Tab. 6.1 with parameter settings according to Tab. 6.2. The different lines correspond to the upper limit in Eq. (6.33) for each scenario. We observe that the constraints for RH-dominated scenarios are a factor $X \approx 20$ stronger than for the corresponding LH-dominated ones due to $(1+X)/(1+1/X) = X$ for $X \neq -1$. The black region in Fig. 6.3 displays the excluded region $M_{Z'} \lesssim 5$ TeV from resonant searches in dilepton spectra [32]. However, the true lower bound for $M_{Z'}$ is different for every solution as it depends on the specific assignments of quark and lepton charges, as well as the overall coupling strength. Thus, part of the parameter space $g_4 < 0.5$ and $M_{Z'} < 5$ TeV might still be allowed or constrained by other searches [163], indicated by the lighter colouring. Figure 6.3 incorporates the updated bound from $D^+ \to \pi^+\mu^+\mu^-$ on the couplings, see Eq. (6.33). Future (more stringent) limits will further reduce the allowed parameters space, entailing smaller $g_4$ or larger $M_{Z'}$. However, as of now, we still find sizeable contributions to charm Wilson coefficients. The idea of hierarchical couplings as realised in this section proves useful to not only relax present mixing bounds, but also reduce the substantial parameter space in $Z'$ model building.

Concluding this section, we compute the contributions to the Wilson coefficients $\mathcal{C}^{(\prime)}_{9/10,\mu}$ for the $Z'$ models. Here, we choose a benchmark value $M_{Z'} = 6$ TeV, while in general the ratio $g_4/M_{Z'}$ fixes the (maximally allowed) value of a Wilson coefficient, constrained by Eq. (6.33). The results are listed in Tab. 6.3. We find that in scenarios, which are either LH- or RH-dominated, substantial

| Model | $\frac{g_4}{M_{Z'}}$ / TeV$^{-1}$ | $\mathcal{C}_{9,\mu}$ | $\mathcal{C}_{10,\mu}$ | $\mathcal{C}'_{9,\mu}$ | $\mathcal{C}'_{10,\mu}$ |
|---|---|---|---|---|---|
| 1 | 0.076 | 0.12 | −0.83 | 0.01 | −0.04 |
| 2 | 0.046 | 0.60 | −0.60 | 0.03 | −0.03 |
| 3′ | 0.019 | −0.04 | −0.01 | −0.86 | −0.19 |
| 3 | 0.083 | −0.82 | −0.18 | −0.04 | −0.01 |
| 4 | 0.130 | −0.80 | −0.27 | −0.04 | −0.01 |
| 5 | 0.164 | −0.84 | 0 | −0.04 | 0 |
| 6 | 0.026 | −0.83 | 0.17 | −0.04 | 0.01 |
| 7 | - | 0 | 0 | 0 | 0 |
| 8′ | 0.015 | 0.02 | −0.04 | 0.41 | −0.81 |
| 8 | 0.067 | 0.38 | −0.75 | 0.02 | −0.04 |

**Table 6.3:** Maximally induced $c\to u\,\mu^+\mu^-$ Wilson coefficients $\mathcal{C}^{(\prime)}_{9/10,\mu}$ for LH- or RH-dominated $Z'$ scenarios listed in Tab. 6.2. We also provide the corresponding ratio $g_4/M_{Z'}$ in units of TeV$^{-1}$ according to Eq. (6.33).

$\mathcal{C}_{9/10,\mu}$ or $\mathcal{C}'_{9/10,\mu}$ can be induced. Due to the hierarchies in Eqs. (6.29) and (6.30), the primed versus unprimed Wilson coefficients differ by the factor $X\approx 20$ (modulo rounding in Tab. 6.3). Notably, model 2 exhibits a $(V-A)$-structure (not only for muons) with $\mathcal{C}^{(\prime)}_{9,\ell}=-\mathcal{C}^{(\prime)}_{10,\ell}$ as U(1)′ charges to lepton singlets $F_{E_i}$ are zero. The challenge of how to detect these NP contributions is approached in the next section, where null test observables in charm decays sensitive to $\mathcal{C}^{(\prime)}_{9/10,\mu}$ are elaborated.

## 6.4 Study of null tests in $D\to P\ell\ell$ decays

In what follows, we review a selection of null test observables predestined to find BSM effects in charm decays. Based on approximate symmetry limits of the SM, such null test searches provide the unique opportunity not only to test the SM, but further confine the underlying NP structure if measured by experiment. We provide a brief overview of the different sets of null test observables in rare semileptonic charm decays. Afterwards, we present tests of lepton universality and $CP$ asymmetries in Secs. 6.4.1 and 6.4.2, respectively, where contributions from $Z'$ scenarios enter prominently and can have pronounced effects.

Let us skim over selected null tests and review their NP sensitivity.

- Angular observables:

  The lepton forward-backward asymmetry $A_{\rm FB}(q^2)$ is mostly sensitive to combinations of (pseudo)scalar and tensor operators, where effects of only scalar or pseudotensors are highly suppressed, *e.g.* $A_{\rm FB}\propto \mathrm{Re}\left(\mathcal{C}_S\mathcal{C}_T^*+(\mathcal{C}_P+\mathcal{C}_P^{\rm R})\,\mathcal{C}_{T5}^*\right)$ for vanishing lepton masses [149].

  The so-called 'flat' term $F_{\rm H}(q^2)$ is enhanced for contributions to (pseudo)tensor and (pseudo)scalar operators as $F_{\rm H}\propto|\mathcal{C}_S|^2+|\mathcal{C}_P+\mathcal{C}_P^{\rm R}|^2\&|\mathcal{C}_T|^2+|\mathcal{C}_{T5}|^2$, while SM-like contributions are $\mathcal{O}\left(10^{-3}\text{-}10^{-2}\right)$ [149]. Large effects in both of these observables would point towards an underlying tensor or scalar nature of NP in these $D\to P\,\ell\ell$ decays. The explicit parametrisations of $A_{\rm FB}$ and $F_{\rm H}$ are given elsewhere [16].

- Lepton flavour violation:

  As indicated by Eqs. (6.14) and (6.15), constraints on lepton flavour violating operators in charm allow for sizeable NP contributions in differential branching ratios of, *e.g.*, $D^+ \to \pi^+ e^\pm \mu^\mp$ or $D_s^+ \to K^+ e^\pm \mu^\mp$ decays. Notably, resonance contributions are absent in those processes, and hence the overall uncertainties are mainly due to form factors. Especially, vector and axial-vector contributions $\mathcal{K}_{9,10} \sim 0.5$ score integrated branching ratios $\mathcal{B}(D^+ \to \pi^+ e^\pm \mu^\mp) \sim 10^{-7}$. While in $Z'$ models LFV effects are model-dependent, we estimate branching ratios up to $\mathcal{O}(10^{-11})$, for instance $\mathcal{B}(D^+ \to \pi^+ e^\pm \mu^\mp) \lesssim \text{few} \cdot 10^{-12}$ assuming $\mathcal{K}_{9,10} \sim 10^{-3}$ [16]. These benchmark values are in agreement with data from $\tau \to (\mu, e)\ell\ell$, with $\ell = e, \mu$, as well as $\mu \to eee$ and $\mu \to e\gamma$ decays [32].

- Lepton universality:

  In the SM, lepton universality (LU) is realised by equal couplings of the electroweak gauge bosons to leptons of different generations. Conversely, NP scenarios can easily induce non-universal effects that can be probed by experiment. Familiar tests of LU have been studied in the beauty sector with experimental data exhibiting notable deviations from the SM prediction, see Sec. 3.4. BSM predictions of LU ratios in $D \to P_1\, P_2\, \ell^+\ell^-$ [164] and $D \to P\ell^+\ell^-$ [16] have been worked out. Examples for the latter are discussed in Sec. 6.4.1.

- $CP$ asymmetries:

  The studies of $CP$-violating effects can help to obtain information on NP Wilson coefficients due to the negligible, CKM-suppressed SM contributions. While large contributions are achieved in the vicinity of resonances, weak phases in the Wilson coefficients and strong phases of the resonances are instrumental to generate $CP$ asymmetries, see Sec. 6.4.2.

### 6.4.1 Tests of lepton universality

Apart from non-universal couplings to $u$ and $c$ quarks, we also allocate different couplings to electrons and muons in our $Z'$ models. This feature can be exploited by defining the ratio of branching ratios analogous to the one for rare $B$-decays, *cf.* Eq. (3.45). It reads [161, 164]

$$R_P^D = \frac{\displaystyle\int_{q^2_{\text{min}}}^{q^2_{\text{max}}} \frac{\mathrm{d}\mathcal{B}(D \to P\mu^+\mu^-)}{\mathrm{d}q^2}\mathrm{d}q^2}{\displaystyle\int_{q^2_{\text{min}}}^{q^2_{\text{max}}} \frac{\mathrm{d}\mathcal{B}(D \to Pe^+e^-)}{\mathrm{d}q^2}\mathrm{d}q^2}\,, \tag{6.34}$$

where $q^2$ denotes the dilepton invariant mass squared, and $q^2_{\text{min}}$ ($q^2_{\text{max}}$) indicates the lower (upper) dilepton mass cut. The SM prediction near unity is given with high precision due to the impeccable cancellation of QCD uncertainties [82]. Here, our focus lies on the observables $R_\pi^D$ testing the ratio of $D^+ \to \pi^+\mu^+\mu^-$ and $D^+ \to \pi^+ e^+ e^-$ decays. While currently no experimental measurements of these modes are available, we can study different NP scenarios and their impact on these LU tests.

First, we discuss generic benchmarks with contributions from different types of Wilson coefficients, while afterwards we analyse the contributions in our $Z'$ set-ups. Assuming only NP contributions to muons, we show the predicted ranges of $R_\pi^D$ in the full, low and high $q^2$-integrated intervals in Tab. 6.4. We include the same resonance parametrisation in Eq. (6.10) for electron and muon

modes, varying the unknown strong phases $\delta_{\phi,\rho,\eta}$ within $[-\pi, \pi]$ that provide the main source of uncertainty. We see that the low-$q^2$ region suffers from the uncertainty of the strong phases, while the full-$q^2$ region remains insensitive to resonance and NP effects with SM-like ratios $R_\pi^D \approx 1$. Conversely, NP effects in the high-$q^2$ region can be quite sizeable. Large deviations from unity can also be achieved in the low-$q^2$ region, while keeping the large uncertainties in mind.

| $R_\pi^D$ | SM | $\lvert\mathcal{C}_9\rvert = 0.5$ | $\lvert\mathcal{C}_{10}\rvert = 0.5$ | $\lvert\mathcal{C}_9\rvert = \pm\lvert\mathcal{C}_{10}\rvert = 0.5$ | $\lvert\mathcal{C}_{S(P)}\rvert = 0.1$ | $\lvert\mathcal{C}_T\rvert = 0.5$ | $\lvert\mathcal{C}_{T5}\rvert = 0.5$ |
|---|---|---|---|---|---|---|---|
| full $q^2$ | $1.00 \pm \mathcal{O}\,(\%)$ | SM-like | SM-like | SM-like | SM-like | SM-like | SM-like |
| low $q^2$ | $0.95 \pm \mathcal{O}\,(\%)$ | $\mathcal{O}\,(100)$ | $\mathcal{O}\,(100)$ | $\mathcal{O}\,(100)$ | $0.9 \ldots 1.4$ | $\mathcal{O}\,(10)$ | $1.0 \ldots 5.9$ |
| high $q^2$ | $1.00 \pm \mathcal{O}\,(\%)$ | $0.2 \ldots 11$ | $3 \ldots 7$ | $2 \ldots 17$ | $1 \ldots 2$ | $1 \ldots 5$ | $2 \ldots 4$ |

**Table 6.4:** $R_\pi^D$ in the SM and in NP scenarios for different $q^2$-bins. Ranges correspond to uncertainties from form factors and resonance parameters. Due to large uncertainties at low $q^2$ in some cases only the order of magnitude of the largest values is given. *Table taken from Ref.* [16].

| $R_\pi^D$ | Model 1 | Model 2 | Model 3 | Model 3′ | Model 4 | Model 5 | Model 6 | Model 8 | Model 8′ |
|---|---|---|---|---|---|---|---|---|---|
| full $q^2$ | SM-like | SM-like | SM-like | SM-like | SM-like | SM-like | SM-like | SM-like | SM-like |
| low $q^2$ | $1.8 \ldots 5.5$ | $\mathcal{O}\,(100)$ | $\mathcal{O}\,(50)$ | $\mathcal{O}\,(50)$ | $\mathcal{O}\,(100)$ | $\mathcal{O}\,(100)$ | $1.4 \ldots 16$ | $0.7 \ldots 13$ | $0.8 \ldots 14$ |
| high $q^2$ | $3.0 \ldots 5.3$ | $\mathcal{O}\,(50)$ | $3 \ldots 30$ | $3.5 \ldots 31$ | $2.0 \ldots 36$ | $1.7 \ldots 37$ | $3.5 \ldots 30$ | $1.3 \ldots 17$ | $1.4 \ldots 17$ |

**Table 6.5:** Same as Tab. 6.4, but for hierarchical $Z'$ models. See Tabs. 6.1 and 6.3 for chosen model parameters.

Looking at the $Z'$ models listed in Tab. 6.1, we spot that in most models (except models 4 and 5) NP couplings to electrons exist, and hence Wilson coefficients $\mathcal{C}_{9/10,e}$ are induced in addition to $\mathcal{C}_{9/10,\mu}$ entering Eq. (6.34). However, due to the non-universal charge assignments of electrons and muons, we find similar deviations from unity for $R_\pi^D$, compiled in Tab. 6.5. As before, the full-$q^2$ region is insensitive to NP effects, while huge deviations from the SM prediction can be achieved in the low-$q^2$ region. In addition, it is possible to test specific models, where for instance smaller couplings to muons than to electrons are realised (with U(1)′ charges set accordingly) and induce $R_\pi^D < 1$. While measurements of the resonant-dominated dielectron modes are yet unavailable, the expected future sensitivities at LHCb [165] enable first model-independent LU tests in the upcoming years.

### 6.4.2 *CP* asymmetries

Another null test observable able to probe NP is the $CP$ asymmetry [16, 154, 166], given by

$$A_{CP}(q^2) = \frac{1}{\Gamma + \overline{\Gamma}} \left( \frac{\mathrm{d}\Gamma}{\mathrm{d}q^2} - \frac{\mathrm{d}\overline{\Gamma}}{\mathrm{d}q^2} \right) , \tag{6.35}$$

where $\overline{\Gamma}$ denotes the decay rate of the $CP$-conjugated mode, with the normalisation as in Eq. (E.2). Expressing the difference of differential decay rates as

$$\begin{aligned}\frac{\mathrm{d}\Gamma}{\mathrm{d}q^2} - \frac{\mathrm{d}\overline{\Gamma}}{\mathrm{d}q^2} = \frac{G_\mathrm{F}^2 \alpha_e^2}{256\,\pi^5\, m_D^3} \sqrt{\lambda_{DP}\left(1 - \frac{4m_\ell^2}{q^2}\right)} \Bigg\{ \\ \frac{2}{3}\,\mathrm{Im}\left(\mathcal{C}_9 + 2\,\mathcal{C}_7\,\frac{m_c}{m_D + m_P}\,\frac{f_T}{f_+}\right)\mathrm{Im}\left(\mathcal{C}_9^\mathrm{R}\right)\left(1 + \frac{2m_\ell^2}{q^2}\right)\lambda_{DP}\, f_+^2 \\ + \mathrm{Im}\left(\mathcal{C}_P\right)\mathrm{Im}\left(\mathcal{C}_P^\mathrm{R}\right)\frac{q^2}{m_c^2}(m_D^2 - m_P^2)^2\, f_0^2 \\ + 4\,\mathrm{Im}\left(\mathcal{C}_T\right)\mathrm{Im}\left(\mathcal{C}_9^\mathrm{R}\right)\frac{m_\ell}{m_D + m_P}\,\lambda_{DP}\, f_+\, f_T \\ + 2\,\mathrm{Im}\left(\mathcal{C}_{10}\right)\mathrm{Im}\left(\mathcal{C}_P^\mathrm{R}\right)\frac{m_\ell}{m_c}(m_D^2 - m_P^2)^2\, f_0^2 \Bigg\}\,,\end{aligned} \tag{6.36}$$

we identify the SM contribution $A_{CP}^\mathrm{SM}$ as the first term in Eq. (6.36). This quantity is tiny due to the small phases of the CKM factors in $\mathcal{C}_9$, see Eq. (6.6). Therefore, $A_{CP}$ can be used as a null test of the SM and indicator of BSM physics.

In this chapter, we have confined ourselves to real-valued couplings in the $Z'$ models presented. Thus, no contributions are generated to $A_{CP}$ which is only sensitive to the imaginary part of Wilson coefficients. Therefore, we require weak phases in our $Z'$ framework to utilise this null test. Chapter 7 comprises studies of $CP$ asymmetries and direct $CP$ violation in hadronic charm decays, where $Z'$ models that induce large weak phases and promising patterns of NP are put forward. At this point, we illustrate NP effects by employing such a benchmark scenario, while further details are provided in Chap. 7.

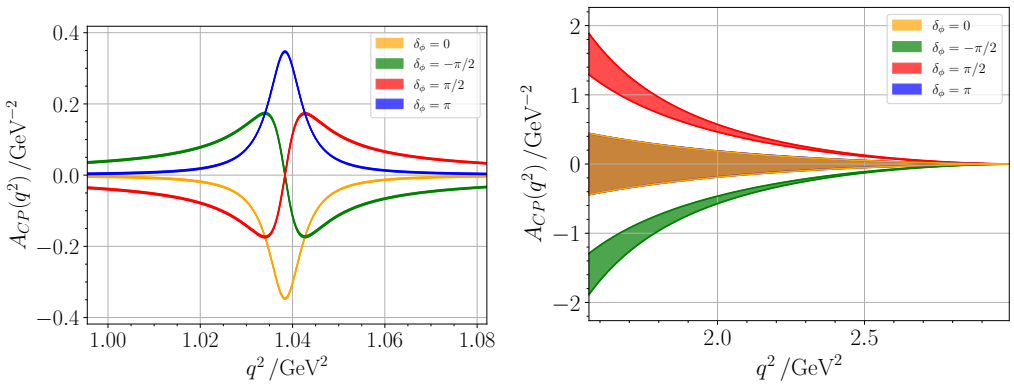


**Figure 6.4:** The $CP$ asymmetry $A_{CP}(q^2)$ in $D^+ \to \pi^+\mu^+\mu^-$ around the $\phi$ resonance, *i.e.* $\left[(m_\phi - 5\,\Gamma_\phi)^2,\, (m_\phi + 5\,\Gamma_\phi)^2\right]$, (left-hand side plot) and at high $q^2$ (right-hand side plot), where $m_\phi = 1.019$ GeV and $\Gamma_\phi = 4.25 \cdot 10^{-3}$ GeV [155]. We choose different values of $\delta_\phi = 0,\, \pm\pi/2,\, \pi$ and employ $\mathcal{C}'_{9,10} = 0.12\,\exp(\mathrm{i}\pi/2)$, a benchmark of model $10\mu$, *cf.* Tabs. 7.4 and 7.8 and details provided in Sec. 7.4. The uncertainties are due to the other strong phases $\delta_{\rho,\eta}$, the form factors and the $c$-quark mass $m_c$.

We note that enhanced strong phases entering $\mathcal{C}_{9,P}^\mathrm{R}$ as resonance effects are vital to generate a sizeable $CP$ asymmetry [166]. In Fig. 6.4, we show $A_{CP}$ in $D^+ \to \pi^+\mu^+\mu^-$ around the $\phi$-resonance region (left-hand side plot) and at high-$q^2$ (right-hand side plot) for different values of

$\delta_\phi$ employing a benchmark value of $\mathcal{C}'_{9,10} = 0.12\,\exp(\mathrm{i}\pi/2)$. This benchmark is realised in model $10\mu$, see Tabs. 7.3 and 7.4. The band width corresponds to $1\,\sigma$ uncertainties by varying the phases $\delta_{\rho,\eta}$ within $[-\pi, \pi]$, while uncertainties from form factors and $m_c$ are also included. In general, large NP effects are induced by contributions to $\mathcal{C}_9$, while $\mathcal{C}_T$ and $\mathcal{C}_{10,P}$ are suppressed by the light lepton mass and the completely negligible $\mathrm{Im}(\mathcal{C}_P^{\mathrm{R}}(q^2 \simeq m_\phi^2))$ at the $\phi$ resonance, respectively [16]. We find that regardless of the value of $\delta_\phi$ strong BSM effects can emerge, while measuring $A_{CP}$ as a binned observable is necessary to avoid a vanishing integrated asymmetry, which may occur due to sign changes around $q^2 \sim m_\phi^2$.

Chapter

7

# $CP$ asymmetries in rare charm decays

This chapter comprises studies of $CP$-violating NP in hadronic and semileptonic rare charm $\Delta c = \Delta u = 1$ transitions based on the author's publication [17]. We consider flavourful, anomaly-free $Z'$ models with non-universal couplings to $c$ and $u$ quarks. Before that, we review the $CP$ phenomenology and present patterns of $CP$-violating NP in Sec. 7.1. The $\Delta A_{CP}$ contributions are discussed in Sec. 7.2 utilising $Z'$ model building. Afterwards, we present $U$-spin and isospin patterns which emerge in such models and report on correlations of $CP$-violating effects connecting hadronic and semileptonic charm decays in Secs. 7.3 and 7.4, respectively. In closing this chapter, we review benchmark models in the light of recently updated limits concerning $D^0$-$\overline{D}^0$ mixing parameters in Sec. 7.5. We conclude in Sec. 7.6.

In the late of 2011, direct $CP$ violation in SCS $D$-decays was evidenced in the observable

$$\Delta A_{CP} = A_{CP}\left(K^+K^-\right) - A_{CP}\left(\pi^+\pi^-\right) . \tag{7.1}$$

The measurement by the LHCb experiment [167], $\Delta A_{CP}^{\text{LHCb'11}} = (-82 \pm 24) \cdot 10^{-4}$ with a $3.5\,\sigma$ significance of the measured deviation from zero, provided the first evidence for $CP$ violation in the charm sector. Here, the time-integrated $CP$ asymmetry for a final $CP$ eigenstate $f$ is given by [168]

$$A_{CP}(f) = \frac{\Gamma(D^0 \to f) - \Gamma(\overline{D}^0 \to f)}{\Gamma(D^0 \to f) + \Gamma(\overline{D}^0 \to f)} , \tag{7.2}$$

and effects of indirect $CP$ violation approximately cancel in $\Delta A_{CP}$. In 2019, LHCb reported on the observation of direct $CP$ violation with an updated measurement of [169]

$$\Delta A_{CP}^{\text{LHCb'19}} = (-15.4 \pm 2.9) \cdot 10^{-4} , \tag{7.3}$$

being $5.3\,\sigma$ away from zero, while the corresponding world average reads [123]

$$\Delta A_{CP}^{\text{HFLAV}} = (-16.4 \pm 2.8) \cdot 10^{-4} . \tag{7.4}$$

Even though $\Delta A_{CP}$ is a manifestation of $CP$ violation in decay, it constitutes no clear-cut sign of possible NP. The SM contribution to the individual $A_{CP}$ is CKM-suppressed by a factor of [170]

$$I_{\text{CKM}} \equiv 2\,\text{Im}\left(\frac{V_{cb}^* V_{ub}}{V_{cs}^* V_{us}}\right) \approx 1.4 \cdot 10^{-3} , \tag{7.5}$$

and hence we naively estimate $\Delta A_{CP}^{\text{SM}} \sim \mathcal{O}\left(\alpha_s/\pi\right) \cdot I_{\text{CKM}} \sim 10^{-4}$, one order of magnitude below

Eq. (7.3). An $\mathcal{O}(10)$ enhancement from hadronic effects cannot be ruled out as well [171–175], in which case Eq. (7.3) is accounted for by the SM alone. However, other groups derive smaller estimates utilising first principle QCD methods [125, 176], *i.e.* $|\Delta A_{CP}^{\text{SM}}| \leq 3.6 \cdot 10^{-4}$, which deviates significantly from the experimental result favouring sizeable NP contributions to $\Delta A_{CP}$.

Due to this ongoing debate, we aim to generate NP contributions $\Delta A_{CP}^{\text{NP}} \sim 10^{-3}$ that can accommodate the current measurement alone, assuming a negligible SM contribution.

## 7.1 $CP$ phenomenology and $Z'$ models in charm

### 7.1.1 Parametrisation of $CP$-violating new physics

The SCS decay amplitudes $\mathcal{A}_f$ and $\overline{\mathcal{A}}_f$ for the $D^0$ and $\overline{D}^0$ meson, respectively, are given by [168]

$$\mathcal{A}_f = \mathcal{A}_f^{\text{tree}}\, \mathrm{e}^{\mathrm{i}\,\phi_f^{\text{tree}}} \left(1 + r_f\, \mathrm{e}^{\mathrm{i}\,(\delta_f + \phi_f)}\right), \quad \overline{\mathcal{A}}_f = \eta_{CP}\, \mathcal{A}_f^{\text{tree}}\, \mathrm{e}^{-\mathrm{i}\,\phi_f^{\text{tree}}} \left(1 + r_f\, \mathrm{e}^{\mathrm{i}\,(\delta_f - \phi_f)}\right). \tag{7.6}$$

Here, $\eta_{CP} = +(-)1$ denotes the eigenvalue of $CP$ even (odd) states. The parameters $\delta_f$ and $\phi_f$ denote the strong ($CP$-conserving) and weak ($CP$-violating) relative phases, respectively. The term $\mathcal{A}_f^{\text{tree}}\, \mathrm{e}^{\pm \mathrm{i}\,\phi_f^{\text{tree}}}$ refers to the dominant tree-level contribution in the SM, whereas the relative magnitude of all subleading amplitudes are described by the parameter $r_f$. Using Eqs. (7.2) and (7.6), we can write the $CP$ asymmetry $A_{CP}(f)$ as

$$A_{CP}(f) = -\frac{2\, r_f\, \sin(\delta_f)\, \sin(\phi_f)}{1 + r_f^2 + 2\, r_f\, \cos(\delta_f)\, \cos(\phi_f)} = -2\, r_f\, \sin(\delta_f)\, \sin(\phi_f) + \mathcal{O}\left(r_f^2\right), \tag{7.7}$$

where we have assumed $r_f \ll 1$ in the last step [1]. We observe that both non-vanishing strong and weak phases are needed to generate contributions to $A_{CP}(f)$, while the tree-level amplitude $\mathcal{A}_f^{\text{tree}}$ cancels. Since we are interested in NP effects contributing to this observable, we add a BSM term to the $D^0$ decay amplitude as

$$\mathcal{A}_f = \sum_{q=d,s,b} \lambda_q\, (\mathcal{A}_f^q)_{\text{SM}} + \mathcal{A}_f^{\text{NP}}. \tag{7.8}$$

The first term denotes the SM contribution with CKM factors $\lambda_q = V_{cq}^* V_{uq}$ and the second term incorporates NP. Here and in the following, we employ the notation $f = K$ and $f = \pi$ for the subscripts referring to the final states $\pi^+\pi^-$ and $K^+K^-$, respectively. By exploiting the unitarity of the CKM matrix, see Eq. (2.38), we obtain

$$\begin{aligned} \mathcal{A}_K &= \lambda_s \left(\mathcal{A}_K^s - \mathcal{A}_K^d\right)_{\text{SM}} + \lambda_b \left(\mathcal{A}_K^b - \mathcal{A}_K^d\right)_{\text{SM}} + \mathcal{A}_K^{\text{NP}}, \\ \mathcal{A}_\pi &= \lambda_d \left(\mathcal{A}_\pi^d - \mathcal{A}_\pi^s\right)_{\text{SM}} + \lambda_b \left(\mathcal{A}_\pi^b - \mathcal{A}_\pi^s\right)_{\text{SM}} + \mathcal{A}_\pi^{\text{NP}}, \end{aligned} \tag{7.9}$$

where the first and second terms correspond to SCS and penguin contributions in the SM, respectively. The latter contributions induce only small Wilson coefficients as they are strongly CKM-suppressed compared to the SCS ones. Using Eq. (7.9) together with Eqs. (7.6) and (7.7),

[1] Since $r_f \propto |\lambda_b/\lambda_{d,s}| \approx 6 \cdot 10^{-4}$, then $\mathcal{O}(r_f^2)$ corrections can be safely neglected.

we derive the formula

$$\Delta A_{CP} = \Delta A_{CP}^{\rm SM} + \Delta A_{CP}^{\rm NP} = \Delta A_{CP}^{\rm SM} - \frac{2}{|\lambda_{s,d}|}\,\Delta r^{\rm NP}\,. \tag{7.10}$$

The NP effects are embedded in

$$\Delta r^{\rm NP} = r_K^{\rm NP}\,\sin(\delta_K)\,\sin(\phi_K) + r_\pi^{\rm NP}\,\sin(\delta_\pi)\,\sin(\phi_\pi)\,, \tag{7.11}$$

with

$$r_K^{\rm NP} = \left|\frac{\mathcal{A}_K^{\rm NP}}{(\mathcal{A}_K^s - \mathcal{A}_K^d)_{\rm SM}}\right|, \quad r_\pi^{\rm NP} = \left|\frac{\mathcal{A}_\pi^{\rm NP}}{(\mathcal{A}_\pi^d - \mathcal{A}_\pi^s)_{\rm SM}}\right|, \tag{7.12}$$

where the plus sign between the pion and kaon amplitudes in Eq. (7.11) emerges due to $\lambda_d = -\lambda_s + \mathcal{O}(\lambda_b)$. Maximal NP effects in $\Delta A_{CP}$ are generated for $|\sin(\delta_{K,\pi})| \approx 1$ and $|\sin(\phi_{K,\pi})| \approx 1$. Note that no information on the sign of $\Delta r^{\rm NP}$ can be inferred a priori as it depends on the product of strong and weak phases. Therefore, we set $\sin(\delta_{K,\pi}) \sim 1$ (meaning either sign possible) in our analysis. Moreover, we choose for the weak phases $\sin(\phi_{K,\pi}) \sim 1$ following a similar guideline, which is elaborated in Sec. 7.1.4.

To determine possible NP effects in $\Delta A_{CP}$, we also need the modulus of the leading SM amplitudes $(\mathcal{A}_K^s - \mathcal{A}_K^d)_{\rm SM}$ and $(\mathcal{A}_\pi^d - \mathcal{A}_\pi^s)_{\rm SM}$, which can be extracted from data on branching ratios of $D \to f$ modes. In this chapter, we also study the related $D^+ \to \pi^+\pi^0$ and $D^0 \to \pi^0\pi^0$ decays, and hence introduce the subscripts $P = \pi'$ and $P = \pi^0$, respectively, to distinguish the different decay modes in the following. The branching ratio for $D \to f$ modes reads [168]

$$\mathcal{B}(D \to P_1\,P_2) = \tau_D \sqrt{1 - \frac{4\,m_P^2}{m_D^2}}\,\frac{|\mathcal{A}_P|^2}{16\,\pi\,m_D}\,, \tag{7.13}$$

where $\tau_D$ denotes the lifetime of the $D$ meson. The amplitude is parametrised as

$$\mathcal{A}_P = n_P\,\lambda_P\,a_P\,\frac{G_{\rm F}}{\sqrt{2}}\left(m_D^2 - m_P^2\right)\,f_0^{DP}\left(m_P^2\right)\,f_P\,, \tag{7.14}$$

where $\lambda_\pi = \lambda_d$, $\lambda_K = \lambda_s$ and

$$n_P = \begin{cases} 1 & P = \pi, \pi^0, K \\ \frac{1}{\sqrt{2}} & P = \pi' \end{cases}. \tag{7.15}$$

Numerical values of the decay constants $f_P$, form factors $f_0^{DP}$ as well as the respective lifetimes $\tau_D$ are provided in Tab. B.3. With current experimental data on branching ratios [32] we compute the parameters $a_P$ for the four decay modes, summarised in Tab. 7.1.

| Mode | $P$ | $\mathcal{B}$ (Mode) | $a_P$ |
|---|---|---|---|
| $D^0 \to K^+K^-$ | $K$ | $(4.08 \pm 0.06) \cdot 10^{-3}$ | $1.19 \pm 0.04$ |
| $D^0 \to \pi^+\pi^-$ | $\pi$ | $(1.453 \pm 0.024) \cdot 10^{-3}$ | $0.94 \pm 0.07$ |
| $D^0 \to \pi^0\pi^0$ | $\pi^0$ | $(8.26 \pm 0.25) \cdot 10^{-4}$ | $0.71 \pm 0.05$ |
| $D^+ \to \pi^+\pi^0$ | $\pi'$ | $(1.247 \pm 0.033) \cdot 10^{-3}$ | $0.77 \pm 0.05$ |

**Table 7.1:** Measured branching ratios [32] and parameters $a_P$ from Eq. (7.14) for different $D \to f$ decay modes. *Table taken from Ref.* [17].

### 7.1.2 $CP$ violation with $Z'$ models

The $Z'$ couplings of interest are included in the effective Hamiltonian

$$\mathcal{H}_{Z'}^{cu\ell\ell} \supset \left(g_L^{cu}\,\overline{u}_L\gamma^\mu c_L Z'_\mu + g_R^{cu}\,\overline{u}_R\gamma^\mu c_R Z'_\mu + \text{h.c.}\right) + g_L^{\ell\ell}\,\overline{\ell}_L\gamma^\mu\ell_L Z'_\mu + g_R^{\ell\ell}\,\overline{\ell}_R\gamma^\mu\ell_R Z'_\mu + \sum_{q=u,d,s}\left(g_L^{qq}\,\overline{q}_L\gamma^\mu q_L Z'_\mu + g_R^{qq}\,\overline{q}_R\gamma^\mu q_R Z'_\mu\right), \tag{7.16}$$

which enhances the interaction previously considered in Eq. (6.16) by flavour-diagonal quark couplings to the $Z'$ boson, $g_{L,R}^{qq}$. In analogy to the lepton couplings, they are constructed by taking the U(1)′ coupling $g_4$ times the associated U(1)′ charge $F_f$ as outlined in Sec. 5.1.2. The FCNC couplings are given by

$$g_L^{cu} = g_4\,\Delta F_L\,\lambda_{\text{CKM}}\,, \tag{7.17}$$

$$g_R^{cu} = g_4\,\Delta F_R\,\cos(\theta_u)\,\sin(\theta_u)\,\exp(\mathrm{i}\phi_R)\,, \tag{7.18}$$

as defined in Eqs. (5.12) and (5.14), respectively. The difference of U(1)′ charges to the doublet (singlet) $c$ and $u$ quark is encoded in $\Delta F_L = F_{Q_2} - F_{Q_1}$ ($\Delta F_R = F_{U_2} - F_{U_1}$) as introduced in Eq. (6.27). To induce $CP$-violating effects we explicitly maintain the $CP$ phase $\phi_R$ in the right-handed coupling, while for $g_L^{cu}$ only small (SM-like) phases are realised.

In Fig. 7.1, the tree-level Feynman diagrams for the relevant hadronic charm decays involving a $Z'$ boson are displayed. Therein, the diagrams in the top row display the contributions to $D^0 \to \pi^+\pi^-$ and $D^0 \to K^+K^-$ that enter $\Delta A_{CP}^{\text{NP}}$, but also induce $U$-spin breaking, whereas the diagrams in the middle row can induce isospin breaking in $D^+ \to \pi^+\pi^0$, see discussion in Sec. 7.3.1.

### 7.1.3 Effective theory description of $Z'$ contributions

By inducing the non-universal quark couplings in Eqs. (7.17) and (7.18), additional NP four-quark operators are generated in an EFT framework. The corresponding weak Hamiltonian at the scale $m_b < \mu < \mu_{\text{EW}}$ is given by [177]

$$\mathcal{H}_{\text{eff}}^{|\Delta c|=1} \supset \frac{G_{\text{F}}}{\sqrt{2}} \sum_i \widetilde{C}_i^{(\prime)}\,\widetilde{Q}_i^{(\prime)} + \text{h.c.}\,, \tag{7.19}$$

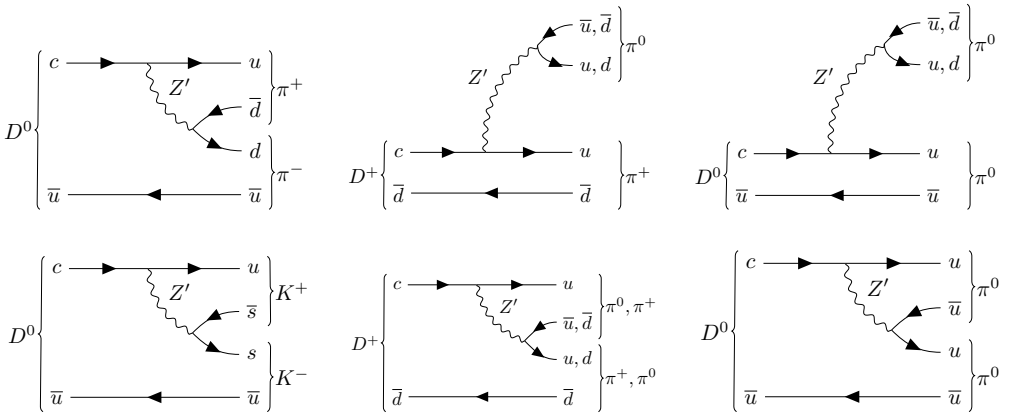


**Figure 7.1:** NP tree-level contributions via a $Z'$ boson for hadronic $D$-decays, that is $D^0 \to \pi^+\pi^-$, $D^0 \to K^+K^-$, $D^0 \to \pi^+\pi^-$ and $D^+ \to \pi^+\pi^0$ decays.

with the operators

$$
\begin{aligned}
\widetilde{Q}_7 &= (\overline{u}c)_{V-A} \sum_q F_{U_i,D_i}\,(\overline{q}q)_{V+A}\,, & \widetilde{Q}'_7 &= (\overline{u}c)_{V+A} \sum_q F_{Q_i}\,(\overline{q}q)_{V-A}\,,\\
\widetilde{Q}_8 &= (\overline{u}_\alpha c_\beta)_{V-A} \sum_q F_{U_i,D_i}\,(\overline{q}_\beta q_\alpha)_{V+A}\,, & \widetilde{Q}'_8 &= (\overline{u}_\alpha c_\beta)_{V+A} \sum_q F_{Q_i}\,(\overline{q}_\beta q_\alpha)_{V-A}\,,\\
\widetilde{Q}_9 &= (\overline{u}c)_{V-A} \sum_q F_{Q_i}\,(\overline{q}q)_{V-A}\,, & \widetilde{Q}'_9 &= (\overline{u}c)_{V+A} \sum_q F_{U_i,D_i}\,(\overline{q}q)_{V+A}\,,\\
\widetilde{Q}_{10} &= (\overline{u}_\alpha c_\beta)_{V-A} \sum_q F_{Q_i}\,(\overline{q}_\beta q_\alpha)_{V-A}\,, & \widetilde{Q}'_{10} &= (\overline{u}_\alpha \overline{c}_\beta)_{V+A} \sum_q F_{U_i,D_i}\,(\overline{q}_\beta q_\alpha)_{V+A}\,.
\end{aligned}
\tag{7.20}
$$

Here, the subscript $(V \pm A)$ is a shorthand notation that refers to the Dirac structures $\gamma_\mu(1 \pm \gamma_5)$, $q = u, c, d, s, b$ and $\alpha, \beta$ are the colour indices. The primed operators are obtained by interchanging the chirality $L \leftrightarrow R$ of the currents in the unprimed operators as $P_{L/R} = (1 \mp \gamma_5)/2$, while also accounting for the different U(1)$'$ charges of quark doublet or singlets. The full Hamiltonian is given in App. F.

By comparing the two Hamiltonians in Eqs. (7.16) and (7.19), we can write the corresponding Wilson coefficients at the $Z'$-boson mass scale $\mu = M_{Z'}$ as

$$
\widetilde{\mathcal{C}}_7^{(\prime)}\,(M_{Z'}) = \widetilde{\mathcal{C}}_9^{(\prime)}\,(M_{Z'}) = \frac{\sqrt{2}\,g_4\,g_{L(R)}^{cu}}{4\,G_\mathrm{F}\,M_{Z'}^2}\,, \quad \widetilde{\mathcal{C}}_8^{(\prime)}\,(M_{Z'}) = \widetilde{\mathcal{C}}_{10}^{(\prime)}\,(M_{Z'}) = 0\,. \tag{7.21}
$$

These coefficients are evolved down to the charm scale at LO in the strong coupling $\alpha_s$ via RGEs. This induces non-zero values of $\widetilde{\mathcal{C}}_{8,10}^{(\prime)}$ at $\mu = m_c$, see App. F.2 for supplementary calculations and

details. In doing so, we obtain the Wilson coefficients at the charm scale

$$\begin{aligned}
\widetilde{\mathcal{C}}_7^{(\prime)}(m_c) &= \sqrt{r_1}\,\widetilde{\mathcal{C}}_7^{(\prime)}(M_{Z'})\,,\\
\widetilde{\mathcal{C}}_8^{(\prime)}(m_c) &= \frac{\widetilde{\mathcal{C}}_7^{(\prime)}(M_{Z'})\left(1-r_1^{\frac{9}{2}}\right)+3\,\widetilde{\mathcal{C}}_8^{(\prime)}(M_{Z'})}{3\,r_1^4}\,,\\
\widetilde{\mathcal{C}}_9^{(\prime)}(m_c) &= \frac{\widetilde{\mathcal{C}}_9^{(\prime)}(M_{Z'})-\widetilde{\mathcal{C}}_{10}^{(\prime)}(M_{Z'})+r_1^3\left(\widetilde{\mathcal{C}}_9^{(\prime)}(M_{Z'})+\widetilde{\mathcal{C}}_{10}^{(\prime)}(M_{Z'})\right)}{2\,r_1^2}\,,\\
\widetilde{\mathcal{C}}_{10}^{(\prime)}(m_c) &= \frac{\widetilde{\mathcal{C}}_{10}^{(\prime)}(M_{Z'})-\widetilde{\mathcal{C}}_9^{(\prime)}(M_{Z'})+r_1^3\left(\widetilde{\mathcal{C}}_9^{(\prime)}(M_{Z'})+\widetilde{\mathcal{C}}_{10}^{(\prime)}(M_{Z'})\right)}{2\,r_1^2}\,,
\end{aligned} \tag{7.22}$$

with the renormalisation factor $r_1 = r_1(\mu = m_c, M_{Z'})$ defined in Eq. (5.34). For illustrative purposes, we evaluate Eq. (7.22) for a benchmark value of $M_{Z'} = 6$ TeV, which yields

$$\begin{aligned}
\widetilde{\mathcal{C}}_7^{(\prime)}(m_c) &= \;\;0.83\,\widetilde{\mathcal{C}}_7^{(\prime)}(M_{Z'})\,,\\
\widetilde{\mathcal{C}}_8^{(\prime)}(m_c) &= \;\;1.22\,\widetilde{\mathcal{C}}_7^{(\prime)}(M_{Z'})+4.50\,\widetilde{\mathcal{C}}_8^{(\prime)}(M_{Z'})\,,\\
\widetilde{\mathcal{C}}_9^{(\prime)}(m_c) &= \;\;1.40\,\widetilde{\mathcal{C}}_9^{(\prime)}(M_{Z'})-0.72\,\widetilde{\mathcal{C}}_{10}^{(\prime)}(M_{Z'})\,,\\
\widetilde{\mathcal{C}}_{10}^{(\prime)}(m_c) &= -0.72\,\widetilde{\mathcal{C}}_9^{(\prime)}(M_{Z'})+1.40\,\widetilde{\mathcal{C}}_{10}^{(\prime)}(M_{Z'})\,.
\end{aligned} \tag{7.23}$$

Furthermore, we define the functions

$$R_1\left(m_c, M_{Z'}\right) = \frac{r_1^{-4}}{3\sqrt{2}\,G_{\rm F}\,\lambda_s}\,, \quad R_2\left(m_c, M_{Z'}\right) = \frac{2\,r_1 - r_1^{-2}}{3\sqrt{2}\,G_{\rm F}\,\lambda_s}\,, \tag{7.24}$$

which incorporate the running of different combinations of Wilson coefficients and are of use in subsequent calculations.

To compute the NP decay amplitudes $\mathcal{A}_f^{\rm NP}$, we need to determine the respective HMEs for each operator in Eq. (7.20). For the sake of brevity, we provide the necessary details on the derivation of the HMEs in App. F.3. The results for $D^0 \to K^+K^-$ and $D^0 \to \pi^+\pi^-$ decays, as well as the related $D^+ \to \pi^+\pi^0$ and $D^0 \to \pi^0\pi^0$ decays, are compiled in Tab. 7.2. Therein, we utilise the shorthand notation

$$\begin{aligned}
\langle \ldots \rangle_K &= \langle K^+K^-| \ldots |D^0\rangle\,, \quad & \langle \ldots \rangle_\pi &= \langle \pi^+\pi^-| \ldots |D^0\rangle\,,\\
\langle \ldots \rangle_{\pi'} &= \langle \pi^+\pi^0| \ldots |D^+\rangle\,, \quad & \langle \ldots \rangle_{\pi^0} &= \langle \pi^0\pi^0| \ldots |D^0\rangle\,.
\end{aligned} \tag{7.25}$$

The HMEs are expressed in terms of the associated SM matrix elements, that is $\langle Q_1^s\rangle_K$ and $\langle Q_1^d\rangle_\pi$, with $Q_1^p = (\overline{u}p)_{V-A}(\overline{p}c)_{V-A}$, for $D^0 \to K^+K^-$ and $D^0 \to \pi^+\pi^-$, respectively. For $D^+ \to \pi^+\pi^0$ and $D^0 \to \pi^0\pi^0$ decays the SM contributions are proportional to $\langle Q_1^u\rangle_u = \langle \overline{u}u|\, Q_1^u\, |D^0\rangle$. Moreover, we employ the chiral enhancements $\chi_K(m_c) \approx 3.626$ and $\chi_\pi(m_c) \approx 3.655$ generated by $(V-A)\times(V+A)$ operators at the charm mass scale, see Eq. (B.2). All entries in Tab. 7.2 are obtained in the isospin limit, $m_u = m_d$ and $e = 0$. We impose this limit as isospin breaking corrections from NP, $F_{Q_i,U_i,D_i} \neq 0$, fully dominate compared to the ones within the SM. Then, $\langle Q_1^u\rangle_u = \langle Q_1^d\rangle_d$ and the $\langle \widetilde{Q}_{9,10}\rangle_{\pi',\pi^0}$ vanish as they are proportional to $(F_{Q_1} - F_{Q_1}) = 0$.

The parametrisation of the HMEs in terms of SM contributions is convenient since in the formula for $A_{CP}^{\rm NP}$ in Eq. (7.10) only the ratio of NP and SM amplitudes enters, and therefore the elements $\langle Q_1^{s,d}\rangle_{K,\pi}$ cancel.

| | $P = K$ | $P = \pi$ | $P = \pi'$ | $P = \pi^0$ |
|---|---|---|---|---|
| $\langle \widetilde{Q}_7 \rangle_P$ | $\frac{F_{D_2}\,\chi_K}{N_C}\,\langle Q_1^s \rangle_K$ | $\frac{F_{D_1}\,\chi_\pi}{N_C}\,\langle Q_1^d \rangle_\pi$ | $\frac{\left(F_{U_1}-F_{D_1}\right)\chi_\pi}{\sqrt{2}\,N_C}\,\langle Q_1^u \rangle_u$ | $\frac{\left(F_{U_1}-F_{D_1}\right)\chi_\pi}{2\,N_C}\,\langle Q_1^u \rangle_u$ |
| $\langle \widetilde{Q}_8 \rangle_P$ | $F_{D_2}\,\chi_K\,\langle Q_1^s \rangle_K$ | $F_{D_1}\,\chi_\pi\,\langle Q_1^d \rangle_\pi$ | $\frac{\left(F_{U_1}-F_{D_1}\right)\chi_\pi}{\sqrt{2}}\,\langle Q_1^u \rangle_u$ | $\frac{\left(F_{U_1}-F_{D_1}\right)\chi_\pi}{2}\,\langle Q_1^u \rangle_u$ |
| $\langle \widetilde{Q}_9 \rangle_P$ | $\frac{F_{Q_2}}{N_C}\,\langle Q_1^s \rangle_K$ | $\frac{F_{Q_1}}{N_C}\,\langle Q_1^d \rangle_\pi$ | 0 | 0 |
| $\langle \widetilde{Q}_{10} \rangle_P$ | $F_{Q_2}\,\langle Q_1^s \rangle_K$ | $F_{Q_1}\,\langle Q_1^d \rangle_\pi$ | 0 | 0 |
| $\langle \widetilde{Q}'_7 \rangle_P$ | $\frac{F_{Q_2}\,\chi_K}{N_C}\,\langle Q_1^s \rangle_K$ | $\frac{F_{Q_1}\,\chi_\pi}{N_C}\,\langle Q_1^d \rangle_\pi$ | 0 | 0 |
| $\langle \widetilde{Q}'_8 \rangle_P$ | $F_{Q_2}\,\chi_K\,\langle Q_1^s \rangle_K$ | $F_{Q_1}\,\chi_\pi\,\langle Q_1^d \rangle_\pi$ | 0 | 0 |
| $\langle \widetilde{Q}'_9 \rangle_P$ | $\frac{F_{D_2}}{N_C}\,\langle Q_1^s \rangle_K$ | $\frac{F_{D_1}}{N_C}\,\langle Q_1^d \rangle_\pi$ | $\frac{F_{U_1}-F_{D_1}}{\sqrt{2}\,N_C}\,\langle Q_1^u \rangle_u$ | $\frac{F_{U_1}-F_{D_1}}{2\,N_C}\,\langle Q_1^u \rangle_u$ |
| $\langle \widetilde{Q}'_{10} \rangle_P$ | $F_{D_2}\,\langle Q_1^s \rangle_K$ | $F_{D_1}\,\langle Q_1^d \rangle_\pi$ | $\frac{F_{U_1}-F_{D_1}}{\sqrt{2}}\,\langle Q_1^u \rangle_u$ | $\frac{F_{U_1}-F_{D_1}}{2}\,\langle Q_1^u \rangle_u$ |

**Table 7.2:** List of HMEs for the operators in Eq. (7.20) where $\chi_P = \chi_P(\mu)$, $P = K, \pi$, denote the chiral enhancements and $F_f$ is the associated U(1)′ charge. For more details, see the main text and App. F.

## 7.1.4 Avoiding $D^0$-$\overline{D}^0$ mixing constraints

Following Eqs. (5.37) and (5.38), the constraint from $D$-mixing on the couplings $g_{L,R}^{cu}$ is given by

$$\left| \left(g_L^{cu}\right)^2 + \left(g_R^{cu}\right)^2 - X\, g_L^{cu}\, g_R^{cu} \right| \lesssim 6.4 \cdot 10^{-7} \left(\frac{M_{Z'}}{\text{TeV}}\right)^2 , \tag{7.26}$$

assuming complex-valued couplings, and $X \approx 20$ for $M_{Z'}$ in the TeV-range. The parameter $X$ has been determined in Eq. (5.36). The bound in Eq. (7.26) can be circumvented by inducing both non-zero couplings $g_L^{cu}$, $g_R^{cu}$ that exhibit the hierarchy $g_L^{cu} = 1/X\, g_R^{cu}$ or $g_L^{cu} = X\, g_R^{cu}$, see Sec. 5.3.1. Notably, Eq. (7.26) forces the $CP$ phases of both couplings to be aligned, *i.e.* $\arg\left(g_L^{cu}\right) \sim \arg\left(g_R^{cu}\right)$. As only SM-like $CP$ phases in $g_L^{cu}$ are allowed, *cf.* Eq. (7.17), we find that possible $CP$-violating effects in charm are irrelevant in the case of both non-zero couplings $g_L^{cu} \neq 0$ and $g_R^{cu} \neq 0$. This is the main difference compared to the $Z'$ model set-up discussed in Sec. 6.3, where $CP$ phases have not been included, assuming real-valued, hierarchical couplings instead. Therefore, we choose $g_L^{cu} = 0$ to generate sizeable $CP$ phases in $g_R^{cu}$, which is possible by setting $\Delta F_L = F_{Q_2} - F_{Q_1} = 0$ while $\Delta F_R = F_{U_2} - F_{U_1} \neq 0$ needs to hold at the same time. This can be achieved for a selection of the $Z'$ models listed in Tab. 6.1, where it is possible to rearrange U(1)′ charges due to permutation invariance. We additionally consider new models 9 and 10 that feature large $\Delta F_R$ and, conversely, $\Delta F_L = 0$ by construction. All models are compiled in Tab. 7.3. In models 9 and 10($\mu$), no U(1)′ charges $F_{Q_i}$ are present. Model 10$\mu$ is constructed from model 10 while choosing smaller couplings to muons, $F_{L_2}$ and $F_{E_2}$. As we consider only the complex-valued coupling $g_R^{cu} \neq 0$, the bound in Eq. (7.26) simplifies to

$$\left| g_R^{cu} \right| \lesssim 8.0 \cdot 10^{-4} \left(\frac{M_{Z'}}{\text{TeV}}\right) . \tag{7.27}$$

| Model | $F_{Q_i}$ | | | $F_{U_i}$ | | | $F_{D_i}$ | | | $F_{L_i}$ | | | $F_{E_i}$ | | | $F_{\nu_i}$ | | |
|---|---|---|---|---|---|---|---|---|---|---|---|---|---|---|---|---|---|---|
| 2 | 3 | 3 | -6 | -8 | 4 | 4 | -10 | 10 | 0 | -6 | 5 | 1 | 0 | 0 | 0 | 0 | 0 | 0 |
| 4 | -1 | -1 | 2 | -1 | 2 | -1 | 0 | 0 | 0 | -1 | 1 | 0 | -2 | 2 | 0 | -2 | -1 | 3 |
| 5 | -1 | -1 | 2 | -1 | 2 | -1 | 2 | -1 | -1 | -1 | 1 | 0 | -1 | 1 | 0 | 0 | 0 | 0 |
| 9 | 0 | 0 | 0 | -11 | -2 | 13 | 7 | 7 | -14 | -8 | 3 | 5 | -6 | 16 | -10 | 0 | 0 | 0 |
| 10 | 0 | 0 | 0 | -13 | 6 | 7 | -1 | -14 | 15 | -15 | 15 | 0 | -14 | 18 | -4 | 0 | 0 | 0 |
| $10\mu$ | 0 | 0 | 0 | -13 | 6 | 7 | -1 | -14 | 15 | -15 | 0 | 15 | -14 | -4 | 18 | 0 | 0 | 0 |

**Table 7.3:** Selected $Z'$ models taken from Tab. 6.1 where $\Delta F_L = 0$ and $\Delta F_R \neq 0$ are possible through permutation of $\mathrm{U}(1)'$ charges, see main text for details. We add models 9 and $10(\mu)$, where all $F_{Q_i} = 0$. Model $10\mu$ refers to model 10 with the smallest couplings to muons, *i.e.* $F_{L_2}$ and $F_{E_2}$. *Table taken from Ref.* [17].

Additionally, the $CP$-violating observable $x_{12}\sin(\phi_{12})$ in Eq. (5.28) provides an even stronger bound on the phase of $g_R^{cu}$,

$$x_{12}\sin(\phi_{12}) \lesssim 1.98\cdot 10^{-4}\,. \tag{7.28}$$

However, it can be circumvented for certain choices of $\phi_R = \arg(g_R)$ around $\pi/2$ (or $3\pi/2$), where $\sin(\phi_{12}) = \sin(2\,\phi_R) \simeq 0$ [17, 177]. Then, the contributions to $\Delta A_{CP}$ are maximized while the constraints from $D$-mixing are satisfied at the same time. We illustrate this interplay in Fig. 7.2, where NP contributions to $\Delta A_{CP}$ are shown in the $\phi_R$-$g_4/M_{Z'}$ plane for the selected models 2 and $10(\mu)$. The induced $\Delta A_{CP}^{\mathrm{NP}}$ is worked out in Eq. (7.30) and shown as green bands. We also display the regions excluded by $D$-mixing, distinguishing between the bound on the absolute value $x_{12}$ (red hatched region) and the imaginary part $x_{12}\sin(\phi_{12})$ (red region). In each plot a dedicated benchmark point taken from Tab. 7.4 indicates a value of $\Delta A_{CP}^{\mathrm{NP}} \sim 10^{-3}$ and $\phi_R \sim \pi/2$, reproducing the world average of $\Delta A_{CP}$ in Eq. (7.4).

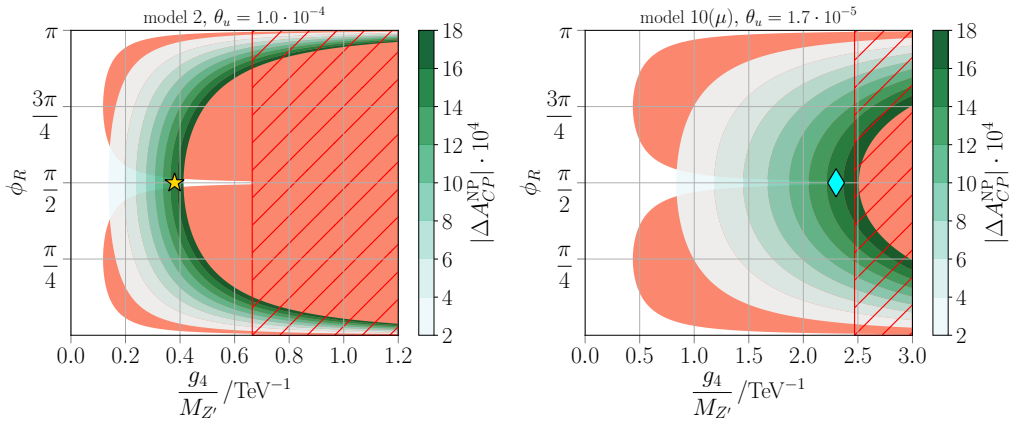


**Figure 7.2:** Exclusion regions from $D^0$-$\overline{D}^0$ mixing (red regions) and contributions $|\Delta A_{CP}^{\mathrm{NP}}|$ (green bands) in the $\phi_R$-$g_4/M_{Z'}$ plane. Constraints on the absolute value $x_{12}$ are indicated by the red hatched rectangle, whereas the parameter space excluded by constraints on the imaginary part $x_{12}\sin(\phi_{12})$ is displayed by the red region, *cf.* Eqs. (7.27) and (7.28), respectively. The coloured markers indicate benchmarks listed in Tab. 7.4. *Figure adapted from Ref.* [17].

| Benchmark marker | Model | $\frac{g_4}{M_{Z'}}$ / TeV$^{-1}$ | $\theta_u \cdot 10^4$ | $\Delta F_R$ | $\phi_R$ | $\lvert\Delta A_{CP}^{\rm NP}\rvert \cdot 10^3$ |
|---|---|---|---|---|---|---|
| golden star ☆ | model 2 | 0.38 | 1.0 | 12 | $\pi/2$ | 1.5 |
| brown star ★ | model 4 | 1.40 | 1.0 | 3 | $\pi/2$ | 1.7 |
| blue star ★ | model 5 | 1.30 | 1.0 | 3 | $\pi/2$ | 1.5 |
| purple diamond ♦ | model 9 | 2.30 | 0.36 | 9 | $\pi/2$ | 1.6 |
| pink diamond ♦ | model 10 | 2.30 | 0.17 | 19 | $\pi/2$ | 1.5 |
| cyan diamond ♦ | model 10$\mu$ | 2.30 | 0.17 | 19 | $\pi/2$ | 1.5 |

**Table 7.4:** List of benchmarks for $Z'$ models given in Tab. 7.3 with parameter settings that generate $\Delta A_{CP}^{\rm NP} \sim 10^{-3}$.

In what follows, we present a study involving $Z'$ models that feature only RH couplings with a $CP$ phase $\phi_R = \pi/2$ and generate sizeable effects in $\Delta A_{CP}$. We reveal and discuss NP patterns for benchmark scenarios that suffice the input from Eq. (7.27).

## 7.2 Study of $\Delta A_{CP}$ in $Z'$ models

Using Eq. (7.10), we can parametrise NP effects to $\Delta A_{CP}$ as

$$\Delta A_{CP}^{\rm NP} = A_{CP}^{\rm NP}\left(K^+K^-\right) - A_{CP}^{\rm NP}\left(\pi^+\pi^-\right) , \tag{7.29}$$

with

$$\begin{aligned} A_{CP}^{\rm NP}\left(K^+K^-\right) &\sim \frac{g_4^2}{M_{Z'}^2}\theta_u\,\Delta F_R\left[c_K\,F_{Q_2} + d_K\,F_{D_2}\right] , \\ A_{CP}^{\rm NP}\left(\pi^+\pi^-\right) &\sim \frac{g_4^2}{M_{Z'}^2}\theta_u\,\Delta F_R\left[c_\pi\,F_{Q_1} + d_\pi\,F_{D_1}\right] . \end{aligned} \tag{7.30}$$

Here, we have employed $\sin(\theta_u)\cos(\theta_u) \approx \theta_u \ll 1$ in Eq. (7.18) and set $g_L^{cu} = 0$ in accordance with the assumptions outlined in Sec. 7.1.4. The parameters $c_{\pi,K}$ and $d_{\pi,K}$ encode the LO running of the strong coupling via the functions $R_{1,2}$ as well as the tree-level contributions $a_{K,\pi}$ fixed by experiment, *cf.* Eq. (7.24) and Tab. 7.1, respectively. In addition, the parameters $c_{\pi,K}$ include the chiral enhancements $\chi_{K,\pi}$ induced by the operators $\widetilde{Q}'_{7,8}$. The exact form of these parameters is given by

$$c_{K(\pi)} = (-)\,\frac{\chi_{K(\pi)}}{a_{K(\pi)}}\,R_1\left(m_c, M_{Z'}\right) , \quad d_{K(\pi)} = (-)\,\frac{1}{a_{K(\pi)}}\,R_2\left(m_c, M_{Z'}\right) , \tag{7.31}$$

where numerical values for different $Z'$ masses are given in Tab. 7.5.

Note that the sign of $A_{CP}^{\rm NP}(f)$, with $f = K^+K^-, \pi^+\pi^-$, is always chosen to match the experimental value of $\Delta A_{CP}$. This is possible since no information on the strong phases $\delta_{K,\pi}$ is available. Therefore, $\sin(\delta_{K,\pi})\sin(\phi_R) \sim 1$ is used in Eq. (7.30). We remark that flipping the sign of $\theta_u$ or choosing, *e.g.*, $\phi_R = 3\pi/2$ would have the same effect, but we do not consider this possibility here.

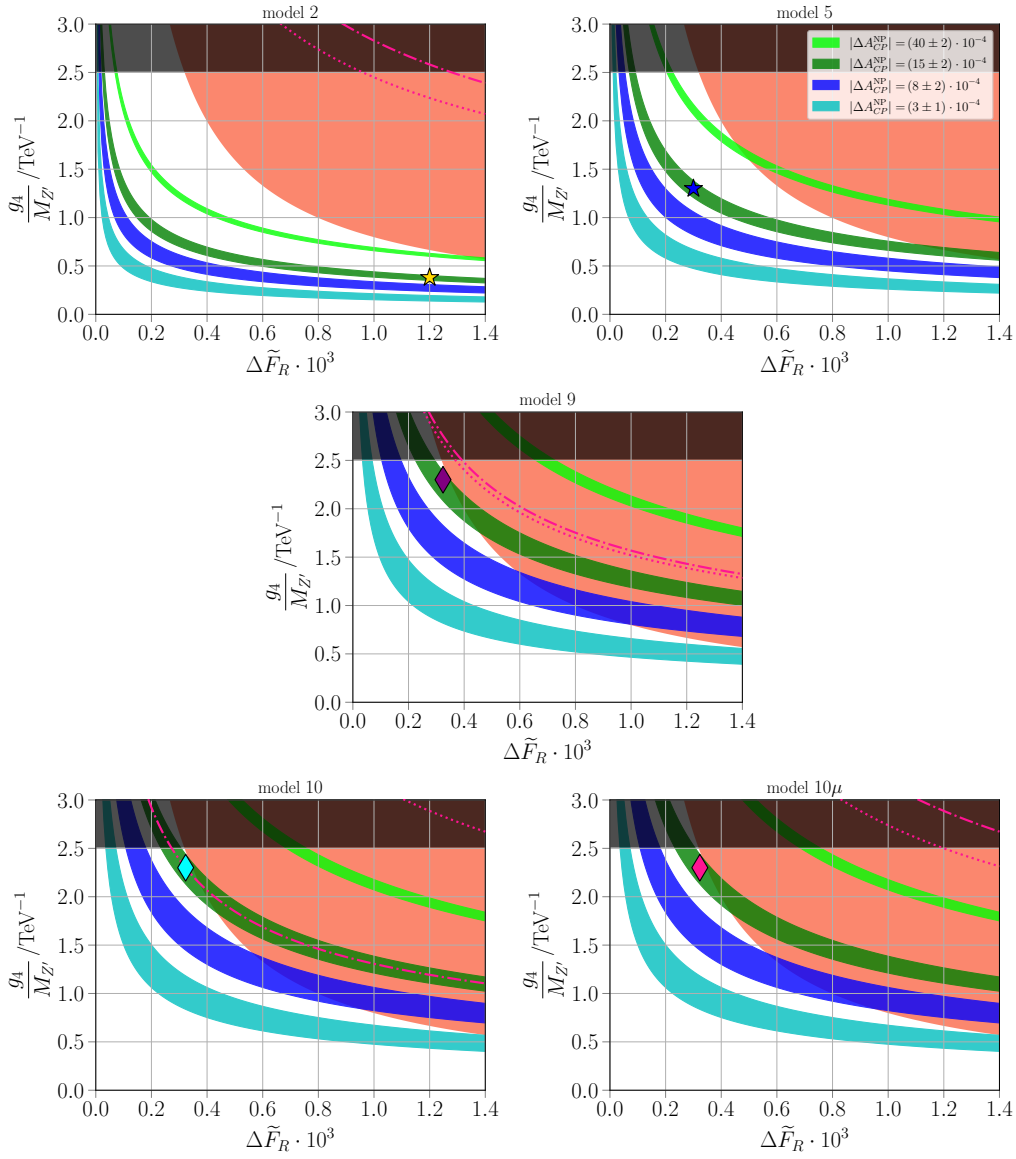


**Figure 7.3:** $|\Delta A_{CP}^{\rm NP}|$ for different $Z'$ models (see plot titles) in the plane of $g_4/M_{Z'}$ versus the parameter $\Delta \widetilde{F}_R = \Delta F_R \cdot \theta_u$, together with the excluded region from $D^0$-$\overline{D}^0$ mixing (red), see Eq. (7.27). The pink dashed-dotted and dotted lines indicate the bounds from Eqs. (7.32) and (7.33), respectively. The black region is excluded due to bounds coming from perturbativity and direct searches in dimuon and dielectron spectra [32], that is $g_4 \leq 4\pi$ and $M_{Z'} \geq 5$ TeV, respectively. The markers (stars, diamonds) refer to benchmark points in Tab. 7.4. *Expanded version of a figure taken from Ref.* [17].

| $M_{Z'}$ / TeV | 2 | 4 | 6 | 8 | 10 |
|---|---|---|---|---|---|
| $c_K$ | 1.133 | 1.217 | 1.266 | 1.302 | 1.330 |
| $d_K$ | −0.046 | −0.054 | −0.058 | −0.061 | −0.063 |
| $c_\pi$ | −1.446 | −1.553 | −1.616 | −1.661 | −1.698 |
| $d_\pi$ | 0.058 | 0.068 | 0.074 | 0.077 | 0.080 |
| $d_{\pi'}$ | 0.071 | 0.083 | 0.090 | 0.094 | 0.098 |
| $d_{\pi 0}$ | 0.077 | 0.090 | 0.097 | 0.102 | 0.106 |

**Table 7.5:** Numerical values of parameters $c_{K,\pi}, d_{K,\pi}$ and $d_{\pi',\pi^0}$ in units of TeV$^2$ as defined in Eqs. (7.31) and (7.46), respectively, for different $Z'$ masses. *Table taken from Ref.* [17].

In Fig. 7.3, we display contributions to $\Delta A_{CP}^{\rm NP}$ using Eq. (7.29) for the $Z'$ models 2, 5, 9, 10, and 10$\mu$, see Tab. 7.3. We plot different contours in the plane of $g_4/M_{Z'}$ versus the parameter $\Delta\widetilde{F}_R = \Delta F_R \cdot \theta_u$. The exclusion region from the $D$-mixing constraint in Eq. (7.27) is shown in red. The corresponding plot of model 4 is omitted in Fig. 7.3 as only marginal differences to model 5 are present in terms of $\Delta A_{CP}^{\rm NP}$-bands and exclusion bounds due to identical $F_{Q_{1,2}}$. We show both plots for models 10 and 10$\mu$ since different bounds coming from (semi)muonic $D$-decays, shown as pink (dash-)dotted lines, are obtained. These bounds are extracted from upper limits on branching ratios of $D^+ \to \pi^+\mu^+\mu^-$ and $D^0 \to \mu^+\mu^-$ decays that have been worked out in Eqs. (6.19) and (6.20), respectively. For $g_L^{cu} = 0$, they can be rewritten as [2]

$$\left|g_R^{cu}\right| \sqrt{(g_L^{\mu\mu})^2 + (g_R^{\mu\mu})^2} = g_4^2 \left|\Delta\widetilde{F}_R\right| \sqrt{F_{L_2}^2 + F_{e_2}^2} \lesssim 0.04 \left(\frac{M_{Z'}}{\text{TeV}}\right)^2 , \tag{7.32}$$

$$\left|g_R \left(g_L^{\mu\mu} - g_R^{\mu\mu}\right)\right| = g_4^2 \left|\Delta\widetilde{F}_R \left(F_{L_2} - F_{E_2}\right)\right| \lesssim 0.03 \left(\frac{M_{Z'}}{\text{TeV}}\right)^2 . \tag{7.33}$$

As shown in Fig. 7.3, these bounds are in general weaker than those from $D$-mixing, however they become relevant for models with large lepton couplings, *i.e.* models 9 and 10, close to the (black) non-perturbativity region. On that account, model 10$\mu$ is constructed to evade the muon constraints by choosing the smallest $F_{L_2}$ and $F_{E_2}$ through permutation of lepton charges. Hence, improved bounds from future measurements would still allow for $\Delta A_{CP}^{\rm NP} \sim 10^{-3}$ in this model. Notably, models 2, 4, and 5 are the least affected by the constraints as they exhibit small couplings to leptons (but also to quarks) compared to the other models. In consequence, they provide a larger viable parameter space, allowing for $\Delta A_{CP}^{\rm NP} \sim 4 \cdot 10^{-3}$ (lime green band). We also show the selected benchmark points for each model in Fig. 7.3 that pass the aforementioned constraints while inducing $\Delta A_{CP}^{\rm NP} \sim 10^{-3}$.

## 7.3 Symmetry patterns in hadronic charm decays

Flavour-breaking signatures are realised in $Z'$ models due to the non-universal U(1)$'$ charges. They entail large breaking effects that can significantly alter relations based on approximate SU(3)$_F$ symmetries between hadronic charm decays. As put forward in Sec. 2.5, $U$-spin and isospin

[2] Here, we present $Z'$ scenarios employing the outdated upper limit on $\mathcal{B}\left(D^+ \to \pi^+\mu^+\mu^-\right)$ as stated in Eq. (6.19) in brackets. Section 7.5 discusses the impact of updated measurements of observables on the $Z'$ benchmarks studied in this chapter.

| Model | $\beta_{\pi^0}$ | $\beta_{\pi'}$ | $\mathrm{U}^{\mathrm{tot}}_{\mathrm{break}}$ | $\mathrm{U}^{\mathrm{NP}}_{\mathrm{break}}$ |
|---|---|---|---|---|
| 2 | −0.02 | −0.02 | 0.42 | 0.24 |
| 4 | −0.03 | −0.03 | 0.22 | 0 |
| 5 | −0.10 | −0.09 | 0.32 | 0.11 |
| 9 | −1.89 | −1.75 | 0.22 | 0 |
| 10($\mu$) | 1.31 | 1.22 | 0.91* | 1.19* |

**Table 7.6:** Values of $\beta_{\pi'}$,$\beta_{\pi^0}$ in $\mathrm{TeV}^{-2}$ for selected $Z'$ models as defined in Eqs. (7.48) and (7.52), respectively. The quantities $\mathrm{U}^{\mathrm{tot}}_{\mathrm{break}}$ and $\mathrm{U}^{\mathrm{NP}}_{\mathrm{break}}$ are also provided, see Eqs. (7.36), (7.40), and (7.41) for their definitions. All values are given for $M_{Z'} = 6$ TeV. The asterisk indicates values obtained with swapped modes in the definition of $u_{K\pi}$ in Eq. (7.35), see Footnote 3. *Table adapted from Ref.* [17].

breaking is already realised in the SM. However, they can experience enhancements in the presence of NP contributions [173, 178, 179]. We present such breaking patterns induced by $Z'$ models in Secs. 7.3.1 and 7.3.2, and work out the $CP$ asymmetry of $D^0 \to \pi^0\pi^0$ decays in Sec. 7.3.3.

### 7.3.1 $U$-spin breaking patterns in $D^0 \to K^+K^-$ and $D^0 \to \pi^+\pi^-$

The relevant $U$-spin sum rule reads [178]

$$A_{CP}\left(K^+K^-\right) + A_{CP}\left(\pi^+\pi^-\right) = 0\,, \tag{7.34}$$

which holds in the $\mathrm{SU}(3)_F$ limit but is broken for $F_{Q_1} \neq F_{Q_2}$ or $F_{D_1} \neq F_{D_2}$ in a $\mathrm{U}(1)'$ extension, where different charges to $d$ and $s$ quarks are present. Deviations from this relation indicate $U$-spin breaking and can be expressed as [3]

$$U^{\mathrm{tot}}_{\mathrm{break}} = |1 + u_{K\pi}|\,, \quad u_{K\pi} = \frac{A_{CP}\left(K^+K^-\right)}{A_{CP}\left(\pi^+\pi^-\right)}\,, \tag{7.35}$$

where $\mathrm{U}^{\mathrm{tot}}_{\mathrm{break}} = 0$ holds in the $U$-spin limit in Eq. (7.34). Employing our parametrisation of $A_{CP}$ from Eq. (7.30), we obtain

$$U^{\mathrm{tot}}_{\mathrm{break}} = \left|1 + \frac{c_K\, F_{Q_2} + d_K\, F_{D_2}}{c_\pi\, F_{Q_1} + d_\pi\, F_{D_1}}\right|\,, \tag{7.36}$$

where numerical values for models 2, 4, 5, 9, and 10($\mu$), for $M_{Z'} = 6$ TeV, are provided in Tab. 7.6. The variation of $U^{\mathrm{tot}}_{\mathrm{break}}$ due to the $M_{Z'}$-dependence of the parameters $c_{K,\pi}$ , $d_{K,\pi}$ is at the (few) percent level.

To study how $U$-spin breaking is generated in $Z'$ models in more detail, we perform a Taylor expansion in Eq. (7.36) up to $\mathcal{O}\left(d_K, d_\pi\right)$. This is a valid approximation since the parameters $d_{K,\pi}$

[3] To avoid large values $\mathrm{U}^{\mathrm{tot}}_{\mathrm{break}} > 1$, we set $u_{K\pi} = A_{CP}\left(\pi^+\pi^-\right)/A_{CP}\left(K^+K^-\right)$ for model 10($\mu$). In this case, the subscripts $K, Q_2, D_2$ and $\pi, Q_1, D_1$ in Eq. (7.36) and following need to be swapped.

are small compared to the chirally-enhanced $c_{K,\pi}$ , that is $d_{K,\pi}/c_{K,\pi} \approx -0.05$. We obtain

$$\mathrm{U}_{\mathrm{break}}^{\mathrm{tot}} = \left|1 + \frac{c_K\, F_{Q_2}}{c_\pi\, F_{Q_1}} - \frac{c_K\, d_\pi\, F_{Q_2}\, F_{D_1}}{c_\pi^2\, F_{Q_1}^2} + \frac{d_K\, F_{D_2}}{c_\pi\, F_{Q_1}}\right| + \mathcal{O}\left(d_K^2, d_\pi^2, d_K d_\pi\right), \tag{7.37}$$

which can be simplified considering the two cases

$$\text{(i)}\, F_{Q_1} = F_{Q_2} \neq 0: \quad \mathrm{U}_{\mathrm{break}}^{\mathrm{tot}} \approx \left|1 + \frac{c_K}{c_\pi} - \frac{c_K\, d_\pi\, F_{D_1}}{c_\pi^2\, F_{Q_1}} + \frac{d_K F_{D_2}}{c_\pi F_{Q_1}}\right|, \tag{7.38a}$$

$$\text{(ii)}\, F_{Q_1} = F_{Q_2} = 0: \quad \mathrm{U}_{\mathrm{break}}^{\mathrm{tot}} = \left|1 + \frac{d_K\, F_{D_2}}{d_\pi\, F_{D_1}}\right| = \left|1 + \frac{d_K}{d_\pi} + \frac{d_K\, (F_{D_2} - F_{D_1})}{d_\pi\, F_{D_1}}\right|. \tag{7.38b}$$

Case (i) holds for models 2, 4, and 5, whereas case (ii) is valid in models 9 and 10($\mu$). Note that $\mathrm{U}_{\mathrm{break}}^{\mathrm{tot}} = 0$ is recovered for $c_K = -c_\pi$, $d_K = -d_\pi$ and universal U(1)′ charges in the $\mathrm{SU}(3)_F$ limit.

In the following, we discuss the two cases. For $F_{Q_1} = F_{Q_2} \neq 0$, we identify different sources of $U$-spin breaking. The second term in Eq. (7.38a) is responsible for effects coming from the interference between SM amplitude and NP charges $F_{Q_{1,2}}$. This contribution accounts for 22 % $U$-spin breaking, comparable to the expected breaking uncertainty of the SM. Conversely, the last two terms in Eq. (7.38a) are pure NP $U$-spin breaking effects. However, they are suppressed which can be seen by further simplifying Eq. (7.38a). We substitute $d_K \approx c_K/c_\pi\, d_\pi$, which holds numerically at the (sub-)percent level due to $\chi_\pi \approx \chi_K$, and obtain

$$\mathrm{U}_{\mathrm{break}}^{\mathrm{tot}} \approx \left|1 + \frac{c_K}{c_\pi} + \frac{d_K}{c_\pi}\left(\frac{F_{D_2} - F_{D_1}}{F_{Q_1}}\right)\right|. \tag{7.39}$$

The pure NP $U$-spin breaking effects are given by

$$\mathrm{U}_{\mathrm{break}}^{\mathrm{NP}}(F_{Q_{1,2}} \neq 0) = \frac{d_K}{c_\pi}\left|\frac{F_{D_2} - F_{D_1}}{F_{Q_1}}\right| \approx 0.04\left|\frac{F_{D_2} - F_{D_1}}{F_{Q_1}}\right|, \tag{7.40}$$

suppressed by the pion chiral enhancement and the function $R_2$, see Eq. (7.31). Regarding case (ii), where $F_{Q_{1,2}} = 0$, we can express the pure NP-induced $U$-spin breaking as

$$\mathrm{U}_{\mathrm{break}}^{\mathrm{NP}}(F_{Q_{1,2}} = 0) = \left|\frac{d_K\, (F_{D_2} - F_{D_1})}{d_\pi\, F_{D_1}}\right| \approx 0.78\left|\frac{F_{D_2} - F_{D_1}}{F_{D_1}}\right|. \tag{7.41}$$

In Tab. 7.6, the values of $\mathrm{U}_{\mathrm{break}}^{\mathrm{NP}}$ for the $Z'$ models are listed.

For models that obey case (i), we find $U$-spin breaking effects within the range of the expected SM $U$-spin breaking $\lesssim 30\,\%$ for values of $F_{D_2} - F_{D_1} \sim \mathcal{O}(1)$ as in model 5. The $U$-spin breaking in model 4 is SM-like due to $F_{D_i} = 0$, hence $\mathrm{U}_{\mathrm{break}}^{\mathrm{NP}} = 0$. In contrast, large effects are possible for $F_{D_2} - F_{D_1} \sim \mathcal{O}(10)$ as in model 2, which would be observable with future sensitivities for $A_{CP}\,(K^+K^-)$ and $A_{CP}\,(\pi^+\pi^-)$ collected in Tab. 7.7.

For models of case (ii), the NP $U$-spin breaking effects in Eq. (7.41) are unsuppressed. For instance, in model 10($\mu$) large $\mathrm{U}_{\mathrm{break}}^{\mathrm{NP}}$ is generated, though the SM-interference term with an opposite sign slightly reduces the total $U$-spin breaking. Model 9 features $F_{Q_1} = F_{Q_2} = 0$ as well. However, $U$-spin breaking emerges from $d_K \neq -d_\pi$ only due to $F_{D_1} = F_{D_2}$ in this model, which yields SM-like effects as in model 4.

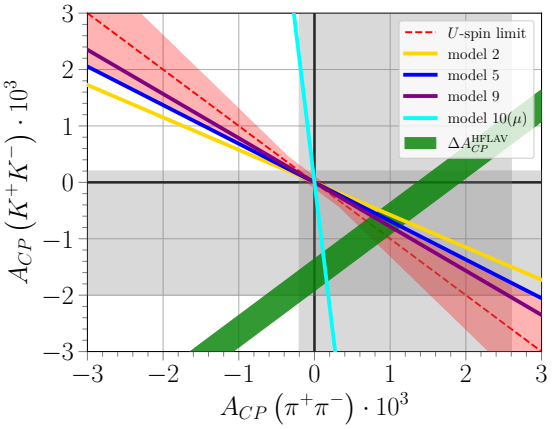


**Figure 7.4:** Individual $CP$ asymmetries $A_{CP}\left(K^+K^-\right)$ versus $A_{CP}\left(\pi^+\pi^-\right)$ with NP contributions of models 2, 5, 9, and 10($\mu$) indicated by yellow, blue, purple and cyan lines, respectively. The green band denotes the experimental world average of $\Delta A_{CP}$ in Eq. (7.4) at $1\,\sigma$, while the present $1\,\sigma$ regions of the individual asymmetries listed in Tab. 7.7 are shown as grey bands. The $U$-spin limit in Eq. (7.34) is shown as a red dashed line, while SM-like $U$-spin breaking $\leq 30\,\%$ is indicated by the red region for comparison. *Figure adapted from Ref.* [17].

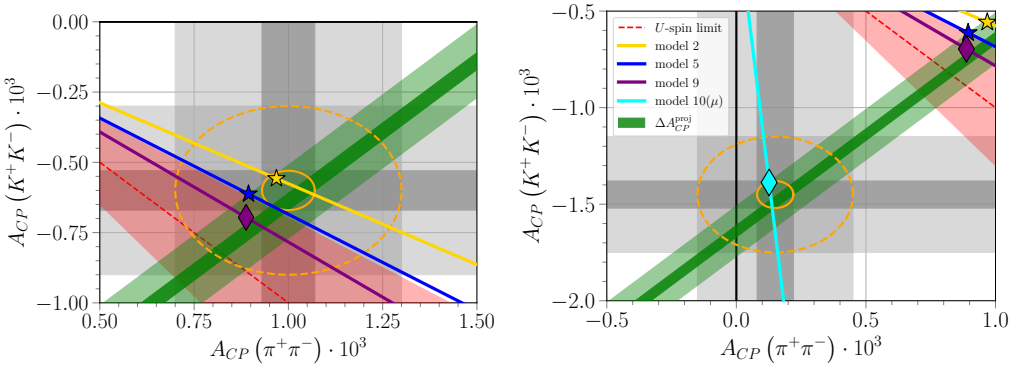


**Figure 7.5:** Future projections for $A_{CP}\left(K^+K^-\right)$ versus $A_{CP}\left(\pi^+\pi^-\right)$ with predictions in the $Z'$ models 2, 5, 9, and 10($\mu$) in yellow, blue, purple and cyan lines, respectively. The green band denotes the experimental world average of $\Delta A_{CP}$ in Eq. (7.4) with projected $1\,\sigma$ sensitivities according to Tab. 7.7. Indicated by the grey bands are two future measurements of the individual asymmetries, *i.e. future* I (left-hand side plot) and *future* II (right-hand side plot), with central values given in Eqs. (7.42) and (7.43), respectively, and uncertainties scaled according to Tab. 7.7. The markers denote benchmark points listed in Tab. 7.4. Light and dark grey bands correspond to LHCb Run 1-3 and Run 1-5, respectively. Around the benchmark points of model 2 (left-hand side plot) and model 10$\mu$ (right-hand side plot) dashed and solid ellipses are drawn for LHCb Run 1-3 and Run 1-5 sensitivities, respectively, assuming Gaussian errors for simplicity. The $U$-spin limit in Eq. (7.34) is shown as a red dashed line, while SM-like $U$-spin breaking $\leq 30\,\%$ is indicated by the red region for comparison. *Figure adapted from Ref.* [17].

| $\cdot 10^{-4}$ | Data | $\sigma_{\text{LHCb}}$ | $\sigma_{\text{BelleII}}$ |
|---|---|---|---|
| $\Delta A_{CP}^{\text{LHCb}}$ | $-15.4 \pm 2.9$ [169] | 1.3 (0.3) | – |
| $\Delta A_{CP}^{\text{HFLAV}}$ | $-16.4 \pm 2.8$ [123] | 1.3 (0.3) | – |
| $A_{CP}\,(D^0 \to K^+K^-)$ | $-9 \pm 11$ [123] | 3 (0.7) | 3 |
| $A_{CP}\,(D^0 \to \pi^+\pi^-)$ | $12 \pm 14$ [123] | 3 (0.7) | 5 |
| $A_{CP}\,(D^0 \to \pi^0\pi^0)$ | $-3 \pm 64$ [123] | – | 9 |
| $A_{CP}\,(D^+ \to \pi^+\pi^0)$ | $+290 \pm 290 \pm 30$ [180] | – | 17 |

**Table 7.7:** $CP$ asymmetries and future sensitivities $\sigma$ in units of $10^{-4}$ at LHCb Run 1-3 (Run 1-5) with $23\,\text{fb}^{-1}(300\,\text{fb}^{-1})$ [165] and Belle II with $50\,\text{ab}^{-1}$ [85]. *Table adapted from Ref.* [17].

The contributions of models 2, 5, 9, and 10($\mu$) to the individual $CP$ asymmetries $A_{CP}\,(K^+K^-)$ and $A_{CP}\,(\pi^+\pi^-)$ are depicted in Figs. 7.4 and 7.5 as yellow, blue, purple, and cyan lines, respectively. Model 4 is not shown as it features $U$-spin breaking similar to model 9. The $U$-spin limit in Eq. (7.34) is indicated by the red dashed line, while the red contour highlights $U$-spin breaking of 30 %. In Fig. 7.4, we show the current experimental bounds listed in Tab. 7.7 as $1\,\sigma$ regions in grey and green for the individual asymmetries and $\Delta A_{CP}$, respectively. Figure 7.5 illustrates two possible measurements denoted as *future* I (left-hand side plot) and *future* II (right-hand side plot). Therein, the light and dark grey bands indicate the projected sensitivities for the individual asymmetries from LHCb Run 1-3 and Run 1-5, respectively. In a similar manner, the green bands highlight the projections for $\Delta A_{CP}$. The central values of the measurements are chosen as

$$\begin{gathered} \textit{future}\ \text{I}: \\ A_{CP}^{\text{cen}}\left(K^-K^+\right) = -0.60 \cdot 10^{-3}\,, \quad A_{CP}^{\text{cen}}\left(\pi^-\pi^-\right) = 1.00 \cdot 10^{-3}\,, \end{gathered} \tag{7.42}$$

$$\begin{gathered} \textit{future}\ \text{II}: \\ A_{CP}^{\text{cen}}\left(K^-K^+\right) = -1.45 \cdot 10^{-3}\,, \quad A_{CP}^{\text{cen}}\left(\pi^-\pi^-\right) = 0.15 \cdot 10^{-3}\,. \end{gathered} \tag{7.43}$$

They coincide approximately with values generated by two benchmark points, labelled by a golden star (model 2) and a cyan diamond (model 10($\mu$)), whereas the uncertainties are scaled according to Tab. 7.7. For completion, we also display the benchmark points for the other models taken from Tab. 7.4. To illustrate the NP sensitivity, we show the $1\,\sigma$ regions of the projected uncertainties of $A_{CP}\,(K^+K^-)$ and $A_{CP}\,(\pi^+\pi^-)$ as dashed (solid) orange ellipses for LHCb Run 1-3 (1-5) assuming no correlations. We stress that future analyses that incorporate such correlations between the individual asymmetries and $\Delta A_{CP}$ are likely to be more powerful and distinguish between different NP scenarios.

In the $Z'$ models presented various amounts of $U$-spin breaking are realised. For instance, model 10($\mu$) features a 90 % breaking that easily exceeds the expected amount present within the SM of 30 %. Conversely, the $U$-spin symmetry in model 2 is broken at the level of 40 %, in the same ballpark as the SM. The projected sensitivities of LHCb and Belle II in Tab. 7.7 have the potential to signal NP in $A_{CP}\,(K^+K^-)$ and $A_{CP}\,(\pi^+\pi^-)$.

### 7.3.2 Isospin breaking patterns in $D^+ \to \pi^+\pi^0$

In the following, we examine the isospin breaking induced by flavourful $Z'$ models for $F_{U_1} \neq F_{D_1}$, which can be probed studying the $D^+ \to \pi^+\pi^0$ decay. Its $CP$ asymmetry $A_{CP}\left(D^+ \to \pi^+\pi^0\right)$, defined by

$$A_{CP}\left(\pi^+\pi^0\right) = \frac{\Gamma(D^+ \to f^+) - \Gamma(D^- \to f^-)}{\Gamma(D^+ \to f^+) + \Gamma(D^- \to f^-)}\,, \tag{7.44}$$

with $f^\pm = \pi^\pm\pi^0$, is of special concern as it constitutes a clean null test of the SM [181]. Following Sec. 7.2, we can parametrise the NP contribution as

$$A_{CP}^{\rm NP}\left(\pi^+\pi^0\right) \sim \frac{g_4^2}{M_{Z'}^2}\,\theta_u\,\Delta F_R\,d_{\pi'}\left(F_{D_1} - F_{U_1}\right)\,, \tag{7.45}$$

where we have inserted the corresponding HMEs from Tab. 7.2, and assumed $\theta_u \ll 1$. The parameter

$$d_{\pi'} = -\frac{1}{a_{\pi'}}\,R_2\left(m_c, M_{Z'}\right) \tag{7.46}$$

includes the SM tree-level contribution to $D^+ \to \pi^+\pi^0$, $a_{\pi'}$, given in Tab. 7.1. Numerical values of $d_{\pi'}$ for different $Z'$ masses are collected in Tab. 7.5. By comparing Eq. (7.45) with the $\Delta A_{CP}^{\rm NP}$ formula in Eq. (7.10), we find

$$A_{CP}^{\rm NP}\left(\pi^+\pi^0\right) \sim \beta_{\pi'} \cdot \Delta A_{CP}^{\rm NP}\,, \tag{7.47}$$

where

$$\beta_{\pi'} = \frac{d_{\pi'}\,\left(F_{D_1} - F_{U_1}\right)}{c_K\,F_{Q_2} + d_K\,F_{D_2} - c_\pi\,F_{Q_1} - d_\pi\,F_{D_1}}\,. \tag{7.48}$$

In Tab. 7.6, values of $\beta_{\pi'}$ for $M_{Z'} = 6$ TeV and different $Z'$ models are provided. Note that we have lost information about the signs of the leading SM decay amplitudes which interfere with possible NP. Therefore, we are unable to predict the relative sign between $A_{CP}^{\rm NP}\left(\pi^+\pi^0\right)$ and $\Delta A_{CP}^{\rm NP}$ in Eq. (7.47) without a robust determination of the strong phases.

Nevertheless, we can study $\beta_{\pi'}$ in our NP models and the asymmetry induced for $\Delta A_{CP}^{\rm NP} \sim 10^{-3}$ in the light of future measurements compiled in Tab. 7.7, which yields interesting findings. In models 9 and 10($\mu$), values of $A_{CP}^{\rm NP}\left(\pi^+\pi^0\right) \sim (1-2)\cdot\Delta A_{CP}^{\rm NP}$ are generated which are within the projected sensitivities of Belle II with $50\,{\rm ab}^{-1}$ [85]. However, models 2, 4, and 5 only induce $A_{CP}^{\rm NP}\left(\pi^+\pi^0\right) \lesssim 0.1\cdot\Delta A_{CP}^{\rm NP} \sim 10^{-4}$ which is beyond the reach of Belle II and LHCb. Additional insight into this behaviour is gained by expanding Eq. (7.48) in the $d_i$ up to $\mathcal{O}\left(d_i\right)$. Again, we distinguish between the two cases $F_{Q_1} = F_{Q_2} = 0$ and $F_{Q_1} = F_{Q_2} \neq 0$. Barring extra enhancements or suppressions for certain choices of U(1)$'$ charges, we parametrise the leading contributions as

$$\text{(i)}:\ \beta_{\pi'}(F_{Q_{1,2}} \neq 0) = \frac{d_{\pi'}}{(c_K - c_\pi)}\cdot\frac{F_{D_1} - F_{U_1}}{F_{Q_1}} + \mathcal{O}\left(d_i^2, d_i d_j\right) \approx 0.03\cdot\frac{F_{D_1} - F_{U_1}}{F_{Q_1}}\,, \tag{7.49}$$

$$\text{(ii)}:\ \beta_{\pi'}(F_{Q_{1,2}} = 0) = \frac{d_{\pi'}}{d_K}\cdot\frac{F_{D_1} - F_{U_1}}{F_{D_2}} + \mathcal{O}\left(d_i^2, d_i d_j\right) \approx -1.55\cdot\frac{F_{D_1} - F_{U_1}}{F_{D_2}}\,, \tag{7.50}$$

with $i = K, \pi, \pi'$. We observe that a suppression factor $d_{\pi'}/\left(c_K - c_\pi\right)$ is present in models with

$F_{Q_1} = F_{Q_2} \neq 0$. This is due to the chiral enhancement of the $(V-A)\times(V+A)$ operators, and yields $\beta_{\pi'} \sim \mathcal{O}\left(10^{-2}\text{-}10^{-1}\right)$. In contrast, the charge assignment $F_{Q_1} = F_{Q_2} = 0$, realised in models 9 and 10($\mu$), enables sizeable isospin breaking effects $\sim \mathcal{O}(1)$ as the leading contributions scale with $d_{\pi'}/d_K$.

### 7.3.3 *CP* asymmetry for $D^0 \to \pi^0\pi^0$

In our $Z'$ models, the $CP$ asymmetry for the $D^0 \to \pi^0\pi^0$ decay is given by

$$A_{CP}^{\text{NP}}\left(\pi^0\pi^0\right) \sim \beta_{\pi^0} \cdot \Delta A_{CP}^{\text{NP}}\,, \tag{7.51}$$

where

$$\beta_{\pi^0} = \frac{d_{\pi^0}\,\left(F_{D_1} - F_{U_1}\right)}{c_K\,F_{Q_2} + d_K\,F_{D_2} - c_\pi\,F_{Q_1} - d_\pi\,F_{D_1}}\,. \tag{7.52}$$

Here, we have simply replaced the subscripts $\pi' \to \pi^0$ in Eqs. (7.45) and (7.46) to obtain Eq. (7.51). Numerical values for $\beta_{\pi^0}$ are given in Tab. 7.6. Promising patterns to detect NP employing with this $CP$ asymmetry have been worked out in, *e.g.*, Ref. [182]. Moreover, Tab. 7.7 highlights the pronounced experimental prospect at Belle II for $A_{CP}\left(\pi^0\pi^0\right)$, with a future sensitivity of $\sigma_{\text{BelleII}} = 9\cdot 10^{-4}$, nearly a factor of two better compared to $A_{CP}\left(\pi^+\pi^0\right)$. Values of $A_{CP}^{\text{NP}}\left(\pi^0\pi^0\right) \sim (1-2)\cdot\Delta A_{CP}^{\text{NP}}$ emerge in models 9 and 10($\mu$), which are within the sensitivity of Belle II with $50\,\text{ab}^{-1}$ [85] provided $\Delta A_{CP}^{\text{NP}} \sim 10^{-3}$.

As an additional test of our $Z'$ framework, we define the ratio

$$\frac{A_{CP}^{\text{NP}}\left(\pi^0\pi^0\right)}{A_{CP}^{\text{NP}}\left(\pi^+\pi^0\right)} \sim \frac{\beta_{\pi^0}}{\beta_{\pi'}} = \frac{a_{\pi'}}{a_{\pi^0}} = 1.08 \pm 0.10\,, \tag{7.53}$$

valid for all models with $F_{U_1} \neq F_{D_1}$. However, Eq. (7.53) can be altered by uncertainties coming from possible large, unknown strong phases.

## 7.4 Correlations between semileptonic and hadronic *D*-decays

In the following, we investigate the interplay between NP contributions to hadronic observables, *i.e.* $CP$ asymmetries, with those of rare semileptonic decays in charm. To this end, we take a look at the Wilson coefficients $\mathcal{C}^{(\prime)}_{9/10,\ell}$ dominant in $c\to u\,\ell^+\ell^-$ transitions, defined in Sec. 6.3. As outlined in Sec. 7.1.4, we have $g_L^{cu} = 0$ and therefore only the primed coefficients in Eq. (6.17) remain,

$$\mathcal{C}'_{9/10,\ell} = -\frac{\pi}{\sqrt{2}\,G_{\text{F}}\,\alpha_e}\,\frac{g_R^{cu}\left(g_R^{\ell\ell} \pm g_L^{\ell\ell}\right)}{M_{Z'}^2}\,. \tag{7.54}$$

Here, $g_R^{\ell\ell} = g_4\,F_{E_i}$ and $g_L^{\ell\ell} = g_4\,F_{L_i}$ as defined in Eq. (5.23), whereas the coupling $g_R^{cu}$ is given by Eq. (7.18).

With Eq. (7.54) and utilising the parametrisation of $\Delta A_{CP}^{\rm NP}$ in Eq. (7.30), we obtain

$$\text{Im}\left(\mathcal{C}'_{9/10,\ell}\right) \sim \frac{\pi}{\sqrt{2}\, G_{\rm F}\, \alpha_e}\, \beta^{\ell\ell}_{9/10} \cdot \Delta A_{CP}^{\rm NP}\,, \tag{7.55}$$

where

$$\beta^{\ell\ell}_{9/10} = \frac{F_{E_i} \pm F_{L_i}}{c_K\, F_{Q_2} + d_K\, F_{D_2} - c_\pi\, F_{Q_1} - d_\pi\, F_{D_1}}\,. \tag{7.56}$$

Numerical values of $\beta^{\ell\ell}_{9/10}$ for $\ell = e,\, \mu$ in units of $\text{TeV}^{-2}$ are given in Tab. 7.8 for $M_{Z'} = 6$ TeV. Assuming a benchmark value $\Delta A_{CP}^{\rm NP} \sim 10^{-3}$ in Eq. (7.55), we find

$$\text{Im}\left(\mathcal{C}'_{9/10,\ell}\right) \sim 0.03\ \text{TeV}^{-2} \cdot \beta^{\ell\ell}_{9/10}\,. \tag{7.57}$$

This implies $\mathcal{C}'_{9/10,\ell} = \mathcal{O}\left(10^{-2}\right)$ for models 2, 4, and 5 that feature $g_L^{cu} = 0$, $g_R^{cu} \neq 0$ and $\beta^{\ell\ell}_{9/10} = \mathcal{O}\left(1\ \text{TeV}^{-2}\right)$, consistent with results derived in Sec. 6.3. However, models with large couplings to leptons in combination with $F_{Q_1} = F_{Q_2} = 0$, such as models 9 and $10(\mu)$, can generate $\mathcal{C}'_{9/10,\ell} \lesssim \mathcal{O}\left(10^{-1}\right)$ where $\beta^{\ell\ell}_{9/10} = \mathcal{O}\left(10\ \text{TeV}^{-2}\right)$. The caveat remains that such models are at the edge of semileptonic exclusion limits, as depicted in Fig. 7.3. They are confronted with updated bounds on the Wilson coefficients in Sec. 7.5.

| Model | $\beta_9^{\mu\mu}$ | $\beta_{10}^{\mu\mu}$ | $\beta_9^{ee}$ | $\beta_{10}^{ee}$ |
|---|---|---|---|---|
| 2 | 0.57 | −0.57 | −0.68 | 0.68 |
| 4 | −1.04 | −0.35 | 1.04 | 0.35 |
| 5 | −0.67 | 0 | 0.67 | 0 |
| 9 | −20.56 | −14.07 | 15.15 | −2.17 |
| 10 | 37.25 | 3.39 | −32.73 | 1.13 |
| $10\mu$ | −4.52 | −4.52 | −32.73 | 1.13 |

**Table 7.8:** Values of $\beta^{\ell\ell}_{9/10}$ in $\text{TeV}^{-2}$, see Eq. (7.56), for $\ell = \mu, e$ and evaluated at $M_{Z'} = 6$ TeV. *Table taken from Ref.* [17].

Signals of NP in $CP$ asymmetries of semileptonic $D$-decays are indicated by $\text{Im}(\mathcal{C}'_{9/10,\ell}) \gtrsim \mathcal{O}(10^{-2}\text{-}10^{-1})$ [16, 164, 166]. Hence, all models presented in Tab. 7.3 can generate NP patterns in $c \to u\,\ell^+\ell^-$ decays with $\Delta A_{CP}^{\rm NP} \sim 10^{-3}$.

In Figs. 7.6 and 7.7, we visualise the correlation between NP effects in $\Delta A_{CP}$ and charm Wilson coefficients $\text{Im}(\mathcal{C}'_{9/10,\ell})$. Plots on the left-hand side are for $\ell = e$, while the case $\ell = \mu$ is shown in the right-hand side plots. In Fig. 7.6, the coloured lines represent values for $\text{Im}(\mathcal{C}'_{10,\ell})$ versus $\text{Im}(\mathcal{C}'_{9,\ell})$, while allowing for $|\Delta A_{CP}^{\rm NP}| \leq 2 \cdot 10^{-3}$. The dashed grey line indicates the scenario $\text{Im}(\mathcal{C}'_{9,\ell}) = -\text{Im}(\mathcal{C}'_{10,\ell})$, which is realised by model 2 with vanishing $F_{E_i}$. Models 2, 4, and 5 (yellow, brown, and blue lines) score smaller values $\text{Im}(\mathcal{C}'_{9/10,\ell}) \lesssim \mathcal{O}\left(10^{-2}\right)$ compared to models 9, 10, and $10(\mu)$ (purple, cyan, and pink lines). Model 5 features vector-like $\text{U}(1)'$ charges to electrons and muons, *i.e.* $F_{L_i} = F_{E_i}$. In this case, we find $\text{Im}(\mathcal{C}'_{10,e}) = \text{Im}(\mathcal{C}'_{10,\mu}) = 0$. The charge assignment $F_{L_2} = 0$ in model $10\mu$ entails $\text{Im}(\mathcal{C}'_{9,\mu}) = \text{Im}(\mathcal{C}'_{10,\mu})$, and able to generate both sizeable vector and axial-vector contributions. Conversely, model 10 features $F_{L_i} \approx -F_{E_i}$ for both muon and electron couplings. Hence, the axial-vector contributions are suppressed compared to purely vector ones, that is $|\mathcal{C}'_{10,\ell}| \ll |\mathcal{C}'_{9,\ell}|$ and close to zero.

The induced absolute value $\left|\mathrm{Im}(\mathcal{C}'_{9/10,\ell})\right|$ as a function of $\Delta A_{CP}^{\mathrm{NP}}$ is shown in Fig. 7.7. Using the same colour scheme as in Fig. 7.6, we present the contributions for vector (axial-vector) Wilson coefficients as solid (dashed) lines, proportional to $\beta^{\ell\ell}_{9(10)}$. To avoid clutter, we do not show model 5 in Fig. 7.7 since very similar values of $\beta_9^{\ell\ell}$ as in model 2 are generated. We also display dedicated benchmark points taken from Tab. 7.4 for the different $Z'$ models. The dashed grey regions highlight the upper limits on the corresponding Wilson coefficients obtained from high-$p_{\mathrm{T}}$ data and experimental bounds on branching ratios [154, 183] barring cancellations,

$$|\mathcal{C}^{(\prime)}_{9/10,\mu}| \lesssim 1\,, \quad |\mathcal{C}^{(\prime)}_{9/10,e}| \lesssim 3\,. \tag{7.58}$$

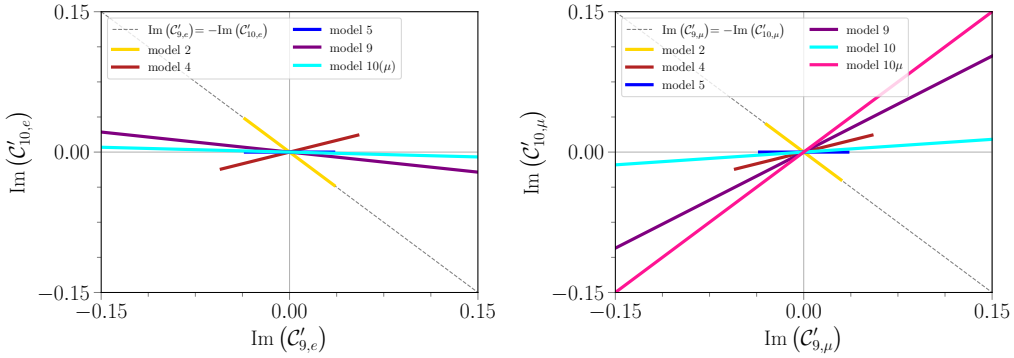


**Figure 7.6:** Induced contributions $\mathrm{Im}(\mathcal{C}'_{10,\ell})$ versus $\mathrm{Im}(\mathcal{C}'_{9,\ell})$ for different $Z'$ models, where $\ell = e$ and $\ell = \mu$ is shown in the left-hand and right-hand side plot, respectively. The dashed grey line corresponds to $\mathrm{Im}(\mathcal{C}'_{9,\ell}) = -\mathrm{Im}(\mathcal{C}'_{10,\ell})$. *Figures adapted from Ref.* [17].

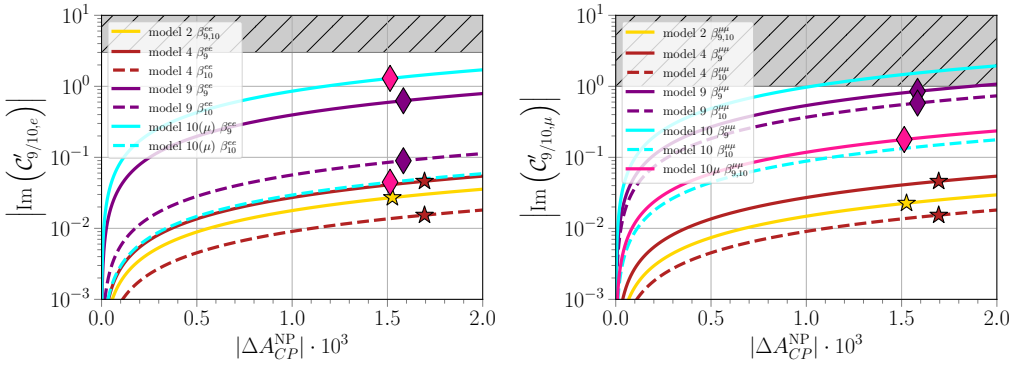


**Figure 7.7:** $\left|\mathrm{Im}(\mathcal{C}'_{9/10,\ell})\right|$ as a function of $\Delta A_{CP}^{\mathrm{NP}}$ for different $Z'$ models, where $\ell = e$ and $\ell = \mu$ is shown in the left-hand and right-hand side plot, respectively. Solid (dashed) lines correspond to contributions to vector (axial-vector) lepton couplings $\mathcal{C}'_{9(10),\ell}$. The coloured markers indicate the benchmark points of model 2 (golden star), model 4 (brown star), model 9 (purple diamond), and 10$\mu$ (pink diamond) listed in Tab. 7.4. The dashed grey region depicts exclusion limits, see Eq. (7.58). *Figures adapted from Ref.* [17].

## 7.5 Discussing updated limits of flavour observables

Since the publication of our work [16], the HFLAV collaboration has provided a recent update on their global fit of $D$-mixing observables [124], which incorporates 2021 experimental data of LHCb [184]. The update is given in Eq. (B.6). Relevant for our analysis are the updated values

$$x_{12} \in [0.314\,,\,0.503]\ \%\,, \quad \phi_{12} \in [-1.2°,\,2.42°]\ . \tag{7.59}$$

The upper limit on $g_R^{cu}$, previously given by Eq. (7.27), thus reduces to

$$|g_R^{cu}| \lesssim 7.1 \cdot 10^{-4} \left(\frac{M_{Z'}}{\text{TeV}}\right)\ . \tag{7.60}$$

The updated value of $\phi_{12}$ in Eq. (7.59) allows for slightly larger phases. However, since we employ $\phi_R = 2\,\phi_{12} \sim \pi/2$ to avoid constraints from $x_{12}\,\sin(\phi_{12})$ in our analysis, we merely have to debate the tightened bound on $g_R^{cu}$ in Eq. (7.60).

In the studies presented in Secs. 7.2 to 7.4, we have employed the less restrictive limit on the $Z'$ couplings in Eq. (6.19) coming from upper limits on $D^+ \to \pi^+\mu^+\mu^-$. The improved bound (by roughly a factor of two) also affects some $Z'$ benchmarks, especially models with large couplings to muons, *i.e.* models 9 and 10. The construction of model 10$\mu$ featuring small U(1)$'$ muon charges evades this bound. For the full list of $Z'$ models and dedicated benchmarks, see Tabs. 7.3 and 7.4, respectively.

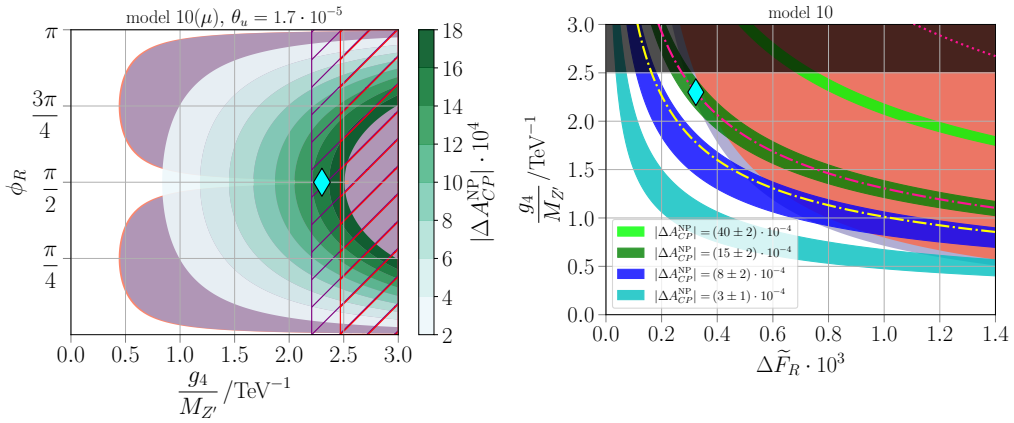


**Figure 7.8:** Updated version of selected plots of Figs. 7.2 and 7.3 for model 10. In the left-hand side plot, we add the exclusion regions from updated the $D^0$-$\overline{D}^0$ mixing constraints, that is $x_{12}\,\sin(\phi_{12})$ (purple region) and the absolute value $x_{12}$ (purple hatched rectangle). In the right-hand side plot, we additionally show the improved exclusion region from updated $D^0$-$\overline{D}^0$ mixing constraints (purple region) and the improved bound from $D^+ \to \pi^+\mu^+\mu^-$ in Eq. (6.19) (yellow dash-dotted line). The cyan diamond marker refers to the benchmark point chosen in Tab. 7.4. For discussions see the main text.

In Fig. 7.8, we give an updated version of the Figs. 7.2 and 7.3 for model 10, where the NP contributions to $\Delta A_{CP}$ in the $\phi_R$-$g_4/M_{Z'}$ and $g_4$-$\Delta\widetilde{F}_R$ plane are displayed, respectively. In the left-hand side plot, the overdrawn exclusion regions denote the updated $D^0$-$\overline{D}^0$ mixing constraints. The purple region is excluded from $x_{12}\,\sin(\phi_{12})$, whereas the purple hatched rectangle indicates absolute values $x_{12}$ that exceed the experimental limit. We observe that the allowed parameter

space is shifted and forbids values of $|\Delta A_{CP}^{\text{NP}}| \gtrsim 14 \cdot 10^{-4}$. Therefore, the benchmark point selected for model 10 (cyan diamond) is excluded. The same conclusions are drawn in the right-hand side plot of Fig. 7.8, where the improved bound from $D^+ \to \pi^+\mu^+\mu^-$ is depicted as a yellow dash-dotted line. However, we still find viable parameter space for smaller values of $\Delta A_{CP}^{\text{NP}} \sim \text{few} \cdot 10^{-4}$. Similar implications can be obtained for model 9 and its benchmark, which also features large $Z'$ couplings to muons. Conversely, the impact on the remaining models discussed in this chapter (models 2, 4, and 5) is significantly smaller and benchmark points remain viable due to small couplings and ratio $g_4/M_{Z'}$, see corresponding plots in Figs. 7.2 and 7.3.

While certain benchmark points might be at the edge of being excluded (or excluded by future data), they still provide insight into connections of $CP$-violating observables. We point out that a possible interference between SM and NP contributions, which has been neglected in this study, can enhance $CP$-violating effects. Then, even smaller NP contributions may become relevant in the light of future measurements of $\Delta A_{CP}$ and theory developments.

## 7.6 Summary and conclusion

The flavourful, anomaly-free $Z'$ scenarios presented in Tab. 7.3 are viable candidates to induce both $\Delta A_{CP}^{\text{NP}} \sim 10^{-3}$ in hadronic charm decays as well as measurable $CP$ asymmetries in semileptonic $c \to u\,\ell^+\ell^-$ modes above the SM. The underlying correlation between the two sectors has been worked out in Sec. 7.4. Therein, we studied $Z'$ models with couplings only to RH quark currents featuring a weak phase $\phi_R = \pi/2$. While the scenarios put forward in Chap. 6 evade $D^0$-$\overline{D}^0$ mixing constraints completely, they necessitate SM-like phases. Conversely, for models with only $g_R^{cu} \neq 0$ these mixing bounds provide tight constraints on our models. However, a NP interpretation of $\Delta A_{CP}$ can be achieved that suffices bounds from mixing and semi(muonic) experimental limits, see Fig. 7.2. Relaxing our assumptions on the negligible SM contributions to $\Delta A_{CP}$, the implications derived in this study can be used as upper limits on the $Z'$ model parameters.

Supplementary cross-checks are given by $CP$ asymmetries in $D^0 \to \pi^+\pi^-$ and $D^0 \to K^+K^-$ decays, where $U$-spin breaking beyond the SM can be probed. We refer to Figs. 7.4 and 7.5 for benchmarks employing present data and future sensitivities from colliders, respectively. Furthermore, related $CP$ asymmetries in $D^+ \to \pi^+\pi^0$ and $D^0 \to \pi^0\pi^0$ decays can even exceed $\Delta A_{CP}^{\text{NP}}$ contributions, making observations of isospin-violating NP accessible. Projected sensitivities at Belle II are provided in Tab. 7.7.

As put forward in Sec. 6.4, the non-universality of lepton couplings in our $Z'$ framework can be probed in LU ratios, such as $R_\pi^D$ and $R_{K^*}^{D_s}$. For instance, model 9 can achieve $R_\pi^D \gg 1$ due to large muon couplings, while simultaneously inducing $A_{CP}^{\text{NP}}\left(\pi^+\pi^0\right) \sim A_{CP}^{\text{NP}}\left(\pi^0\pi^0\right) \lesssim 2\,\Delta A_{CP}^{\text{NP}}$. Conversely, model $10\mu$ generates $R_\pi^D < 1$ with sizeable NP $U$-spin breaking $A_{CP}^{\text{NP}}\left(\pi^+\pi^-\right) \ll A_{CP}^{\text{NP}}\left(K^+K^-\right) \sim \Delta A_{CP}^{\text{NP}}$ [17]. We stress the importance of working out and testing correlations between $CP$ asymmetries to pin down the specific NP model. Hence, future $CP$ studies of both rare semileptonic and hadronic charm decays with improved data and sensitivities will help disentangle the different NP patterns, with LHCb and Belle II as the main players.

Regarding future work of $Z'$ models in this sector, the issue of Landau poles emerging in the RG running needs to be addressed. Due to sizeable U(1)$'$ charges and coupling strength at the charm scale, diverging couplings arise way below the Planck scale. One possibility to tame this UV behaviour is devised by the Planck safety approach. It ensures the predictivity and stability of the theory until the Planck scale, see Sec. 5.5.

Chapter

8

# Planck-safe U(1)′ explanations for the $B$-anomalies

As previously discussed in Sec. 3.4, the keen interest for the $B$-anomalies hinting at NP effects in $b\to s\,\ell^+\ell^-$ transitions persists and motivates BSM model building in this sector. A plethora of NP scenarios has been put forward to account for the deviations in these observables. Here, $Z'$ models are prime candidates due to possible non-universal couplings to quarks and leptons at tree level. While U(1)′ extensions are able to address the neutral-current $b\to s\,\ell^+\ell^-$ anomalies, they fall short of explaining the anomalies in the charged-current $b\to c\,\ell\nu$ decays.

In this chapter, we present a study of anomaly-free $Z'$ models, based on the findings published in Ref. [21]. These models can account for the $B$-anomalies while providing a stable and predictive theory up to Planckian energies. We outline the necessary BSM particle content and discuss viable models in Secs. 8.1 and 8.2. Section 8.3 encompasses an analysis of viable RG trajectories for a selected benchmark model, while phenomenological implications are provided in Sec. 8.4. We summarise in Sec. 8.5.

## 8.1 The $Z'$ model set-up

In our investigation we consider $Z'$ models that generate sizeable contributions to the Wilson coefficients of the weak Hamiltonian in Eq. (3.41). They are induced at tree level with couplings to $b$, $s$ quarks and leptons as shown in Fig. 8.1.

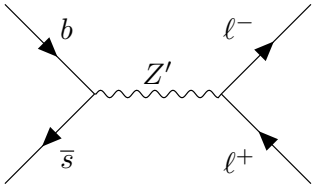


**Figure 8.1:** Tree-level diagram of a $b\to s\,\ell^+\ell^-$ transition via a $Z'$ boson.

The relevant $Z'$ couplings are given by

$$\mathcal{L}_{Z'}^{bs\ell\ell} \supset \left(g_L^{bs}\,\bar{s}_L\gamma^\mu b_L Z'_\mu + g_R^{bs}\,\bar{s}_R\gamma^\mu b_R Z'_\mu + \text{h.c.}\right) + g_L^{\ell\ell}\,\bar{\ell}_L\gamma^\mu\ell_L Z'_\mu + g_R^{\ell\ell}\,\bar{\ell}_R\gamma^\mu\ell_R Z'_\mu\,, \tag{8.1}$$

where $\ell = e,\mu,\tau$ is understood. By integrating out the $Z'$ boson in Eq. (8.1) we obtain the effective

Hamiltonian [128]

$$\mathcal{H}_{\text{eff}}^{Z'} \supset \frac{1}{2\,M_{Z'}^2}\Big[\quad g_L^{bs}(\bar{s}_L\gamma^\mu b_L) + g_L^{bs*}(\bar{b}_L\gamma^\mu s_L) + g_R^{bs}(\bar{s}_R\gamma^\mu b_R) + g_R^{bs*}(\bar{b}_R\gamma^\mu s_R) \\ + g_L^{\ell\ell}(\bar{\ell}_L\gamma^\mu \ell_L) \; + g_R^{\ell\ell}(\bar{\ell}_R\gamma^\mu \ell_R)\Big]^2, \tag{8.2}$$

which evokes contributions to the Wilson coefficients $\mathcal{C}_{9/10,\ell}^{(\prime)}$. As previously reviewed in Sec. 5.3.2, the couplings $g_{L,R}^{bs}$ entail additional $B_s$-mixing contributions, which are constrained by experimental data. The NP Wilson coefficients relevant for $b\to s\,\ell^+\ell^-$ transitions can be extracted by comparing the effective Hamiltonians in Eqs. (3.41) and (8.2). We find

$$\mathcal{C}_{9/10,\ell}^{(\prime)} = -\frac{\pi}{\sqrt{2}\,G_{\text{F}}\,\alpha_e\,V_{tb}V_{ts}^*}\,\frac{g_{L(R)}^{bs}\,\left(g_R^{\ell\ell} \pm g_L^{\ell\ell}\right)}{M_{Z'}^2}\,, \tag{8.3}$$

where $g_{L(R)}^{\ell\ell}$ refer to the flavour-diagonal $Z'$ couplings to leptons given by Eq. (5.23). The non-diagonal coupling of $b$- and $s$-quark doublets has been worked out in Sec. 5.1.3, and is given in Eq. (5.19). It reads

$$g_L^{bs} = (F_{Q_3} - F_{Q_2})\;V_{ts}^*V_{tb}\,g_4\,, \tag{8.4}$$

with $V_{tb}V_{ts}^* \approx -0.04$. The global fit of $b\to s$ Wilson coefficients discussed in Sec. 4.2 indicates that the $B$-anomalies can be explained with NP in left-handed FCNC quark couplings only. Therefore, we set

$$g_R^{bs} = 0\,. \tag{8.5}$$

This setting can be realised by choosing $\theta_d = 0$ in Eq. (5.9), which entails a trivial rotation matrix between flavour and mass eigenstates in the down-sector.

### 8.1.1 Beyond the standard model particle content and interactions

In what follows, we review the particle content in our $Z'$ model set-up. In analogy to our previous studies in Chaps. 6 and 7, we introduce generation-dependent U(1)′ charges $F_f$ for the SM quarks ($f = Q, U, D$) and leptons ($f = L, E$), as well as for three RH neutrino fields ($f = \nu_R$). Moreover, in this analysis we explicitly involve the SM Higgs $H$ and a $N_f \times N_f$ BSM scalar $S$, with corresponding U(1)′ charges $F_H$ and $F_S$, respectively. The scalar $S$ is assumed to be a SM singlet with trivial representations under the SM gauge group. The fermion sector is supplemented by $N_f$ BSM fermions $\psi_{L,R}$ carrying universal U(1)′ charges.

In order to generate the heavy mass ($\sim$ TeV) of the $Z'$ boson, we introduce a BSM scalar $\phi$ as a SM singlet with $F_\phi \neq 0$, which is responsible for the SSB of the U(1)′ symmetry. In Tab. 8.1, the relevant matter fields and their representations under the extended gauge group $\text{U}(1)_Y \times \text{SU}(2)_L \times \text{SU}(3)_C \times \text{U}(1)'$ are collected. Moreover, we make the following simplifying assumptions. To avert additional gauge anomalies emerging from BSM fermions, see Sec. 5.2, we consider only vector-like fermions that are complete SM singlets. In addition, those fermions come

in three generations while $S$ has vanishing $\mathrm{U}(1)'$ charge. In summary, these conditions read

$$N_f = 3\,, \quad F_\psi = F_{\psi_L} = F_{\psi_R}\,, \quad F_S = 0\,, \quad Y_\psi = 0\,, \quad r_2 = 1\,, \quad r_3 = 1\,. \tag{8.6}$$

| | Field | Gen. | $\mathrm{U}(1)_Y$ | $\mathrm{SU}(2)_L$ | $\mathrm{SU}(3)_C$ | $\mathrm{U}(1)'$ |
|---|---|---|---|---|---|---|
| SM fermions | $Q$ | 3 | $+\frac{1}{6}$ | 2 | 3 | $F_{Q_i}$ |
| | $L$ | 3 | $-\frac{1}{2}$ | 2 | 1 | $F_{L_i}$ |
| | $U$ | 3 | $+\frac{2}{3}$ | 1 | 3 | $F_{U_i}$ |
| | $D$ | 3 | $-\frac{1}{3}$ | 1 | 3 | $F_{D_i}$ |
| | $E$ | 3 | $-1$ | 1 | 1 | $F_{E_i}$ |
| Higgs scalar | $H$ | 1 | $+\frac{1}{2}$ | 2 | 1 | $F_H$ |
| BSM fermions | $\nu_R$ | 3 | 0 | 1 | 1 | $F_{\nu_i}$ |
| | $\psi_L$ | $N_f$ | $Y_\psi$ | $r_2$ | $r_3$ | $F_{\psi_L}$ |
| | $\psi_R$ | $N_f$ | $Y_\psi$ | $r_2$ | $r_3$ | $F_{\psi_R}$ |
| BSM scalars | $S$ | $N_f \times N_f$ | 0 | 1 | 1 | $F_S$ |
| | $\phi$ | 1 | 0 | 1 | 1 | $F_\phi$ |

**Table 8.1:** SM and BSM fields with multiplicities (number of generations $i$) and representations under $\mathrm{U}(1)_Y \times \mathrm{SU}(2)_L \times \mathrm{SU}(3)_C \times \mathrm{U}(1)'$. In our analysis, we further impose Eqs. (8.6), (8.19), and (8.20), as well as Eqs. (8.12) and (8.22), see main text. *Table taken from Ref.* [21].

### 8.1.2 The Yukawa sector

The SM Yukawa interaction in Eq. (2.19) is extended by a pure BSM Yukawa vertex as well as by the coupling of RH neutrinos to the Higgs, $Y^\nu$. Thus, the Yukawa sector becomes

$$\mathcal{L}_{\text{Yuk}} = Y_u^{ij}\,\overline{Q}_i\,\tilde{H}\,U_j + Y_d^{ij}\,\overline{Q}_i\,H\,D_j + Y_e^{ij}\,\overline{L}_i\,H\,E_j + Y_\nu^{ij}\,\overline{L}_i\,\tilde{H}\,\nu_{R,j} + y\,\bar{\psi}_{L,i}\,S_{ij}\,\psi_{R,j} + \text{h.c.}\,. \tag{8.7}$$

In particular, the BSM Yukawa is described by a single universal coupling $y$, which is protected by a $\mathrm{U}(3)_{\psi_L} \times \mathrm{U}(3)_{\psi_R}$ flavour symmetry. We choose the $F_{\psi_{L,R}}$ charges to be universal, which ensures that this symmetry is only softly broken.

This symmetry further prohibits additional Yukawa interactions between SM or RH neutrino fields and the BSM sector of $\psi_{L,R}$ and $S$. While Majorana-like Yukawa couplings of neutrinos are allowed for some models, we do not consider such scenarios here [21].

### 8.1.3 The scalar potential

With the BSM scalars $S$ and $\phi$, we can extend the scalar potential in Eq. (2.11). We write the occurring mass and cubic terms as

$$V^{(2)} + V^{(3)} = m_H^2\,\left(H^\dagger H\right) + m_S^2\,\mathrm{tr}\left(S^\dagger S\right) + m_\phi^2\,\left(\phi^\dagger \phi\right) + \mu_{\text{det}}\left[\det\left(S\right) + \det\left(S^\dagger\right)\right]\,, \tag{8.8}$$

where the last term involves determinants in flavour space and the trilinear coupling $\mu_{\rm det}$. The quartic interactions read

$$\begin{aligned} V^{(4)} = \lambda\,(H^\dagger H)^2 + s\,(\phi^\dagger\phi)^2 + u\,\mathrm{tr}\left(S^\dagger S S^\dagger S\right) + v\,\mathrm{tr}\left(S^\dagger S\right)\mathrm{tr}\left(S^\dagger S\right) \\ + \delta\,(H^\dagger H)\,\mathrm{tr}\left(S^\dagger S\right) + \tilde{\delta}\,(H^\dagger H)(\phi^\dagger\phi) + w\,(\phi^\dagger\phi)\,\mathrm{tr}\left(S^\dagger S\right)\,, \end{aligned} \tag{8.9}$$

featuring the Higgs ($\lambda$) and BSM ($u, v, s$) self-interactions as well as portal couplings ($\delta, \tilde{\delta}, w$). In the BSM sector, two types of vacuum configurations are realised; a flavour-symmetric one ($V^+$) with quartic $u > 0$, and a symmetry-broken one ($V^-$) with $u < 0$ [139, 140]. In the former setting, the BSM scalar vev is flavour-diagonal, while $V^-$ possesses a vev only in one diagonal component of $S$. At large, it can be shown that the classical potential in Eq. (8.9) is bounded from below whenever the conditions [185–187]

$$\begin{aligned} &\lambda > 0\,, \quad \Delta > 0\,, \quad s > 0\,, \quad \delta' = \delta + 2\sqrt{\lambda\Delta} > 0\,, \quad \tilde{\delta}' = \tilde{\delta} + 2\sqrt{\lambda s} > 0\,, \\ &w' = w + 2\sqrt{s\Delta} > 0\,, \quad 2\sqrt{\lambda\Delta s} + \delta\sqrt{s} + \tilde{\delta}\sqrt{\Delta} + w\sqrt{\lambda} + \sqrt{\delta'\,\tilde{\delta}'\,w'} > 0\,, \end{aligned} \tag{8.10}$$

are satisfied. The parameter

$$\Delta = \begin{cases} \frac{u}{3} + v > 0 & \text{for } u > 0 \quad (V^+) \\ u + v > 0 & \text{for } u < 0 \quad (V^-) \end{cases} \tag{8.11}$$

depends on the ground state for the BSM scalars. These *stability conditions* ensure a stable scalar potential, and is one of the key elements of the Planck safety strategy, which guides the analysis presented here. We refer to Sec. 5.5 for a brief discussion on Planck safety.

### 8.1.4 Gauge-kinetic mixing and scalar symmetry breaking

To ensure that the scales and mechanisms of the electroweak symmetry and the U(1)′ breaking are independent, we fix

$$F_H = 0\,. \tag{8.12}$$

This assumption also avoids additional kinetic mixing contributions which would affect the $\rho$ parameter as outlined in Sec. 5.4. Nonetheless, kinetic mixing between the two abelian sectors is induced in our models via the parameter $\eta \neq 0$, see Eq. (5.53). In our analysis, we avert large mixing contributions by imposing the constraint on $\eta$ put forward in Eq. (5.56), $|\eta| \lesssim \mathcal{O}\left(10^{-2}\right)$. This ensures kinetic mixing to be subleading at the electroweak scale. Moreover, corrections to the photon and $Z$ couplings $g_f^{\gamma,Z} \propto \eta\, F_f\, g_4$ of SM fermions $f$ can be evaded for small values of $g_4$ or $\eta$ at the electroweak scale [21]. In what follows, we outline the SSB of the U(1)′ symmetry and its implications on BSM parameters. After EWSB, *cf.* Eq. (2.13), we find

$$H = \frac{1}{\sqrt{2}} \begin{pmatrix} 0 \\ v_h + h \end{pmatrix}\,, \quad \phi = \frac{1}{\sqrt{2}}(v_\phi + \varphi)\,, \tag{8.13}$$

where the real modes $h$, $\varphi$ are rotated into mass eigenstates via

$$\begin{pmatrix} h' \\ \varphi' \end{pmatrix} = \begin{pmatrix} \cos(\beta) & -\sin(\beta) \\ \sin(\beta) & \cos(\beta) \end{pmatrix} \begin{pmatrix} h \\ \varphi \end{pmatrix} , \tag{8.14}$$

and the scalar portal couplings induce the mixing angle

$$\tan(2\beta) = \frac{\tilde{\delta}\, v_h\, v_\phi}{s\, v_\phi^2 - \lambda\, v_h^2} \approx \frac{\tilde{\delta}}{s}\, \frac{v_h}{v_\phi} . \tag{8.15}$$

By acquiring a vev $\langle \phi \rangle = v_\phi/\sqrt{2} \neq 0$, we generate a $Z'$ mass

$$M_{Z'} = |F_\phi|\, g_4\, v_\phi , \tag{8.16}$$

where no contribution from the SM Higgs appears stipulated by Eq. (8.12). Due to the new decay channels of $\phi'$ into SM fermions and gauge bosons introduced by the scalar mixing, the decay width of the $h'$ to SM final states is reduced in consequence. The mixing angle is constrained by combined Higgs signal strength measurements [32], which imply

$$\sin^2(\beta) \leq 0.01 . \tag{8.17}$$

Employing Eqs. (8.15) to (8.17), we estimate

$$|F_\phi|\, g_4\, \frac{\tilde{\delta}}{s} < \begin{cases} 4.1 & \text{for } M_{Z'} = 5 \text{ TeV} \\ 2.4 & \text{for } M_{Z'} = 3 \text{ TeV} \end{cases} . \tag{8.18}$$

While a non-vanishing vev of the scalar $S$ may also be realised [140], the resulting mixing into mass eigenstates becomes more elaborate but can be adjusted by the size of the scalar portal couplings, $|\delta|$, $|\tilde{\delta}|$, and $|w|$.

### 8.1.5 Phenomenological constraints on $Z'$ model parameters

To conclude this section, we summarise additional constraints on the $Z'$ model parameters. In accordance with phenomenological reasoning, we further impose the following charge assignments. First, we avoid severe constraints from $K^0$-$\overline{K}^0$ oscillations [32] by fixing

$$F_{Q_1} = F_{Q_2} , \quad F_{D_1} = F_{D_2} . \tag{8.19}$$

This prohibits kaon FCNCs due to universal $s$ and $d$ quarks couplings, see discussion in Sec. 5.3. Moreover, we forbid couplings of the $Z'$ boson to electrons,

$$F_{L_1} = F_{E_1} = 0 . \tag{8.20}$$

This setting is considered due to the following reasons. By choosing vanishing U(1)$'$ charges to electrons, we can induce the required $\mu$-$e$ non-universality by construction, provided that appropriate $Z'$ couplings to muons are present. In addition, a $Z'$ boson coupled to electrons with sizeable $g_4 \gtrsim \mathcal{O}(1)$ could affect electroweak observables at tree level measured at LEP [10, 188]. While such bounds are of course model-dependent, we evade possible constraints by neglecting U(1)$'$ charges to electrons.

### Gauge invariance conditions in the Yukawa sector

The BSM Yukawa coupling $y$ in Eq. (8.7) is assured to be gauge invariant due to the charge assignments proposed in Eq. (8.6). Conversely, this is not given by default for the SM Yukawa couplings but would necessitate the following conditions, $i, j = 1, 2, 3$,

$$\begin{aligned} Y_u^{ij}: &\quad F_{Q_i} + F_H - F_{U_j} = 0\,, \\ Y_d^{ij}: &\quad F_{Q_i} - F_H - F_{D_j} = 0\,, \\ Y_e^{ij}: &\quad F_{L_i} + F_H - F_{E_j} = 0\,, \\ Y_\nu^{ij}: &\quad F_{L_i} - F_H - F_{\nu_j} = 0\,. \end{aligned} \tag{8.21}$$

In our analysis, however, we relax some of those constraints. We know that the necessary tree-level FCNC via the $Z'$-$b$-$s$ quark vertex requires non-universal charges, *i.e.* $F_{Q_3} \neq F_{Q_2}$ in Eq. (8.4). Yet, this charge assignment cannot be realised if all conditions in Eq. (8.21) have to be met. Instead, solving Eq. (8.21) for non-diagonal entries in $Y_u^{ij}$ and $Y_d^{ij}$ yields universal charge assignments $F_{Q_1} = F_{Q_2} = F_{Q_3}$, while similar implications manifest themselves in the lepton sector.

As we are guided in our approach to explain the $B$-anomalies and ensure a stable RG flow that includes the dominant (top and bottom) Yukawa couplings, we only impose the gauge invariance conditions for the diagonal quark Yukawa elements in Eq. (8.21). Hence, we fix

$$\begin{aligned} Y_u^{ii}: &\quad F_{Q_i} + F_H - F_{U_i} = 0\,, \\ Y_d^{ii}: &\quad F_{Q_i} - F_H - F_{D_i} = 0\,, \end{aligned} \tag{8.22}$$

allowing for the corresponding mass terms. In doing so, we drop the related conditions for the lepton sector, neglecting charged lepton and neutrino masses. For the same reasons, only the top coupling $Y_u^{33}$ is essential for the RG evolution, whereas other Yukawa couplings remain naturally orders of magnitude smaller under the RG running.

### Constraints on $g_L^{bs}$ from $B_s$-mixing

A $Z'$ coupling $g_L^{bs} \neq 0$ invariably generates a tree-level contribution to $\Delta M_s$, *i.e.* to $B_s$-mixing, see Sec. 5.3.2. As we confine ourselves to $g_R^{bs} = 0$, we use the bound in Eq. (5.49),

$$\frac{\left|g_L^{bs}\right|^2}{M_{Z'}^2} \lesssim 1.24 \cdot 10^{-5}\ \text{TeV}^{-2} \equiv I_{\max}\,. \tag{8.23}$$

While this limit is quite strong, it can be met by $Z'$ benchmark scenarios that are introduced in Sec. 8.2. To quantify the $B_s$-mixing contribution, we define the ratio of induced over maximally allowed mixing as

$$r_{B_s} = \frac{\left|g_L^{bs}\right|^2}{M_{Z'}^2} \cdot \frac{1}{I_{\max}}\,, \tag{8.24}$$

where $r_{B_s} \leq 1$ is understood. In Sec. 5.3.2, we have put forward a certain hierarchy of couplings, that is $g_L^{bs} = g_R^{bs}\, X_s$, with $X_s \approx 10$. In these scenarios, small RH currents $g_R^{bs} \neq 0$ are present, which allows to evade $B_s$-mixing constraints completely. We discuss this possibility in Sec. 8.4.3.

## 8.2 Benchmark models explaining the $B$-anomalies

In this section, we present viable scenarios that induce NP effects accounting for the $B$-anomalies. We employ selected fit results on the Wilson coefficients $\mathcal{C}_{9,\mu}$ and $\mathcal{C}_{10,\mu}$, which have been presented in Sec. 4.2. We determine three benchmark models (BMs) that predict NP near the matching scale $\mu_0 \simeq 5$ TeV. Furthermore, a fourth scenario with a lower matching scale $\mu_0 \simeq 3$ TeV is identified as well. The explicit U(1)′ charge assignments are compiled in Tab. 8.2.

| model | $F_{Q_i}$ | | | $F_{U_i}$ | | | $F_{D_i}$ | | | $F_{L_i}$ | | | $F_{E_i}$ | | | $F_{\nu_i}$ | | | $F_H$ | $F_\psi$ | $F_\phi$ |
|---|---|---|---|---|---|---|---|---|---|---|---|---|---|---|---|---|---|---|---|---|---|
| BM$_1$ | $\frac{1}{20}$ | $\frac{1}{20}$ | $-\frac{1}{10}$ | $\frac{1}{20}$ | $\frac{1}{20}$ | $-\frac{1}{10}$ | $\frac{1}{20}$ | $\frac{1}{20}$ | $-\frac{1}{10}$ | 0 | $-\frac{9}{10}$ | $\frac{9}{10}$ | 0 | $-\frac{9}{10}$ | $\frac{9}{10}$ | 0 | 0 | 0 | 0 | 1 | $\frac{1}{5}$ |
| BM$_2$ | $-\frac{1}{4}$ | $-\frac{1}{4}$ | $\frac{1}{6}$ | $-\frac{1}{4}$ | $-\frac{1}{4}$ | $\frac{1}{6}$ | $-\frac{1}{4}$ | $-\frac{1}{4}$ | $\frac{1}{6}$ | 0 | 1 | 0 | 0 | 0 | 1 | $\frac{1}{12}$ | $-\frac{1}{12}$ | 1 | 0 | $\frac{11}{12}$ | $\frac{1}{9}$ |
| BM$_3$ | $-\frac{1}{8}$ | $-\frac{1}{8}$ | 0 | $-\frac{1}{8}$ | $-\frac{1}{8}$ | 0 | $-\frac{1}{8}$ | $-\frac{1}{8}$ | 0 | 0 | $\frac{1}{2}$ | $\frac{1}{4}$ | 0 | $\frac{1}{4}$ | $\frac{1}{2}$ | 0 | $\frac{1}{4}$ | $\frac{1}{2}$ | 0 | 1 | $\frac{1}{8}$ |
| BM$_4$ | 0 | 0 | $\frac{1}{9}$ | 0 | 0 | $\frac{1}{9}$ | 0 | 0 | $\frac{1}{9}$ | 0 | $\frac{1}{3}$ | $-\frac{2}{3}$ | 0 | $\frac{1}{3}$ | $-\frac{2}{3}$ | 0 | $\frac{1}{3}$ | $-\frac{2}{3}$ | 0 | 1 | $\frac{1}{6}$ |

**Table 8.2:** U(1)′ charge assignments in the four benchmark models BM$_{1-4}$. Note that the charges are not given as integers, but instead are normalised by scaling the largest value of each solution to one. *Table taken from Ref.* [21].

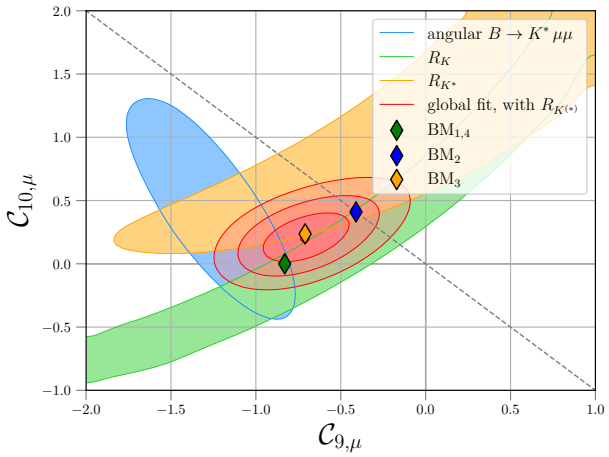


**Figure 8.2:** Likelihood contours as in the left-hand side plot of Fig. 4.2, with additional four benchmarks given in Tabs. 8.2 and 8.4 and displayed as diamond-shaped markers. The dashed line indicates $\mathcal{C}_{9,\mu} = -\mathcal{C}_{10,\mu}$. Note that BM$_1$ and BM$_4$ generate identical values of $\mathcal{C}_{(9,10),\mu}$, see main text for further details. *Figure adapted from Ref.* [21].

To generate the desired NP contributions via the semimuonic Wilson coefficients in Eq. (8.3), we study different patterns that distinguish the four models presented. Motivated by the 1d and 2d fit results in Tab. 4.2, we choose

$$\begin{aligned} &\text{BM}_{1,4}: \quad \mathcal{C}_{9,\mu} \neq 0 \quad \text{and} \quad \mathcal{C}_{10,\mu} = 0\,, \\ &\text{BM}_2: \quad \mathcal{C}_{9,\mu} = -\mathcal{C}_{10,\mu}\,, \\ &\text{BM}_3: \quad -\mathcal{C}_{9,\mu} \gg \mathcal{C}_{10,\mu} > 0\,, \end{aligned} \tag{8.25}$$

where BM$_4$ is constructed as a minimal model with only the necessary U(1)′ charges to third-

generation quarks. The model generates the same Wilson coefficients as $\mathrm{BM}_1$, see Tab. 8.2.

In Fig. 8.2, we display the corresponding Wilson coefficients together with selected likelihood contours in the $\mathcal{C}_{9,\mu}$-$\mathcal{C}_{10,\mu}$ plane. Moreover, these models are compliant with the theoretical and phenomenological constraints brought forward in Sec. 8.1. In particular, we employ the ACCs introduced in Eq. (5.24) to obtain anomaly-free $Z'$ models. The gauge invariance of quark mass terms and constraints from $B_s$-mixing in Eqs. (8.22) and (8.23), respectively, are satisfied as well. The solutions presented also obey Eqs. (8.19) and (8.20) in accordance with kaon mixing and electroweak precision measurements, respectively.

In the following, we discuss the different benchmarks beginning with some general remarks. To generate NP scenarios with $\mathcal{C}_{9,\mu} = -\mathcal{C}_{10,\mu}$ (as in $\mathrm{BM}_2$), we require $g_R^{\mu\mu} = 0$, that is $F_{E_2} = 0$. Conversely, models with $\mathcal{C}_{10,\mu} = 0$ (as in $\mathrm{BM}_{1,4}$) are only possible with vector-like muon charges $F_{L_2} = F_{E_2}$, *cf.* Eq. (8.3). The pattern that emerges for the 1d and 2d fit results in Tab. 4.2 reads

$$-\mathcal{C}_{9,\mu} \geq \mathcal{C}_{10,\mu} \geq 0\,, \tag{8.26}$$

and yields constraints on the relative sign of the quark and lepton charges. Viable $Z'$ models that match the pattern in Eq. (8.26) need to satisfy

$$\begin{aligned} &F_{Q_3} > F_{Q_2} \quad \text{and} \quad F_{L_2} \geq F_{E_2} \geq 0 \\ \text{or} \quad &F_{Q_3} < F_{Q_2} \quad \text{and} \quad F_{L_2} \leq F_{E_2} \leq 0\,, \end{aligned} \tag{8.27}$$

following the input of the known signs of the relevant CKM elements and $g_4^2 > 0$ in Eq. (8.3).

Moreover, the inclusion of RH neutrino charges $F_\nu$ has a profound impact on which scenarios are accessible. In the case of vanishing RH neutrino charges $F_{\nu_i} = 0$, the theoretical and phenomenological constraints necessitate

$$F_H = 0\,, \quad F_{q_3} = -2\,F_{q_1} = -2\,F_{q_2}\,, \quad F_{L_3} = -F_{L_2}\,, \quad F_{E_3} = -F_{E_2} = \mp F_{L_2}\,, \tag{8.28}$$

where $q_i = Q_i,\, U_i,\, D_i$ . The desired pattern of Wilson coefficients in Eqs. (8.26) and (8.27) can only be achieved by setting $F_{L_2} = F_{E_2}$ in Eq. (8.28). While NP scenarios with $\mathcal{C}_{9,\mu} \neq 0$ are allowed, such vector-like muon charges stipulate $\mathcal{C}_{10,\mu} = 0$. Therefore, $\mathcal{C}_{10,\mu} \neq 0$ requires RH neutrinos in our $Z'$ framework that enter the ACCs in Eq. (5.24) and consequently relax the conditions in Eq. (8.28). We observe that non-vanishing charges $F_{\nu_i}$ are mandatory for $\mathrm{BM}_{2,3}$ where $\mathcal{C}_{10,\mu} \neq 0$. In $\mathrm{BM}_4$ the inclusion of RH neutrinos is also required to couple the $Z'$ boson to third-generation quarks only. Conversely, RH neutrinos are not needed in $\mathrm{BM}_1$, which is both compliant with $\mathcal{C}_{10,\mu} = 0$ and Eq. (8.28).

$\mathrm{BM}_1$ exhibits a distinct structure where the same U(1)′ charge for all representations of quarks ($q_i = Q_i,\, U_i,\, D_i$) and leptons ($\ell_i = L_i,\, E_i$) for a given generation $i$ emerge, that is

$$F_{q_3} = -2\,F_{q_2} = -2\,F_{q_1}\,, \quad F_{\ell_1} = 0\,, \quad F_{\ell_3} = -F_{\ell_2}\,. \tag{8.29}$$

In addition to quark masses, this particular choice of charges also allows for diagonal lepton Yukawa elements $Y_e^{ii}$, see Eq. (8.21). To reproduce the best-fit value $\mathcal{C}_{9,\mu} = -0.83$ given in Tab. 4.2, we employ Eq. (8.3) and derive the matching condition $\alpha_4(\mu_0) = g_4^2/(4\pi)^2 = 1.87 \cdot 10^{-2}$ for the rescaled U(1)′ gauge coupling. In this case, the constraint from $B_s$-mixing in Eq. (8.24) is satisfied with moderate $r_{B_s} = 0.35$.

In $\mathrm{BM}_2$, we have $F_{E_2} = 0$ which provokes the best-fit values $\mathcal{C}_{9,\mu} = -\mathcal{C}_{10,\mu} = -0.41$, see Tab. 4.2.

This leads to $\alpha_4(\mu_0) = 5.97 \cdot 10^{-3}$ and $r_{B_s} = 0.86$, near to but lower than the current $B_s$-mixing bound in Eq. (8.23).

The pattern $-\mathcal{C}_{9,\mu} \gg \mathcal{C}_{10,\mu} > 0$ is realised in $\text{BM}_3$. We generate

$$\mathcal{C}_{9,\mu} = -0.71\,, \quad \mathcal{C}_{10,\mu} = +0.24\,, \tag{8.30}$$

with $\alpha_4(\mu_0) = 4.60 \cdot 10^{-2}$, which is in excellent agreement with the respective fit result in Tab. 4.2. In contrast to the other benchmark models $\text{BM}_{1,2,4}$, we have to adjust for two coefficients simultaneously. We fix $\mathcal{C}_{9,\mu}$ to its best-fit value, while allowing $\mathcal{C}_{10,\mu}$ to be within the $1\,\sigma$ uncertainty of its central fit value, *i.e.* $\mathcal{C}_{10,\mu} = 0.20 \pm 0.13$. Notably, no charges to third-generation quarks are present In $\text{BM}_3$. The required $Z'$ couplings to the (mass eigenstate) $b$ quarks are induced after flavour rotations as detailed in Sec. 5.1.3.

In benchmark model $\text{BM}_4$, we choose a lower matching scale than in $\text{BM}_{1,2,3}$ as the vanishing first- and second-generation quark charges yield a suppressed $Z'$ production in $pp$-collisions, and allow to mitigate constraints on the $Z'$ mass [21]. Following this argument, $\text{BM}_4$ can also be considered minimal as it features fewer couplings compared to the other benchmarks. We provide more details on the phenomenological implication of our $Z'$ benchmarks in Sec. 8.4. As in $\text{BM}_1$, we have $F_{L_2} = F_{E_2}$, and hence $\mathcal{C}_{10,\mu} = 0$. For identical $\mathcal{C}_{9,\mu} = -0.83$, we obtain $\alpha_4(\mu_0 = 3\text{ TeV}) = 2.46 \cdot 10^{-2}$. A model with a similar minimal set-up as $\text{BM}_4$ has been studied in Ref. [134]. Yet, a large tuning in flavour rotations is necessary in their set-up, while CKM-like $bs$-mixing as in $\text{BM}_4$ would violate the pattern in Eq. (8.27) and predict the wrong sign of $\mathcal{C}_{9,\mu}$. For convenience, we collect all features of the benchmark models in Tab. 8.4, at the end of this chapter.

## 8.3 Planck safety in U(1)′ extensions

After presenting phenomenologically viable U(1)′ extensions that account for the $B$-anomalies in Sec. 8.2, we move to the Planck safety analysis of these benchmarks models. We outline our Planck safety analysis under general considerations in Sec. 8.3.1. Afterwards, dedicated results for the benchmark model $\text{BM}_3$ are presented in Sec. 8.3.2. We refer to Ref. [21] for details on the other benchmark models.

In Sec. 5.5, we have discussed Landau poles that arise at energies $\mu_{\text{LP}} \lesssim 10^{13}$ GeV when U(1)′ gauge interactions $\alpha_4(\mu_0) \simeq \mathcal{O}\left(10^{-2}\right)$ with minimal U(1)′ charge assignments are included into the RG flow. This limit lies well below the Planck scale $\mu_{\text{Pl}} \sim 10^{19}$ GeV, and is lowered even further in scenarios with a beyond-minimal U(1)′ charge assignment, illustrated in Fig. 5.4. To obtain a stable and predictive theory until the Planck scale, we consider a rich BSM particle sector and new interactions put forward in Sec. 8.1. Following Sec. 5.5.1, we utilise the Planck safety approach to ensure the predictivity and stability of our models up to the Planck scale.

### 8.3.1 Critical surface of model parameters and general considerations

The RG running of the couplings determines possible Planck-safe trajectories, which can be extracted for the different benchmark models $\text{BM}_{1,2,3,4}$ introduced in Sec. 8.2. We consider the

running of the gauge, Yukawa, quartic and portal couplings employing the rescaled couplings $\alpha_i$ given in Eqs. (A.33) and (A.37). In App. A.4, we provide the numerical values of the SM couplings at the matching scale in Tab. A.1, which are extracted from experimental data. The RG evolution of these couplings up to the matching scale remains unchanged. Moreover, we include the running of the kinetic mixing parameter $\eta$, see Sec. 8.1.4, being constrained by Eq. (5.56). For the quartic coupling $\alpha_s$ we impose Eq. (8.18). As stated in Eq. (8.22), we only take into account the SM Yukawa couplings of the $t$ and $b$ quark, denoted by $y_t$ and $y_b$, respectively. The remaining Yukawa couplings of the SM can safely be neglected due to their numerical smallness and (technical) naturalness. Viable RG trajectories are given by finite and well-defined values of all couplings for energies from the matching scale up to the Planck scale. Here, we fix the matching scale to

$$\mu_0 = \begin{cases} 5 \text{ TeV} & \text{for BM}_{1,2,3} \\ 3 \text{ TeV} & \text{for BM}_4 \end{cases} . \tag{8.31}$$

Furthermore, we demand a stable scalar potential by imposing the conditions in Eq. (8.10) to hold all the way up to Planckian energies.

Following the approach outlined in Ref. [140], the RG running is evolved numerically at two-loop accuracy for all couplings starting at the matching scale. Then, the evolution of the couplings via the corresponding $\beta$-functions is computed until the Planck scale. During this procedure, we monitor the stability of the quantum vacuum and ensure the absence of Landau poles for any RG trajectory. Since in each benchmark model the value of $\alpha_4(\mu_0)$ is determined by the Wilson coefficients needed to account for the $B$-anomalies, *cf.* Eq. (8.3), we define the set of initial conditions

$$\mathcal{P}_C = \left\{\alpha_y,\, \alpha_\delta,\, \alpha_{\tilde{\delta}},\, \alpha_u,\, \alpha_v,\, \alpha_w,\, \alpha_s\right\}|_{\mu=\mu_0} . \tag{8.32}$$

This set includes the values of the remaining couplings at the matching scale in Eq. (8.31). Then, the BSM *critical surface* of parameters constitutes a set $\mathcal{P}_C$ that leads to well-defined RG trajectories up to the Planck scale.

To move arising Landau poles past the Planck scale through BSM Yukawa interactions, we require a contribution

$$F_\psi^2 \cdot \alpha_y(\mu_0) \gtrsim \mathcal{O}\left(10^{-1}\right) . \tag{8.33}$$

Simultaneously, the growth of $\alpha_4$ needs to be decelerated by choosing sufficiently small absolute values of all other U(1)′ charges relative to $|F_\psi|$. Due to their colour and isospin multiplicities the quark charges heavily influence the growth of the U(1)′ gauge couplings. However, these considerations coincide with the phenomenological constraints from $B_s$-mixing that demand $F_{Q_{2,3}}/F_\psi \ll 1$, see Tab. 8.2. Conversely, sizeable U(1)′ charges to leptons are needed in Eq. (8.3) to accommodate the $B$-anomalies after all.

In the scalar sector, substantial contributions from at least one of the portals couplings $\delta$ or $\tilde{\delta}$ to the scalars $S$ and $\phi$ are necessary to stabilise the Higgs potential in Eq. (8.9). We estimate the preferred ranges

$$\mathcal{O}\left(10^{-3}\right) \lesssim \alpha_{\delta,\tilde{\delta}} \lesssim \mathcal{O}\left(10^{-1}\right) , \tag{8.34}$$

where it is sufficient if one of the Higgs portals fulfils one of the conditions above, while the other one can be chosen freely. The conditions in Eqs. (8.33) and (8.34) provide a major advantage in

obtaining viable RG trajectories. Hence, they are key results of our RG analysis as in general the parameter region is dominated by poles (and instabilities) [21].

## 8.3.2 Planck-safe trajectories in benchmark model 3

In $BM_3$, the value of $\alpha_4(\mu_0) = 4.60 \cdot 10^{-2}$ dictates a putative Landau pole at $\mu_{LP} \approx 25$ TeV. The location of the naive Landau pole bounds the masses of the $\psi$ and $S$ fields, $M_\psi$, $M_S < \mu_{LP}$. Previously, in Fig. 5.4 we have displayed the RG running of the same benchmark while disabling the BSM fields $\psi$, $S$, and $\phi$. This explains why in that scenario the Landau pole is located at larger energies around $3 \cdot 10^4$ TeV. We remark that the addition of BSM fields lowers the potential scale of the Landau pole due to additional U(1)′ charge carriers. However, the associated BSM Yukawa interactions are able to move divergences past the Planck scale.

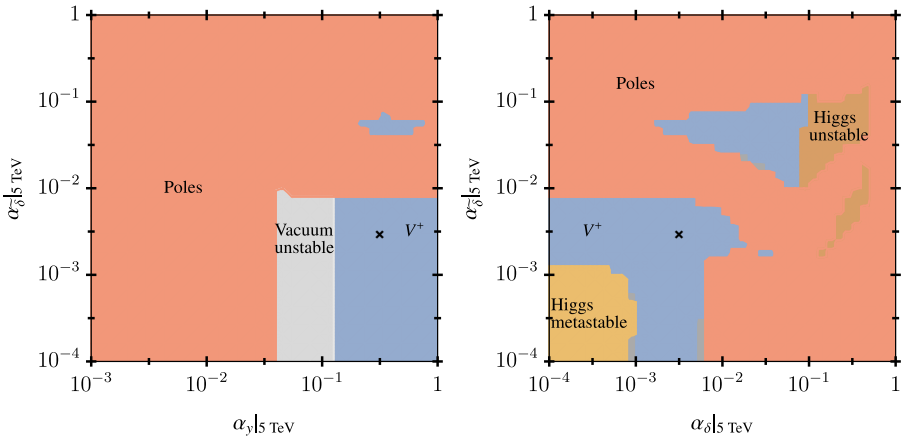


**Figure 8.3:** Critical surface of parameters for the benchmark model $BM_3$, projected onto the $\{\alpha_y, \alpha_{\tilde{\delta}}\}|_{\mu_0}$ (left-hand side plot) and the $\{\alpha_\delta, \alpha_{\tilde{\delta}}\}|_{\mu_0}$ (right-hand side plot) plane of parameters. We set the matching scale $\mu_0 = 5$ TeV and $\alpha_\delta|_{\mu_0} = 10^{-2.5}$ (left-hand side plot), $\alpha_y|_{\mu_0} = 10^{-0.5}$ (right-hand side plot), together with $\{\alpha_4, \eta, \alpha_u, \alpha_v, \alpha_w, \alpha_s\}|_{\mu_0} = \{4.60 \cdot 10^{-2}, 0, 10^{-4}, 10^{-5}, 10^{-6}, 10^{-3.5}\}$. The black cross corresponds to the sample trajectory displayed in Fig. 8.4. The colour coding is as follows. An unstable vacuum (stable vacuum $V^+$) at the Planck scale is indicated in grey (blue). Brown and yellow regions illustrate an unstable ($\alpha_\lambda < -10^{-4}$) and a metastable ($-10^{-4} < \alpha_\lambda < 0$) Higgs at the Planck scale. Landau poles that emerge at or before the Planck scale are shown in red. *Figure taken from Ref.* [21].

Viable RG trajectories are obtained, scanning over the set of initial conditions $\mathcal{P}_C$ in Eq. (8.32). The prior estimates made under general considerations in Eqs. (8.33) and (8.34) are adjusted in the latter case, where we find

$$10^{-1} \lesssim \alpha_y(\mu_0)\,, \tag{8.35}$$

$$10^{-4} \lesssim \alpha_\delta(\mu_0) \lesssim 10^{-1} \quad \text{or} \quad 10^{-2.5} \lesssim \alpha_{\tilde{\delta}}(\mu_0) \lesssim 10^{-1}\,. \tag{8.36}$$

Results for $BM_3$ are displayed in Fig. 8.3, where the UV critical surface at the Planck scale is shown in terms of the couplings $\alpha_y$, $\alpha_\delta$ and $\alpha_{\tilde{\delta}}$ at the matching scale. We observe that many parameters settings are excluded due to poles (shown in red) and instabilities of the scalar potential (brown,

yellow). However, we find a fair range of parameters space that allows for a stable ground state $V^+$ (blue) at the Planck scale, while pushing Landau poles beyond Planckian energies. Visible in both projections, we observe two disconnected pieces of the vacuum only separated by the occurrence of poles for parameters in between. We further deduce that both Higgs portal couplings become sizeable at $\mu_0$ in one of the regions, but remain within the limits established in Eq. (8.36).

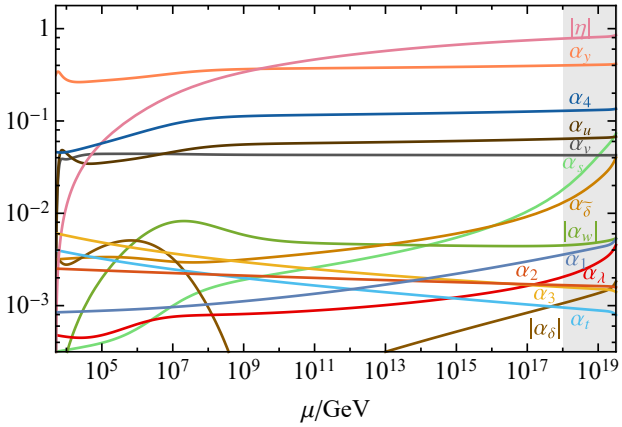


**Figure 8.4:** Sample running of couplings for the benchmark model $\mathrm{BM}_3$ up to the Planck scale $\mu_{\mathrm{Pl}}$ (grey area) showing trajectories for all couplings and the kinetic mixing parameter $\eta$ for $\mu_0 = 5$ TeV alongside $\{\alpha_4, \eta, \alpha_y, \alpha_\delta, \alpha_{\tilde{\delta}}, \alpha_u, \alpha_v, \alpha_w, \alpha_s\}|_{\mu_0} = \{4.60 \cdot 10^{-2}, 0, 10^{-0.5}, 10^{-2.5}, 10^{-2.5}, 10^{-4}, 10^{-5}, 10^{-6}, 10^{-3.5}\}$. *Figure taken from Ref.* [21].

In Fig. 8.4, a sample Planck-safe trajectory of $\mathrm{BM}_3$ is depicted, with parameters settings corresponding to the black cross in Fig. 8.3. Overall, we find a moderate but slow evolution of all couplings between the matching and the Planck scale. Kinetic mixing reaches an $\mathcal{O}(1)$ value, while the BSM Yukawa and U(1)′ coupling score values of $\mathcal{O}(10^{-1})$. All other couplings remain roughly within the range of $\mathcal{O}(10^{-3}\text{-}10^{-2})$. We also identify the so-called 'walking regime' in Fig. 8.4, where the growth of couplings comes almost to a halt. Such regimes can be observed in all viable trajectories and prove to be an essential feature of our model building. Comparable RG trajectories are obtained when considering different Planck-safe parameter regions of Fig. 8.3. The corresponding results for the other benchmark models $\mathrm{BM}_{1,2,4}$ are discussed in Ref. [21].

## 8.4 Phenomenological implications

In this section, we present phenomenological implications of our benchmark models. To this end, we study predictions for dineutrino modes and discuss collider signatures that emerge in $Z'$ models. We also entertain the possibility of RH quark couplings and their impact on $R_{K^{(*)}}$ observables.

### 8.4.1 Predictions for dineutrino modes $B \to K^{(*)}\nu\bar{\nu}$

A detailed parametrisation of SM and NP contributions to dineutrino modes $q' \to q\,\nu\bar{\nu}$ is provided in, *e.g.*, Ref. [20] and also discussed in Chap. 9. It can be shown that a universal impact for

all $B \to H\nu\bar{\nu}$, with $H = K, K^*, \ldots$, branching ratios is present for vanishing RH quark currents. This setting is realised for the $Z'$ models considered in this analysis, see Sec. 8.2. Therefore, we write [20]

$$\frac{\mathcal{B}(B \to H\nu\bar{\nu})}{\mathcal{B}(B \to H\nu\bar{\nu})_{\rm SM}} = \frac{1}{3}\left(\sum_i |1 + F_{L_i}\, a|^2 + |F_{\nu_i}\, a|^2\right) , \tag{8.37}$$

where $a = 2\mathcal{N}^{-1}\, g_L^{bs} / \left(M_{Z'}^2\, X_{\rm SM}\right)$ and $|a| \ll 1$. Here, $X_{\rm SM} = -12.64$ encodes the SM contribution, see definition in Eq. (9.6). Inserting the U(1)′ charges and Wilson coefficients of the respective benchmarks into Eq. (8.37), we obtain the values 1.003 ,1.05 ,1.08, 0.97 for $\rm BM_1$, $\rm BM_2$, $\rm BM_3$ and $\rm BM_4$, respectively. The tiny deviation from one in $\rm BM_1$ is due to a certain cancellation of contributions. To be precise, the chosen second- and third-generation charges $F_{L_2} = -F_{L_3}$ provoke an cancellation of the interference term with the SM, *cf.* Tab. 8.2. Only the second term in Eq. (8.37) encodes contributions from light RH neutrinos which is missing SM interference. Therefore, only negligible contributions at the permille level are realised in $\rm BM_{2,3,4}$. We find that $b \to s$ dineutrino branching ratios are generally enhanced in NP scenarios addressing the $B$-anomalies, although a mild suppression is obtained in $\rm BM_4$ where $a > 0$ and $F_{L_3} < 0$. While current sensitivities of the Belle II experiment allow for an observation of $B^0 \to K^0\nu\bar{\nu}$ and $B^0 \to K^{*0}\nu\bar{\nu}$ decays at the SM-level, the NP effects in our benchmarks are indistinguishable from the SM prediction within present precision, see Tab. 9.3. Nevertheless, the study of branching ratios in dineutrino modes allows for different patterns of NP that can validate or falsify concrete models, see Chap. 9.

### 8.4.2 Collider signatures

The $Z'$ models in Sec. 8.2 provide a rich phenomenology that can be probed at different colliders. In what follows, we present two key signatures, while expanded discussions can be found in Ref. [21].

The decay width of a $Z'$ boson decaying into fermion-antifermion pairs is given by [189]

$$\begin{aligned}\Gamma\left(Z' \to f_i \bar{f}_i\right) = \frac{2\pi N_C^f}{3}\alpha_4\, M_{Z'}\sqrt{1 - \frac{4m_{f_i}^2}{M_{Z'}^2}} \\ \cdot \left[\left(F_{f_{Li}}^2 + F_{f_{Ri}}^2\right) - \frac{m_f^2}{M_{Z'}^2}\left(F_{f_{Li}}^2 - 6F_{f_{Li}}F_{f_{Ri}} + F_{f_{Ri}}^2\right)\right] .\end{aligned} \tag{8.38}$$

Here, kinetic mixing has been neglected, and the colour factor reads $N_C^f = 3$ for quarks and $N_C^f = 1$ otherwise. The decay $Z' \to \psi\bar{\psi}$ is kinematically allowed and becomes dominant if $M_{Z'} > 2M_\psi$. We find that the phase space suppression of the partial decay width $\Gamma(Z' \to \psi\bar{\psi})$ remains small ($< 5\,\%$) as long as $M_\psi \lesssim 0.3\, M_{Z'}$. The $Z'$ cannot decay to SM gauge bosons at LO if kinetic mixing is neglected. For $F_s \neq 0$, the decay $Z' \to ss$ with $s = h, \phi$ can arise and its corresponding decay width reads [189]

$$\Gamma\left(Z' \to ss\right) \simeq \frac{\pi}{3}\,\alpha_4\, M_{Z'}\, F_s^2 \left(1 - 4\,\frac{m_s^2}{M_{Z'}^2}\right)^{\frac{3}{2}} . \tag{8.39}$$

The branching ratios $\mathcal{B}\left(Z' \to f_i\bar{f}_i,\, ss\right)$ can be computed via Eqs. (8.38) and (8.39), employing

the charge assignments in Tab. 8.2 for the benchmark models $\mathrm{BM}_{1-4}$. The results are compiled in Tab. 8.3.

| Model | jets | $b$ | $t$ | $e$ | $\mu$ | $\tau$ | $\nu_{e,\mu,\tau}$ | $h$ | $\psi_{1,2,3}$ | $\phi$ | $\Gamma^{\mathrm{tot}}(Z')$ |
|---|---|---|---|---|---|---|---|---|---|---|---|
| $\mathrm{BM}_1$ | 0.5 | 0.5 | 0.5 | 0 | 15 | 15 | 15 | 0 | 54 | 0.2 | $0.43\,M_{Z'}$ |
| $\mathrm{BM}_2$ | 14 | 1.5 | 1.5 | 0 | 9 | 9 | 18 | 0 | 46 | 0.1 | $0.14\,M_{Z'}$ |
| $\mathrm{BM}_3$ | 5 | 0 | 0 | 0 | 4 | 4 | 8 | 0 | 79 | 0.1 | $0.73\,M_{Z'}$ |
| $\mathrm{BM}_4$ | 0 | 0.9 | 0.9 | 0 | 3 | 11 | 14 | 0 | 72 | 0.2 | $0.43\,M_{Z'}$ |

**Table 8.3:** Tree-level branching ratios in % for the different $Z'$ decay modes to fermion-antifermion pairs and pairs of scalars, neglecting fermionic as well as kinetic mixing. The last column displays the total $Z'$-width. The numerical values correspond to the scenario where the decays $Z' \to \psi_i\bar{\psi}_i, \phi\phi$ are kinematically allowed and hardly phase space suppressed (i.e. $M_{\psi,\phi} \lesssim 0.3\,M_{Z'}$). If the decay to $\psi\bar{\psi}$ is kinematically suppressed at a significant level or forbidden, the other branching ratios increase by up to roughly a factor of 2, 4 and 5 in $\mathrm{BM}_{1,2}$, $\mathrm{BM}_3$ and $\mathrm{BM}_4$, respectively. *Table adapted from Ref.* [21].

Therein, we also show the corresponding total $Z'$-width $\Gamma^{\mathrm{tot}}(Z')$ obtained in the limit $M_\psi \lesssim 0.3\,M_{Z'}$. We find that the decay mode $Z' \to \psi\bar{\psi}$ (if kinematically allowed) provides the dominant contribution in all benchmarks with a branching ratio of approximately 50 %, 80 % and 70 % in $\mathrm{BM}_{1,2}$, $\mathrm{BM}_3$ and $\mathrm{BM}_4$, respectively. Another observation made in all scenarios is the substantial branching ratio to dineutrinos $\mathcal{B}(Z' \to \nu\bar{\nu})$ ranging from 8 to 18 %. Thus, both these decay modes yield missing energy signatures at colliders, $Z' \to$ invisible with a branching ratio of $\sim$ 65-85 %. Such signatures can be studied with future LHC searches.

The four benchmarks can be distinguished by their different branching ratios to leptons (muons and tauons) but also to dijets, where $\mathrm{BM}_2$ provides the largest ratio of 14 %. Conversely, in $\mathrm{BM}_4$ no dijets are produced via $Z'$ decays due to the vanishing first- and second-generation $Z'$ couplings. Thus, a distinction of benchmarks is possible when measuring $Z'$ branching ratios with an accuracy of $\sim 10\,\%$.

Another finding in the benchmarks presented is their promising implications for future muon colliders [190–193]. The $Z'$ boson can be directly produced, either on- or off-shell, in the $s$-channel. The cross section is enhanced by the large U(1)′ coupling as well as the requisite muon coupling $F_{L_2}$. In the following, we study the $Z'$ production in dominant subsequent decays to invisibles which provides a formidable discovery potential via $\mu^+\mu^- \to Z' \to \psi\bar{\psi}, \nu\bar{\nu}$. To lowest order, the corresponding cross section is given as

$$\sigma\left(\mu^+\mu^- \to Z' \to \psi\bar{\psi}, \nu\bar{\nu}\right) = \frac{s\,\left(F_{L_2}^2 + F_{E_2}^2\right)}{\left(M_{Z'}^2 - s\right)^2 + M_{Z'}^2\Gamma_{Z'}^2} \cdot \frac{g_4^4}{48\pi}\left[2N_f F_\psi^2 + \sum_i (F_{L_i}^2 + F_{\nu_i}^2)\right], \quad (8.40)$$

which is about 880, 72, 560 and 4800 times larger in the respective models $\mathrm{BM}_{1-4}$ compared to the SM cross section $\sigma_{\mathrm{SM}}(\mu^+\mu^- \to Z \to \nu\bar{\nu}) \approx 1.94 \cdot 10^{-11}$ GeV$^{-2}$ for $\sqrt{s} = 3$ TeV [21]. For recent muon collider studies of $Z'$ models explaining the $B$-anomalies, we refer to Refs. [194, 195].

### 8.4.3 Impact of right-handed quark currents

Throughout this chapter, we have focussed U(1)′ extensions that feature NP Wilson coefficients $\mathcal{C}_{(9,10),\mu}$ with only LH quark couplings $g_L^{bs}$. While this assumption works perfectly to explain the $B$-anomalies, it restricts $R_K \simeq R_{K^*}$ [83]. The latest experimental data from LHCb [8, 84], collected in Tab. C.5, suggests in particular $R_{K^+} > R_{K^{*0}}$ in the $q^2$-bin $[1.1, 6.0]$ GeV$^2$ at a level of approximately $1\,\sigma$. The first measurement of $R_{K^0_S}$ [9] does not follow this trend, but is subject to sizeable uncertainties.

In the following, we consider simultaneous contributions of LH and RH quark couplings, $g_L^{bs}$ and $g_R^{bs}$, respectively. In Eq. (3.50), we have put forward a double ratio sensitive to primed Wilson coefficients. This ratio can be simplified in the case of vanishing electron couplings and reads

$$\frac{R_{K^*}}{R_K} \simeq 1 - 0.41 \, \left(\mathcal{C}'_{9,\mu} - \mathcal{C}'_{10,\mu}\right) \, . \tag{8.41}$$

The semileptonic Wilson coefficients obey the relation

$$\frac{\mathcal{C}'_{9,\mu}}{\mathcal{C}_{9,\mu}} = \frac{\mathcal{C}'_{10,\mu}}{\mathcal{C}_{10,\mu}} = \frac{g_R^{bs}}{g_L^{bs}} \equiv r \, , \tag{8.42}$$

see Eq. (8.3). The 4d fit results in Tab. 4.2 favour $r < 0$, but they also remain consistent with $r = 0$ varying uncertainties within 1-2 $\sigma$. However, we can derive additional implications assuming that $\mathcal{C}_{9,\mu} < 0$ remains true in future updated global fits and that NP contributions to electrons are tiny. Under these assumptions, we can distinguish

$$\begin{cases} r > 0 \text{ (hence } \mathcal{C}'_{9,\mu} < 0) : & R_{K^*} > R_K \, , \\ r < 0 \text{ (hence } \mathcal{C}'_{9,\mu} > 0) : & R_{K^*} < R_K \, . \end{cases}$$

Interestingly, $Z'$ contributions to $B_s$-mixing can be cancelled in a LH-dominated scenario $g_L^{bs} = g_R^{bs} \, X_s$, with $X_s \approx 10$, which has been put forward in Eq. (5.48). In this case, Eq. (8.42) can be rewritten inserting the definition of $g_L^{bs}$ Eq. (8.4). We obtain

$$\sin\left(2\,\theta_d\right) = \frac{2\,V_{tb}\,V_{ts}^*}{X_s} \frac{F_{Q_3} - F_{Q_2}}{F_{D_3} - F_{D_2}} \approx \left(-8 \cdot 10^{-3}\right) \cdot \frac{F_{Q_3} - F_{Q_2}}{F_{D_3} - F_{D_2}} \, , \tag{8.43}$$

where $\theta_d$ denotes the $bs$-mixing angle for the down-type quark singlets, *cf.* Eq. (5.20). Hence, $\theta_d$ is small in models with $F_{Q_3} - F_{Q_2}$ of the same order or smaller as $F_{D_3} - F_{D_2}$. The ratios of Wilson coefficients are strictly positive, that is $r = 1/X_s > 0$ in the preferred LH-dominated scenario.

In summary, we find that $Z'$ models can be uniquely probed by a combined analysis of $b \to s\,\ell^+\ell^-$ transitions, $B_s$-mixing constraints, and universality ratios $R_K$ versus $R_{K^*}$. Moreover, related muon-to-electron ratios, such as $R_\phi$ or $R_{K_1}$, can help pinpoint the underlying chirality of the NP quark currents [83].

## 8.5 Summary of Planck-safe benchmark models

We have studied new flavourful U(1)′ extensions of the SM that account for the $B$-anomalies presently hinting at NP in $b\to s\,\mu^+\mu^-$ transitions. In doing so, we have enforced stability and predictivity of the theory parameters via RG evolution up to the Planck scale. This is necessary to avert Landau poles emerging well below Planckian energies when adding the U(1)′ coupling to the RG flow, and further remedies the metastability of the scalar potential. We have extended the particle content by including vector-like fermions, meson-like scalars and (in some models) RH neutrinos, see Sec. 8.1.1. The new Yukawa couplings tame Landau poles while portal couplings are crucial to stabilise the scalar potential, as illustrated in Sec. 8.3.2 for a sample RG trajectory.

The benchmark models presented each describe a viable fit scenario from Tab. 4.2, addressing the $B$-anomalies. The main features are summarised in Tab. 8.4. We have explored the phenomenology of these benchmark models, where distinct signatures for (future) lepton and hadron colliders have been discussed in Sec. 8.4. Notably, we find that the $Z'$ predominantly decays into invisibles, where $Z'\to\psi\bar{\psi}$ dominates if kinematically allowed, see Tab. 8.3. Moreover, these models can be extended and tested to accommodate future measurements.

| Model | $\mu_0$ | $\alpha_4(\mu_0)$ | $\mathcal{C}_{9,\mu}$ | $\mathcal{C}_{10,\mu}$ | $Y^{ii}_{u,d}$ | $Y^{ii}_{e}$ | $Y^{ii}_{\nu}$ | $r_{B_s}$ | $\mathcal{B}\,(Z'\to\text{inv.})$ | $\nu_R$ |
|---|---|---|---|---|---|---|---|---|---|---|
| $\text{BM}_1$ | 5 TeV | $1.87\cdot10^{-2}$ | $-0.83$ | 0 | ✓ | ✓ | ✗ | 0.35 | 73 % | ✗ |
| $\text{BM}_2$ | 5 TeV | $5.97\cdot10^{-3}$ | $-0.41$ | $-\mathcal{C}_{9,\mu}$ | ✓ | ✗ | ✗ | 0.86 | 64 % | ✓ |
| $\text{BM}_3$ | 5 TeV | $4.60\cdot10^{-2}$ | $-0.71$ | $+0.24$ | ✓ | ✗ | ✗ | 0.60 | 87 % | ✓ |
| $\text{BM}_4$ | 3 TeV | $2.46\cdot10^{-2}$ | $-0.83$ | 0 | ✓ | ✓ | ✓ | 0.70 | 86 % | ✓ |

**Table 8.4:** Key features of Planck-safe benchmark models (with charge assignments listed in Tab. 8.2), showing the values of the matching scale $\mu_0$, the Wilson coefficients $\mathcal{C}_{(9,10),\mu}$, the gauge coupling $\alpha_4$, and the diagonal Yukawa interactions $Y^{ii}_{u,d,e,\nu}$ as in Sec. 8.2. In addition, we list the branching ratio for $Z'$ decays to missing energy, whether RH neutrinos $\nu_R$ are included, and the room left by the $B_s$-mixing constraint $r_{B_s}\leq 1$ before RH currents need to be invoked, with $r_{B_s}$ defined in Eq. (8.24). *Table taken from Ref.* [21].

While $Z'$ models with large $M_{Z'}$ in the TeV-range are able to account for the $B$-anomalies, they fall short of simultaneously explaining the $(g-2)_\mu$ discrepancy [196] due to tiny $Z'$ one-loop contribution to $(g-2)_\mu$ [197, 198]. This apparent mismatch can be interpreted as different types of NP entering these anomalies, see, *e.g.*, Refs. [199, 200]. This motivates future studies where the $Z'$ boson teams up with other NP particles, such as leptoquarks or vector-like fermions [201] that can collectively explain flavour anomalies in different sectors.

Chapter

9

# Lepton universality tests in dineutrino modes

Probing lepton universality (LU) in rare semileptonic decays provides an excellent opportunity to find deviations from the SM. Regarding the current status of the persistent $B$-anomalies, it is well motivated to construct additional tests involving other decay modes not only as a cross-check, but also to pinpoint possible BSM scenarios that can account for those effects. Therefore, related FCNC quark transitions into dineutrinos modes $q' \to q\,\nu\bar{\nu}$ are ideal for testing universality and discovering NP due to several reasons. Firstly, these modes are subject to similar loop and CKM suppressions as $q' \to q\,\ell^+\ell^-$ transitions, while neutrino masses require SM extensions. The flavour of neutrinos cannot be tagged experimentally, and thus a measurement of dineutrino observables involves an incoherent sum over all neutrino flavours $i, j = e, \mu, \tau$. In particular, the dineutrino branching ratio is expressed as

$$\mathcal{B}\left(q' \to q\,\nu\bar{\nu}\right) = \sum_{i,j} \mathcal{B}\left(q' \to q\,\nu_j\bar{\nu}_i\right) \,. \tag{9.1}$$

Notably, contributions from lepton universality violation, or lepton flavour violation, are included by construction. This way, complementary experimental tests of LU and charged lepton flavour conservation (cLFC) can be formulated. In this chapter, we study different lepton flavour structures connecting the charged dilepton couplings to those of dineutrinos by $\mathrm{SU}(2)_L$-invariance in a model-independent way. A clean environment to probe dineutrino modes is available at $e^+e^-$-facilities such as Belle II and the BES III experiment, with promising expected yields for measurements of missing energy [85, 202]. Furthermore, planned experiments like the Future Circular Collider (FCC) with collider signatures of positron-electron collisions FCC-ee [203] will also advance NP searches in these modes.

This chapter is based on collective findings first presented in Refs. [18–20]. Therein, detailed studies in different flavour sectors, such as charm and $B$-physics, have been conducted, while results for kaon and top couplings have been worked out as well. In what follows, we aim to present the general idea of these studies. To this end, we review the correlation of dineutrino and charged dilepton couplings present in the SMEFT framework in Sec. 9.1. This link is put to use in Sec. 9.2, where predictions for dineutrino modes are worked out in the charm and $B$-sector. Subsequently, in Sec. 9.3 we discuss novel tests probing LU in $b \to s\,\nu\bar{\nu}$ transitions in a model-independent way. Results for $Z'$ models are described as well.

## 9.1 SU(2)$_L$-link between dineutrino and charged lepton couplings

Here, we present a unified description of FCNC interactions between two quarks and two leptons, separating contributions of charged leptons and neutrinos. Compared to the previously considered EFT framework in Eq. (3.41) and Eq. (6.2), we utilise a slightly adapted notation where the different flavour indices of quarks and leptons are made explicit. Below the electroweak scale, $\mu < \mu_{\rm EW}$, the Hamiltonian involving charged leptons is given by

$$\mathcal{H}_{\rm eff}^{\ell_i^-\ell_j^+} \supset -\frac{4G_{\rm F}}{\sqrt{2}}\,\frac{\alpha_e}{4\pi}\sum_{A=L,R}\mathcal{K}_A^{P_{\alpha\beta}ij}\,O_A^{\alpha\beta ij} + \text{h.c.}\,, \tag{9.2}$$

whereas for neutrinos we have

$$\mathcal{H}_{\rm eff}^{\nu_i\bar{\nu}_j} = -\frac{4G_{\rm F}}{\sqrt{2}}\,\frac{\alpha_e}{4\pi}\sum_{A=L,R}\mathcal{C}_A^{P_{\alpha\beta}ij}\,Q_A^{\alpha\beta ij} + \text{h.c.}\,, \tag{9.3}$$

where the indices $\alpha$, $\beta$ and $i$, $j$ denote the flavours of quarks and leptons, respectively. The superscript $P = D$ ($P = U$) refers to the down-quark sector (up-quark sector), for instance $P_{\alpha\beta} = D_{13}$ ($U_{12}$) indicates $b\to s$ ($c\to u$) transitions. The dimension-six operators $O_A^{\alpha\beta ij}$ and $Q_A^{\alpha\beta ij}$ cover the low-energy dynamics, where the relevant semileptonic operators read

$$O_L^{\alpha\beta ij} = (\bar{q}_L^\alpha\gamma_\mu q_L^\beta)(\bar{\ell}_L^j\gamma^\mu\ell_L^i)\,, \quad O_R^{\alpha\beta ij} = (\bar{q}_R^\alpha\gamma_\mu q_R^\beta)(\bar{\ell}_L^j\gamma^\mu\ell_L^i)\,, \tag{9.4}$$

while, in absence of RH neutrinos like in the SM, only the two dineutrino operators

$$Q_L^{\alpha\beta ij} = (\bar{q}_L^\alpha\gamma_\mu q_L^\beta)(\bar{\nu}_L^j\gamma^\mu\nu_L^i)\,, \quad Q_R^{\alpha\beta ij} = (\bar{q}_R^\alpha\gamma_\mu q_R^\beta)(\bar{\nu}_L^j\gamma^\mu\nu_L^i)\,, \tag{9.5}$$

appear in Eq. (9.3). The short-distance dynamics are encoded in the Wilson coefficients $\mathcal{K}_k^{P_{\alpha\beta}ij} = \mathcal{K}_{A,\rm SM}^{P_{\alpha\beta}ij} + \mathcal{K}_{A,\rm NP}^{P_{\alpha\beta}ij}$ and $\mathcal{C}_k^{P_{\alpha\beta}ij} = \mathcal{C}_{A,\rm SM}^{P_{\alpha\beta}ij} + \mathcal{C}_{A,\rm NP}^{P_{\alpha\beta}ij}$, where the separation between SM and BSM contributions is made explicit. The SM Wilson coefficients are lepton (flavour) universal, which gives

$$\mathcal{C}_{L,\rm SM}^{D_{bs}ij} = V_{ts}\,V_{tb}^*\,X_{\rm SM}\,\delta_{ij}\,, \tag{9.6}$$

particularising for the $b\to s$ transition. In Eq. (9.6), we have introduced the coefficient $X_{\rm SM} = -2\,X_t/\sin^2(\theta_{\rm W}) = -12.64 \pm 0.15$, which is known with a high accuracy, including two-loop electroweak contributions [204] and NLO QCD corrections [205, 206]. Details on the derivation of the function $X_t$ is given in Refs. [131, 204]. The contributions $\mathcal{C}_{R,\rm SM}^{D_{\alpha\beta}ij}$ are negligible [207], and hence are not considered in our studies. The semileptonic Wilson coefficients $\mathcal{K}_{L,R}^{D_{23}ij}$ are related to the rare $B$-decay ones, previously defined in Eq. (3.44), as

$$\mathcal{K}_L^{D_{23}ij} = V_{tb}\,V_{ts}^*\left(\mathcal{C}_9^{ij} - \mathcal{C}_{10}^{ij}\right)\,, \quad \mathcal{K}_R^{D_{23}ij} = V_{tb}\,V_{ts}^*\left(\mathcal{C}_9^{\prime ij} - \mathcal{C}_{10}^{\prime ij}\right)\,. \tag{9.7}$$

Assuming $\mu_{\rm EW} \lesssim \Lambda_{\rm NP}$, we can describe the set of FCNC transitions $q_\beta \to q_\alpha(\ell_i^-\ell_j^+, \nu_i\bar{\nu}_j)$ in SMEFT introduced in Sec. 3.3. The LO contributions are given by the four-fermion operators

embedded in [61]

$$\begin{aligned}\mathcal{L}_{\text{SMEFT}} \supset & \frac{\mathcal{C}_{lq}^{(1)}}{v_h^2}\,(\overline{L}\gamma_\mu L)(\overline{Q}\gamma^\mu Q) + \frac{\mathcal{C}_{lq}^{(3)}}{v_h^2}\,(\overline{L}\gamma_\mu \sigma^a L)(\overline{Q}\gamma^\mu \sigma^a Q) \\ & + \frac{\mathcal{C}_{lu}}{v_h^2}\,(\overline{L}\gamma_\mu L)(\overline{U}\gamma^\mu U) + \frac{\mathcal{C}_{ld}}{v_h^2}\,(\overline{L}\gamma_\mu L)(\overline{D}\gamma^\mu D)\,,\end{aligned} \tag{9.8}$$

where $\sigma^a$ are Pauli matrices and $v_h$ denotes the Higgs vev. We have suppressed the flavour indices of the SU(2)$_L$-doublet leptons $L$ and quarks $Q$ as well as the RH up-singlet (down-singlet) quarks $U$ ($D$) to avoid clutter. We remark that operators featuring charged lepton singlets $E$, such as $(\overline{Q}\gamma_\mu Q)(\overline{E}\gamma^\mu E)$, are disconnected from the dineutrino processes and break the relation $\mathcal{C}_9 = -\mathcal{C}_{10}$ in WET. Additional operators that induce $Z$-penguins at tree level, such as $(\overline{Q}\gamma_\mu Q)(H^\dagger D^\mu H)$ involving two Higgs fields $H$ and a covariant derivate $D^\mu$, are constrained by, *e.g.*, electroweak and top observables [208, 209]. They are negligible for the purpose of our investigations. Therefore, the (axial-)vector operators in Eq. (9.8) provide a suitable model-independent basis for the description of dineutrino modes due to their invariance under QCD-evolution [210], while corrections from electroweak RG running [211] are not significant, see Ref. [20] for details.

By splitting the operators in Eq. (9.8) into SU(2)$_L$-components, we derive the following link between the couplings to dineutrinos ($C_A^P$) and to charged dileptons ($K_A^P$) in the gauge basis

$$\begin{aligned} C_L^U = K_L^D &= \frac{2\pi}{\alpha_e}\left(\mathcal{C}_{lq}^{(1)} + \mathcal{C}_{lq}^{(3)}\right)\,, \quad C_R^U = K_R^U = \frac{2\pi}{\alpha_e}\mathcal{C}_{lu}\,, \\ C_L^D = K_L^U &= \frac{2\pi}{\alpha_e}\left(\mathcal{C}_{lq}^{(1)} - \mathcal{C}_{lq}^{(3)}\right)\,, \quad C_R^D = K_R^D = \frac{2\pi}{\alpha_e}\mathcal{C}_{ld}\,. \end{aligned} \tag{9.9}$$

A one-to-one map between the dineutrino and dilepton Wilson coefficients is realised for RH quark currents, $C_R^{U,D} = K_R^{U,D}$ in *both* up-quark and down-quark sectors. In contrast, we obtain $C_L^D = K_L^U$ and $C_L^U = K_L^D$ in the gauge basis for the LH quark currents, due to the relative minus signs between $\mathcal{C}_{lq}^{(1)}$ and $\mathcal{C}_{lq}^{(3)}$. This SU(2)$_L$-link in the gauge basis is visualised in Fig. 9.1.

Appropriate field rotations are necessary to express $K_L^P$ and $C_L^P$ in the mass basis, which are denoted by calligraphic $\mathcal{K}_A^P$ and $\mathcal{C}_A^P$ included in Eq. (9.2) and Eq. (9.3), respectively. Employing the unitary rotations introduced in Eq. (2.21), we obtain the relations

$$\mathcal{C}_R^P = (U_{\text{PMNS}})^\dagger\ \mathcal{K}_R^P\, U_{\text{PMNS}}\,, \tag{9.10}$$

$$\mathcal{C}_L^P = (U_{\text{PMNS}})^\dagger\ \mathcal{K}_L^{P'}\, U_{\text{PMNS}} + \mathcal{O}\left(\lambda_{\text{CKM}}\right), \tag{9.11}$$

where $U_{\text{PMNS}}$ is the PMNS matrix, and $P = U, D$ for $P' = D, U$. By summing over the lepton flavours $i$, $j$ incoherently, as put forward in Eq. (9.1), a link between the couplings $\mathcal{C}_A^P$ and $\mathcal{K}_R^P$ is established [18]

$$\begin{aligned} &\sum_{\nu=i,j}\left(|\mathcal{C}_L^{Pij}|^2 + |\mathcal{C}_R^{Pij}|^2\right) \\ = \text{tr}\left(\mathcal{C}_L^P\ \left(\mathcal{C}_L^P\right)^\dagger + \mathcal{C}_R^P\ \left(\mathcal{C}_R^P\right)^\dagger\right) &= \text{tr}\left(\mathcal{K}_L^P\ \left(\mathcal{K}_L^{P'}\right)^\dagger + \mathcal{K}_L^P\ \left(\mathcal{K}_R^P\right)^\dagger\right) + \mathcal{O}\left(\lambda_{\text{CKM}}\right) \\ &= \sum_{\ell=i,j}\left(|\mathcal{K}_L^{P'ij}|^2 + |\mathcal{K}_R^{Pij}|^2\right) + \mathcal{O}\left(\lambda_{\text{CKM}}\right). \end{aligned} \tag{9.12}$$

Further details on this SU(2)$_L$-link and the incorporated flavour rotations and assumptions are

collected in App. G.

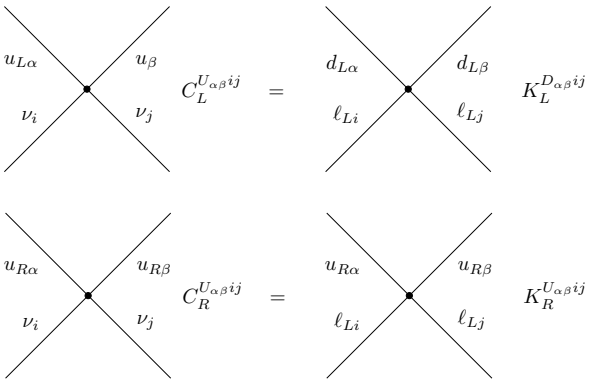


**Figure 9.1:** Diagrams that display the NP contributions to up- and down-quark transitions with dineutrinos $C^U_{L,R}$ and dileptons $K^D_{L,R}$, from the operators in Eq. (9.8) in the gauge basis, with flavour indices $\alpha$, $\beta$, $i$, $j$. The $\mathrm{SU}(2)_L$-link between neutrino and charged lepton operators is exploited in Eq. (9.12) in the mass basis. *Figure taken from Ref.* [18].

Equation (9.12) provides the unique possibility to predict dineutrino rates for different lepton flavour structures $\mathcal{K}^{Pij}_{L,R}$, which can be probed with lepton-specific measurements. We determine the following structures

- lepton flavour universality (LFU) or equivalently called just lepton universality (LU):

$$\mathcal{K}^P_{L,R} = \begin{pmatrix} k & 0 & 0 \\ 0 & k & 0 \\ 0 & 0 & k \end{pmatrix} , \tag{9.13}$$

- charged lepton flavour conservation (cLFC):

$$\mathcal{K}^P_{L,R} = \begin{pmatrix} k_{ee} & 0 & 0 \\ 0 & k_{\mu\mu} & 0 \\ 0 & 0 & k_{\tau\tau} \end{pmatrix} , \tag{9.14}$$

- general, including charged lepton flavour violation (cLFV):

$$\mathcal{K}^P_{L,R} = \begin{pmatrix} k_{ee} & k_{e\mu} & k_{e\tau} \\ k_{\mu e} & k_{\mu\mu} & k_{\mu\tau} \\ k_{\tau e} & k_{\tau\mu} & k_{\tau\tau} \end{pmatrix} . \tag{9.15}$$

## 9.2 Correlations of different flavour sectors

In the following, we explore the rich playground of dineutrino modes using the $\mathrm{SU}(2)_L$-link in Eq. (9.12). The differential branching ratio of dineutrino modes can be written as

$$\frac{\mathrm{d}\mathcal{B}\,(q' \to q\,\nu\bar{\nu})}{\mathrm{d}q^2} = a_+(q^2)\,x_P^+ + a_-(q^2)\,x_P^-\,, \tag{9.16}$$

which is related to the final state hadron's energy distribution in the initial state hadron rest frame as $\mathrm{d}\mathcal{B}/\mathrm{d}q^2 = 1/(2\,m_M)\,\mathrm{d}\mathcal{B}/\mathrm{d}E$. Here, $m_M$ denotes the mass of the initial state hadron and $q^2$ indicates the dineutrino invariant mass squared. In Eq. (9.16), the factors $a_\pm(q^2)$ are decay mode specific. and include the form factors and kinematics of the respective decay, see, *e.g.*, Refs. [19, 20] for definitions. Consequently, all branching ratios depend on at most two combinations of Wilson coefficients that can be chosen as

$$x_P^\pm = \sum_{i,j} |\mathcal{C}_L^{Pij} \pm \mathcal{C}_R^{Pij}|^2\,. \tag{9.17}$$

Here, it proves useful to define the quantity

$$x_P = \frac{x_P^+ + x_P^-}{2} = \sum_{i,j} \left(|\mathcal{C}_L^{Pij}|^2 + |\mathcal{C}_R^{Pij}|^2\right)\,, \quad x_P^\pm \leq 2\,x_P\,, \tag{9.18}$$

which for instance enters in inclusive decays. The integrated branching ratio of dineutrino modes is readily obtained as

$$\mathcal{B}\,(q' \to q\,\nu\bar{\nu}) = A_+\,x_P^+ + A_-\,x_P^-\,, \tag{9.19}$$

with

$$A_\pm = \int_{q^2_{\mathrm{min}}}^{q^2_{\mathrm{max}}} a_\pm(q^2)\,\mathrm{d}q^2\,, \tag{9.20}$$

where $q^2_{\mathrm{min}}$ and $q^2_{\mathrm{max}}$ denote the allowed kinematic range which depends on the specific decay mode, *e.g.* $q^2_{\mathrm{min}} = 0$ and $q^2_{\mathrm{max}} = (m_{B^0} - m_{K^0})^2$ for the exclusive $B^0 \to K^0\nu\bar{\nu}$ decay. In Tab. 9.3, we provide central values of $A_\pm$ with their symmetrised uncertainties for selected $b\to s$ decay modes. Interestingly, $A_- = 0$ for decays into pseudoscalar mesons $B \to P$, while $A_+ \ll A_-$ for vector mesons $B \to V$. Moreover, the relation $A_+ = A_-$ holds in inclusive $B \to X_{(s)}$ decays. This complementarity between different decay modes is a result of parity conservation in the strong interaction as well as Lorentz invariance. It can be exploited for instance to construct tests of LU, see Sec. 9.3.

We discuss the implications of the $\mathrm{SU}(2)_L$-link for charm and beauty dineutrino modes in Secs. 9.2.1 and 9.2.2, respectively.

### 9.2.1 Predictions for charm

Due to the efficient GIM-cancellation in charm decays, the SM amplitude of $c\to u$ dineutrino transitions is perfectly negligible and therefore constitutes a clean null test of the SM. Recently,

| $D^0 \to F$ | $A_+$ $[10^{-8}]$ | $A_-$ $[10^{-8}]$ | $\mathcal{B}^{\max}_{\text{LU}}$ $[10^{-7}]$ | $\mathcal{B}^{\max}_{\text{cLFC}}$ $[10^{-6}]$ | $\mathcal{B}^{\max}$ $[10^{-6}]$ | $N^{\max}_{\text{LU}}/\eta_{\text{eff}}$ | $N^{\max}_{\text{cLFC}}/\eta_{\text{eff}}$ | $N^{\max}/\eta_{\text{eff}}$ |
|---|---|---|---|---|---|---|---|---|
| $D^0 \to \pi^0$ | 0.9 | 0 | 6.1 | 3.5 | 13 | 47 k (395 k) | 270 k (2.3 M) | 980 k (8.3 M) |
| $D^0 \to \pi^0\pi^0$ | $0.7 \cdot 10^{-3}$ | 0.21 | 1.5 | 0.8 | 3.1 | 11 k (95 k) | 64 k (540 k) | 230 k (2.0 M) |
| $D^0 \to \pi^+\pi^-$ | $1.4 \cdot 10^{-3}$ | 0.41 | 2.8 | 1.6 | 5.9 | 22 k (180 k) | 120 k (1.0 M) | 450 k (3.8 M) |
| $D^0 \to K^+K^-$ | $4.7 \cdot 10^{-6}$ | 0.004 | 0.03 | 0.02 | 0.06 | 0.2 k (1.9 k) | 1.3 k (11 k) | 4.8 k (40 k) |

**Table 9.1:** Coefficients $A_\pm$ as defined in Eq. (9.20) for selected $D^0$-meson decays into final states $F$ for central values of input [19]. Utilising Eq. (9.19), we provide the upper limits on branching ratios $\mathcal{B}^{\max}_{\text{LU}}$, $\mathcal{B}^{\max}_{\text{cLFC}}$ and $\mathcal{B}^{\max}$ corresponding to Eqs. (9.23) to (9.25), respectively. The expected number of events, see Eq. (9.22), per reconstruction efficiency $\eta_{\text{eff}}$ for Belle II with $50\,\text{ab}^{-1}$ (FCC-ee yields in parentheses) are given in the last three columns. *Table taken from Ref.* [19].

the BES III experiment performed the first experimental search of the $c \to u\,\nu\bar{\nu}$ process, where the upper limit [212]

$$\mathcal{B}\left(D^0 \to \pi^0\,\nu\bar{\nu}\right) < 2.1 \cdot 10^{-4} \tag{9.21}$$

at 90 % C.L. has been obtained. Current experiments like BES III [202], Belle II [85] as well as other future $e^+e^-$-colliders such as the FCC-ee [203] are perfect for analyses of the corresponding missing energy modes, with charm production rates from $\mathcal{B}\,(Z \to c\bar{c}) \simeq 0.12$ [32] for the latter. More quantitatively, we can parametrise the expected event rate for a decay $h_c \to F\,\nu\bar{\nu}$, with a charged hadron $h_c$ and final state $F$, as

$$N_F^{\text{exp}} = \eta_{\text{eff}}\,N(h_c)\,\mathcal{B}\,(h_c \to F\,\nu\bar{\nu})\ , \tag{9.22}$$

where $\eta_{\text{eff}}$ denotes the reconstruction efficiency. The number of charmed hadrons $N(h_c)$ can be fetched from Tab. G.8 with expected magnitudes of $\mathcal{O}\left(10^{10}\right)$.

Utilising the $\text{SU}(2)_L$-link in Eq. (9.12) together with data on the charged lepton couplings $\mathcal{K}_L^{sd\ell\ell'}$ and $\mathcal{K}_R^{cu\ell\ell'}$, we are able to computed upper limits on the quantity $x_{cu} \equiv x_{U_{12}}$. Here, we have adapted the notation $U_{12} \equiv cu$ and $D_{12} \equiv sd$, while also $i,j \to \ell,\ell'$ is understood. We employ high-$p_{\text{T}}$ data provided in Tabs. G.1 and G.2 to obtain the upper limits [19]

$$x_{cu} \lesssim 34 \quad (\text{LU})\,, \tag{9.23}$$

$$x_{cu} \lesssim 196 \quad (\text{cLFC})\,, \tag{9.24}$$

$$x_{cu} \lesssim 716 \quad (\text{general})\,, \tag{9.25}$$

assuming the inherent flavour structures of the lepton couplings, see Eqs. (9.13) to (9.15), in each of those limits. Notably, we have included the $\mathcal{O}\,(\lambda_{\text{CKM}})$ corrections in Eq. (9.12), where an explicit derivation of the upper limits is provided in App. G.3. We remark that more stringent bounds are obtained when including data from rare kaon decays in addition to those from (high-$p_{\text{T}}$) Drell-Yan processes. However, they are subject to cancellations and may not be considered fully model-independent. We focus on the bounds given in Eqs. (9.23) to (9.25) for our subsequent studies, whereas limits also including low energy constraints are listed in App. G.4.

In Fig. 9.2, we display the resulting upper bounds on selected charm dineutrino branching ratios, employing Eq. (9.19) together with $x_{cu}^{\pm} \leq 2\,x_{cu}$. The corresponding $A_\pm$ factors as well as the maximal branching ratio for the specific flavour structures denoted by $\mathcal{B}^{\max}_{\text{LU}}$, $\mathcal{B}^{\max}_{\text{cLFC}}$, and $\mathcal{B}^{\max}$

are provided in Tab. 9.1. In Fig. 9.2, we additionally show the relative statistical uncertainty $\delta\mathcal{B} = 1/\sqrt{\eta_{\text{eff}}\, N(h_c)\, \mathcal{B}}$ against the branching ratio $\mathcal{B}$, where the former scales as $1/\sqrt{N_F^{\text{exp}}}$, for Belle II (green region) and FCC-ee (lilac region). We choose $\eta_{\text{eff}} = 10^{-3}$ as a benchmark efficiency shown as tilted lines, whereas the left-most boundaries of the respective regions correspond to the ideal, no loss case $\eta_{\text{eff}} = 1$. All relevant values of $N_F^{\text{exp}}$ are listed in Tab. 9.1. We find that for efficiencies of a permille or better, branching ratios of $\mathcal{O}\left(10^{-6}\right)$ down to $\mathcal{O}\left(10^{-8}\right)$ can be discovered at $5\,\sigma$ (that is $\delta\mathcal{B} = 1/5$) in $D^0$-modes. Similar yields are obtained for other charm modes given elsewhere [19]. Certainly, given corroborated estimates of $\eta_{\text{eff}}$ and reduced systematic uncertainties in the future, the reach of future measurements at charm factories can be worked out more quantitatively. However, regions with branching ratios $\mathcal{O}\left(10^{-6}\text{-}10^{-5}\right)$ already cover interesting physics as can be inferred from the computed maximal branching ratio limits. We observe that all limits shown here are above $\sim 10^{-6}$, except for $D^0 \to K^+K^-\,\nu\bar{\nu}$. Notably, the branching ratio $\mathcal{B}^{\text{max}}(D^0 \to \pi^0\,\nu\bar{\nu}) = 1.3 \cdot 10^{-5}$ is only one order of magnitude smaller than the available experimental limit, see Eq. (9.21).

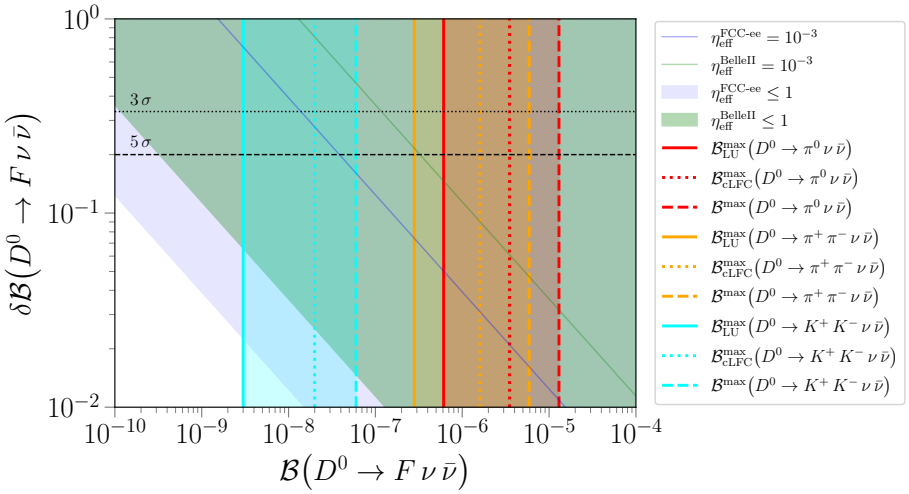


**Figure 9.2:** Relative statistical uncertainty of the branching ratio $\delta\mathcal{B}$ versus the branching ratio $\mathcal{B}$ for dineutrino decays of the $D^0$ meson. The shaded areas correspond to the reach of the reconstruction efficiency $\eta_{\text{eff}} = 1$, while the solid tilted lines depict the impact of $\eta_{\text{eff}} = 10^{-3}$ for FCC-ee (lilac) and Belle II (green). Horizontal $3\,\sigma$ (dotted) and $5\,\sigma$ (dashed) black lines illustrate $\delta\mathcal{B} = 1/3$ and $\delta\mathcal{B} = 1/5$, respectively. Vertical lines represent upper limits assuming LU (solid), cLFC (dotted) and generic lepton flavour (dashed) for decay modes, compiled in Tab. 9.1. To improve readability, the three lines for each decay mode are grouped together by a shaded band. *Figure adapted from Ref.* [19].

The upper limits satisfy $\mathcal{B}_{\text{LU}}^{\text{max}} < \mathcal{B}_{\text{cLFC}}^{\text{max}} < \mathcal{B}^{\text{max}}$, and we can therefore infer that, *e.g.*, a branching ratio measurement $\mathcal{B}_{\text{exp}}$ in some mode with $\mathcal{B}_{\text{LU}}^{\text{max}} < \mathcal{B}_{\text{exp}} < \mathcal{B}_{\text{cLFC}}^{\text{max}}$ would be an indication of LU violation. In contrast, a breakdown of cLFC is inferred by a branching ratio above $\mathcal{B}_{\text{cLFC}}^{\text{max}}$.

### Reach of $Z'$ models in charm dineutrino modes

Specific BSM extensions, such as leptoquarks or $Z'$ scenarios, feature a generic alignment between the Wilson coefficients in the gauge basis

$$\begin{aligned} &\mathcal{C}_{lq}^{(3)} = \alpha\, \mathcal{C}_{lq}^{(1)}\,, \\ &K_L^D = \gamma\, C_L^D = (1+\alpha)\left(\frac{2\pi}{\alpha_e}\right)\mathcal{C}_{lq}^{(1)}\,, \quad K_L^U = \frac{1}{\gamma}\, C_L^U = (1-\alpha)\left(\frac{2\pi}{\alpha_e}\right)\mathcal{C}_{lq}^{(1)}\,, \end{aligned} \tag{9.26}$$

where $\gamma = (1+\alpha)/(1-\alpha)$. In $Z'$ models, where $\alpha = 0$ (hence $\gamma = 1$), the Eq. (9.26) can be simplified to

$$K_L^{U,D} = C_L^{U,D}\,. \tag{9.27}$$

Similar results and implications arise for leptoquark representations [19]. In particular, for $c \to u$ transitions it holds

$$x_{cu}^{Z'} < \sum_{i,j}\left(|\mathcal{K}_R^{U_{12}ij}|^2 + |\mathcal{K}_L^{U_{12}ij}|^2\right)\,. \tag{9.28}$$

utilising the bounds on charged lepton couplings from high-$p_{\mathrm{T}}$ data, we obtain

$$x_{cu}^{Z'} \lesssim 15 \quad (\mathrm{LU})\,, \tag{9.29}$$

$$x_{cu}^{Z'} \lesssim 85 \quad (\mathrm{cLFC})\,, \tag{9.30}$$

$$x_{cu}^{Z'} \lesssim 288 \quad (\mathrm{general})\,, \tag{9.31}$$

which are stronger than the model-independent limits in Eqs. (9.23) to (9.25), nevertheless within the same order of magnitude. The resulting upper limits on dineutrino branching ratios follow the same reasoning and are compiled in Tab. 9.2.

| | $Z'$ models: $K_L^U = C_L^U$ | | |
|---|---|---|---|
| $h_c \to F$ | $\mathcal{B}_{\mathrm{LU}}^{\mathrm{max}}$ $[10^{-7}]$ | $\mathcal{B}_{\mathrm{cLFC}}^{\mathrm{max}}$ $[10^{-6}]$ | $\mathcal{B}^{\mathrm{max}}$ $[10^{-6}]$ |
| $D^0 \to \pi^0$ | 2.7 | 1.5 | 5.1 |
| $D^0 \to \pi^0\pi^0$ | 0.6 | 0.4 | 1.2 |
| $D^0 \to \pi^+\pi^-$ | 1.2 | 0.7 | 2.4 |
| $D^0 \to K^+K^-$ | 0.01 | 0.007 | 0.03 |

**Table 9.2:** Upper limits $\mathcal{B}_{\mathrm{LU}}^{\mathrm{max}}$, $\mathcal{B}_{\mathrm{cLFC}}^{\mathrm{max}}$ and $\mathcal{B}^{\mathrm{max}}$ extracted from the LU, cLFC and general bounds on $x_{cu}^{Z'}$ in Eqs. (9.29) to (9.31), respectively, see Eq. (9.19). *Table taken from Ref.* [19].

## 9.2.2 Predictions for beauty

To study the phenomenological implications in the $B$-sector, it is convenient to utilise the following notation,

$$\mathcal{K}_{A,\,\mathrm{NP}}^{U_{23}} = \mathcal{K}_A^{tc}\,, \quad \mathcal{K}_{A,\,\mathrm{NP}}^{D_{23}} = \mathcal{K}_A^{bs}\,, \quad \mathcal{K}_{A,\,\mathrm{NP}}^{U_{13}} = \mathcal{K}_A^{tu}\,, \quad \mathcal{K}_{A,\,\mathrm{NP}}^{D_{13}} = \mathcal{K}_A^{bd}\,. \tag{9.32}$$

| Mode | $A_+$ | $A_-$ | $\mathcal{B}\,(\text{Mode})_{\text{SM}}$ | $\mathcal{B}\,(\text{Mode})_{\text{exp}}$ upper limit | derived EFT limit | Belle II @ $5\,\text{ab}^{-1}$ ($50\,\text{ab}^{-1}$) |
|---|---|---|---|---|---|---|
| | $[10^{-8}]$ | $[10^{-8}]$ | $[10^{-8}]$ | $[10^{-6}]$ | $[10^{-6}]$ | % |
| $B^0 \to K^0$ | $516 \pm 68$ | 0 | $391 \pm 52$ | 26 [213] | 15 | – |
| $B^+ \to K^+$ | $558 \pm 74$ | 0 | $423 \pm 56$ | 16 [214] | $16^i$ | 30 (11) |
| $B^0 \to K^{*0}$ | $200 \pm 29$ | $888 \pm 108$ | $824 \pm 99$ | 18 [213] | $18^i$ | 26 (9.6) |
| $B^+ \to K^{*+}$ | $217 \pm 32$ | $961 \pm 116$ | $893 \pm 107$ | 40 [215] | 19 | 25 (9.3) |
| $B_s \to \phi$ | $184 \pm 9$ | $1110 \pm 85$ | $981 \pm 69$ | 5400 [216] | 23 | – |
| $B^0 \to X_s$ | $1834 \pm 193$ | $1834 \pm 193$ | $2800 \pm 300$ | 640 [216] | 78 | – |
| $B^+ \to X_s$ | $1978 \pm 208$ | $1978 \pm 208$ | $3000 \pm 300$ | 640 [216] | 84 | – |

**Table 9.3:** SM predictions of dineutrino branching ratios of $B \to K\nu\bar{\nu}$ and $B \to K^*\nu\bar{\nu}$ decays, as well as related modes with underlying $b \to s\,\nu\bar{\nu}$ transition. Also provided are the $A_\pm$ parameters [21], see Eq. (9.19), and the current experimental upper limits on the branching ratio at 90% C.L. in the fifth column. Derived EFT limits using Eq. (9.35) are displayed in the sixth column, while projected Belle II sensitivities [85] for $5\,\text{ab}^{-1}$ ($50\,\text{ab}^{-1}$) are given in the last column. The superscript $i$ denotes limits used as input in Eq. (9.35). *Table adapted from Ref.* [21].

This highlights the respective quark transition and eases the notation of the dilepton couplings, where we have omitted the subscript 'NP'. In addition, we reduce clutter by using rescaled versions of these quantities

$$\kappa_R^{bqij} = \mathcal{K}_R^{bqij} \cdot \left(V_{tb}\, V_{tq}^*\right)^{-1} , \quad \kappa_L^{tcij} = \mathcal{K}_L^{tcij} \cdot \left(V_{tb} V_{ts}^*\right)^{-1} , \quad \kappa_L^{tuij} = \mathcal{K}_L^{tuij} \cdot \left(V_{tb} V_{td}^*\right)^{-1} , \tag{9.33}$$

where the dependence of the CKM matrix elements has been factorised. Similar changes in notation can be implemented for the corresponding dineutrino Wilson coefficients.

In Tab. 9.3, we summarise the SM branching ratios for selected $b \to s$ modes that are computed using Eq. (9.19). In this case, Eq. (9.17) reads

$$x_{bs}^{\pm} = \sum_{i,j} |\mathcal{C}_{L,\text{SM}}^{bsij} + \mathcal{K}_L^{tcij} \pm \mathcal{K}_R^{bsij}|^2 . \tag{9.34}$$

Here, we have inserted the connected dilepton couplings, neglecting $\mathcal{O}\left(\lambda_{\text{CKM}}^2\right)$ corrections that stem from the $\text{SU}(2)_L$-link in Eq. (9.12). Different sensitivities of Wilson coefficients in $x_\pm$ enter the branching ratio parametrisation given in Eq. (9.19) for $B \to P\,\nu\bar{\nu}$, $B \to V\,\nu\bar{\nu}$, and inclusive $B \to X_s\,\nu\bar{\nu}$ decays. This fact can be exploited by using current experimental upper limits to constrain

$$x_{bs}^+ \lesssim 2.9 , \quad x_{bs}^- + 0.2\, x_{bs}^+ \lesssim 2.0 , \tag{9.35}$$

extracted from the experimental limits on $B^+ \to K^+\nu\bar{\nu}$ and $B^0 \to K^{*0}\nu\bar{\nu}$, see Tab. 9.3. Using Eq. (9.35), we find indirect limits on the branching ratios of *other* dineutrino modes that hold within our EFT framework. Exemplary EFT limits are collected in Tab. 9.3 for selected decay modes, that is $B \to K^{(*)}\nu\bar{\nu}$, $B_s \to \phi\nu\bar{\nu}$ and inclusive $B \to X_s\nu\bar{\nu}$ decays. An extended list that also involves decay modes with underlying $b \to d$ transitions is provided in Ref. [21]. We note that a

| $bs\,\ell\ell'$ | $ee$ | $\mu\mu$ | $\tau\tau$ | $e\mu$ | $e\tau$ | $\mu\tau$ |
|---|---|---|---|---|---|---|
| $\lvert\kappa_{L,R}^{bs\ell\ell'}\rvert_{\rm DY}$ | 331 | 178 | 637 | 200 | 688 | 748 |
| $\kappa_L^{bs\ell\ell'}$ | 1 | $[-1.6, -1.1]$ | 806 | 2.5 | 71 | 86 |
| $\kappa_R^{bs\ell\ell'}$ | 1 | $[0.2, 0.8]$ | 806 | 2.5 | 71 | 86 |
| $\lvert\kappa_R^{bs\ell\ell'}\rvert_{\nu\bar{\nu}}$ | 35 | 35 | 35 | 45 | 45 | 45 |

**Table 9.4:** Upper limits on charged dilepton couplings $\kappa_{L,R}^{bs\ell\ell'}$ from high–$p_T$ [183, 217] (top row), charged dilepton $B$-decays (mid rows) and derived ones from three-body rare $B$-decays to dineutrinos (bottom row). Numbers without ranges correspond to a limit on the modulus. The $\mu\mu$ ranges are derived from the global fit results of Ref. [20], see Sec. 4.2 and Tab. 4.1 for details, with the departures from zero in $\mathcal{K}_L^{bs\mu\mu}$ corresponding to the $B$-anomalies. The LFV-bounds are quoted as flavour-summed, $\sqrt{|\kappa^{\ell^+\ell'^-}|^2 + |\kappa^{\ell^-\ell'^+}|^2}$, whereas the other bounds are for a single coupling. Corresponding rescaled values for couplings $\mathcal{K}_{L,R}^{bs\mu\mu} = V_{tb}V_{ts}^*\,\kappa_{L,R}^{bs\mu\mu}$ are given in Tab. G.3 for completion. *Table entries taken from Refs.* [20, 21].

violation of these limits would be a sign of NP which is not embedded in our EFT description, such as light BSM particles.

In the following, we study the impact of the dineutrino limits on flavour-specific charged dilepton couplings. Afterwards, we compare them with direct limits extracted from high-$p_{\rm T}$ data and rare $B$-decays to charged leptons. The bound in Eq. (9.35) can be rewritten in terms of the rescaled couplings $\kappa_L^{tcij}$ and $\kappa_R^{bsij}$, see Eq. (9.33), which yields

$$\sum_{i,j} |X_{\rm SM}\,\delta_{ij} + \kappa_L^{tcij} + \kappa_R^{bsij}|^2 \lesssim 1.8\cdot 10^3\,, \quad \sum_{i,j} |X_{\rm SM}\,\delta_{ij} + \kappa_L^{tcij} - \kappa_R^{bsij}|^2 \lesssim 1.3\cdot 10^3\,. \tag{9.36}$$

By assuming different lepton flavour structures we can utilise Eq. (9.36) to obtain limits on $\kappa_L^{tcij}$ and $\kappa_R^{bsij}$. For the three dedicated scenarios (LU, cLFC, and a general flavour structure) we obtain the constraints [21]

$$\begin{aligned} \text{LU}: &\quad |\kappa_R^{bs\ell\ell}| \lesssim 23\,, &\quad -10 \lesssim\ & \kappa_L^{tc\ell\ell} \lesssim 35\,, \\ \text{cLFC}: &\quad |\kappa_R^{bs\ell\ell}| \lesssim 35\,, &\quad -22 \lesssim\ & \kappa_L^{tc\ell\ell} \lesssim 47\,, \\ \text{general}: &\quad |\kappa_R^{bs\ell\ell'}| \lesssim 32\,, & & |\kappa_L^{tc\ell\ell'}| \lesssim 32\,, \end{aligned} \tag{9.37}$$

assuming real-valued couplings. A comprehensive list that incorporates the various limits on the couplings $\kappa_L^{bs\ell\ell'}$ is given in Tab. 9.4, where the limits in Eq. (9.37) are displayed in the bottom row. Bounds extracted from Drell-Yan data and rare $B$-decays to charged leptons are given in the top row and middle rows, respectively. Note that we quote the LFV-bounds as flavour-summed, where the limits obtained in the general case (allowing for cLFV) in Eq. (9.37) are scaled as $|\kappa_R^{bs\ell\ell'}|_{\nu\bar{\nu}} = \sqrt{32^2 + 32^2} \approx 45$. The bounds from (semi)leptonic rare $B$-decays are computed using `flavio` [91] with experimental upper limits taken from Ref. [32], assuming one coupling at a time, $|\mathcal{C}_9| = |\mathcal{C}_{10}| = \kappa_L/2$ or $|\mathcal{C}'_9| = |\mathcal{C}'_{10}| = \kappa_R/2$. Supplementary tables that list upper limits on charged dilepton couplings $\mathcal{K}_{L,R}$ for other quark transitions can be found in App. G.2. We observe that limits on couplings with dimuons $\kappa_{L,R}^{bs\mu\mu}$ from charged $B$-decays are the strongest, which have been extracted from our global fit to $b\to s$ data, see Sec. 9.3. Moreover, the bounds from dineutrinos surpass the ones obtained via the direct dilepton data for $\tau\tau$ as well as $e\tau$ and $\mu\tau$ by a factor of 23, 2, and 2, respectively, whereas weaker constraints follow for $ee$ and $e\mu$. Comparing our findings to Drell-Yan data, the dineutrino bounds on $\kappa_{L,R}^{bs\ell\ell'}$ are a factor of 4 or more stronger (depending on

the coupling) than those from high-$p_{\rm T}$. Similar results follows for limits on $\kappa_{L,R}^{bd\ell\ell'}$ couplings [21].

Since the SU(2)$_L$-link enables us to extract limits on LH top couplings $\kappa_L^{tc\ell\ell'}$ as well, we can compare such limits to those obtained by the 2021 analysis of CMS [218] with top quark productions plus leptons (admixture of dielectrons and dimuons), $\kappa_L^{tt\ell\ell} = [-196, 243]$, with $\ell = e, \mu$. Assuming a top-philic flavour pattern [219] with FCNC couplings in the down mass basis we find $\kappa_L^{tc\ell\ell} \sim V_{tb}V_{ts}^*\,\kappa_L^{tt\ell\ell} = [-8, 10]$ somewhat stronger than the corresponding dineutrino limits, $\kappa_L^{tc\ell\ell} = [-22, 47]$. However, those limits from dineutrinos are available for all flavours $\ell\ell'$, as opposed to collider limits from CMS, which are limited to $ee$ and $\mu\mu$ only.

## 9.3 Universality tests with $b\to s\,\nu\bar{\nu}$ transitions

As the SU(2)$_L$-link is bidirectional, we can utilise data of charged dileptons to obtain bounds on dineutrino modes. In what follows, we provide tests of lepton universality, where we focus on $B\to K\nu\bar{\nu}$ and $B\to K^*\nu\bar{\nu}$ decays, featuring an underlying $b\to s$ transition.

In the LU limit, the branching ratio in Eq. (9.19) can be parametrised as

$$\mathcal{B}\left(B\to K\nu\bar{\nu}\right)_{\rm LU} = A_+^{BK}\, x_{bs,\rm LU}^+\,, \tag{9.38}$$

$$\mathcal{B}\left(B\to K^*\nu\bar{\nu}\right)_{\rm LU} = A_+^{BK^*}\, x_{bs,\rm LU}^+ + A_-^{BK^*}\, x_{bs,\rm LU}^-\,, \tag{9.39}$$

with $x_{bs,\rm LU}^\pm = 3|V_{tb}V_{ts}^*|^2\left(X_{\rm SM} + \kappa_L^{tc\ell\ell} \pm \kappa_R^{bs\ell\ell}\right)^2$ and $\ell$ fixed to the flavour with the strongest constraints. As present rare top data is not able to put useful constraints on the couplings $\kappa_L^{tc\ell\ell}$ [18], we instead solve $\mathcal{B}\left(B\to K\nu\bar{\nu}\right)_{\rm LU}$ in Eq. (9.38) for this coupling and insert the two solutions into Eq. (9.39). This yields a correlation between the branching ratios,

$$\begin{aligned}\mathcal{B}\left(B\to K^*\nu\bar{\nu}\right)_{\rm LU} = {}& \frac{A_+^{BK^*}}{A_+^{BK}}\,\mathcal{B}\left(B\to K\nu\bar{\nu}\right)_{\rm LU} \\ & + 3\,A_-^{BK^*}\,|V_{tb}V_{ts}^*|^2\left(\sqrt{\frac{\mathcal{B}\left(B\to K\nu\bar{\nu}\right)_{\rm LU}}{3\,|V_{tb}V_{ts}^*|^2\,A_+^{BK}}} \mp 2\,\kappa_R^{bs\ell\ell}\right)^2\,,\end{aligned} \tag{9.40}$$

which holds for any combination of charged and/or neutral decay modes with appropriate substitution of the parameters $A_\pm$, see Tab. 9.3.

As the most stringent limits on $\kappa_R^{bs\ell\ell}$ are given for $\ell = \mu$, we utilise the global fit approach outlined in Chap. 4. In the following, we consider the 6d fit results of the NP Wilson coefficients $\mathcal{C}_{(7,9,10),\mu}^{(\prime)}$ listed in Tab. 4.1 where only pure $b\to s$ data has been included. Matching to the dineutrino basis, we find

$$\begin{aligned}\kappa_L^{bs\mu\mu} &= \mathcal{C}_{9,\mu} - \mathcal{C}_{10,\mu} = -1.45 \pm 0.29\,,\\ \kappa_R^{bs\mu\mu} &= \mathcal{C}'_{9,\mu} - \mathcal{C}'_{10,\mu} = \phantom{-}0.46 \pm 0.26\,,\end{aligned} \tag{9.41}$$

with an deviation from the SM hypothesis, $\kappa_{L,R}^{bs\mu\mu} = 0$, at $4.6\,\sigma$.

We use Eqs. (9.40) and (9.41) to display the correlations between $\mathcal{B}\left(B^0\to K^{*0}\nu\bar{\nu}\right)$ versus $\mathcal{B}\left(B^0\to K^0\nu\bar{\nu}\right)$ and $\mathcal{B}\left(B^0\to K^{*0}\nu\bar{\nu}\right)$ versus $\mathcal{B}\left(B^+\to K^+\nu\bar{\nu}\right)$ shown in the left-hand and right-

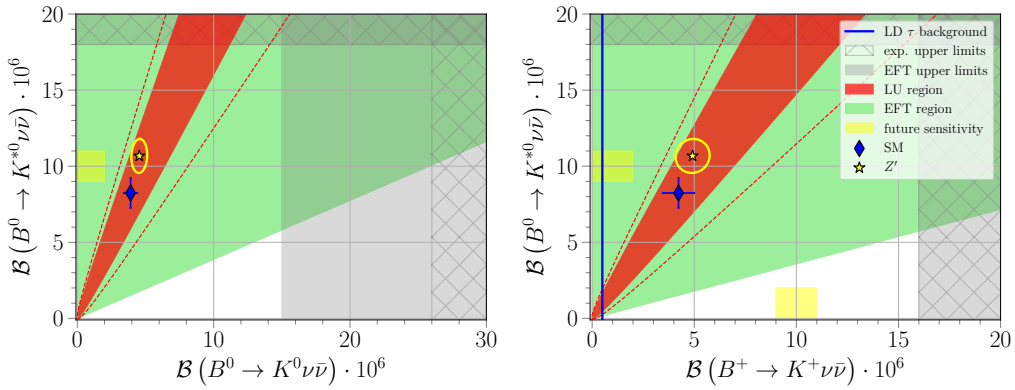


**Figure 9.3:** $\mathcal{B}\left(B^0 \to K^{*0}\nu\bar{\nu}\right)$ versus $\mathcal{B}\left(B^0 \to K^0\nu\bar{\nu}\right)$ (left-hand side plot) and $\mathcal{B}\left(B^0 \to K^{*0}\nu\bar{\nu}\right)$ versus $\mathcal{B}\left(B^+ \to K^+\nu\bar{\nu}\right)$ (right-hand side plot). SM predictions (blue diamond) with their uncertainties (blue bars) from Tab. 9.3, where the resonant $\tau$-background in the charged mode is included as an additional uncertainty and the solid blue line indicates the scale of the pure resonant contribution. The dark red regions (dashed red lines) represent the LU region given by Eq. (9.40) where $\kappa_R^{bs\mu\mu}$ and $A_\pm$ have been scanned within their $1\,\sigma$ ($2\,\sigma$) uncertainties. The light green region represents the validity of the EFT framework as in Eq. (9.35). Assuming the couplings in Eq. (9.27), we display a specific BSM benchmark, which results in best-fit values (yellow star) and $1\,\sigma$ regions (yellow ellipses) for a $Z'$ boson from $b\to s$ global fits, see main text for details. Hatched grey bands correspond to the current experimental 90% C.L. upper limits, whereas the yellow boxes illustrate the projected experimental sensitivity (10 % at the chosen point) of Belle II with $50\,\text{ab}^{-1}$ in Tab. 9.3. *Figure adapted from Ref.* [19].

hand side plot of Fig. 9.3, respectively. Scanning $\kappa_R^{bs\mu\mu}$ and the prefactors $A_\pm$, see Tab. 9.3, within their $1\,\sigma$ ($2\,\sigma$) uncertainties, one identifies

$$\frac{\mathcal{B}\left(B^0 \to K^{*0}\nu\bar{\nu}\right)_{\text{LU}}}{\mathcal{B}\left(B^0 \to K^0\nu\bar{\nu}\right)_{\text{LU}}} = 1.7 \ldots 2.6 \quad (1.3 \ldots 2.9)\,. \tag{9.42}$$

$$\frac{\mathcal{B}\left(B^0 \to K^{*0}\nu\bar{\nu}\right)_{\text{LU}}}{\mathcal{B}\left(B^+ \to K^+\nu\bar{\nu}\right)_{\text{LU}}} = 1.6 \ldots 2.4 \quad (1.2 \ldots 2.7)\,. \tag{9.43}$$

These limits are shown as the red LU regions in Fig. 9.3. Two measurements outside this region would indicate a breakdown of LU. However, a measurement inside this region does not necessarily imply LU. To avoid a double counting of uncertainties in the derivation of the LU region, we separate branching ratio contributions into those coming from the SM, NP, and their interference terms. Then, only the central values of the respective $A_\pm$ factors in Tab. 9.3 are inserted for the pure NP contributions, whereas the SM term even incorporates correlations between the $A_\pm$ factors. The interference term is scaled with $A \sim \sqrt{A^{\text{cen}} \cdot A^{\text{unc}}}$, where $A^{\text{cen}}$ and $A^{\text{unc}}$ refer to the central value and the value including uncertainties of the corresponding $A_\pm$, respectively. The SM predictions are shown with their uncertainties as blue markers, taken from Tab. 9.3. The green region represents the validity of our EFT framework, given by Eq. (9.35). The hatched grey bands correspond to the currently available experimental 90 % C.L. upper limits, while the unhatched grey regions indicate the derived EFT limits, see Tab. 9.3. Then, a measurement between those two areas would infer a clear hint of BSM physics not covered by the EFT framework. The widths of the yellow boxes illustrate the projected experimental sensitivity (10 % at the chosen point) of Belle II with $50\,\text{ab}^{-1}$ [85].

The solid blue line (in the right-hand side plot) corresponds to the resonant branching ratio of a $B^+$ meson annihilating via $\tau^+\nu \to K^+\nu\bar{\nu}$, $\mathcal{B}\left(D^+ \to K^+\bar{\nu}_\tau\nu_\tau\right)_{\text{LD}} \sim 5\cdot 10^{-7}$, such that the region left of this line loses any sensitivity to possible NP. Correlations that include only neutral mesons as in the left-hand side plot are not affected. Similar procedures can also be applied to perform tests of cLFC. However, current limits on $\tau\tau$ couplings as given in Tab. 9.4 are unable to provide information beyond the already established EFT limit, *i.e.* the green region.

### $Z'$ boson benchmark

In $Z'$ models, the alignment of Wilson coefficients $K_L^D = C_L^D$ is present, *cf.* Eq. (9.27). By giving up the model-independent framework from our previous discussions, we gain the possibility to predict LU branching ratios for all possible decay modes only using information from global fits. For $Z'$ models, where also RH quark couplings $C_R^D \neq 0$ emerge, we employ the global fit results in Eq. (9.41). In Fig. 9.3, the corresponding best-fit branching ratio prediction is displayed as a yellow star while $1\,\sigma$ uncertainties (computed in a similar manner as the LU region) are indicated by the enclosing ellipse. In this $Z'$ scenario, predictions of the LU branching ratios of $B\to K^{(*)}\nu\bar{\nu}$ decays read

$$\begin{aligned} \mathcal{B}\left(B^0\to K^0\nu\bar{\nu}\right) &= (4.5\pm 0.6)\cdot 10^{-6}\,, \qquad \mathcal{B}\left(B^+\to K^+\nu\bar{\nu}\right) = (4.9\pm 0.8)\cdot 10^{-6}\,, \\ \mathcal{B}\left(B^0\to K^{*0}\nu\bar{\nu}\right) &= (10.7\pm 1.1)\cdot 10^{-6}\,, \quad \mathcal{B}\left(B^+\to K^{*+}\nu\bar{\nu}\right) = (11.6\pm 1.2)\cdot 10^{-6}\,, \end{aligned} \tag{9.44}$$

which can be compared with their SM predictions and corresponding (experimental) limits provided in Tab. 9.3.

## 9.4 Summary and conclusion

We have worked out a striking connection between dilepton and charged dineutrino couplings established by the $\text{SU}(2)_L$-invariance studied in SMEFT. While this link is applicable in many flavour sectors, it allows us to probe the lepton flavour structure in dineutrino observables, *e.g.* branching ratios related to missing energies measurements. We identify three different structures, that is lepton universality, charged lepton flavour conservation, and an arbitrary structure allowing for lepton flavour violation. Assuming these flavour structures, upper limits for charm dineutrino branching ratios and $b\to s$ couplings have been determined, see Tabs. 9.1 and 9.4, respectively.

As currently no direct observations of BSM physics have been made at colliders, synergies and correlations across all flavour sectors provide the possibility to analyse existing data and hunt towards NP patterns in these rare decay modes. Meanwhile, future refined theoretical work is also vital, and can profoundly impact and improve the tests that have been put forward in this chapter. In particular, improved data of form factors can significantly reduce the uncertainties of branching ratio predictions.

The $\text{SU}(2)_L$-link in Eq. (9.12) can be exploited in both directions, meaning limits from dineutrino data directly affect dilepton couplings and vice versa. By including global fit results of $b\to s\,\mu^+\mu^-$ Wilson coefficients, we can study a relation between dineutrino branching ratios of $B\to$ vector and pseudoscalar mesons to probe lepton universality. We have presented the LU regions in Eqs. (9.42) and (9.43), which are further illustrated in Fig. 9.3. Furthermore, tests of the EFT framework can be established, *e.g.* Eq. (9.35) for $b\to s$ transitions, where a violation hints at light

BSM particles such as RH neutrinos. Refs. [19, 20] provide estimates on the impact of additional dimension-six operators induced by light RH neutrinos where improved (future) experimental limits on $\mathcal{B}(D^0 \to \nu\bar{\nu})$ and $\mathcal{B}(B^0_{(s)} \to \nu\bar{\nu})$ can further constrain scalar and pseudoscalar operators in charm and $B$-physics, respectively.

The data-driven bounds on branching ratios presented for rare charm dineutrino modes of up to $\mathcal{O}\left(10^{-5}\right)$ can be probed by $e^+e^-$-facilities as displayed in Fig. 9.2. Limits on dineutrino branching ratios in flavourful $Z'$ models with a simplified SMEFT framework, see Eq. (9.27), are stronger than the model-independent ones, but within the same order of magnitude. We very much look forward to updated analyses of Belle II and LHCb and improved theoretical input to further elaborate on the suggested null and lepton universality tests able to disentangle different NP scenarios.

*Chapter*

# 10

# Summary and conclusion

In this thesis, we exploited the rich phenomenology of $Z'$ models. A notable aspect of these extensions is the presence of non-universal fermionic U(1)$'$ charges. Due to flavour rotations large effects in FCNC transitions can be induced, which in contrast are strongly GIM-suppressed in the SM. However, the new charges are subject to constraints from gauge anomaly cancellation that have to be met, while also stringent phenomenological bounds on NP parameters from, *e.g.*, meson mixing supplement the model-building approach presented in Chap. 5.

Prompted by the enduring $B$-anomalies with a plethora of $b\to s\,\ell^+\ell^-$ and $b\to s\,\gamma$ data available, we performed global fits of $b\to s$ Wilson coefficients in Chap. 4. The results obtained point towards the evidence of lepton universality violation which can be realised by the presence of NP in left-handed quark currents, see Tabs. 4.1 and 4.2. A minimal extension to account for these deviations is given by $Z'$ models that have been extensively studied in the literature. However, these models are prone to Landau poles emerging before the Planck scale which need to be addressed. We tackled this issue in Chap. 8, proposing the *Planck safety* approach that comes with a great predictive power as only a small subset of models achieves a stable behaviour until the Planck scale. Such viable $Z'$ models were worked out in Secs. 8.2 and 8.3.

The previous studies can be complemented by information from FCNCs in the up-quark sector. In Chap. 6, we studied rare charm decays where null test observables are instrumental to evade the unknown description of the long-distance dynamics. Sizeable contributions to Wilson coefficients present in these observables can be generated by certain sets of $Z'$ models compiled in Tab. 6.1. In particular, deviations from the lepton universality limit $R_P^D = 1$ are readily induced in such models. The predictions are outlined in Sec. 6.4.1 and provide a clear-cut sign of NP if confirmed by experiments. In addition, we worked out the implications of new sources of $CP$ violation in Chap. 7. We exploited $CP$ asymmetries in hadronic charm decays, where a link between a NP-dominated $\Delta A_{CP}$ and semileptonic $D$-decays allows to probe different patterns in $Z'$ models within the reach of future LHCb and Belle II sensitivities [85, 165]. Furthermore, large $U$-spin and isospin breaking effects are realised in these models and can also be accessed by the same experiments.

Thanks to the SU(2)$_L$-invariance in the SMEFT, a genuine connection between quark transitions into dineutrinos with those into charged dileptons emerges. We investigated this link in Chap. 9 across multiple FCNC transitions in a model-independent way, but also in $Z'$ scenarios that provide more restrictive predictions. Using Drell-Yan and rare decay data, we derived upper limits on various $c\to u\,\nu\bar{\nu}$ branching ratios for distinct lepton flavour assumptions, see Tab. 9.1. The link can also be applied to $b\to s$ transitions, which in contrast yields improved limits on charged $\tau$-lepton couplings, see Tab. 9.4. In addition, we presented novel universality tests in $B\to K\nu\bar{\nu}$ and $B\to K^*\nu\bar{\nu}$ decays illustrated in Fig. 9.3. Predictions for $Z'$ models were also worked out.

Clear signs of NP are yet to be discovered at colliders, however the future experimental prospects,

both in the up- and down-sector, are promising and highly anticipated by the community. For example, the first measurements by the Belle II experiment of the LU ratios $R_{K^{(*)}}$ are expected in the near future [85], and will provide independent validations of the current deviations by LHCb [8, 84]. While global fits are already well-established in the $B$-sector, future implementations comprising observables in the up-sector are welcome, and indeed will be crucial to disentangle the whole picture of the underlying BSM theory.

*Appendix*

# A

# Notations and conventions

Throughout this thesis, we work in natural units, *i.e.* redefining the speed of light and Planck's constant as $c = 1$ and $\hbar = 1$, respectively. This gives all quantities dimensions of energy $E$ (in electron volt eV) to some power. Equivalently, we can define the mass dimension of a quantity using $E = m\,c^2$. For example, momentum $p$ and masses $m$ of particles are given in units of GeV, whereas (life)times $\tau$ and lengths $x$ have units $1/\,\mathrm{GeV}$. Their mass dimension is then given by $[p] = [m] = 1$ (positive mass dimension) and $[\tau] = [x] = -1$ (negative mass dimension), respectively. Common examples are

$$\begin{aligned} &[\mathrm{d}x] = [x] = [\tau] = -1\,, \quad [\partial_\mu] = [p_\mu] = 1\,, \\ &[S] = \left[\int \mathrm{d}^4x\,\mathcal{L}\right] = 0\,, \quad [\mathcal{L}] = 4\,, \quad [\psi] = \frac{3}{2}\,, \quad [\phi] = 1\,, \end{aligned} \tag{A.1}$$

where the action $S$ is assumed dimensionless. In Eq. (A.1), $\mathcal{L}$ denotes a Lagrangian (or Lagrangian density), while $\psi$ and $\phi$ refer to fermion and scalar fields, respectively.

Furthermore, we follow the conventions (except when explicitly noted otherwise) described in this appendix that are commonly employed in the literature, *e.g.* Ref. [26].

## A.1 Dirac algebra and spinors

We define the metric tensor as

$$g_{\mu\nu} = \mathrm{diag}\,(+1, -1, -1, -1)\,. \tag{A.2}$$

The Dirac or *gamma* matrices $\gamma_\mu$ with $\mu = 0, 1, 2, 3$ satisfy the anticommutation relation

$$\{\gamma_\mu, \gamma_\nu\} = \gamma_\mu\,\gamma_\nu + \gamma_\nu\gamma_\mu = 2\,g_{\mu\nu}\,, \tag{A.3}$$

where explicit expressions of $\gamma_\mu$ and $\gamma_5$ are given elsewhere [23, 24, 26]. This implies a Dirac algebra with 16 elements

$$\boldsymbol{S} = \mathbb{1}_{4\times4}, \quad \boldsymbol{P} = \gamma_5, \quad \boldsymbol{V} = \gamma_\mu, \quad \boldsymbol{A} = \gamma_\mu\,\gamma_5, \quad \boldsymbol{T} = \sigma_{\mu\nu}\,, \tag{A.4}$$

where

$$\gamma_5 = \mathrm{i}\gamma^0\gamma^1\gamma^2\gamma^3 = \gamma^5\,, \tag{A.5}$$

$$\sigma_{\mu\nu} = \frac{\mathrm{i}}{2}\,[\gamma_\mu, \gamma_\nu] = \frac{\mathrm{i}}{2}\,(\gamma_\mu\gamma_\nu - \gamma_\nu\gamma_\mu)\,. \tag{A.6}$$

In Eq. (A.4), we organise the different structures as *scalar* ($\boldsymbol{S}$), *pseudoscalar* ($\boldsymbol{P}$), *vector* ($\boldsymbol{V}$), *axial vector* ($\boldsymbol{A}$) and *tensor* ($\boldsymbol{T}$). The following relations are useful

$$\begin{aligned} \left(\gamma^0\right)^\dagger &= +\gamma^0\,, & \left(\gamma^i\right)^\dagger &= -\gamma^i\,, \\ \left(\gamma^\mu\right)^\dagger &= \gamma^0\gamma^\mu\gamma^0\,, & \left(\gamma_0\right)^2 &= \mathbb{1}\,, \qquad \left(\gamma_i\right)^2 = -\mathbb{1}\,, \\ \{\gamma_5,\gamma_\mu\} &= 0\,, & \left(\gamma_5\right)^\dagger &= \gamma_5\,, \end{aligned} \tag{A.7}$$

with $i = 1, 2, 3$.

The *chirality projectors* are defined as

$$P_{L/R} = \frac{1 \mp \gamma_5}{2}\,, \quad \left(P_A\right)^\dagger = P_A\,, \quad P_A\,\gamma_\mu = \gamma_\mu\,P_{-A}\,, \tag{A.8}$$

with $A = L, R$, where $-L = R$ and $-R = L$ is understood. Furthermore, we give the *charge conjugation matrix* $C = \mathrm{i}\gamma^2\,\gamma^0$ with selected properties

$$C\left(\gamma_5\right)^{\mathsf{T}}\,C^{-1} = +\gamma_5, \quad C^{\mathsf{T}} = -C\,, \quad C^\dagger = C^{-1}\,, \quad C\left(P_A\right)^{\mathsf{T}} = P_A\,C\,. \tag{A.9}$$

A fermion is described by a four-component *Dirac spinor* and its adjoint which are denoted by $\psi$ and $\bar{\psi} \equiv \left(\psi\right)^\dagger\gamma^0$, respectively. Then, left-handed (LH) and right-handed (RH) fermions are defined as chiral fields

$$\psi_{L/R} \equiv P_{L/R}\,\psi = \frac{1 \mp \gamma_5}{2}\,\psi\,, \tag{A.10}$$

$$\bar{\psi}_A \equiv \overline{\psi_A} = \bar{\psi}\,P_{-A}\,. \tag{A.11}$$

Employing Eq. (A.9), we define the charge-conjugated spinors as

$$\psi^c \equiv C\,\overline{\psi}^{\mathsf{T}}\,, \quad \left(\psi^c\right)^c = \psi\,, \tag{A.12}$$

with chiral properties according to

$$\psi^c_A \equiv \left(\psi_A\right)^c = \left(\psi^c\right)_{-A} = P_{-A}\,\psi^c\,, \tag{A.13}$$

$$\bar{\psi}^c_A \equiv \overline{\psi^c_A} = \overline{\left(\psi_A\right)^c} = \overline{\left(\psi^c\right)_{-A}} = \overline{\psi^c}\,P_A\,. \tag{A.14}$$

By expressing a Dirac fermion as

$$\psi = \psi_L + \psi_R\,, \quad \bar{\psi} = \bar{\psi}_L + \bar{\psi}_R\,, \tag{A.15}$$

we can identify the following properties

$$\bar{\psi}\gamma_\mu\psi = \bar{\psi}_L\gamma_\mu\psi_L + \bar{\psi}_R\gamma_\mu\psi_R \qquad \text{(vector)}\,, \tag{A.16}$$

$$\bar{\psi}\psi = \bar{\psi}_L\psi_R + \bar{\psi}_R\psi_L \qquad \text{(scalar)}\,, \tag{A.17}$$

$$\bar{\psi}\gamma_\mu\gamma_5\psi = -\bar{\psi}_L\gamma_\mu\psi_L + \bar{\psi}_R\gamma_\mu\psi_R \qquad \text{(axial vector)}\,, \tag{A.18}$$

$$\bar{\psi}\gamma_5\psi = \bar{\psi}_L\psi_R - \bar{\psi}_R\psi_L \qquad \text{(pseudoscalar)}\,. \tag{A.19}$$

We note that vector-type terms with $\gamma_\mu$ and $\gamma_\mu\gamma_5$ connect only fields of the same helicity, *i.e.* LH or RH fields. Conversely, a helicity flip occurs for scalar-type terms only linking fields of opposite helicity.

These features manifest themselves when examining interaction and mass terms of fermionic Lagrangians [26]

$$\mathcal{L}_{\text{mass}} = -m \left(\bar{\psi}_R \psi_L + \bar{\psi}_L \psi_R\right) , \tag{A.20}$$

$$\mathcal{L}_{\text{int}} = +g\, F_\psi \, \left(\bar{\psi}_L \gamma_\mu A^\mu \psi_L + \bar{\psi}_R \gamma_\mu A^\mu \psi_R\right) , \tag{A.21}$$

where $g$ and $F_\psi$ denote the gauge coupling and charge under a U(1) symmetry, respectively, and $m$ is the fermion mass. A helicity flip is needed to dynamically generate a mass term. This statement generally holds for charged fermions while an exception marks the introduction of so-called Majorana mass terms for neutral fermions, *e.g.* neutrinos as in Eq. (2.29). Gauge interactions connect fields of the same helicity, and hence without a separate mass term it is not possible to generate fermion masses radiatively through interactions.

## A.2 Pauli matrices

The Pauli matrices $\sigma^i$ are defined via the Lie algebra following

$$\left[\sigma^i, \sigma^j\right] = 2\,\mathrm{i}\,\epsilon_{ijl}\,\sigma^l, \quad \left\{\sigma^i, \sigma^j\right\} = 2\,\mathrm{i}\,\delta_{ij}\,\mathbb{1}\,, \tag{A.22}$$

tacitly employing the Einstein summation notation. Here, the structure constant $\epsilon_{ijl}$ is the Levi-Civita tensor normalised as $\epsilon_{123} = +1$, while $\delta_{ij}$ denotes the Kronecker delta. The four Pauli matrices can be written as

$$\sigma^0 = \begin{pmatrix} 1 & 0 \\ 0 & 1 \end{pmatrix} , \quad \sigma^1 = \begin{pmatrix} 0 & 1 \\ 1 & 0 \end{pmatrix} , \quad \sigma^2 = \begin{pmatrix} 0 & -\mathrm{i} \\ \mathrm{i} & 0 \end{pmatrix} , \quad \sigma^3 = \begin{pmatrix} 1 & 0 \\ 0 & -1 \end{pmatrix} . \tag{A.23}$$

## A.3 Fierz identities

Fierz identities or Fierz relations transfer a given chain of spinors into another one. They prove useful when a calculation of matrix elements between external states is easier to perform using a certain arrangement of spinors. The relevant Fierz identities at *operator level* [26, 220] read

$$\left(\bar{\psi}_1\, \gamma_\mu\, P_A\, \psi_2\right) \left(\bar{\psi}_3\, \gamma^\mu\, P_A\, \psi_4\right) = \left(\bar{\psi}_1\, \gamma_\mu\, P_A\, \psi_4\right) \left(\bar{\psi}_3\, \gamma^\mu\, P_A\, \psi_2\right) , \tag{A.24}$$

$$\left(\bar{\psi}_1\, \gamma_\mu\, P_A\, \psi_2\right) \left(\bar{\psi}_3\, \gamma^\mu\, P_B\, \psi_4\right) = (-2) \left(\bar{\psi}_1\, \gamma_\mu\, P_B\, \psi_4\right) \left(\bar{\psi}_3\, \gamma^\mu\, P_A\, \psi_2\right) , \tag{A.25}$$

with the projection operators $P_A \neq P_B$ as in Eq. (A.8). Using an improved notation, the identities above can be compactly written as

$$\left[\gamma^\mu\, P_A\right]_{ij} \left[\gamma_\mu\, P_A\right]_{kl} = \left[\gamma^\mu\, P_A\right]_{il} \left[\gamma_\mu\, P_A\right]_{kj} , \tag{A.26}$$

$$\left[\gamma^\mu\, P_A\right]_{ij} \left[\gamma_\mu\, P_B\right]_{kl} = (-2) \left[P_B\right]_{il} \left[P_A\right]_{kj} , \tag{A.27}$$

with fermion indices $i$, $j$, $k$, $l$ in flavour space.

## A.4 Details on the definition of couplings

The renormalisation factor $r_1$ in Eq. (5.34) is evaluated via the running of the *effective* strong coupling $\alpha_s = g_s^2/(4\pi)$ at one loop [44, 221]. The corresponding RGE is given by

$$\frac{\mathrm{d}\alpha_s}{\mathrm{d}\ln(\mu)} = -2\,\beta_0^{\mathrm{QCD}}\,\frac{\alpha_s^2}{4\pi}\,, \tag{A.28}$$

with $\beta_0^{\mathrm{QCD}} = 11 - 2/3\,n_f$ as in Eq. (3.21). As quark masses $m_q$ create additional higher-order perturbation terms, they indirectly affect $\alpha_s$ via the number of active quark flavours at the scale $\mu$, denoted as $n_f$. A quark flavour $f$ is referred to as active if $m_q < \mu$. At the quark thresholds, we impose the boundary conditions

$$\alpha_s^{(n_f-1)}(\mu = m_q) = \alpha_s^{(n_f)}(\mu = m_q)\,. \tag{A.29}$$

In the studies of Chaps. 6 and 7, we employ

$$\alpha_s^{(n_f)}(\mu) = \frac{\alpha_s^{(n_f)}(\mu_0)}{1 + \tilde{\beta}_0(n_f)\,\alpha_s^{(n_f)}(\mu_0)\,\ln\left(\frac{\mu^2}{\mu_0^2}\right)}\,, \tag{A.30}$$

where $\tilde{\beta}_0 = \beta_0^{\mathrm{QCD}}/(4\pi)$. To compute the running while passing quark thresholds, we employ the experimental input $\alpha_s(M_Z) = \alpha_s^{(5)}(M_Z)$ provided in Tab. B.1. For example, we obtain

$$\alpha_s^{(4)}(m_b) = \alpha_s^{(5)}(m_b) = \frac{\alpha_s(M_Z)}{1 + \tilde{\beta}_0(5)\,\alpha_s(M_Z)\,\ln\left(\frac{m_b^2}{M_Z^2}\right)}\,, \tag{A.31}$$

$$\alpha_s^{(4)}(m_c) = \frac{\alpha_s^{(4)}(m_b)}{1 + \tilde{\beta}_0(4)\,\alpha_s^{(4)}(m_b)\,\ln\left(\frac{m_c^2}{m_b^2}\right)}\,. \tag{A.32}$$

### Rescaling of gauge couplings

In what follows, we provide the notation of the rescaled couplings used in Chap. 8, where we follow the notation of, *e.g.*, Refs. [21, 137, 141, 142]. The gauge couplings read

$$\alpha_X = \frac{X^2}{(4\,\pi)^2} \quad \text{with} \quad X = \{g_1,\, g_2,\, g_3,\, g_4\}\,, \tag{A.33}$$

where the scaling differs from the convention commonly used in literature by a factor $4\pi$. Due to this rescaling, the RGE of the strong coupling in Eq. (A.28) gets modified and reads

$$\frac{\mathrm{d}\alpha_3}{\mathrm{d}\ln(\mu)} = B_3\,\alpha_3^2\,, \tag{A.34}$$

| | $\mu_0 = 3$ TeV | $\mu_0 = 5$ TeV |
|---|---|---|
| $\alpha_1(\mu_0)$ | $8.40 \cdot 10^{-4}$ | $8.46 \cdot 10^{-4}$ |
| $\alpha_2(\mu_0)$ | $2.54 \cdot 10^{-3}$ | $2.52 \cdot 10^{-3}$ |
| $\alpha_3(\mu_0)$ | $6.37 \cdot 10^{-3}$ | $6.09 \cdot 10^{-3}$ |
| $\alpha_t(\mu_0)$ | $4.17 \cdot 10^{-3}$ | $4.00 \cdot 10^{-3}$ |
| $\alpha_b(\mu_0)$ | $1.07 \cdot 10^{-6}$ | $1.02 \cdot 10^{-6}$ |
| $\alpha_\lambda(\mu_0)$ | $5.18 \cdot 10^{-4}$ | $4.80 \cdot 10^{-4}$ |

**Table A.1:** Numerical values of SM parameters at matching scales $\mu_0 = 3$ TeV and $\mu_0 = 5$ TeV. *Table taken from Ref.* [21].

with $B_3 = -2\,\beta_0^{\rm QCD}$. The solution can be written as

$$\alpha_3(\mu) = \frac{\alpha_3(\mu_0)}{1 - \frac{B_3}{2}\,\alpha_3(\mu_0)\,\ln\left(\frac{\mu^2}{\mu_0^2}\right)}\,, \tag{A.35}$$

suppressing the active quark flavours for brevity. However, we avoid unnecessary confusion by using the default notation for the fine-structure constant

$$\alpha_e \equiv \frac{e^2}{4\,\pi}\,. \tag{A.36}$$

where $e$ denotes the elementary charge. Then, $\alpha_e(m_e) \approx 1/137$ at $\mu = m_e$.

For completion, we give the corresponding rescaled Yukawa, quartic and portal couplings as utilised in the Planck safety analysis of Ref. [21] and discussed in Sec. 8.3,

$$\begin{aligned} \alpha_Y &= \frac{Y^2}{(4\,\pi)^2} \quad \text{with} \quad Y = \{y_t,\, y_b,\, y\}\,, \\ \alpha_Z &= \frac{Z}{(4\,\pi)^2} \quad \text{with} \quad Z = \{\lambda,\, \delta,\, \tilde{\delta},\, u,\, v,\, w,\, s\}\,. \end{aligned} \tag{A.37}$$

In Tab. A.1, we provide the SM parameters at the matching scales $\mu_0 = 3$ TeV and $\mu_0 = 5$ TeV, employed in the analysis of Chap. 8.

*Appendix*

# B

# Numerical constants and input parameters

In this appendix, we summarise the input parameters which are employed in the main calculations of this thesis. In Tabs. B.1 to B.3, we list values of coupling constants, CKM parameters, masses, and lifetimes divided into three separate tables. Therein, central values and the respective uncertainties are given. Yet, we generally consider only the central values in our computations if not noted otherwise. For instance, the uncertainties of the Fermi constant $G_{\rm F}$ and the fine-structure constant $\alpha_e$ quoted in Tab. B.1 are minuscule and only stated here for the sake of completion. We also provide useful functions and input on meson mixing parameters.

In Tab. B.1, we quote two numbers each for the CKM parameters in the Wolfenstein notation. The first numbers are taken from the Particle Data Group (PDG) of 2018 [155], whereas the numbers in brackets refer to the latest PDG input available in Ref. [32]. While the updated values have only minor impact on the results presented herein, we clarify that Chaps. 6 and 7 utilise the older numbers, while the updated numbers are included in the analyses of Chaps. 8 and 9.

For the conversion from seconds to GeV the following relation proves useful

$$6.5821 \cdot 10^{-13}\,\text{ps GeV} = 6.5821 \cdot 10^{-25}\,\text{s GeV} = 1\,. \tag{B.1}$$

We define the chiral enhancements [168]

$$\begin{aligned} \chi_K(\mu) &= \frac{2\,m_{K^0}^2}{m_c(\mu)\,m_s(\mu)}\,, \\ \chi_\pi(\mu) &= \frac{2\,m_{\pi^0}^2}{m_c(\mu)\,(m_d+m_u)(\mu)}\,, \end{aligned} \tag{B.2}$$

with values $\chi_K(m_c) \approx 3.626$ and $\chi_\pi(m_c) \approx 3.655$ at the charm scale.

The Källén function is defined as

$$\lambda(a,b,c) \equiv a^2 + b^2 + c^2 - 2(ab + ac + bc)\,. \tag{B.3}$$

Moreover, we employ the kinematic function

$$\lambda_{DP} = \lambda_{DP}(q^2) = \lambda(m_D^2, m_P^2, q^2)\,, \tag{B.4}$$

with units $[\,\text{GeV}]^4$. Here, $q^2$ is the dilepton invariant mass squared, while $m_D$ and $m_P$ denote constituent decay masses.

### $D^0$-$\overline{D}^0$ mixing parameters

For the mixing parameters we use the latest *published* world averages of the HFLAV collaboration [123]

$$x_{12} \in [0.22\,,\,0.63]\ \%\,, \quad y_{12} \in [0.50\,,\,0.75]\ \%\,, \quad \phi_{12} \in [-2.5^\circ,\,1.8^\circ]\,, \tag{B.5}$$

quoting the allowed 95 % C.L. intervals. However, a recent global fit update of the $D$-mixing parameters is provided online awaiting publication. The updated values as of December 2021 read [124]

$$x_{12} \in [0.314\,,\,0.503]\ \%\,, \quad y_{12} \in [0.495\,,\,0.715]\ \%\,, \quad \phi_{12} \in [-1.2^\circ,\,2.42^\circ]\,. \tag{B.6}$$

We discuss the impact of this update on the parameter space of $Z'$ models in Sec. 7.5.

The HMEs of the operators $Q_{1-3}$ and $Q_6$ in Eq. (5.31) are computed at $\mu = 3$ GeV. The numerical values can be extracted from Ref. [222] and read

$$\begin{aligned} \langle Q_1 \rangle &= \ \ 0.0805(55)\ \text{GeV}^4 = \langle Q_6 \rangle\,, \\ \langle Q_2 \rangle &= -0.2070(142)\ \text{GeV}^4\,, \\ \langle Q_3 \rangle &= \ \ 0.2747(129)\ \text{GeV}^4\,. \end{aligned} \tag{B.7}$$

### $B^0$-$\overline{B}^0$ mixing parameters

The experimental world averages of the mass differences of the neutral $B_{(s)}$ mesons read [123]

$$\Delta M_d^{\text{exp}} = (0.5065 \pm 0.0019)\ \text{ps}^{-1}\,, \tag{B.8}$$

$$\Delta M_s^{\text{exp}} = (17.757 \pm 0.021)\ \text{ps}^{-1}\,. \tag{B.9}$$

For the SM predictions we employ the weighted averages [128]

$$\Delta M_d^{\text{SM}} = \left(0.533^{+0.022}_{-0.036}\right)\ \text{ps}^{-1}\,, \tag{B.10}$$

$$\Delta M_s^{\text{SM}} = \left(18.4^{+0.7}_{-1.2}\right)\ \text{ps}^{-1}\,. \tag{B.11}$$

| Quantity | Symbol | Value | | Unit | Reference |
|---|---|---|---|---|---|
| Fermi constant | $G_\mathrm{F}$ | 1.1663787(6) | $\cdot 10^{-5}$ | $\mathrm{GeV}^{-2}$ | PDG [32] |
| inv. fine-structure constant | $\alpha_e(m_e)^{-1}$ | 137.035999150(33) | | | PDG [32] |
| 137.036 strong coupling constant | $\alpha_s(M_Z)$ | 0.1182(8) | | | FLAG [223] |
| Wolfenstein parameter | $\lambda_\mathrm{CKM}$ | 0.22453(44) [0.22650(48)] | | | PDG [155], [32] |
| | $A$ | 0.836(15) [0.790(17)] | | | PDG [155], [32] |
| | $\bar{\rho}$ | 0.122(18) [0.141(17)] | | | PDG [155], [32] |
| | $\bar{\eta}$ | 0.355(12) [0.357(11)] | | | PDG [155], [32] |

**Table B.1:** Numerical values of input parameters used in this thesis. The values in parentheses denote the respective uncertainty up to the given significant figure, *e.g.* $1.0(2) = 1.0 \pm 0.2$. For the CKM input, we give the errors as symmetrised ones by taking the largest value of the upper and lower uncertainties.

| Quantity | Symbol | Value | | Unit | Reference |
|---|---|---|---|---|---|
| $W$-boson mass | $M_W$ | 91.1876(21) | | GeV | PDG [155] |
| $Z$-boson mass | $M_Z$ | 80.379(12) | | GeV | PDG [155] |
| Higgs-boson mass | $M_H$ | 125.18(16) | | GeV | PDG [155] |
| electron mass | $m_e$ | 0.5109989461(31) | $\cdot 10^{-3}$ | GeV | PDG [155] |
| muon mass | $m_\mu$ | 0.1056583745(24) | | GeV | PDG [155] |
| tauon mass | $m_\tau$ | 1.77686(12) | | GeV | PDG [155] |
| $u$-quark mass | $m_u(2\ \mathrm{GeV})$ | 2.2(5) | $\cdot 10^{-3}$ | GeV | PDG [155] |
| $d$-quark mass | $m_d(2\ \mathrm{GeV})$ | 4.7(5) | $\cdot 10^{-3}$ | GeV | PDG [155] |
| averaged $u$, $d$ mass at charm scale | $\frac{m_u+m_d}{2}\ (m_c)$ | 3.894(49) | $\cdot 10^{-3}$ | GeV | Our analysis[†] |
| $s$-quark mass | $m_s(2\ \mathrm{GeV})$ | 95(9) | $\cdot 10^{-3}$ | GeV | PDG [155] |
| $s$-quark mass at charm scale | $m_s(m_c)$ | 106.71(78) | $\cdot 10^{-3}$ | GeV | Our analysis[†] |
| $c$-quark mass at charm scale | $m_c(m_c)$ | 1.275(25) | | GeV | PDG [155] |
| $b$-quark mass at $b$-scale | $m_b(m_b)$ | 4.198(12) | | GeV | PDG [32] |
| $t$-quark mass at $t$-scale | $m_t(m_t)$ | 160(5) | | GeV | PDG [155] |
| $B^0$-meson mass | $m_{B^0}$ | 5.27965(12) | | GeV | PDG [32] |
| $B^+$-meson mass | $m_{B^+}$ | 5.27934(12) | | GeV | PDG [32] |
| $B_s$-meson mass | $m_{B_s}$ | 5.36688(14) | | GeV | PDG [32] |
| $D^0$-meson mass | $m_{D^0}$ | 1.86484(5) | | GeV | PDG [32] |
| $D^+$-meson mass | $m_{D^+}$ | 1.86966(5) | | GeV | PDG [32] |
| $D_s$-meson mass | $m_{D_s}$ | 1.96835(7) | | GeV | PDG [32] |

**Table B.2:** Continuation of Tab. B.1, which lists numerical values of the input parameters used in this thesis. The quark masses are given in the $\overline{\mathrm{MS}}$ scheme [32]. [†]We have computed the masses using the `rundec` package [224] available in Python and Mathematica.

| Quantity | Symbol | Value | | Unit | Reference |
|---|---|---|---|---|---|
| muon lifetime | $\tau_\mu$ | 2.1969811(22) | $\cdot 10^{-6}$ | s | PDG [32] |
| tauon lifetime | $\tau_\tau$ | 2.903(5) | $\cdot 10^{-12}$ | s | PDG [32] |
| $D^0$-meson lifetime | $\tau_{D^0}$ | 0.4101(15) | $\cdot 10^{-12}$ | s | PDG [32] |
| $D^+$-meson lifetime | $\tau_{D^+}$ | 1.040(7) | $\cdot 10^{-12}$ | s | PDG [32] |
| $D_s$-meson lifetime | $\tau_{D_s}$ | 0.504(4) | $\cdot 10^{-12}$ | s | PDG [32] |
| $B^0$-meson lifetime | $\tau_{B^0}$ | 1.519(4) | $\cdot 10^{-12}$ | s | PDG [32] |
| $B^+$-meson lifetime | $\tau_{B^+}$ | 1.638(4) | $\cdot 10^{-12}$ | s | PDG [32] |
| $B_s$-meson lifetime | $\tau_{B_s}$ | 1.515(4) | $\cdot 10^{-12}$ | s | PDG [32] |
| $\pi$-meson decay constant | $f_\pi$ | 130.2(8) | $\cdot 10^{-3}$ | GeV | FLAG [223] |
| $K$-meson decay constant | $f_K$ | 155.7(7) | $\cdot 10^{-3}$ | GeV | FLAG [223] |
| $D$-meson decay constant | $f_D$ | 212.0(7) | $\cdot 10^{-3}$ | GeV | FLAG [223] |
| $D_s$-meson decay constant | $f_{D_s}$ | 249.9(5) | $\cdot 10^{-3}$ | GeV | FLAG [223] |
| $B$-meson decay constant | $f_B$ | 188(7) | $\cdot 10^{-3}$ | GeV | FLAG [223] |
| $B_s$-meson decay constant | $f_{B_s}$ | 227(7) | $\cdot 10^{-3}$ | GeV | FLAG [223] |
| $D \to \pi$ form factor | $f_0^{D\pi}(0)$ | 0.612(35) | | | [225]$^\dagger$ |
| | $f_0^{D\pi}(m_\pi^2)$ | 0.614(35) | | | [225]$^\dagger$ |
| $D \to K$ form factor | $f_0^{DK}(0)$ | 0.765(31) | | | [225]$^\dagger$ |
| | $f_0^{DK}(m_K^2)$ | 0.789(28) | | | [225]$^\dagger$ |

**Table B.3:** Continuation of Tabs. B.1 and B.2, which comprises lifetimes of leptons and mesons, as well as meson decay constants and $D \to P$ form factors. $^\dagger$Values are obtained using the fit results of the z-expansion parameters in Ref. [225] including correlations, see App. E.3 for details.

*Appendix*

# C

# Details on $b \to s$ global fits

In this appendix, we provide details on the global fit of $b \to s$ Wilson coefficients that is performed using the `flavio` and `iminuit` packages available in Python [91, 95]. We summarise the observables included in our fit and present results in Apps. C.1 and C.2, respectively. The correlation matrices for the fit scenarios are given in App. C.3.

## C.1 List of observables and data included

In our global fit, we study observables featuring little sensitivity to long-distance physics, which provide an enhanced potential in NP searches. Such observables are often referred to as (theoretically) *clean*, where hadronic uncertainties of, *e.g.*, form factors cancel at LO in the effective theory considered. In addition, the experimental accessibility of these observables is formidable [226]. Incorporating a large number of such (binned and unbinned) observables in our fit is necessary to sufficiently constrain the FCNC operators in $b \to s$ transitions.

In the following, we give the complete list of observables and datasets used in the global fit, where we follow Refs. [93, 94]. We provide several tables that include different sets of observables, *e.g.* angular observables and (differential) branching ratios in Tabs. C.1 and C.2, respectively. We include the observables listed in Table B.1-B.3 of Ref. [93], while additionally including the recent measurements of $R_{K^0_S}$ and $R_{K^{*+}}$ from LHCb [9], displayed in Tab. C.4 herein. In our analysis, we focus on observables sensitive to the $b \to s$ transition. Hence, we do not include charged-current $B$-decays ($b \to (c,u)\,\ell\nu$), strange, charm or $\tau$-lepton decays as well as LFV decays, such as $B^+ \to K^+\tau\mu$, *cf.* Tables B.4 to B.9 in Ref. [93]. Conversely, we include observables of radiative modes, $B^0_{(s)} \to \mu^+\mu^-$and $\Lambda_b$-decays, which are already implemented in `flavio`, see Tab. C.3. To minimise confusion, we highlight observables that are *only* included in our analysis (and *not* implemented in the analysis of Ref. [93]) with a $\circ$ in Tabs. C.1 to C.4.

For the binned $b \to s\,\mu^+\mu^-$ observables compiled in Tabs. C.1 and C.2, we take into account all available data on angular observables in the *optimised* basis [1] [226], where we refer to, *e.g.*, Ref. [249] for details on angular observables. The different (sub)sets of observables and bins included vary depending on the experiment providing the data. Notably, in the region of the $c\bar{c}$ resonances non-factorisable contributions diminish the validity of the QCD factorisation [70]. Thus, we do not take into account $q^2$-bins between 6 and 8 GeV$^2$. Moreover, we omit the $q^2$-bin $[0.1, 0.98]$ GeV$^2$ in our fit since different form factor treatments in `flavio` and Ref. [226] lead to considerable discrepancies in the associated theoretical uncertainties in this bin. In contrast, a

[1] The *optimised* basis represents a sound trade-off between theoretical cleanliness and simplicity in their experimental accessibility, see Ref. [226] and references therein.

| Observables | $q^2$-bins in GeV$^2$ | Datasets | |
|---|---|---|---|
| $\langle\mathcal{O}\rangle\,(B^0\to K^{*0}\mu^+\mu^-)$ | | | |
| $\langle F_{\rm L}\rangle, \langle P_1\rangle, \langle P_2\rangle, \langle P_3\rangle,$ $\langle P_4'\rangle, \langle P_5'\rangle, \langle P_6'\rangle, \langle P_8'\rangle$ | $[1.1, 2.5], [2.5, 4],$ $[4, 6], [15, 19]$ | LHCb'15 [227], LHCb'20 [228] | |
| $\langle F_{\rm L}\rangle, \langle P_1\rangle, \langle P_4'\rangle,$ $\langle P_5'\rangle, \langle P_6'\rangle, \langle P_8'\rangle$ | $[0.04, 2], [2, 4],$ $[4, 6]$ | ATLAS'17 [229] | |
| $\langle F_{\rm L}\rangle, \langle A_{\rm FB}\rangle,$ $\langle P_1\rangle, \langle P_5'\rangle$ | $[1, 2], [2, 4.3],$ $[4.3, 6], [16, 19]$ | CMS'17 [230] | |
| $\langle F_{\rm L}\rangle, \langle A_{\rm FB}\rangle$ | $[0, 2], [2, 4.3], [16, 19.3]$ | CDF'12 [231] | |
| $\langle\mathcal{O}\rangle\,(B^+\to K^{*+}\mu^+\mu^-)$ | | | |
| $\langle F_{\rm L}\rangle, \langle P_1\rangle, \langle P_2\rangle, \langle P_3\rangle$ $\langle P_4'\rangle, \langle P_5'\rangle, \langle P_6'\rangle, \langle P_8'\rangle$ | $[1.1, 2.5], [2.5, 4],$ $[4, 6], [15, 19]$ | LHCb'20 [232] | |
| $\langle A_{\rm FB}\rangle$ | $[1.1, 2.5], [4, 6], [15, 19]$ | LHCb'20 [232] | ∘ |
| $\langle\mathcal{O}\rangle\,(B^+\to K^+\mu^+\mu^-)$ | | | |
| $\langle A_{\rm FB}\rangle, \langle F_{\rm H}\rangle$ | $[1.1, 2], [2, 3], [3, 4],$ $[4, 5], [5, 6], [15, 22]$ | LHCb'14 [233] | ∘ |
| $\langle\mathcal{O}\rangle\,(\Lambda_b\to \Lambda\,\mu^+\mu^-)$ | | | |
| $\langle A_{\rm FB}^h\rangle, \langle A_{\rm FB}^l\rangle, \langle A_{\rm FB}^{lh}\rangle$ | $[15, 20]$ | LHCb'18 [234] | ∘ |
| $\langle\mathcal{O}\rangle\,(B_s\to \phi\,\mu^+\mu^-)$ | | | |
| $\langle F_{\rm L}\rangle, \langle S_3\rangle, \langle S_4\rangle, \langle S_7\rangle$ | $[0.1, 2], [2, 5], [15, 19]$ | LHCb'15 [235] | |

**Table C.1:** Datasets on angular $b\to s\mu^+\mu^-$ observables used in our fit. This list comprises 126 different observables. The ∘ highlights observables that are *not* included in the analysis of Ref. [93].

good agreement is reached in all other bins. Following the set-up in Ref. [93], we always take into account the narrow bins (if provided by the experiment) in the region of large hadronic recoil (low-$q^2$ region), while for low hadronic recoil (high-$q^2$ region) we consider larger bin sizes averaging over the kinematic region above the resonances. Observables of radiative $B$-decays as well as the branching ratios of $B_s\to\mu^+\mu^-$ and $B^0\to\mu^+\mu^-$ (due to their strong correlation) are also included in our fit, where we provide the corresponding SM predictions and measurements in Tab. C.3.

While the previously presented observables are obtained from *pure* $b\to s\,\mu^+\mu^-$ data, we list a special set of observables that violate LFU in Tab. C.4. Assuming that electron modes do not suffer from NP effects, we include observables with couplings to electrons that set strong constraints on the Wilson coefficients $\mathcal{C}_7^{(\prime)}$ [97]. We include the datasets from LHCb and Belle, where the measurements on the ratios of (differential) branching ratios $R_{K^{(*)}}$ provided by LHCb yield stronger constraints on our fit due to their significantly smaller statistical and systematic uncertainties. We refer to Tab. C.5 for a comparison and Sec. 3.4 for more details on the LU ratios. The Belle

| Observables | $q^2$-bins in GeV$^2$ | Datasets | |
|---|---|---|---|
| $\langle \frac{d\mathcal{B}}{dq^2} \rangle (B^0 \to K^{*0}\mu^+\mu^-)$ | $[1.1, 2.5], [2.5, 4], [4, 6], [15, 19]$ | LHCb'16 [236] | |
| $\langle \frac{d\mathcal{B}}{dq^2} \rangle (B^+ \to K^{*+}\mu^+\mu^-)$ | $[0.1, 2], [2, 4], [4, 6], [15, 19]$ | LHCb'14 [237] | |
| $\langle \frac{d\mathcal{B}}{dq^2} \rangle (B^0 \to K^{0}\mu^+\mu^-)$ | $[0.1, 2], [2, 4], [4, 6], [15, 22]$ | LHCb'14 [237] | |
| $\langle \frac{d\mathcal{B}}{dq^2} \rangle (B^+ \to K^{+}\mu^+\mu^-)$ | $[1.1, 2], [2, 3], [3, 4], [4, 5], [5, 6], [15, 22]$ | LHCb'14 [237] | |
| $\langle \frac{d\mathcal{B}}{dq^2} \rangle (B_s \to \phi\,\mu^+\mu^-)$ | $[0.1, 2], [2, 5], [15, 19], [1.1, 2.5], [2.5, 4], [4, 6]$ | LHCb'15 [235], LHCb'21 [99] | □ |
| $\langle \frac{d\mathcal{B}}{dq^2} \rangle (\Lambda_b \to \Lambda\,\mu^+\mu^-)$ | $[2, 4], [4, 6], [15, 20]$ | LHCb'15 [238] | ∘ |

**Table C.2:** Datasets on binned differential branching ratios in $b\to s\mu^+\mu^-$ observables used in our fit. This list comprises 27 different observables. The ∘ highlights observables that are *not* included in the analysis of Ref. [93]. The □ indicates new/updated measurements of observables compared to the analysis of Ref. [20], see comments in the main text.

results are measured in more bins compared to LHCb [2]. Additionally, we take into account the observables

$$Q_{4,5} \equiv P'^{\mu}_{4,5} - P'^{e}_{4,5}\,. \tag{C.1}$$

They measure the difference of angular observables $P'_i$ between electrons and muons in the final state, and thus constitute a null test of the SM. The list in Tab. C.4 is complemented by a set of $B^0\to K^{*0}\,e^+e^-$ observables, also included in the analysis of Ref. [93].

### Updated measurements compared to the analysis in Ref. [20]

Since the publication of Ref. [20], where this global fit to $b\to s$ data was presented first, updated measurements of some observables have been made available to `flavio`. Hence, in this appendix we perform an updated fit that includes the following changes compared to the analysis in Ref. [20]:

- We additionally include the latest LHCb measurement [99] of $\langle \frac{d\mathcal{B}}{dq^2} \rangle (B_s\to \phi\,\mu^+\mu^-)$ with $q^2$ bins $[1, 2.5], [2.5, 4]$ and $[4, 6]$ GeV$^2$, see Tab. C.2.
- We use the updated combined measurement of $B^0_{(s)} \to \mu^+\mu^-$ branching ratios [98] with a Gaussian distribution fitted to the numerical combination of ATLAS, CMS and LHCb results, see Tab. C.3. In Ref. [20], the 2020 combination [250] has been employed instead.
- We include the (first) LHCb measurements [9] of $R_{K^{*+}}$ (and $R_{K^0_S}$) which were not available when our original analysis was realised.

[2] We remark that for the Belle measurements of $R_{K^0_S}$ and $R_{K^+}$ the updated values taken from the published version of Ref. [245] are employed in our fit. The measurements list provided by `flavio` v2.3.3 only incorporates the *outdated* values of version 1 as of May 2022. However, such changes have no noticeable impact on the fit due to the large uncertainties of those measurements.

| Observables | SM prediction | Measurement/Limit | | |
|---|---|---|---|---|
| $\mathcal{B}(B_s \to \mu^+\mu^-)$ | $(3.67 \pm 0.14) \cdot 10^{-9}$ | $(2.9 \pm 0.3) \cdot 10^{-9}$ | combination 2021$^\dagger$ [98] | ∘ □ |
| $\mathcal{B}(B^0 \to \mu^+\mu^-)$ | $(1.14 \pm 0.11) \cdot 10^{-10}$ | $(0.6 \pm 0.7) \cdot 10^{-10}$ | combination 2021$^\dagger$ [98] | ∘ □ |
| $\mathcal{B}(B^0 \to K^{*0}\gamma)$ | $(41.8 \pm 7.4) \cdot 10^{-6}$ | $(43.3 \pm 1.5) \cdot 10^{-6}$ | HFLAV'14 [239] | ∘ |
| $\mathcal{B}(B^+ \to K^{*+}\gamma)$ | $(42.5 \pm 8.0) \cdot 10^{-6}$ | $(42.1 \pm 1.8) \cdot 10^{-6}$ | HFLAV'14 [239] | ∘ |
| $\mathcal{B}(B \to X_s\gamma)$ | $(329 \pm 23) \cdot 10^{-6}$ | $(327 \pm 14) \cdot 10^{-6}$ | Belle'16 [240, 241] | ∘ |
| $\mathcal{B}(B_s \to \phi\gamma)$ | $(4.0 \pm 0.5) \cdot 10^{-5}$ | $(3.6 \pm 0.5 \pm 0.3 \pm 0.6) \cdot 10^{-5}$ | Belle'14 [242] | ∘ |
| $\frac{\mathcal{B}(B_s \to K^{*0}\gamma)}{\mathcal{B}(B_s \to \phi\gamma)}$ | $1.04 \pm 0.19$ | $1.19 \pm 0.06 \pm 0.04 \pm 0.07$ | LHCb'12 [243] | ∘ |
| $A_{CP}(B^0 \to K^{*0}\gamma)$ | $0.005 \pm 0.002$ | $-0.002 \pm 0.015$ | HFLAV'14 [239] | ∘ |
| $A_{CP}(B_s \to \phi\gamma)$ | $0.004 \pm 0.002$ | $0.11 \pm 0.29 \pm 0.11$ | LHCb'19 [244] | ∘ |
| $A_{CP}^{\Delta}(B_s \to \phi\gamma)$ | $0.03 \pm 0.02$ | $-0.67^{+0.37}_{-0.41} \pm 0.17$ | LHCb'19 [244] | ∘ |
| $S_{\phi\gamma}$ | $(-2 \pm 2) \cdot 10^{-4}$ | $0.43 \pm 0.30 \pm 0.11$ | LHCb'19 [244] | ∘ |
| $S_{K^*\gamma}$ | $-0.023 \pm 0.014$ | $-0.16 \pm 0.22$ | HFLAV'14 [239] | ∘ |

**Table C.3:** Datasets on observables of $B^0_{(s)} \to \mu^+\mu^-$and $B \to X\gamma$ decays, where their SM predictions are obtained using `flavio`. This list comprises 12 different observables. The ∘ highlights observables that are *not* included in the analysis of Ref. [93]. The □ indicates new/updated measurements of observables compared to the analysis of Ref. [20]. $^\dagger$Latest combination of ATLAS'18, CMS'19 and LHCb'21 results using a Gaussian distribution implemented in `flavio`.

| Observables | $q^2$-bins in GeV$^2$ | Datasets | |
|---|---|---|---|
| $\langle R_{K^0_S} \rangle$ | $[0.1, 4]$, $[1.0, 6.0]$, $[14.18, 19]$ | Belle'19 [245] | |
| $\langle R_{K^0_S} \rangle$ | $[1.1, 6]$ | LHCb'21 [9] | ∘ □ |
| $\langle R_{K^+} \rangle$ | $[0.1, 4]$, $[1, 6]$, $[14.18, 19]$ | Belle'19 [245] | |
| $\langle R_{K^+} \rangle$ | $[1.1, 6]$ | LHCb'21 [8] | |
| $\langle R_{K^{*0}} \rangle$ | $[0.045, 1.1]$, $[1.1, 6]$, $[15, 19]$ | Belle'19 [86] | |
| $\langle R_{K^{*0}} \rangle$ | $[0.045, 1.1]$, $[1.1, 6]$ | LHCb'17 [84] | |
| $\langle R_{K^{*+}} \rangle$ | $[0.045, 1.1]$, $[1.1, 6]$, $[15, 19]$ | Belle'19 [86] | |
| $\langle R_{K^{*+}} \rangle$ | $[0.045, 6.0]$ | LHCb'21 [9] | ∘ □ |
| LU-violating observables | | | |
| $\langle Q_4 \rangle, \langle Q_5 \rangle$ | [0.1, 4], [1, 6], [14.18, 19] | Belle'16 [246] | |
| $B^0 \to K^{*0} e^+e^-$ observables | | | |
| $\langle F_L \rangle, \langle P_1 \rangle, \langle P_2 \rangle, \langle \mathrm{Im}(A_T) \rangle$ | [0.002, 1.12], [0.0008, 0.257] | LHCb'15 [247], LHCb'20 [248] | |

**Table C.4:** Datasets on observables in $B \to K^{(*)}\ell^+\ell^-$ decays sensitive to LFU violation. This list comprises 29 different observables. The ∘ highlights observables that are *not* included in the analysis of Ref. [93]. The □ indicates new/updated measurements of observables compared to the analysis of Ref. [20].

| | $q^2$-bin in GeV$^2$ | SM prediction | Measurement | Dataset | Deviation |
|---|---|---|---|---|---|
| $R_{K^0_S}$ | $[0.1, 4.0]$ | $1.00 \pm 0.01$ | $1.62^{+1.31}_{-1.01}\,(\text{stat}) \pm 0.02\,(\text{syst})$ | Belle'19 [245] | $< 1.0\,\sigma$ |
| | $[1.0, 6.0]$ | $1.00 \pm 0.01$ | $0.55^{+0.46}_{-0.34}\,(\text{stat}) \pm 0.01\,(\text{syst})$ | Belle'19 [245] | $< 1.0\,\sigma$ |
| | $[1.1, 6.0]$ | $1.00 \pm 0.01$ | $0.66^{+0.20}_{-0.14}\,(\text{stat})\,^{+0.02}_{-0.04}\,(\text{syst})$ | LHCb'21 [9] | $\sim 1.5\,\sigma$ |
| | $[14.18, 19.0]$ | $1.00 \pm 0.01$ | $1.57^{+1.28}_{-1.00}\,(\text{stat}) \pm 0.02\,(\text{syst})$ | Belle'19 [245] | $< 1.0\,\sigma$ |
| $R_{K+}$ | $[0.1, 4.0]$ | $1.00 \pm 0.01$ | $0.98^{+0.29}_{-0.26}\,(\text{stat}) \pm 0.02\,(\text{syst})$ | Belle'19 [245] | $< 1.0\,\sigma$ |
| | $[1.0, 6.0]$ | $1.00 \pm 0.01$ | $1.39^{+0.36}_{-0.33}\,(\text{stat}) \pm 0.02\,(\text{syst})$ | Belle'19 [245] | $< 1.0\,\sigma$ |
| | $[1.1, 6.0]$ | $1.00 \pm 0.01$ | $0.846^{+0.042}_{-0.039}\,(\text{stat})\,^{+0.013}_{-0.012}\,(\text{syst})$ | LHCb'21 [8] | $\sim 3.1\,\sigma$ |
| | $[14.18, 19.0]$ | $1.00 \pm 0.01$ | $1.13^{+0.31}_{-0.28}\,(\text{stat}) \pm 0.01\,(\text{syst})$ | Belle'19 [245] | $< 1.0\,\sigma$ |
| $R_{K*0}$ | $[0.045, 1.1]$ | $0.91 \pm 0.03$ | $0.46^{+0.55}_{-0.27}\,(\text{stat}) \pm 0.13\,(\text{syst})$ | Belle'19 [86] | $< 1.0\,\sigma$ |
| | | | $0.66^{+0.11}_{-0.07}\,(\text{stat}) \pm 0.03\,(\text{syst})$ | LHCb'17 [84] | $\sim 2.2\,\sigma$ |
| | $[1.1, 6.0]$ | $1.00 \pm 0.01$ | $1.06^{+0.63}_{-0.38}\,(\text{stat}) \pm 0.14\,(\text{syst})$ | Belle'19 [86] | $< 1.0\,\sigma$ |
| | | | $0.69^{+0.11}_{-0.07}\,(\text{stat}) \pm 0.05\,(\text{syst})$ | LHCb'17 [84] | $\sim 2.5\,\sigma$ |
| | $[15, 19]$ | $1.00 \pm 0.01$ | $1.12^{+0.61}_{-0.36}\,(\text{stat}) \pm 0.10\,(\text{syst})$ | Belle'19 [86] | $< 1.0\,\sigma$ |
| $R_{K*+}$ | $[0.045, 1.1]$ | $0.91 \pm 0.03$ | $0.62^{+0.60}_{-0.36}\,(\text{stat}) \pm 0.09\,(\text{syst})$ | Belle'19 [86] | $< 1.0\,\sigma$ |
| | $[0.045, 6.0]$ | $0.98 \pm 0.02$ | $0.70^{+0.18}_{-0.13}\,(\text{stat})\,^{+0.03}_{-0.04}\,(\text{syst})$ | LHCb'21 [9] | $\sim 1.4\,\sigma$ |
| | $[1.1, 6.0]$ | $1.00 \pm 0.01$ | $0.72^{+0.99}_{-0.44}\,(\text{stat}) \pm 0.15\,(\text{syst})$ | Belle'19 [86] | $< 1.0\,\sigma$ |
| | $[15, 19]$ | $1.00 \pm 0.01$ | $1.40^{+1.99}_{-0.68}\,(\text{stat}) \pm 0.12\,(\text{syst})$ | Belle'19 [86] | $< 1.0\,\sigma$ |

**Table C.5:** List of $R_{K^{(*)}}$ observables for selected $q^2$-bins used in our fit. We state the experimental results while also indicating the corresponding collaboration and year of publication, *e.g.* LHCb'21. The theoretical predictions in the SM are taken from Refs. [82, 87]. The deviation of a measurement compared to its SM prediction, *i.e.* the pull from the SM in terms of standard deviations, is also provided. Notably, the experimental results from Belle are compatible with the SM due to their large uncertainties.

## C.2 Fit results and supplementary plots

In what follows, we display all results following the fit procedure outlined in Chap. 4. In doing so, we iterate the fit results of Chap. 4 in Tabs. C.7 and C.8 for clarity. Revised fit results employing updated measurements of some observables are compiled in Tabs. C.9 and C.10. Additional information can be fetched from Tab. C.6.

| Fit | Fit Table | Updated measurements | $n_{\text{obs}}$ | $\chi^2_{\text{SM}}$ |
|---|---|---|---|---|
| no $R_{K^{(*)}}$ | Table C.7 | ✗ | 162 | 183.33 |
| with $R_{K^{(*)}}$ | Table C.8 | ✗ | 189 | 223.48 |
| no $R_{K^{(*)}}$ | Table C.9 | ✓ | 165 | 189.16 |
| with $R_{K^{(*)}}$ | Table C.10 | ✓ | 194 | 232.93 |

**Table C.6:** Additional meta data for the fit scenarios presented in this thesis. The tick denotes fits that include the updated measurements (see explanation at the end of App. C.1). $n_{\text{obs}}$ denotes the number of observables included in the respective fit approach, whereas $\chi^2_{\text{SM}}$ is the $\chi^2$ function evaluated for SM-like (*i.e.* zero-valued) fit parameters.

The fit results in Tab. C.7 using only pure $b\to s\,\mu^+\mu^-$ data (called 'no $R_{K^{(*)}}$') have been utilised in the work of Ref. [20], and are presented in Chap. 9. Conversely, the best-fit values of scenarios including $R_{K^{(*)}}$ and $B^0\to K^{*0}\,e^+e^-$ observables (called 'with $R_{K^{(*)}}$') in Tab. C.8 feature in the study of Planck-safe $Z'$ models explaining the $B$-anomalies in Ref. [21]. They are discussed in Chap. 8. Dedicated best-fit scenarios and their impact on BSM models are presented in Chap. 4. Therein, Figs. 4.1 and 4.2 display the likelihood contours of global fit results and different (sub)sets of observables for the 6d and 2d fit scenarios, respectively. Additional plots that show different sets of observables are collected in Figs. C.1 and C.2.

Global fits with pure $b\to s\,\mu^+\mu^-$ data ('no $R_{K^{(*)}}$')

| Dim. | $\mathcal{C}_{9,\mu}$ | $\mathcal{C}_{10,\mu}$ | $\mathcal{C}'_{9,\mu}$ | $\mathcal{C}'_{10,\mu}$ | $\mathcal{C}_7$ | $\mathcal{C}'_7$ | red$\chi^2$ | pull$_{\text{SM}}$ |
|---|---|---|---|---|---|---|---|---|
| 1 | $-0.91\pm0.18$ | - | - | - | - | - | 1.00 | $4.5\,\sigma$ |
| 1 | $-0.68\pm0.16$ | $-\mathcal{C}_{9,\mu}$ | - | - | - | - | 0.99 | $4.7\,\sigma$ |
| 2 | $-1.02\pm0.19$ | $0.46\pm0.18$ | - | - | - | - | 0.96 | $4.9\,\sigma$ |
| 4 | $-1.13\pm0.18$ | $0.31\pm0.21$ | $0.29\pm0.33$ | $-0.24\pm0.19$ | - | - | 0.92 | $5.0\,\sigma$ |
| 6 | $-1.15\pm0.18$ | $0.30\pm0.20$ | $0.22\pm0.34$ | $-0.24\pm0.19$ | $0.002\pm0.01$ | $0.02\pm0.02$ | 0.91 | $4.6\,\sigma$ |

**Table C.7:** Duplicate of Tab. 4.1, given here for clarity.
Best-fit values and $1\,\sigma$ uncertainties of the Wilson coefficients from a fit with only pure $b\to s\,\mu^+\mu^-$ data for different NP scenarios. We also provide the respective value of red$\chi^2$ and pull from the SM hypothesis. *Table taken from Ref.* [20].

Global fits including $R_{K^{(*)}}$ data ('with $R_{K^{(*)}}$')

| Dim. | $\mathcal{C}_{9,\mu}$ | $\mathcal{C}_{10,\mu}$ | $\mathcal{C}'_{9,\mu}$ | $\mathcal{C}'_{10,\mu}$ | $\mathcal{C}_7$ | $\mathcal{C}'_7$ | red$\chi^2$ | pull$_{\text{SM}}$ |
|---|---|---|---|---|---|---|---|---|
| 1 | $-0.83 \pm 0.14$ | - | - | - | - | - | 0.98 | $6.0\,\sigma$ |
| 1 | $-0.41 \pm 0.07$ | $-\mathcal{C}_{9,\mu}$ | - | - | - | - | 0.99 | $6.0\,\sigma$ |
| 2 | $-0.71 \pm 0.17$ | $0.20 \pm 0.13$ | - | - | - | - | 0.97 | $5.9\,\sigma$ |
| 4 | $-1.07 \pm 0.17$ | $0.18 \pm 0.15$ | $0.27 \pm 0.32$ | $-0.28 \pm 0.19$ | - | - | 0.90 | $6.5\,\sigma$ |
| 6 | $-1.08 \pm 0.18$ | $0.18 \pm 0.15$ | $0.27 \pm 0.34$ | $-0.28 \pm 0.17$ | $0.0005 \pm 0.01$ | $0.005 \pm 0.006$ | 0.89 | $6.1\,\sigma$ |

**Table C.8:** Duplicate of Tab. 4.2, given here for clarity.
Best-fit values and $1\,\sigma$ uncertainties of the Wilson coefficients from a fit also including the observables listed in Tab. C.4 for different NP scenarios. We also provide the respective value of red$\chi^2$ and pull from the SM hypothesis. *Table taken from Ref.* [20].

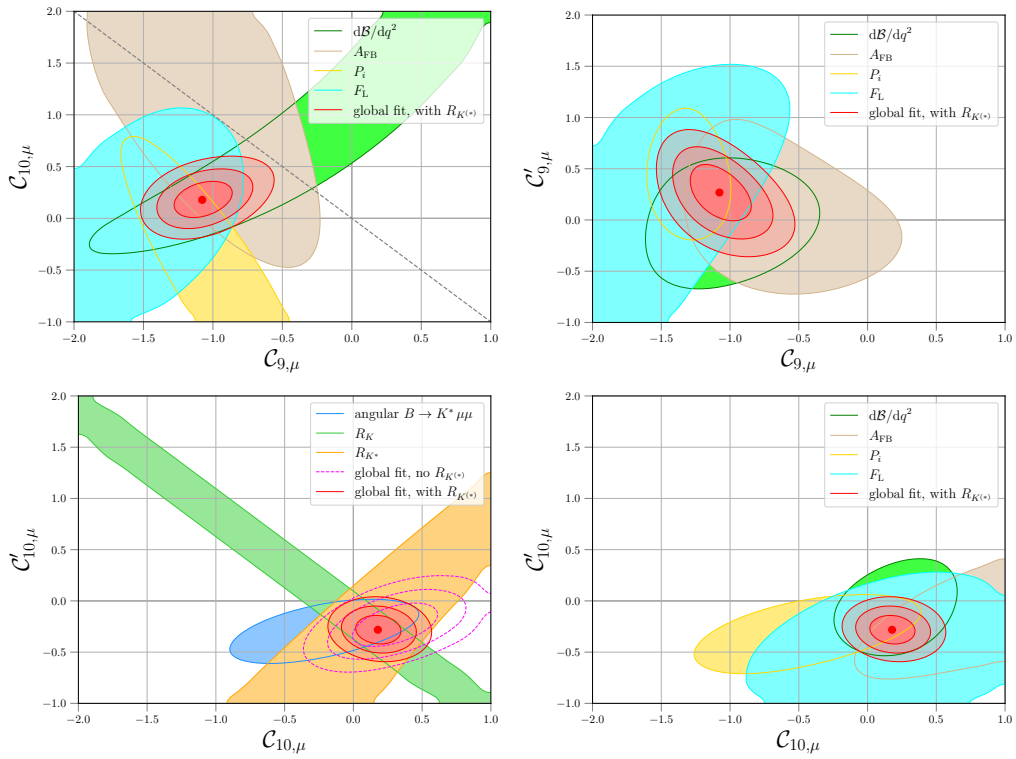


**Figure C.1:** Supplementary contour plots to Fig. 4.1 that show different likelihood contours in the 6d fit scenario 'with $R_{K^{(*)}}$', where the lower two plots display contours in the $\mathcal{C}_{10,\mu}$-$\mathcal{C}'_{10,\mu}$ plane.

## Fit results that include updated measurements

In Tabs. C.9 and C.10, the results using the updated measurements are compiled. In Fig. C.3, the $3\,\sigma$ contours for the 6d fit scenario are shown. We compare the preferred parameter regions to illustrate the small but visible change when including the updated measurements. Nonetheless,

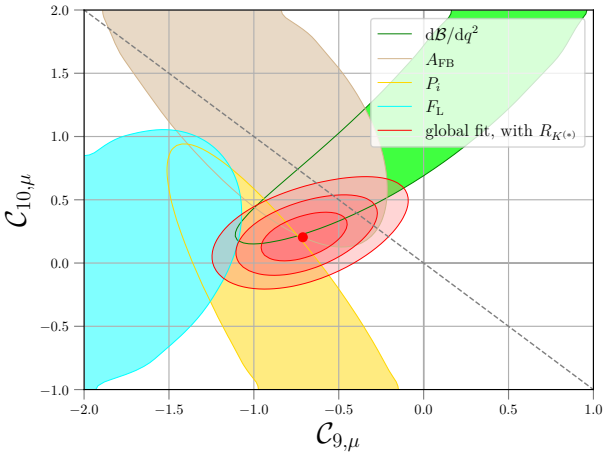


**Figure C.2:** Supplementary contour plot to Fig. 4.2 that shows different likelihood contours in the 2d fit scenario 'with $R_{K^{(*)}}$'.

we stress that this update has no major impact on the overall fit results and implications for the model building in this thesis. Thus, we only present the updated results in this appendix, while the *published* results in Tabs. C.7 and C.8 are employed for all related studies.

Updated global fits with pure $b\to s\,\mu^+\mu^-$ data ('no $R_{K^{(*)}}$')

| Dim. | $\mathcal{C}_{9,\mu}$ | $\mathcal{C}_{10,\mu}$ | $\mathcal{C}'_{9,\mu}$ | $\mathcal{C}'_{10,\mu}$ | $\mathcal{C}_7$ | $\mathcal{C}'_7$ | $\mathrm{red}\chi^2$ | $\mathrm{pull}_{\mathrm{SM}}$ |
|---|---|---|---|---|---|---|---|---|
| 1 | $-0.84 \pm 0.21$ | - | - | - | - | - | 1.07 | $3.5\,\sigma$ |
| 1 | $-0.58 \pm 0.12$ | $-\mathcal{C}_{9,\mu}$ | - | - | - | - | 1.00 | $4.9\,\sigma$ |
| 2 | $-1.07 \pm 0.21$ | $0.50 \pm 0.13$ | - | - | - | - | 0.97 | $5.1\,\sigma$ |
| 4 | $-1.13 \pm 0.19$ | $0.26 \pm 0.20$ | $0.19 \pm 0.33$ | $-0.26 \pm 0.17$ | - | - | 0.93 | $5.1\,\sigma$ |
| 6 | $-1.17 \pm 0.20$ | $0.25 \pm 0.20$ | $0.10 \pm 0.34$ | $-0.27 \pm 0.17$ | $0.002 \pm 0.01$ | $0.02 \pm 0.02$ | 0.93 | $4.7\,\sigma$ |

**Table C.9:** Same as Tab. C.7 but for the *updated* fit.

Updated global fits including $R_{K^{(*)}}$ data ('with $R_{K^{(*)}}$')

| Dim. | $\mathcal{C}_{9,\mu}$ | $\mathcal{C}_{10,\mu}$ | $\mathcal{C}'_{9,\mu}$ | $\mathcal{C}'_{10,\mu}$ | $\mathcal{C}_7$ | $\mathcal{C}'_7$ | $\mathrm{red}\chi^2$ | $\mathrm{pull}_{\mathrm{SM}}$ |
|---|---|---|---|---|---|---|---|---|
| 1 | $-0.81 \pm 0.15$ | - | - | - | - | - | 1.03 | $5.7\,\sigma$ |
| 1 | $-0.42 \pm 0.07$ | $-\mathcal{C}_{9,\mu}$ | - | - | - | - | 0.99 | $6.4\,\sigma$ |
| 2 | $-0.61 \pm 0.17$ | $0.32 \pm 0.10$ | - | - | - | - | 0.98 | $6.2\,\sigma$ |
| 4 | $-1.08 \pm 0.18$ | $0.16 \pm 0.14$ | $0.17 \pm 0.30$ | $-0.31 \pm 0.15$ | - | - | 0.91 | $6.8\,\sigma$ |
| 6 | $-1.09 \pm 0.18$ | $0.15 \pm 0.14$ | $0.16 \pm 0.30$ | $-0.32 \pm 0.15$ | $0.001 \pm 0.01$ | $0.005 \pm 0.004$ | 0.91 | $6.4\,\sigma$ |

**Table C.10:** Same as Tab. C.8 but for the *updated* fit.

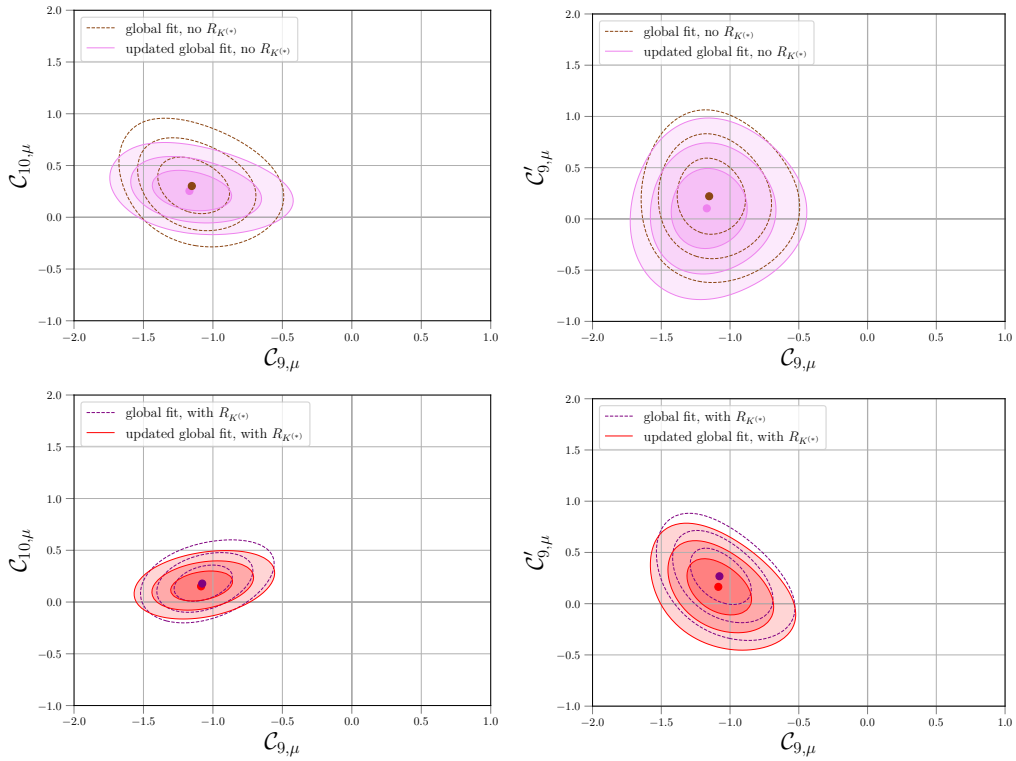


**Figure C.3:** Comparison of likelihood contours (at 1-3 $\sigma$) for 6d fit scenarios where selected planes of Wilson coefficients are displayed.

## C.3 Correlation of the fit parameters

The correlation matrices for the fit results 'no $R_{K^{(*)}}$' in Tab. C.7 are given by

$$\text{Corr}\,(\text{2d}) = \begin{pmatrix} 1.000 & -0.257 \\ -0.257 & 1.000 \end{pmatrix}, \tag{C.2}$$

$$\text{Corr}\,(\text{4d}) = \begin{pmatrix} 1.000 & -0.109 & 0.128 & 0.251 \\ -0.109 & 1.000 & 0.285 & 0.507 \\ 0.128 & 0.285 & 1.000 & 0.664 \\ 0.251 & 0.507 & 0.664 & 1.000 \end{pmatrix}, \tag{C.3}$$

$$\text{Corr}\,(\text{6d}) = \begin{pmatrix} 1.000 & -0.107 & 0.166 & 0.253 & -0.200 & -0.129 \\ -0.107 & 1.000 & 0.307 & 0.515 & 0.098 & -0.070 \\ 0.166 & 0.307 & 1.000 & 0.654 & 0.058 & -0.232 \\ 0.253 & 0.515 & 0.654 & 1.000 & 0.051 & -0.001 \\ -0.200 & 0.098 & 0.058 & 0.051 & 1.000 & 0.046 \\ -0.129 & -0.070 & -0.232 & -0.001 & 0.046 & 1.000 \end{pmatrix}, \tag{C.4}$$

where the columns are ordered as $\{\mathcal{C}_{9,\mu}, \mathcal{C}_{10,\mu}\}$, $\{\mathcal{C}_{9,\mu}, \mathcal{C}_{10,\mu}, \mathcal{C}'_{9,\mu}, \mathcal{C}'_{10,\mu}\}$, and $\{\mathcal{C}_{9,\mu}, \mathcal{C}_{10,\mu}, \mathcal{C}'_{9,\mu}, \mathcal{C}'_{10,\mu}, \mathcal{C}_7, \mathcal{C}'_7\}$ for the 2d, 4d, and 6d scenarios, respectively.

The parameters of the fit 'with $R_{K^{(*)}}$' shown in Tab. C.8 are correlated like so,

$$\text{Corr}\,(\text{2d}) = \begin{pmatrix} 1.000 & 0.479 \\ 0.479 & 1.000 \end{pmatrix}, \tag{C.5}$$

$$\text{Corr}\,(\text{4d}) = \begin{pmatrix} 1.000 & 0.350 & 0.133 & 0.427 \\ 0.350 & 1.000 & 0.562 & 0.502 \\ 0.133 & 0.562 & 1.000 & 0.799 \\ 0.427 & 0.502 & 0.799 & 1.000 \end{pmatrix}, \tag{C.6}$$

$$\text{Corr}\,(\text{6d}) = \begin{pmatrix} 1.000 & -0.486 & -0.366 & 0.107 & -0.212 & 0.011 \\ -0.486 & 1.000 & 0.632 & 0.310 & 0.146 & -0.036 \\ -0.366 & 0.632 & 1.000 & 0.726 & 0.148 & -0.033 \\ 0.107 & 0.310 & 0.726 & 1.000 & 0.055 & 0.001 \\ -0.212 & 0.146 & 0.148 & 0.055 & 1.000 & -0.010 \\ 0.011 & -0.036 & -0.033 & 0.001 & -0.010 & 1.000 \end{pmatrix}. \tag{C.7}$$

For the updated fit results 'no $R_{K^{(*)}}$' in Tab. C.9 the following correlations are present

$$\text{Corr}\,(2\text{d}) = \begin{pmatrix} 1.000 & -0.288 \\ -0.288 & 1.000 \end{pmatrix}, \tag{C.8}$$

$$\text{Corr}\,(4\text{d}) = \begin{pmatrix} 1.000 & -0.047 & 0.123 & 0.168 \\ -0.047 & 1.000 & 0.412 & 0.752 \\ 0.123 & 0.412 & 1.000 & 0.596 \\ 0.168 & 0.752 & 0.596 & 1.000 \end{pmatrix}, \tag{C.9}$$

$$\text{Corr}\,(6\text{d}) = \begin{pmatrix} 1.000 & -0.046 & 0.181 & 0.175 & -0.201 & -0.186 \\ -0.046 & 1.000 & 0.420 & 0.754 & 0.102 & -0.059 \\ 0.181 & 0.420 & 1.000 & 0.593 & 0.054 & -0.280 \\ 0.175 & 0.754 & 0.593 & 1.000 & 0.044 & -0.046 \\ -0.201 & 0.102 & 0.054 & 0.044 & 1.000 & 0.050 \\ -0.186 & -0.059 & -0.280 & -0.046 & 0.050 & 1.000 \end{pmatrix}, \tag{C.10}$$

while the updated fit results 'with $R_{K^{(*)}}$' compiled in Tab. C.10 feature

$$\text{Corr}\,(2\text{d}) = \begin{pmatrix} 1.000 & 0.405 \\ 0.405 & 1.000 \end{pmatrix}, \tag{C.11}$$

$$\text{Corr}\,(4\text{d}) = \begin{pmatrix} 1.000 & 0.444 & 0.171 & 0.484 \\ 0.444 & 1.000 & 0.650 & 0.691 \\ 0.171 & 0.650 & 1.000 & 0.772 \\ 0.484 & 0.691 & 0.772 & 1.000 \end{pmatrix}, \tag{C.12}$$

$$\text{Corr}\,(6\text{d}) = \begin{pmatrix} 1.000 & 0.445 & 0.174 & 0.486 & -0.127 & -0.020 \\ 0.445 & 1.000 & 0.652 & 0.693 & -0.007 & -0.024 \\ 0.174 & 0.652 & 1.000 & 0.773 & 0.040 & -0.022 \\ 0.486 & 0.693 & 0.773 & 1.000 & -0.017 & -0.010 \\ -0.127 & -0.007 & 0.040 & -0.017 & 1.000 & -0.007 \\ -0.020 & -0.024 & -0.022 & -0.010 & -0.007 & 1.000 \end{pmatrix}. \tag{C.13}$$

We point out the apparent strong correlations $\sim 0.5$ in the pairs $(\mathcal{C}_{10,\mu}, \mathcal{C}'_{9,\mu})$, $(\mathcal{C}_{10,\mu}, \mathcal{C}'_{10,\mu})$, $(\mathcal{C}'_{9,\mu}, \mathcal{C}'_{10,\mu})$, where similar findings have been presented for other global fits of, *e.g.*, Ref. [100].

*Appendix*

# D

# A brief review of gauge anomalies

In this appendix, we offer a basic understanding of gauge anomalies and their cancellation to obtain a consistent QFT. Later, we discuss anomaly cancellation in the SM as a useful example. For details on this topic we refer to the literature, *e.g.* Refs. [24, 251–253], while we mostly follow Ref. [254].

## D.1 Gauge anomalies in a quantum field theory

In the description of QFTs symmetries play an important role. A symmetry of the classical action is a transformation of the fields that leaves the action invariant, such as gauge transformations. When promoting the classical formalism to a QFT, these symmetries correspond to Ward and Slavnov-Taylor identities for abelian and non-abelian theories in the path integral formalism, respectively. However, these identities can be violated if the functional integral measure is not invariant under the symmetry, which prohibits a conservation of the associated quantum current. In general terms such a violation is referred to as a *gauge anomaly*.

We review the abelian anomaly as an instructive and simple example introducing a massless (complex) spin-1/2 fermion in some representation $\mathcal{R}$ of the gauge group $\mathcal{G}$ considered. The Lagrangian is given by

$$\mathcal{L} = -\frac{1}{4} F^a_{\mu\nu} F^{\mu\nu,a} + \mathcal{L}_{\text{matter}}[\psi, \bar{\psi}, D_\mu \psi, D_\mu \bar{\psi}] \,, \tag{D.1}$$

where the precise form of the field strength tensor $F^a_{\mu\nu}$ is left unspecified as it is not needed in the present discussion of anomalies. Relevant however is the fermionic part which reads

$$\mathcal{L}_{\text{matter}}[\psi, \bar{\psi}, D_\mu \psi, D_\mu \bar{\psi}] = -\bar{\psi} \not{D} \psi = -\bar{\psi} \left( \not{\partial} - \mathrm{i} \not{A}^{\mathcal{R}} \right) \psi \,. \tag{D.2}$$

Here, we assume standard interactions of the fermion with the gauge field $A$ via a covariant derivative $D_\mu$ that (in this particular example) does not include the chirality matrix $\gamma_5$. Following the path-integral formalism, we study the effect of transformations on the fermion measures $\mathcal{D}\psi$ and $\mathcal{D}\bar{\psi}$ in the effective action

$$e^{\mathrm{i}\, \widetilde{W}[A]} = \int \mathcal{D}\psi \, \mathcal{D}\bar{\psi} \, e^{\mathrm{i} \int \mathcal{L}_{\text{matter}}[\psi, \bar{\psi}, D_\mu \psi, D_\mu \bar{\psi}]} \,. \tag{D.3}$$

While local transformations

$$\begin{aligned} \psi(x) &\to \psi'(x) = U(x)\,\psi(x)\,, \\ \bar{\psi}(x) &\to \bar{\psi}'(x) = \overline{U}(x)\,\bar{\psi}(x)\,, \quad \overline{U}(x) = \mathrm{i}\gamma^0\,U^\dagger(x)\,\mathrm{i}\gamma^0\,, \end{aligned} \tag{D.4}$$

where $U(x)$ denotes a unitary matrix, generally do not leave the effective action invariant, we are interested in the effects of such transformations on the fermion measures $\mathcal{D}\psi$ and $\mathcal{D}\bar{\psi}$ only. As we consider fermion measures for anticommuting fields, they transform according to

$$\mathcal{D}\psi \to \mathcal{D}\psi' = (\det\mathcal{U})^{-1}\,\mathcal{D}\psi\,, \quad \mathcal{D}\bar{\psi} \to \mathcal{D}\bar{\psi}' = \left(\det\overline{\mathcal{U}}\right)^{-1}\,\mathcal{D}\bar{\psi}\,, \tag{D.5}$$

with the operators $\mathcal{U}$ and $\overline{\mathcal{U}}$ obtained by $\langle x|\,\mathcal{U}\,|y\rangle = U(x)\,\delta^4(x-y)$ and $\langle x|\,\overline{\mathcal{U}}\,|y\rangle = \overline{U}(x)\,\delta^4(x-y)$, respectively. In the following, we specify the matrix $U(x)$ considering two cases of non-chiral and chiral transformations.

### D.1.1 Non-chiral versus chiral unitary transformations

First, we let $U$ be a unitary non-chiral transformation of the form

$$U(x) = e^{\mathrm{i}\epsilon^\alpha(x)h_\alpha}\,, \tag{D.6}$$

with Hermitian generators $(h_\alpha)^\dagger = h_\alpha$ and $[\gamma^\mu, h_\alpha] = 0$. We find that since

$$\overline{U}(x) = \mathrm{i}\gamma^0\,e^{-\mathrm{i}\epsilon^\alpha(x)h_\alpha}\,\mathrm{i}\gamma^0 = e^{-\mathrm{i}\epsilon^\alpha(x)h_\alpha}\left(\mathrm{i}\gamma^0\right)^2 = e^{-\mathrm{i}\epsilon^\alpha(x)h_\alpha} = U^{-1}(x)\,, \tag{D.7}$$

also $\overline{\mathcal{U}} = \mathcal{U}^{-1}$, and thus the fermion measure is invariant under the transformation, *cf.* Eq. (D.5):

$$(\det\mathcal{U})^{-1}\left(\det\overline{\mathcal{U}}\right)^{-1} = 1\,. \tag{D.8}$$

We deduce that no gauge anomalies emerge for matter fields that couple non-chirally to the gauge fields. We note that assuming non-chiral couplings in the Lagrangian (D.2) is necessary to ensure gauge invariance when regularising the functional determinants $\det\mathcal{U}$ and $\det\overline{\mathcal{U}}$.

Conversely, in the case of unitary *chiral* transformations

$$U(x) = e^{\mathrm{i}\epsilon^\alpha(x)h_\alpha\,\gamma_5}\,, \tag{D.9}$$

we observe a striking difference compared to the previous case. While the fact that $\gamma_5 = (\gamma_5)^\dagger$ renders the transformation in Eq. (D.9) unitary, it follows due to the anticommutation of $\gamma_5$ and $\gamma^0$ that

$$\overline{U}(x) = \mathrm{i}\gamma^0\,e^{-\mathrm{i}\epsilon^\alpha(x)h_\alpha\gamma_5}\,\mathrm{i}\gamma^0 = e^{+\mathrm{i}\epsilon^\alpha(x)h_\alpha\gamma_5}\left(\mathrm{i}\gamma^0\right)^2 = e^{+\mathrm{i}\epsilon^\alpha(x)h_\alpha\gamma_5} = U(x)\,. \tag{D.10}$$

This yields $\overline{\mathcal{U}} = \mathcal{U}$, and thus the transformation behaviour of the fermion measure is guided by

$$(\det\mathcal{U})^{-1}\left(\det\overline{\mathcal{U}}\right)^{-1} = (\det\mathcal{U})^{-2}\,. \tag{D.11}$$

After performing some algebra [254], the above expression can be written as

$$(\det \mathcal{U})^{-2} = e^{\mathrm{i} \int \mathrm{d}^4 x \, \epsilon^\alpha \, a_\alpha(x)} \,, \tag{D.12}$$

with the local anomaly function

$$a_\alpha(x) = -2 \, \delta^4(0) \, \mathrm{tr} \, (h_\alpha \, \gamma_5) \,. \tag{D.13}$$

It can be shown that the gauge anomaly for chiral transformations can be extracted from a one-loop triangle diagram computation, displayed in Fig. D.1. Furthermore, anomalies only emerge for chiral and massless fermions in non-abelian gauge symmetries, where the contributions of $\psi_L$ and $\psi_R$ are additive and only differ sign-wise.

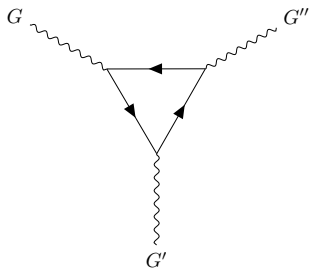


**Figure D.1:** A triangle Feynman diagram coupling to gauge bosons $G$, $G'$ and $G''$ with an inner fermion loop.

## D.1.2 Cancellation of gauge anomalies

We describe the contribution to the anomaly from LH fermions as $D^{\mathcal{R}_i^L}_{\alpha\beta\gamma}$, where $\mathcal{R}_i^L$ denotes the representation of the fermion field $\psi_{L,i}$ under the gauge group $\mathcal{G}$. Similarly, each RH fermion $\psi_{R,i}$ contributes with $-D^{\mathcal{R}_i^R}_{\alpha\beta\gamma}$. The total anomaly can be written as

$$\mathcal{A}_\alpha = \sum_i \mathcal{A}^L_\alpha|_{\psi_{L,i}} + \sum_j \mathcal{A}^R_\alpha|_{\psi_{R,j}} \propto \mathcal{P}^{\beta\gamma} \left( \sum_i D^{\mathcal{R}_i^L}_{\alpha\beta\gamma} - \sum_j D^{\mathcal{R}_j^R}_{\alpha\beta\gamma} \right) , \tag{D.14}$$

which vanishes trivially in the case of non-chiral fermions (often referred to as vector-like fermions). Here, $\mathcal{P}^{\beta\gamma}$ denotes an expression involving a partial derivative acting on combinations of gauge fields, where the explicit form is given in Ref. [254]. We define the group theoretical factor

$$\mathcal{D}^{\mathcal{R}}_{\alpha\beta\gamma} = \mathrm{str}_{\mathcal{R}} \, (h_\alpha \, h_\beta \, h_\gamma) \tag{D.15}$$

which denotes the symmetrised trace of the generators $h_\alpha$ of a corresponding gauge interaction $G$. This quantity parametrises the anomaly illustrated in Fig. D.1. Then, gauge anomalies are present if the trace in Eq. (D.15) is non-vanishing.

As there are many possible combinations of generators that can appear in Eq. (D.15), it proves crucial to know which gauge group (factors) and which representations lead to anomalies. In the following, we study possible sources of anomalies utilising the SM gauge group as an instructive

example. We refer to Refs. [253, 254] for in-depth group theoretical discussions and details on more general group structures.

## D.2 Anomaly cancellation in the standard model

The SM gauge group in the unbroken phase reads

$$\mathcal{G}_{\rm SM} = \mathrm{U}(1) \times \mathrm{SU}(2) \times \mathrm{SU}(3)\,, \tag{D.16}$$

where we have dropped the usual subscripts as in Eq. (2.1) to ease the readability in this discussion.

Naively, the following combinations can give rise to anomalies:

(1) $[\mathrm{SU}(3)]^2 \times \mathrm{SU}(2)$
(2) $\mathrm{SU}(3) \times [\mathrm{SU}(2)]^2$
(3) $\mathrm{SU}(3) \times \mathrm{SU}(2) \times \mathrm{U}(1)$
(4) $\mathrm{SU}(3) \times \mathrm{U}(1) \times \mathrm{U}(1)$
(5) $\mathrm{SU}(2) \times [\mathrm{U}(1)]^2$
(6) $[\mathrm{SU}(2)]^3$
(7) $[\mathrm{SU}(3)]^3$
(8) $[\mathrm{SU}(3)]^2 \times \mathrm{U}(1)$
(9) $[\mathrm{SU}(2)]^2 \times \mathrm{U}(1)$
(10) $[\mathrm{U}(1)]^3$
(11) U(1)-gravity

Following the labelling in Fig. D.1, we refer to the anomalies that arise from these different possibilities as $G - G' - G''$ anomalies. That being said, it is useful to distinguish between the simple U(1) factor and $G_s = \mathrm{SU}(2)$, SU(3), with traceless generators for the latter [255]:

$$\mathrm{tr}\,(h_\delta) = 0 \quad \text{for any SU}(N) \text{ Lie algebra.} \tag{D.17}$$

To this end, it is convenient to redefine the Lie algebra generators satisfying

$$\mathrm{tr}_{\mathcal{R}}\,(h_\alpha\, h_\beta) = \mathrm{tr}\left(h^{\mathcal{R}}_\alpha\, h^{\mathcal{R}}_\beta\right) = g_i^2\, C^{(i)}_{\mathcal{R}}\, \delta_{\alpha\beta}\,, \tag{D.18}$$

for each simple and $G_i$ factor. Here, $g_i$ and $C^{(i)}_{\mathcal{R}}$ denote the associated gauge coupling and the Casimir, respectively, with, *e.g.*, $C_N = C_{\overline{N}} = 1/2$ for $G_i = \mathrm{SU}(N)$. We can dismiss certain cases above. The cases $(1) - (5)$ yield vanishing contributions, where the trace can be factorised as always one non-abelian factor $G_s$ appears alone. Moreover, only non-zero contributions arise if a U(1) *and* SU($N$) with $n \geq 3$ are involved, which renders $D^{\mathcal{R}}_{\alpha\beta\gamma} = 0$ for case (6). While (7) also gives no contribution, it is not obvious at first glance on why this is true. Here, we make use of the fact that also for groups with only real or pseudoreal representations no contributions appear. Then, considering the SM fermions in Tab. 2.1 (reading the table from top to bottom) the total (reducible) SU(3) representations that occur are given by $R = (3+3) + \overline{3} + \overline{3} + (1+1)$. As $\overline{3}$ is the complex conjugate of 3, we find only real representations entailing $D^{\mathcal{R}}_{\alpha\beta\gamma} = 0$.

For the four remaining cases we need to check if anomalies emerge by evaluating the trace of generators explicitly. Using the group theoretical properties defined above, we obtain dedicated equations for each of the cases which we collectively call anomaly cancellation conditions (ACCs).

Obviously, all these conditions need to hold for a consistent QFT. We summarise

$$[\mathrm{SU}(3)]^2 \times \mathrm{U}(1): \quad A_{331} = \mathrm{tr}_{\mathcal{R}}\left(t_\alpha\, t_\beta\, Y\right), \tag{D.19}$$

$$[\mathrm{SU}(2)]^2 \times \mathrm{U}(1): \quad A_{221} = \mathrm{tr}_{\mathcal{R}}\left(T_\alpha\, T_\beta\, Y\right), \tag{D.20}$$

$$[\mathrm{U}(1)]^3: \quad A_{111} = \mathrm{tr}_{\mathcal{R}}\left(Y\, Y\, Y\right), \tag{D.21}$$

$$\mathrm{U}(1)\text{-gravity}: \quad A_{gg1} = \mathrm{tr}_{\mathcal{R}}\left(Y\right), \tag{D.22}$$

where $Y$, $T$, and $t$ denote the generators of U(1), SU(2), and SU(3), respectively, see Eq. (2.6). Starting with Eq. (D.19), we confirm that indeed the SM with its known fermions is free of any gauge anomaly. For brevity, we consider only one generation of fermions while utilising the fermion charges and representations listed in Tab. 2.1.

For the combination $[\mathrm{SU}(3)]^2 \times \mathrm{U}(1)$ only fermions charged under both SU(3) and U(1) contribute (in this case the quarks), where we need to consider the *multiplicity* (of SU(2)) of each fermion. Rewriting the trace yields

$$\begin{aligned} A_{331} = \mathrm{tr}\left(t_\alpha^{\mathcal{R}}\, t_\beta^{\mathcal{R}}\, Y^{\mathcal{R}}\right) &= 2\,\mathrm{tr}\left(t_\alpha^3\, t_\beta^3\right)\cdot\left(-\frac{1}{6}\,g_1\right) \\ &\quad + \mathrm{tr}\left(t_\alpha^{\bar{3}}\, t_\beta^{\bar{3}}\right)\cdot\left(\frac{2}{3}\,g_1\right) + \mathrm{tr}\left(t_\alpha^{\bar{3}}\, t_\beta^{\bar{3}}\right)\cdot\left(-\frac{1}{3}\,g_1\right) \\ &= g_3\, g_1\, C_3\, \delta_{\alpha\beta}\left(-2\cdot\frac{1}{6} + \frac{2}{3} - \frac{1}{3}\right) = 0\,. \end{aligned} \tag{D.23}$$

In an analogous manner, we obtain for Eq. (D.20) the expression

$$\begin{aligned} A_{221} = \mathrm{tr}\left(T_\alpha^{\mathcal{R}}\, T_\beta^{\mathcal{R}}\, Y^{\mathcal{R}}\right) &= \mathrm{tr}\left(T_\alpha^2\, T_\beta^2\right)\cdot\left(\frac{1}{2}\,g_1\right) + 3\,\mathrm{tr}\left(T_\alpha^2\, T_\beta^2\right)\cdot\left(-\frac{1}{6}\,g_1\right) \\ &= g_2\, g_1\, C_2\, \delta_{\alpha\beta}\left(\frac{1}{2} + 3\cdot\left(-\frac{1}{6}\right)\right) = 0\,, \end{aligned} \tag{D.24}$$

where solely SU(2) doublets contribute accounting for the multiplicity of SU(3). For the two remaining combinations in Eq. (D.21) and Eq. (D.22) we find vanishing contributions in both cases,

$$\begin{aligned} A_{111} = \mathrm{tr}\left(Y^{\mathcal{R}}\, Y^{\mathcal{R}}\, Y^{\mathcal{R}}\right) &= 2\cdot\left(\frac{1}{2}\,g_1\right)^3 + (-g_1)^3 + 3\cdot 2\cdot\left(-\frac{1}{6}\,g_1\right)^3 \\ &\quad + 3\cdot\left(\frac{2}{3}\,g_1\right)^3 + 3\cdot\left(-\frac{1}{3}\,g_1\right)^3 = 0\,, \end{aligned} \tag{D.25}$$

$$\begin{aligned} A_{gg1} = \mathrm{tr}\left(Y^{\mathcal{R}}\right) &= 2\cdot\left(\frac{1}{2}\,g_1\right) + (-g_1) + 3\cdot 2\cdot\left(-\frac{1}{6}\,g_1\right) \\ &\quad + 3\cdot\left(\frac{2}{3}\,g_1\right) + 3\cdot\left(-\frac{1}{3}\,g_1\right) = 0\,. \end{aligned} \tag{D.26}$$

This demonstrates that each generation of the SM is an anomaly-free set, and therefore the full SM with all three generations features no gauge anomalies. The same holds true for the broken phase of the SM following similar reasoning for anomaly cancellation in $\mathrm{SU}(3)_C \times \mathrm{U}(1)_{\mathrm{em}}$.

## D.3 Anomaly cancellation in new physics scenarios

This work focuses on NP models that involve an extended gauge group with a new $Z'$ gauge boson. The absence of gauge anomalies enforces new conditions on this interaction, in particular on the associated charges of fermions. This concerns not only the SM fermions, but also (possible) new fermions that might be included in BSM model building. We study the details of such ACCs in Sec. 5.2, and give some remarks regarding the general idea of these conditions in terms of BSM physics in the following.

We emphasise that new chiral fermions, which are differently charged under the SM gauge group, add to the gauge anomaly. Hence, they need to be fixed according to the above ACCs. Consequently, BSM fermions are often included as vector-like or even as SM-singlets (meaning trivially charged under the SM gauge group) to evade this issue completely. Then, only the ACCs involving the new gauge group factor need to be taken into account. While also grand unified theories, such as lepton-colour unification in Pati-Salam models [256], can be considered, more commonly studied are extensions of the SM gauge group by an additional $\mathrm{U}(1)'$ factor. In this particular case, six conditions have to be met that are given in Eq. (5.24). These conditions exhibit a similar structure as the SM ones, where instead the new charges play the role of the hypercharge. Indeed, the fermion hypercharges in the SM are chosen such that the ACCs in Eqs. (D.19) to (D.22) are satisfied.

*Appendix*

# E

# Parametrisations of $q^2$-distributions in rare charm decays

In this appendix, we provide the parametrisation of $c \to u\,\ell^+\ell^-$ decay distributions taken from Ref. [16]. Numerical values of the resonance parameters are provided in Tab. E.1, whereas masses, decay constants, and lifetimes can be found in App. B. Some information on $D \to P$ form factors is given at the end of this chapter.

## E.1 Lepton flavour conserving decays

Within the EFT framework outlined in Eq. (6.2), we parametrise the differential semileptonic decay distribution $D \to P\ell^+\ell^-$ as

$$\begin{aligned}
\frac{\mathrm{d}\Gamma}{\mathrm{d}q^2} = \frac{G_\mathrm{F}^2\,\alpha_e^2}{1024\,\pi^5\,m_D^3}\sqrt{\lambda_{DP}\left(1-\frac{4m_\ell^2}{q^2}\right)}\Bigg\{ & \\
& \frac{2}{3}\left|\mathcal{C}_9 + \mathcal{C}_9^\mathrm{R} + \mathcal{C}_7\frac{2m_c}{m_D+m_P}\frac{f_T}{f_+}\right|^2\left(1+\frac{2m_\ell^2}{q^2}\right)\lambda_{DP}f_+^2 \\
& + |\mathcal{C}_{10}|^2\left[\frac{2}{3}\left(1-\frac{4m_\ell^2}{q^2}\right)\lambda_{DP}f_+^2 + \frac{4m_\ell^2}{q^2}(m_D^2-m_P^2)^2 f_0^2\right] \\
& + \left[|\mathcal{C}_S|^2\left(1-\frac{4m_\ell^2}{q^2}\right) + |\mathcal{C}_P+\mathcal{C}_P^\mathrm{R}|^2\right]\frac{q^2}{m_c^2}(m_D^2-m_P^2)^2 f_0^2 \\
& + \frac{4}{3}\left[|\mathcal{C}_T|^2+|\mathcal{C}_{T5}|^2\right]\left(1-\frac{4m_\ell^2}{q^2}\right)\frac{q^2}{(m_D+m_P)^2}\lambda_{DP}f_T^2 \\
& + 8\,\mathrm{Re}\left(\left[\mathcal{C}_9+\mathcal{C}_9^\mathrm{R}+\mathcal{C}_7\frac{2m_c}{m_D+m_P}\frac{f_T}{f_+}\right]\mathcal{C}_T^*\right)\frac{m_\ell}{m_D+m_P}\lambda_{DP}f_+f_T \\
& + 4\,\mathrm{Re}\left(\mathcal{C}_{10}\left(\mathcal{C}_P+\mathcal{C}_P^\mathrm{R}\right)^*\right)\frac{m_\ell}{m_c}(m_D^2-m_P^2)^2 f_0^2 + 16\,|\mathcal{C}_T|^2\frac{m_\ell^2}{(m_D+m_P)^2}\lambda_{DP}f_T^2\Bigg\}\,,
\end{aligned} \tag{E.1}$$

with $\lambda_{DP} = \lambda(m_D^2, m_P^2, q^2)$ defined in Eq. (B.4). In Eq. (E.1), we have neglected the up-quark mass and applied the notation $\mathcal{C}_i \to \mathcal{C}_i + \mathcal{C}_i'$ to condense LH and RH quark-current contributions [16].

The $q^2$-integrated decay rate is readily obtained as

$$\Gamma = \Gamma\left(q^2_{\text{min}}, q^2_{\text{max}}\right) = \int_{q^2_{\text{min}}}^{q^2_{\text{max}}} \frac{\mathrm{d}\Gamma}{\mathrm{d}q^2}\,\mathrm{d}q^2\,. \tag{E.2}$$

The full leptonic $D^0 \to \ell^+\ell^-$ branching ratio reads

$$\begin{aligned}\mathcal{B}\left(D^0 \to \ell^+\ell^-\right) = \tau_{D^0}\frac{G_{\text{F}}^2\,\alpha_e^2\,m_{D^0}^5\,f_D^2}{64\,\pi^3\,m_c^2}\sqrt{1-\frac{4m_\ell^2}{m_{D^0}^2}}\Bigg[\left(1-\frac{4m_\ell^2}{m_{D^0}^2}\right)|\mathcal{C}_S-\mathcal{C}_S'|^2 \\ + \left|\mathcal{C}_P-\mathcal{C}_P'+\frac{2m_\ell\,m_c}{m_{D^0}^2}\left(\mathcal{C}_{10}-\mathcal{C}_{10}'\right)\right|^2\Bigg]\,,\end{aligned} \tag{E.3}$$

where $f_D$ and $\tau_{D^0}$ denote the $D^0$-meson decay constant and lifetime, respectively.

## E.2 Lepton flavour violating decays

The differential distribution for the lepton flavour violating $D \to P e^\pm \mu^\mp$ decays is given as

$$\begin{aligned}\frac{\mathrm{d}\Gamma\left(D\to P e^\pm\mu^\mp\right)}{\mathrm{d}q^2} = \frac{G_{\text{F}}^2\,\alpha_e^2}{1024\,\pi^5\,m_D^3}\sqrt{\lambda_{DP}}\Bigg\{ \\ \frac{2}{3}\left(|\mathcal{K}_9|^2+|\mathcal{K}_{10}|^2\right)\lambda_{DP}\,f_+^2 + \left(|\mathcal{K}_S|^2+|\mathcal{K}_P|^2\right)\frac{q^2}{m_c^2}(m_D^2-m_P^2)^2\,f_0^2 \\ + \frac{4}{3}\left(|\mathcal{K}_T|^2+|\mathcal{K}_{T5}|^2\right)\frac{q^2}{(m_D+m_P)^2}\lambda_{DP}\,f_T^2 \\ + 2\,\text{Re}\left(\pm\mathcal{K}_9\,\mathcal{K}_S^* + \mathcal{K}_{10}\,\mathcal{K}_P^*\right)\frac{m_\mu}{m_c}(m_D^2-m_P^2)^2\,f_0^2 \\ + 4\,\text{Re}\left(\mathcal{K}_9\,\mathcal{K}_T^* \pm \mathcal{K}_{10}\mathcal{K}_{T5}^*\right)\frac{m_\mu}{m_D+m_P}\,\lambda_{DP}\,f_+\,f_T\Bigg\} + \mathcal{O}\left(m_\mu^2\right)\,,\end{aligned} \tag{E.4}$$

where the electron mass has been neglected. Furthermore, $\mathcal{K}_i = \mathcal{K}_{i,\mu e} + \mathcal{K}'_{i,\mu e}$ and $\mathcal{K}_i = \mathcal{K}_{i,e\mu} + \mathcal{K}'_{i,e\mu}$ for $D \to P\,e^+\mu^-$ and $D \to P\,e^-\mu^+$, respectively, is understood. The branching ratio for leptonic decays reads

$$\begin{aligned}\mathcal{B}\left(D^0 \to e^\pm\mu^\mp\right) = \tau_{D^0}\frac{G_{\text{F}}^2\,\alpha_e^2\,m_{D^0}^5\,f_D^2}{64\,\pi^3\,m_c^2}\left(1-\frac{m_\mu^2}{m_{D^0}^2}\right)^2\Bigg[\left|\mathcal{K}_S-\mathcal{K}_S'\pm\frac{m_\mu\,m_c}{m_{D^0}^2}\left(\mathcal{K}_9-\mathcal{K}_9'\right)\right|^2 \\ + \left|\mathcal{K}_P-\mathcal{K}_P'+\frac{m_\mu\,m_c}{m_{D^0}^2}\left(\mathcal{K}_{10}-\mathcal{K}_{10}'\right)\right|^2\Bigg]\,.\end{aligned} \tag{E.5}$$

| | $a_\rho$/ GeV$^{-2}$ | $a_\phi$/ GeV$^{-2}$ | $a_\eta$/ GeV$^{-2}$ | $a_{\eta'}$/ GeV$^{-2}$ |
|---|---|---|---|---|
| $D^+ \to \pi^+$ | $0.18 \pm 0.02$ | $0.23 \pm 0.01$ | $(5.7 \pm 0.4) \times 10^{-4}$ | $\sim 8 \times 10^{-4}$ |
| $D^0 \to \pi^0$ | $0.86 \pm 0.04$ | $0.25 \pm 0.01$ | $(5.3 \pm 0.4) \times 10^{-4}$ | $\sim 8 \times 10^{-4}$ |
| $D_s \to K$ | $0.48 \pm 0.04$ | $0.07 \pm 0.01$ | $(5.9 \pm 0.7) \times 10^{-4}$ | $\sim 7 \times 10^{-4}$ |

**Table E.1:** Phenomenological resonance parameters in Eq. (6.10) extracted from the experimental measurements of $\mathcal{B}(D \to \pi M)$ and $\mathcal{B}(D_s \to K M)$ [155] with resonances $M = \rho, \phi, \eta, \eta'$ decaying to $\mu^+\mu^-$. *Table taken from Ref.* [16].

## E.3 $D \to$ P form factors

The HMEs for $D$-meson decays into a pseudoscalar $P$ can be parametrised as [154]

$$\langle P(k)|\,\overline{u}\,\gamma^\mu\,c\,|D(p)\rangle = \left[(p+k)^\mu - \frac{m_D^2 - m_P^2}{q^2}\,q^\mu\right] f_+(q^2) + q^\mu \frac{m_D^2 - m_P^2}{q^2}\,f_0(q^2)\,, \tag{E.6}$$

$$\langle P(k)|\,\overline{u}\,\sigma^{\mu\nu}\,(1 \pm \gamma_5)\,c\,|D(p)\rangle = -\mathrm{i}\,(p^\mu k^\nu - k^\mu p^\nu \pm \mathrm{i}\,\epsilon^{\mu\nu\rho\sigma}\,p_\rho\,k_\sigma)\frac{2\,f_T(q^2)}{m_D + m_P}\,, \tag{E.7}$$

where $q^\mu = (p_D - p_P)^\mu = (p_{\ell^+} + p_{\ell^-})^\mu$. We identify the form factors $f_{+,0}(q^2)$ and $f_T(q^2)$ in the vector and tensor current, respectively.

In this thesis, we use the $D \to \pi$ and $D \to K$ form factors available in Refs. [225, 257] where lattice QCD methods have been employed. The form factors are described via the $z$-expansion

$$f_i(q^2) = \frac{1}{1 - P_i\,q^2}\left[f_i(0) + c_i\,\big(z(q^2) - z(0)\big)\,\left(1 + \frac{z(q^2) + z(0)}{2}\right)\right], \tag{E.8}$$

for $i = +, 0, T$, and with

$$z(q^2) = \frac{\sqrt{t_+ - q^2} - \sqrt{t_+ - t_0}}{\sqrt{t_+ - q^2} + \sqrt{t_+ - t_0}}\,, \quad t_\pm = (m_D \pm m_P)^2\,, \quad t_0 = \sqrt{t_+}\,(\sqrt{m_D} - \sqrt{m_P})^2\,. \tag{E.9}$$

We refer to Refs. [225, 257] for numerical values of the $f_i(0)$, $c_i$, and $P_i$ parameters, where central values as well as their covariances are provided. Values for the form factor $f_0(q^2)$ at low $q^2$, *i.e.* $q^2 = 0$ and $q^2 = m_P^2$, are given in Tab. B.3. We note that for $D^0 \to \pi^0$ decays the respective form factors receive an additional isospin factor $f_i \to f_i/\sqrt{2}$, following $|\pi^0\rangle = 1/\sqrt{2}\,\big(|\overline{u}u\rangle - |\overline{d}d\rangle\big)$ [1]. Moreover, for $D_s \to K$ decays we use the $D \to \pi$ form factors [16, 258]. See Appendix A of Ref. [16] and references therein for further details.

[1] This normalisation is also employed when computing the branching ratio $\mathcal{B}\left(D^+ \to \pi^+\pi^0\right)$, whereas it cancels for $\mathcal{B}\left(D^0 \to \pi^0\pi^0\right)$ due to identical particles in the final states, see Eq. (7.15).

*Appendix*

# F

# Effective Hamiltonian and hadronic matrix elements for $\Delta c = 1$ processes

In the following, we provide the full effective Hamiltonian relevant for $\Delta c = 1$ processes. We summarise the effective operators as well as NP operators induced by a $Z'$ boson in App. F.1. Details on the RG evolution of the new four-quark operators are provided in App. F.2. In App. F.3, we present calculations of hadronic matrix elements (HMEs) in the naive factorisation ansatz.

## F.1 Overview of effective operators

The relevant contributions to the SCS $D$-meson decays, *i.e.* $D^0 \to K^+K^-$ and $D^0 \to \pi^+\pi^-$, can be described by the following effective Hamiltonian at the scale $m_b < \mu < \mu_{\text{EW}}$ [168, 177]

$$\begin{aligned}\mathcal{H}_{\text{eff}}^{\Delta c=1} = \frac{G_{\text{F}}}{\sqrt{2}}\Bigg[ \sum_p \lambda_p \sum_{i=1}^{2} \left(\mathcal{C}_i^p Q_i^p + \mathcal{C}_i'^p Q_i'^p\right) + \sum_j \left(\mathcal{C}_j Q_j + \mathcal{C}_j' Q_j'\right) \\ + \sum_k \left(\widetilde{\mathcal{C}}_k \widetilde{Q}_k + \widetilde{\mathcal{C}}_k' \widetilde{Q}_k'\right) + \sum_p \sum_l \left(\mathcal{C}_l^{(p)} Q_l^{(p)} + \mathcal{C}_l'^{(p)} Q_l'^{(p)}\right)\Bigg] + \text{h.c.}\,,\end{aligned} \tag{F.1}$$

where the index $p$ runs over all active down-type quark flavours ($p = d, s, b$) and $\lambda_p = V_{cp}V_{up}^*$. Note that $\lambda_{d,s} \sim \lambda_{\text{CKM}} \approx 0.2$, whereas $\lambda_b \sim \lambda_{\text{CKM}}^5 = \mathcal{O}\left(10^{-4}\right)$. In what follows, we define the various operators that appear in the Hamiltonian. The so-called *current-current* operators $Q_i^p$ read

$$Q_1^p = (\overline{u}p)_{V-A}(\overline{p}c)_{V-A}\,, \tag{F.2}$$

$$Q_2^p = (\overline{u}_\alpha p_\beta)_{V-A}(\overline{p}_\beta c_\alpha)_{V-A}\,, \tag{F.3}$$

where $\alpha, \beta$ denote colour indices that are implicitly summed over and $(V \pm A)$ refer to the Dirac structures $\gamma_\mu(1 \pm \gamma_5)$, *e.g.*

$$(\overline{u}p)_{V-A} = \overline{u}\,\gamma_\mu\,(1-\gamma_5)\,p = \overline{u}_\alpha\,\gamma_\mu\,(1-\gamma_5)\,p_\alpha = (\overline{u}_\alpha p_\alpha)_{V-A}\,. \tag{F.4}$$

The operator $Q_1^p$ provides the dominant tree-level SM contribution, $\mathcal{C}_1^p \simeq 1$, at the matching scale $\mu$ via a $W$-boson exchange. The corresponding Feynman diagrams relevant in this thesis are depicted in Fig. F.1. The operators in Eqs. (F.2) and (F.3) are related to the current-current

analogues $O_{1,2}^{d,s}$ introduced in Eq. (6.4) by Fierz identities and employing the colour structure embedded in the $\mathrm{SU}(3)_C$ generators.

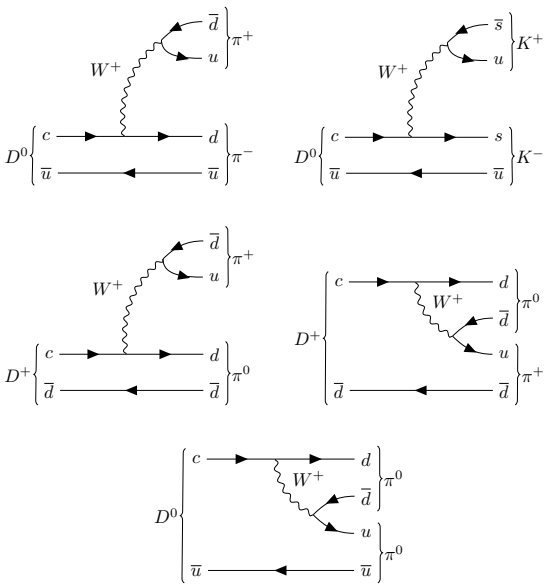


**Figure F.1:** SM tree-level contribution via a $W$ boson for selected hadronic $D$-decays.

The QCD penguin operators $Q_{3,4,5,6}$ and QED penguin operators $Q_{7,8,9,10}$ are given by

$$Q_3 = (\overline{u}c)_{V-A} \sum_q (\overline{q}q)_{V-A} \,, \tag{F.5}$$

$$Q_4 = (\overline{u}_\alpha c_\beta)_{V-A} \sum_q (\overline{q}_\beta q_\alpha)_{V-A} \,, \tag{F.6}$$

$$Q_5 = (\overline{u}c)_{V-A} \sum_q (\overline{q}q)_{V+A} \,, \tag{F.7}$$

$$Q_6 = (\overline{u}_\alpha c_\beta)_{V-A} \sum_q (\overline{q}_\beta q_\alpha)_{V+A} \,, \tag{F.8}$$

$$Q_7 = \frac{3}{2}(\overline{u}c)_{V-A} \sum_q e_q (\overline{q}q)_{V+A} \,, \tag{F.9}$$

$$Q_8 = \frac{3}{2}(\overline{u}_\alpha c_\beta)_{V-A} \sum_q e_q (\overline{q}_\beta q_\alpha)_{V+A} \,, \tag{F.10}$$

$$Q_9 = \frac{3}{2}(\overline{u}c)_{V-A} \sum_q e_q (\overline{q}q)_{V-A} \,, \tag{F.11}$$

$$Q_{10} = \frac{3}{2}(\overline{u}_\alpha c_\beta)_{V-A} \sum_q e_q (\overline{q}_\beta q_\alpha)_{V-A} \,, \tag{F.12}$$

Here, $e_q$ is the electric charge of the quark $q$. The operators $Q_{3,4,5,6}$ are first generated at $\mathcal{O}(\alpha_s)$ and proportional to $V_{ub}V_{cb}^*$. The latter is also true for the operators $Q_{7,8,9,10}$, which are negligible in the SM as they appear at $\mathcal{O}(\alpha_e)$.

The chromomagnetic operator $Q_{8g}$

$$Q_{8g} = \frac{g_s}{8\pi^2} m_c \overline{u}_\alpha \, \sigma^{\mu\nu}(1+\gamma_5)\, c_\beta t^a_{\alpha\beta}\, G^a_{\mu\nu}\,, \tag{F.13}$$

is also generated at $\mathcal{O}(\alpha_s)$, where $G^a_{\mu\nu}$ represents the strong field strength tensor. Scalar and tensor operators are given by

$$Q^{(p)}_{S1} = (\overline{u} P_L p)(\overline{p} P_L c)\,, \tag{F.14}$$
$$Q^{(p)}_{S2} = (\overline{u}_\alpha P_L p_\beta)(\overline{p}_\beta P_L c_\alpha)\,, \tag{F.15}$$
$$Q^{(p)}_{T1} = (\overline{u}\, \sigma_{\mu\nu} P_L p)(\overline{p}\, \sigma^{\mu\nu} P_L c)\,, \tag{F.16}$$
$$Q^{(p)}_{T2} = (\overline{u}_\alpha\, \sigma_{\mu\nu} P_L p_\beta)(\overline{p}_\beta \sigma^{\mu\nu} P_L c_\alpha)\,, \tag{F.17}$$

where tensor operators do not contribute to $D^0 \to K^+K^-$ and $D^0 \to \pi^+\pi^-$ decays in naive factorisation, but can mix with the scalar ones under RG running [177]. Note that the corresponding primed counterparts $Q'$ for the aforementioned operators in Eqs. (F.5) to (F.17) are obtained by the obvious replacement $\gamma_5 \to -\gamma_5$.

In this thesis, our focus lies on the current-current operators $Q^p_i$ and their relation to NP-induced operators $\widetilde{Q}^{(\prime)}_k$, which we outline in the following.

### F.1.1 New physics operators with additional U(1)′ charges

The remaining operators $\widetilde{Q}^{(\prime)}_k$ in Eq. (F.1) describe NP contributions via a $Z'$ boson. We define them as

$$\begin{aligned}\widetilde{Q}_7 &= (\overline{u}c)_{V-A} \sum_q F_{U_i,D_i}\, (\overline{q}q)_{V+A} \\ &= 4\,\bar{u}_L\gamma_\mu c_L \big(F_{U_1}\,\bar{u}_R\gamma^\mu u_R + F_{U_2}\,\bar{c}_R\gamma^\mu c_R + F_{D_1}\,\bar{d}_R\gamma^\mu d_R \\ &\quad + F_{D_2}\,\bar{s}_R\gamma^\mu s_R + F_{D_3}\,\bar{b}_R\gamma^\mu b_R\big)\,,\end{aligned} \tag{F.18}$$
$$\widetilde{Q}'_7 = (\overline{u}c)_{V+A} \sum_q F_{Q_i}\, (\overline{q}q)_{V-A}\,, \tag{F.19}$$
$$\widetilde{Q}_8 = (\overline{u}_\alpha c_\beta)_{V-A} \sum_q F_{U_i,D_i}\, (\overline{q}_\beta q_\alpha)_{V+A}\,, \tag{F.20}$$
$$\widetilde{Q}'_8 = (\overline{u}_\alpha c_\beta)_{V+A} \sum_q F_{Q_i}\, (\overline{q}_\beta q_\alpha)_{V-A}\,, \tag{F.21}$$
$$\widetilde{Q}_9 = (\overline{u}c)_{V-A} \sum_q F_{Q_i}\, (\overline{q}q)_{V-A}\,, \tag{F.22}$$
$$\widetilde{Q}'_9 = (\overline{u}c)_{V+A} \sum_q F_{U_i,D_i}\, (\overline{q}q)_{V+A}\,, \tag{F.23}$$
$$\widetilde{Q}_{10} = (\overline{u}_\alpha c_\beta)_{V-A} \sum_q F_{Q_i}\, (\overline{q}_\beta q_\alpha)_{V-A}\,, \tag{F.24}$$
$$\widetilde{Q}'_{10} = (\overline{u}_\alpha \overline{c}_\beta)_{V+A} \sum_q F_{U_i,D_i}\, (\overline{q}_\beta q_\alpha)_{V+A}\,, \tag{F.25}$$

where $q = u, c, d, s, b$ and $F_f$ denotes the associated U(1)′ charge. In Eq. (F.18), we explicitly write out the sum for the operator $\widetilde{Q}_7$ to illustrate how the different quark currents enter.

## F.2 Matching and running of new physics four-quark operators

We relate the corresponding Wilson coefficients at the $Z'$ mass scale

$$\begin{aligned} \widetilde{\mathcal{C}}_7\left(M_{Z'}\right) &= \widetilde{\mathcal{C}}_9\left(M_{Z'}\right) , \\ \widetilde{\mathcal{C}}'_7\left(M_{Z'}\right) &= \widetilde{\mathcal{C}}'_9\left(M_{Z'}\right) , \\ \widetilde{\mathcal{C}}_8^{(\prime)}\left(M_{Z'}\right) &= \widetilde{\mathcal{C}}_{10}^{(\prime)}\left(M_{Z'}\right) = 0 . \end{aligned} \tag{F.26}$$

These coefficients are evolved down to the charm scale at LO in $\alpha_s$ via RGEs, where the top and bottom quarks are integrated out at their respective hold scales. Following Eq. (3.34), the RGE of the Wilson coefficients is given in general terms by

$$\frac{\mathrm{d}\vec{\widetilde{\mathcal{C}}}(\mu)}{\mathrm{d}\ln(\mu)} - \gamma^{\mathsf{T}}(\mu)\,\vec{\widetilde{\mathcal{C}}}(\mu) = 0 , \tag{F.27}$$

where $\vec{\widetilde{\mathcal{C}}}$ is a vector that includes the Wilson coefficients in question and $\gamma$ is the ADM expressed by a perturbative expansion $\gamma(\mu, \alpha_s) = \gamma^{(0)}\,\frac{\alpha_s}{4\,\pi} + \gamma^{(1)}\left(\frac{\alpha_s}{4\,\pi}\right)^2 + \ldots$ , *cf.* Eq. (3.35). The solution of Eq. (F.27) can be formally written as

$$\vec{\widetilde{\mathcal{C}}}\left(\mu_1\right) = U\left(\mu_1, \mu_2\right)\vec{\widetilde{\mathcal{C}}}\left(\mu_2\right) , \tag{F.28}$$

or expressed as

$$\vec{\widetilde{\mathcal{C}}}\left(m_c\right) = U_4\left(m_c, m_b\right)\,\hat{U}_5\left(m_b, m_t\right)\,\hat{U}_6\left(m_t, M_{Z'}\right)\,\vec{\widetilde{\mathcal{C}}}\left(M_{Z'}\right) , \quad \mu_1 < \mu_2 , \tag{F.29}$$

where $\hat{U}_{n_f}\left(\mu_1, \mu_2\right) \equiv M_{n_f}(\mu_1)\,U_{n_f}\left(\mu_1, \mu_2\right)$. Here, $U_{n_f}\left(\mu_1, \mu_2\right)$ denotes the evolution matrix from scale $\mu_2$ to $\mu_1$ in an EFT with $n_f$ active flavours. The *threshold* matrices $M_{n_f}$ match the associated effective theories with $n_f - 1$ and $n_f$ active flavours, but are given by the identity matrix at LO. The evolution matrix $U_{n_f}$ is computed by [177]

$$U_{n_f}\left(\mu_1, \mu_2\right) = V\left[\left(\frac{\alpha_s^{(n_f)}(\mu_2)}{\alpha_s^{(n_f)}(\mu_1)}\right)^{\vec{a}_0}\right]_D V^{-1} , \tag{F.30}$$

where we have introduced the shorthand notation $\vec{a}_0 \equiv \vec{\gamma}^{(0)}/(2\,\beta_0^{\mathrm{QCD}})$. The vector $\vec{\gamma}^{(0)}$ contains the diagonal elements of the diagonal matrix $\gamma_D^{(0)}$ which is defined via the change of basis

$$\gamma_D^{(0)} = V^{-1}\left(\gamma^{(0)}\right)^{\mathsf{T}} V . \tag{F.31}$$

The ADM describing the RG evolution of the operators in Eq. (7.20) at LO reads [177]

$$\gamma^{(0)} = \begin{pmatrix} \frac{6}{N_C} & -6 & 0 & 0 \\ 0 & \frac{6(1-N_C^2)}{N_C} & 0 & 0 \\ 0 & 0 & -\frac{6}{N_C} & 6 \\ 0 & 0 & 6 & -\frac{6}{N_C} \end{pmatrix} = \begin{pmatrix} 2 & -6 & 0 & 0 \\ 0 & -16 & 0 & 0 \\ 0 & 0 & -2 & 6 \\ 0 & 0 & 6 & -2 \end{pmatrix}, \tag{F.32}$$

where $N_C = 3$ denotes the number of colours. Due to parity conservation in QCD, $\gamma^{(0)}$ is identical for both $\widetilde{Q}_i$ and $\widetilde{Q}'_i$. With $\mu_2 = M_{Z'}$ and $\mu_1 = m_c$, we find the following analytical expression for the running of the Wilson coefficients

$$\begin{aligned} \widetilde{\mathcal{C}}_7^{(\prime)}(m_c) &= \sqrt{r_1}\, \widetilde{\mathcal{C}}_7^{(\prime)}(M_{Z'})\,, \\ \widetilde{\mathcal{C}}_8^{(\prime)}(m_c) &= \frac{\widetilde{\mathcal{C}}_7^{(\prime)}(M_{Z'}) \left(1 - r_1^{\frac{9}{2}}\right) + 3\, \widetilde{\mathcal{C}}_8^{(\prime)}(M_{Z'})}{3\, r_1^4}\,, \\ \widetilde{\mathcal{C}}_9^{(\prime)}(m_c) &= \frac{\widetilde{\mathcal{C}}_9^{(\prime)}(M_{Z'}) - \widetilde{\mathcal{C}}_{10}^{(\prime)}(M_{Z'}) + r_1^3 \left(\widetilde{\mathcal{C}}_9^{(\prime)}(M_{Z'}) + \widetilde{\mathcal{C}}_{10}^{(\prime)}(M_{Z'})\right)}{2\, r_1^2}\,, \\ \widetilde{\mathcal{C}}_{10}^{(\prime)}(m_c) &= \frac{\widetilde{\mathcal{C}}_{10}^{(\prime)}(M_{Z'}) - \widetilde{\mathcal{C}}_9^{(\prime)}(M_{Z'}) + r_1^3 \left(\widetilde{\mathcal{C}}_9^{(\prime)}(M_{Z'}) + \widetilde{\mathcal{C}}_{10}^{(\prime)}(M_{Z'})\right)}{2\, r_1^2}\,, \end{aligned} \tag{F.33}$$

with the renormalisation factor $r_1 = r_1(\mu = m_c,\, M_{Z'})$ defined in Eq. (5.34).

## F.3 Hadronic matrix elements in naive factorisation

In order to derive an estimation of the HMEs, we employ the factorisation of currents for non-leptonic decays which is given by

$$\langle P^+P^-|\, Q_i\, |D^0\rangle = \langle P^+|\, (\bar{q}_{1,\alpha_1}\, \Gamma_1\, q_{2,\alpha_1})\, |0\rangle\ \langle P^-|\, (\bar{q}_{3,\alpha_2}\, \Gamma_2\, q_{4,\alpha_2})\, |D^0\rangle\ B_i^{P^+P^-}\,. \tag{F.34}$$

Here, $P = \pi, K$ and $\Gamma_{1,2}$ refer to possible Dirac structures of the four-quark operator

$$Q_i = (\bar{q}_{1,\alpha_1}\, \Gamma_1\, q_{2,\alpha_1})(\bar{q}_{3,\alpha_2}\, \Gamma_2\, q_{4,\alpha_2}) \equiv (\bar{q}_1^{\alpha_1}\, \Gamma_1\, q_2^{\alpha_1})(\bar{q}_3^{\alpha_2}\, \Gamma_2\, q_4^{\alpha_2})\,, \tag{F.35}$$

exposing the colour indices $\alpha_i$. Note that this factorisation is only possible for quark currents with *same* colour indices. In naive factorisation it is $B^{P^+P^-} = 1$. Nevertheless, in what follows we keep these factors for expediency, while often referring to HMEs as 'matrix elements' or just 'elements'.

In general, three different colour structures emerge

$$\langle Q^{\mathrm{D}}\rangle = \delta_{\alpha_1\alpha_2}\delta_{\alpha_3\alpha_4}\ \langle P^+P^-|\, (\bar{q}_1^{\alpha_1}\, \Gamma_1\, q_2^{\alpha_2})\, (\bar{q}_3^{\alpha_3}\, \Gamma_2\, q_4^{\alpha_4})\, |D^0\rangle\,, \tag{F.36}$$

$$\langle Q^{\mathrm{C}}\rangle = \delta_{\alpha_1\alpha_4}\delta_{\alpha_3\alpha_2}\ \langle P^+P^-|\, (\bar{q}_1^{\alpha_1}\, \Gamma_1\, q_2^{\alpha_2})\, (\bar{q}_3^{\alpha_3}\, \Gamma_2\, q_4^{\alpha_4})\, |D^0\rangle\,, \tag{F.37}$$

$$\langle Q^{\mathrm{M}}\rangle = [t^a]_{\alpha_1\alpha_2}[t^a]_{\alpha_3\alpha_4}\ \langle P^+P^-|\, (\bar{q}_1^{\alpha_1}\, \Gamma_1\, q_2^{\alpha_2})\, (\bar{q}_3^{\alpha_3}\, \Gamma_2\, q_4^{\alpha_4})\, |D^0\rangle\,, \tag{F.38}$$

where the $t^a$ are $\mathrm{SU}(3)_C$ generators. The subscripts of the operators indicate the underlying colour

structures of the currents, *i.e.* $D$ (disconnected), $C$ (connected), and $M$ (mixed).

Employing the colour rearrangement identity [26, 220]

$$[t^a]_{\alpha_1\alpha_2}[t^a]_{\alpha_3\alpha_4} = -\frac{1}{2\,N_C}\,\delta_{\alpha_1\alpha_2}\delta_{\alpha_3\alpha_4} + \frac{1}{2}\,\delta_{\alpha_1\alpha_4}\delta_{\alpha_3\alpha_2}\,, \tag{F.39}$$

which can be viewed as a special Fierz identity, we find that

$$\langle Q^{\rm M}\rangle = -\frac{1}{2\,N_C}\,\langle Q^{\rm D}\rangle + \frac{1}{2}\,\langle Q^{\rm C}\rangle\,. \tag{F.40}$$

It follows that

$$\langle Q^{\rm D}\rangle = N_C\,\langle Q^{\rm C}\rangle\,B^{P^+P^-}\,, \tag{F.41}$$

where $B^{P^+P^-} \equiv 1-b$ with $b = 2\frac{\langle Q^{\rm M}\rangle}{\langle Q^{\rm C}\rangle}$. As a meson state and the vacuum are colourless, we have

$$\begin{aligned}\langle Q^{\rm M}\rangle &= \langle P^+P^-|\,(\bar q_1\,\Gamma_1\,t^a\,q_2)\,(\bar q_3\,\Gamma_2\,t^a\,q_4)\,|D^0\rangle \\ &= \langle P^+|\,(\bar q_1\,\Gamma_1\,t^a\,q_2)\,|0\rangle\;\langle P^-|\,(\bar q_3\,\Gamma_2\,t^a\,q_4)\,|D^0\rangle\;\; B^{P^+P^-} = 0\,,\end{aligned} \tag{F.42}$$

and recover $B^{P^+P^-}|_{\rm naive} = 1$ in naive factorisation. However, beyond naive factorisation the $B^{P^+P^-}$ parameters contain other corrections and are order one [26, 44].

In the next part, the matrix elements for the operators discussed for $D^0\to K^+K^-$ and $D^0\to\pi^+\pi^-$ decays are provided, where we show results for current-current and penguin operators in Apps. F.3.1 and F.3.2, respectively. For more details as well as studies involving, *e.g.*, scalar or chromomagnetic operators we refer to Ref. [177]. The matrix elements for the NP-inducing operators are presented in App. F.3.3. Therein, we also derive the relevant matrix elements of related $D^0\to\pi^0\pi^0$ and $D^+\to\pi^+\pi^0$ decays, extending the shorthand notation for the elements $\langle Q_i\rangle_P$ by $P=\pi^0\,,\pi'$, respectively.

## F.3.1 Current-current operators

### $Q_1^p$ and $Q_2^p$ for $p = d, s$

By comparing the colour structure in Eqs. (F.36) to (F.38) with the current-current operators in Eqs. (F.2) and (F.3), we can directly infer the relations $\langle Q_1^p\rangle \leftrightarrow \langle Q^{\rm D}\rangle$ and $\langle Q_2^p\rangle \leftrightarrow \langle Q^{\rm C}\rangle$ between the matrix elements, and can immediately apply Eq. (F.41). For the $K^+K^-$ final state only $p=s$ gives a non-zero element as $p=d$ only contributes at higher order in $\alpha_s$ via weak annihilation [168], whereas only $p=d$ gives a contribution for the $\pi^+\pi^-$ final state. We find

$P = K$:

$$\langle Q_1^d\rangle_K = 0\,, \tag{F.43}$$
$$\langle Q_1^s\rangle_K = N_C\,\langle Q_2^s\rangle_K\,B_1^s\,, \tag{F.44}$$

$P = \pi$:

$$\langle Q_1^s\rangle_\pi = 0\,, \tag{F.45}$$
$$\langle Q_1^d\rangle_\pi = N_C\,\langle Q_2^d\rangle_\pi\,B_1^d\,. \tag{F.46}$$

## F.3.2 QCD and QED penguin operators

Relating the matrix elements is not as obvious as before in the case of penguin operators. Here, we employ Fierz identities to infer the possible contributions from these operators. The general idea is to relate the matrix elements of all penguin operators back to those of the SM-dominant current-current operators $\langle Q_1^{s,d}\rangle_{K,\pi}$.

### $Q_3$ and $Q_4$

As an example, we start with the HME of the operator $Q_4$ for the $K^+K^-$ final state, where $P = K$. We write

$$\begin{aligned}\langle Q_4\rangle_K &= \langle K^+K^-|\,(\overline{u}_\alpha c_\beta)_{V-A}\sum_q(\overline{q}_\beta q_\alpha)_{V-A}\,|D^0\rangle \\ &= \langle\ldots|\sum_q(\overline{u}_\alpha q_\alpha)_{V-A}(\overline{q}_\beta c_\beta)_{V-A}\,|\ldots\rangle\ ,\end{aligned} \tag{F.47}$$

where we have employed the Fierz identity given in Eq. (A.26) and introduced a simplified *braket* notation for enhanced readability. At this point, we assume that only $q = s$ contributes to $\langle Q_4\rangle_K$ which yields

$$\begin{aligned}\langle Q_4\rangle_K &= \langle\ldots|\sum_q(\overline{u}q)_{V-A}(\overline{q}c)_{V-A}\,|\ldots\rangle = \sum_q\langle\ldots|\,(\overline{u}q)_{V-A}(\overline{q}c)_{V-A}\,|\ldots\rangle \\ &= \langle\ldots|\,(\overline{u}s)_{V-A}(\overline{s}c)_{V-A}\,|\ldots\rangle\ \widehat{B}_s^2 = \langle Q_1^s\rangle_K\,\widehat{B}_s^2\,.\end{aligned} \tag{F.48}$$

In the second line we have identified the operator $\langle Q_1^s\rangle_K$, where the hatted parameter $\widehat{B}_2^s$ accounts for the fact that only $q = s$ in $\langle Q_4\rangle_K$ has been considered.

The calculations for the operator $Q_3$ follow a similar strategy. We apply the Fierz identity in Eq. (A.26) and find for $q = s$

$$\begin{aligned}\langle Q_3\rangle_K &= \langle K^+K^-|\,(\overline{u}_\alpha c_\alpha)_{V-A}(\overline{s}_\beta s_\beta)_{V-A}\,|D^0\rangle \\ &= \langle\ldots|\,(\overline{u}_\alpha s_\beta)_{V-A}(\overline{s}_\beta c_\alpha)_{V-A}\,|\ldots\rangle\ .\end{aligned} \tag{F.49}$$

Then, we employ Eq. (F.41) where only colour indices are interchanged while the quark (flavour) structure remains unchanged. It follows that

$$\begin{aligned}\langle Q_3\rangle_K &= \langle\ldots|\,(\overline{u}_\alpha s_\beta)_{V-A}(\overline{s}_\beta c_\alpha)_{V-A}\,|\ldots\rangle \\ &= \frac{1}{N_C}\,\langle\ldots|\,(\overline{u}_\alpha s_\alpha)_{V-A}(\overline{s}_\beta c_\beta)_{V-A}\,|\ldots\rangle\,\frac{1}{B_2^s} = \frac{1}{N_C}\,\langle Q_4\rangle_K\,\frac{1}{B_2^s}\,,\end{aligned} \tag{F.50}$$

which now has the correct quark content in the factorised currents. This enables us to relate the two HMEs using Eq. (F.41). We obtain

$$\langle Q_4\rangle_K = N_C\,\langle Q_3\rangle_K\,B_2^s\,, \tag{F.51}$$

which we conveniently summarise as

$P = K$:

$$\langle Q_4\rangle_K = N_C\,\langle Q_3\rangle_K\,B_2^s\,, \quad \text{(F.52)}$$
$$\langle Q_4\rangle_K = \langle Q_1^s\rangle_K\,\widehat{B}_2^s\,, \quad \text{(F.53)}$$

$P = \pi$:

$$\langle Q_4\rangle_\pi = N_C\,\langle Q_3\rangle_\pi\,B_2^d\,, \quad \text{(F.54)}$$
$$\langle Q_4\rangle_\pi = \langle Q_1^d\rangle_\pi\,\widehat{B}_2^d\,. \quad \text{(F.55)}$$

Analogous relations hold for the primed counterparts of the penguin operators, which are skipped here for the sake of brevity.

### $Q_5$ and $Q_6$

Here, we follow the same method as before while applying the Fierz identity in Eq. (A.27). As an example, we rewrite

$$\begin{aligned}\langle Q_5\rangle_K &= \langle K^+K^-|\,(\overline{u}c)_{V-A}\sum_q(\overline{q}q)_{V+A}\,|D^0\rangle \\ &= \langle\ldots|\,(-2)\sum_q(\overline{u}_\alpha q_\beta)_{S-P}\,(\overline{q}_\beta c_\alpha)_{S+P}\,|\ldots\rangle\,,\end{aligned} \quad \text{(F.56)}$$

where the shorthand notation $S \pm P$ refer to the Dirac structures $1 \pm \gamma_5$. We obtain

$$\langle Q_5\rangle_K = \frac{1}{N_C}\,\langle Q_6\rangle_K\,\frac{1}{B_s^3}\,. \quad \text{(F.57)}$$

In addition, only $q = s$ contributions to $\langle Q_6\rangle_K$ and after relating $(S-P)\times(S+P)$-terms with the $(V-A)\times(V\mp A)$ ones (see Ref. [168], Eq. (A5) for details) we derive

$$\langle Q_6\rangle_K = \chi_K\,\langle Q_1^s\rangle_K\,\widehat{B}_3^s\,, \quad \text{(F.58)}$$

with the chiral enhancement $\chi_K$ defined in Eq. (B.2). With similar reasoning for $P = \pi$ operators, we obtain

$P = K$:

$$\langle Q_6\rangle_K = N_C\,\langle Q_5\rangle_K\,B_3^s\,, \quad \text{(F.59)}$$
$$\langle Q_6\rangle_K = \chi_K\,\langle Q_1^s\rangle_K\,\widehat{B}_3^s\,, \quad \text{(F.60)}$$

$P = \pi$:

$$\langle Q_6\rangle_\pi = N_C\,\langle Q_5\rangle_\pi\,B_3^d\,, \quad \text{(F.61)}$$
$$\langle Q_6\rangle_\pi = \chi_\pi\,\langle Q_1^d\rangle_\pi\,\widehat{B}_3^d\,. \quad \text{(F.62)}$$

### $Q_i$ for $i = 7, 8, 9, 10$

Analogous derivations for the matrix elements of $Q_{7,8,9,10}$ yield

$P = K$:

$$\langle Q_8\rangle_K = N_C\,\langle Q_7\rangle_K\,B_4^s\,, \tag{F.63}$$
$$\langle Q_8\rangle_K = \frac{3}{2}\,e_s\,\chi_K\,\langle Q_1^s\rangle_K\,\widehat{B}_4^s\,, \tag{F.64}$$
$$\langle Q_{10}\rangle_K = N_C\,\langle Q_9\rangle_K\,B_5^s\,, \tag{F.65}$$
$$\langle Q_{10}\rangle_K = e_s\,\langle Q_1^s\rangle_K\,\widehat{B}_5^s\,, \tag{F.66}$$

$P = \pi$:

$$\langle Q_8\rangle_\pi = N_C\,\langle Q_7\rangle_\pi\,B_4^d\,, \tag{F.67}$$
$$\langle Q_8\rangle_\pi = \frac{3}{2}\,e_d\,\chi_\pi\,\langle Q_1^d\rangle_\pi\,\widehat{B}_4^d\,, \tag{F.68}$$
$$\langle Q_{10}\rangle_\pi = N_C\,\langle Q_9\rangle_\pi\,B_5^d\,, \tag{F.69}$$
$$\langle Q_{10}\rangle_\pi = e_d\,\langle Q_1^d\rangle_\pi\,\widehat{B}_5^d\,, \tag{F.70}$$

where $e_s = e_d = -\frac{1}{3}$ denotes the electric charge of the corresponding quark.

### F.3.3 New physics operators $\widetilde{Q}_i$ for $i = 7, 8, 9, 10$

In the following, we show the results for the NP operators that are of special interest in Sec. 6.3. For better comparison, we set $B_i = 1$ directly working in naive factorisation, and obtain

$P = K$:

$$\langle\widetilde{Q}_7\rangle_K = \frac{1}{N_C}\,\langle\widetilde{Q}_8\rangle_K\,, \tag{F.71}$$
$$\langle\widetilde{Q}_8\rangle_K = F_{D_2}\,\chi_K\,\langle Q_1^s\rangle_K\,, \tag{F.72}$$
$$\langle\widetilde{Q}_9\rangle_K = \frac{1}{N_C}\,\langle\widetilde{Q}_{10}\rangle_K\,, \tag{F.73}$$
$$\langle\widetilde{Q}_{10}\rangle_K = F_{Q_2}\,\langle Q_1^s\rangle_K\,, \tag{F.74}$$

$P = \pi$:

$$\langle\widetilde{Q}_7\rangle_\pi = \frac{1}{N_C}\,\langle\widetilde{Q}_8\rangle_\pi\,, \tag{F.75}$$
$$\langle\widetilde{Q}_8\rangle_\pi = F_{D_1}\,\chi_\pi\,\langle Q_1^d\rangle_\pi\,, \tag{F.76}$$
$$\langle\widetilde{Q}_9\rangle_\pi = \frac{1}{N_C}\,\langle\widetilde{Q}_{10}\rangle_\pi\,, \tag{F.77}$$
$$\langle\widetilde{Q}_{10}\rangle_\pi = F_{Q_1}\,\langle Q_1^d\rangle_\pi\,, \tag{F.78}$$

where $F_{Q_{1,2}}$ and $F_{D_{1,2}}$ refer to the U(1)$'$ charges of the doublet and singlet $d$ ($s$) quarks, respectively. Similarly, we can extract matrix elements for $P = \pi^0, \pi'$ in terms of the current-current operators, *cf.* Eqs. (F.2) and (F.3),

$$Q_1^q = (\overline{u}q)_{V-A}(\overline{q}c)_{V-A}\,, \tag{F.79}$$
$$Q_2^q = (\overline{u}_\alpha q_\beta)_{V-A}(\overline{q}_\beta c_\alpha)_{V-A}\,, \tag{F.80}$$

with $q = u, d$. Together with the shorthand notation $\langle\ldots\rangle_q = \langle\overline{q}q|\ldots|D^0\rangle$, we find the following expressions for the matrix elements

$P = \pi'$:

$$\langle \widetilde{Q}_7 \rangle_{\pi'} = \frac{1}{N_C} \langle \widetilde{Q}_8 \rangle_{\pi'} \,, \tag{F.81}$$

$$\langle \widetilde{Q}_8 \rangle_{\pi'} = \frac{(F_{U_1} - F_{D_1})\, \chi_\pi}{\sqrt{2}} \langle Q_1^u \rangle_u \,, \tag{F.82}$$

$$\langle \widetilde{Q}_9 \rangle_{\pi'} = \frac{1}{N_C} \langle \widetilde{Q}_{10} \rangle_{\pi'} = 0 \,, \tag{F.83}$$

$$\langle \widetilde{Q}_{10} \rangle_{\pi'} = 0 \,, \tag{F.84}$$

$P = \pi^0$:

$$\langle \widetilde{Q}_7 \rangle_{\pi^0} = \frac{1}{N_C} \langle \widetilde{Q}_8 \rangle_{\pi^0} \,, \tag{F.85}$$

$$\langle \widetilde{Q}_8 \rangle_{\pi^0} = \frac{(F_{U_1} - F_{D_1})\, \chi_\pi}{2} \langle Q_1^u \rangle_u \,, \tag{F.86}$$

$$\langle \widetilde{Q}_9 \rangle_{\pi^0} = \frac{1}{N_C} \langle \widetilde{Q}_{10} \rangle_{\pi^0} = 0 \,, \tag{F.87}$$

$$\langle \widetilde{Q}_{10} \rangle_{\pi^0} = 0 \,, \tag{F.88}$$

working in the isospin limit $m_u = m_d$, that is $\langle Q_1^u \rangle_u = \langle Q_1^d \rangle_d$. In this limit, $\langle \widetilde{Q}_{9,10} \rangle_{\pi',\pi^0}$ vanish as they are proportional to $(F_{Q_1} - F_{Q_1}) = 0$. The factor $1/\sqrt{2}$ for $P = \pi^0$ is due to the additional $\pi^0$ meson in the final state.

The results for the primed counterparts are obtained by interchanging the U(1)′ charges $F_{Q_i} \leftrightarrow F_{D_i}$ in the expressions above. They are compiled in Tab. 7.2.

*Appendix*

# G

# Charged lepton and neutrino links via SU(2)$_L$-symmetry

In this appendix, we provide ancillary calculations and details of the SU(2)$_L$-link outlined in Chap. 9. We review the correlations between dineutrino and charged dilepton Wilson coefficients in App. G.1. Supplementary tables listing constraints on charged dilepton couplings $\mathcal{K}_{L,R}$ can be found in App. G.2. They are taken from Ref. [18]. In Apps. G.3 and G.4, we provide details on the derivation of charm dineutrino limits and present updated results of dineutrino branching ratios, respectively.

## G.1 Connection of Wilson coefficients in the mass basis

The dineutrino and dilepton Wilson coefficients in the gauge basis are given by $C_A^P$ and $K_A^P$, respectively, with $A = L, R$ and $P = U, D$. The SU(2)$_L$-link in Eq. (9.9) relates the couplings of dineutrinos and dileptons as $C_L^D = K_L^U, C_L^U = K_L^D$ and $C_R^{U,D} = K_R^{U,D}$ in the gauge basis.

Going to mass basis, we perform a field rotation to obtain the calligraphic $\mathcal{C}_A^P$ and $\mathcal{K}_A^P$ coefficients. Using the biunitary rotations defined in Eq. (2.21), we identify four different unitary rotations in the quark sector, corresponding to the left-handed (right-handed) $V_{u,d}$ ($U_{u,d}$), both for up- and down-type quarks. Conversely, for leptons two rotations are required, $V_\ell$ and $V_\nu$, as we only consider couplings to LH leptons, *cf.* Eqs. (9.4) and (9.5). Employing these rotations, we write the Wilson coefficients in the mass basis as

$$\begin{aligned} \mathcal{C}_L^D &= (V_\nu)^\dagger\,(V_d)^\dagger\,C_L^D\,V_d\,V_\nu\,, \quad \mathcal{C}_R^D = (V_\nu)^\dagger\,(U_d)^\dagger\,C_R^D\,U_d\,V_\nu\,, \\ \mathcal{K}_L^D &= (V_\ell)^\dagger\,(V_d)^\dagger\,K_L^D\,V_d\,V_\ell\,, \quad \mathcal{K}_R^D = (V_\ell)^\dagger\,(U_d)^\dagger\,K_R^D\,U_d\,V_\ell\,, \end{aligned} \tag{G.1}$$

and

$$\begin{aligned} \mathcal{C}_L^U &= (V_\nu)^\dagger\,(V_u)^\dagger\,C_L^U\,V_u\,V_\nu\,, \quad \mathcal{C}_R^U = (V_\nu)^\dagger\,(U_u)^\dagger\,C_R^U\,U_u\,V_\nu\,, \\ \mathcal{K}_L^U &= (V_\ell)^\dagger\,(V_u)^\dagger\,K_L^U\,V_u\,V_\ell\,, \quad \mathcal{K}_R^U = (V_\ell)^\dagger\,(U_u)^\dagger\,K_R^U\,U_u\,V_\ell\,. \end{aligned} \tag{G.2}$$

As $C_R^{U,D} = K_R^{U,D}$, we identify

$$\mathcal{C}_R^D = (V_\nu)^\dagger\,(U_d)^\dagger\,K_R^D\,U_d\,V_\nu = (U_{\text{PMNS}})^\dagger\,\left[\mathcal{K}_R^D\right]\,U_{\text{PMNS}}\,, \tag{G.3}$$

$$\mathcal{C}_R^U = (V_\nu)^\dagger\,(U_u)^\dagger\,K_R^U\,U_u\,V_\nu = (U_{\text{PMNS}})^\dagger\,\left[\mathcal{K}_R^U\right]\,U_{\text{PMNS}}\,, \tag{G.4}$$

where $U_{\rm PMNS} = (V_\ell)^\dagger V_\nu$ is the PMNS matrix, see Eq. (2.27). In the LH quark sector, the analogous relations feature a different structure,

$$\mathcal{C}_L^D = (U_{\rm PMNS})^\dagger \left[(V_{\rm CKM})^\dagger \, \mathcal{K}_L^U \, V_{\rm CKM}\right] U_{\rm PMNS}\,, \tag{G.5}$$

$$\mathcal{C}_L^U = (U_{\rm PMNS})^\dagger \left[V_{\rm CKM} \, \mathcal{K}_L^D \, (V_{\rm CKM})^\dagger\right] U_{\rm PMNS}\,, \tag{G.6}$$

where the CKM matrix $V_{\rm CKM} = (V_u)^\dagger V_d$, see Eq. (2.25), enters prominently due to the link between up- and down-sector. We define

$$L_{\alpha\beta}^D = \left[(V_{\rm CKM})^\dagger \, \mathcal{K}_L^U \, V_{\rm CKM}\right]_{\alpha\beta}\,, \tag{G.7}$$

$$L_{\alpha\beta}^U = \left[V_{\rm CKM} \, \mathcal{K}_L^D \, (V_{\rm CKM})^\dagger\right]_{\alpha\beta}\,, \tag{G.8}$$

where we have made the quark flavours $\alpha, \beta$ explicit. For instance, expanding Eqs. (G.5) and (G.6) in the Wolfenstein parameter $\lambda_{\rm CKM} \approx 0.2$, we obtain

$$L_{23}^D = \mathcal{K}_L^{U_{23}} + \mathcal{O}\left(\lambda_{\rm CKM}\right), \tag{G.9}$$

$$L_{13}^D = \mathcal{K}_L^{U_{13}} + \mathcal{O}\left(\lambda_{\rm CKM}\right), \tag{G.10}$$

for $b \to s$ and $b \to d$ transitions, respectively. Note that switching off mixing between the first and second generation entails suppressed CKM corrections, *i.e.* $\mathcal{O}\left(\lambda_{\rm CKM}^2\right)$ for $L_{23}^D$ and $\mathcal{O}\left(\lambda_{\rm CKM}^3\right)$ for $L_{13}^D$.

## G.2 Bounds on lepton-specific Wilson coefficients

Here, we summarise the various limits on charged dilepton couplings which have been compiled from Ref. [18]. Upper limits on $\mathcal{K}_{L,R}^{sd\ell\ell'}$ and $\mathcal{K}_{L,R}^{cu\ell\ell'}$ are provided in Tabs. G.1 and G.2, respectively. Moreover, Tabs. G.3 and G.4 summarise the derived limits from $b \to s$ and $b \to d$ couplings, respectively. Constraints on top-couplings $\mathcal{K}_{L,R}^{tc\ell\ell'}$ and $\mathcal{K}_{L,R}^{tu\ell\ell'}$ are listed in Tabs. G.5 and G.6, respectively.

| $sd\,\ell\ell'$ | $ee$ | $\mu\mu$ | $\tau\tau$ | $e\mu$ | $e\tau$ | $\mu\tau$ |
|---|---|---|---|---|---|---|
| $\lvert\mathcal{K}_{L,R}^{sd\ell\ell'}\rvert_{\rm DY}$ | 3.5 | 1.9 | 6.7 | 2.0 | 6.1 | 6.6 |
| $\lvert\mathcal{K}_{L,R}^{sd\ell\ell'}\rvert$ | $5 \cdot 10^{-2}$ | $1.6 \cdot 10^{-2}$ | – | $6.6 \cdot 10^{-4}$ | – | – |
| $\lvert\mathcal{K}_{R}^{sd\ell\ell'}\rvert_{\nu\bar{\nu}}^{a}$ | $[-1.9, 0.7] \cdot 10^{-2}$ | $[-1.9, 0.7] \cdot 10^{-2}$ | $[-1.9, 0.7] \cdot 10^{-2}$ | $1.1 \cdot 10^{-2}$ | $1.1 \cdot 10^{-2}$ | $1.1 \cdot 10^{-2}$ |

**Table G.1:** Upper limits on charged dilepton couplings $\mathcal{K}_{L,R}^{sd\ell\ell'}$ from high-$p_{\rm T}$ [183, 217] (top row), charged dilepton $K$-decays (mid row) and derived ones from kaon decays to dineutrinos (bottom row). Numbers correspond to a limit on the modulus. LFV-bounds are quoted as flavour-summed, $\sqrt{|\mathcal{K}^{\ell^+\ell'^-}|^2 + |\mathcal{K}^{\ell^-\ell'^+}|^2}$. [a]Obtained assuming no large cancellations between $\mathcal{K}_R^{sd}$ and $\mathcal{K}_L^{cu}$. *Table taken from Ref.* [18].

| $cu\,\ell\ell'$ | $ee$ | $\mu\mu$ | $\tau\tau$ | $e\mu$ | $e\tau$ | $\mu\tau$ |
|---|---|---|---|---|---|---|
| $\lvert\mathcal{K}_{L,R}^{cu\ell\ell'}\rvert_{\mathrm{DY}}$ | 2.9 | 1.6 | 5.6 | 1.6 | 4.7 | 5.1 |
| $\lvert\mathcal{K}_{L,R}^{cu\ell\ell'}\rvert$ | 4.0 | 0.9 | – | 2.2 | n.a.$^\dagger$ | – |
| $\lvert\mathcal{K}_{L}^{cu\ell\ell'}\rvert_{\nu\bar{\nu}}^{a}$ | $[-1.9, 0.7]\cdot 10^{-2}$ | $[-1.9, 0.7]\cdot 10^{-2}$ | $[-1.9, 0.7]\cdot 10^{-2}$ | $1.1\cdot 10^{-2}$ | $1.1\cdot 10^{-2}$ | $1.1\cdot 10^{-2}$ |

**Table G.2:** Upper limits on charged dilepton couplings $\mathcal{K}_{L,R}^{cu\ell\ell'}$ from high-$p_{\mathrm{T}}$ [183, 217] (top row), charged dilepton $D$-decays (mid row) and derived ones from kaon decays to dineutrinos (bottom row). Numbers correspond to a limit on the modulus. LFV-bounds are quoted as flavour-summed, $\sqrt{|\mathcal{K}^{\ell^+\ell'^-}|^2 + |\mathcal{K}^{\ell^-\ell'^+}|^2}$. $^\dagger$No limit on $D^0 \to e^\pm\tau^\mp$ available. $^a$Obtained assuming no large cancellations between $\mathcal{K}_R^{sd}$ and $\mathcal{K}_L^{cu}$. *Table taken from Ref.* [18].

| $bs\,\ell\ell'$ | $ee$ | $\mu\mu$ | $\tau\tau$ | $e\mu$ | $e\tau$ | $\mu\tau$ |
|---|---|---|---|---|---|---|
| $\lvert\mathcal{K}_{L,R}^{bs\ell\ell'}\rvert_{\mathrm{DY}}$ | 13 | 7.1 | 25 | 8.0 | 27 | 30 |
| $\mathcal{K}_L^{bs\ell\ell'}$ | 0.04 | $[-0.06, -0.04]$ | 32 | 0.1 | 2.8 | 3.4 |
| $\mathcal{K}_R^{bs\ell\ell'}$ | 0.04 | $[-0.03, -0.01]$ | 32 | 0.1 | 2.8 | 3.4 |
| $\lvert\mathcal{K}_R^{bs\ell\ell'}\rvert_{\nu\bar{\nu}}$ | 1.4 | 1.4 | 1.4 | 1.8 | 1.8 | 1.8 |

**Table G.3:** Upper limits on charged dilepton couplings $\mathcal{K}_{L,R}^{bs\ell\ell'}$ from high-$p_{\mathrm{T}}$ [183, 217] (top row), charged dilepton $B$-decays (mid rows) and derived ones from three-body rare $B$-decays to dineutrinos (bottom row). Numbers without ranges correspond to a limit on the modulus. The $\mu\mu$ ranges are derived from the global fit results of Ref. [20], see Sec. 4.2 and Tab. C.7 therein for details, with the departures from zero in $\mathcal{K}_L^{bs\mu\mu}$ corresponding to the $B$-anomalies. LFV-bounds are quoted as flavour-summed, $\sqrt{|\mathcal{K}^{\ell^+\ell'^-}|^2 + |\mathcal{K}^{\ell^-\ell'^+}|^2}$, whereas the other bounds are for a single coupling. *Table taken from Ref.* [18].

| $bd\,\ell\ell'$ | $ee$ | $\mu\mu$ | $\tau\tau$ | $e\mu$ | $e\tau$ | $\mu\tau$ |
|---|---|---|---|---|---|---|
| $\lvert\mathcal{K}_{L,R}^{bd\ell\ell'}\rvert_{\mathrm{DY}}$ | 5.0 | 2.7 | 9.6 | 3.1 | 9.6 | 11 |
| $\mathcal{K}_L^{bd\ell\ell'}$ | 0.09 | $[-0.07, 0.02]$ | 21 | 0.2 | 3.4 | 2.4 |
| $\mathcal{K}_R^{bd\ell\ell'}$ | 0.09 | $[-0.03, 0.03]$ | 21 | 0.2 | 3.4 | 2.4 |
| $\lvert\mathcal{K}_R^{bd\ell\ell'}\rvert_{\nu\bar{\nu}}$ | 1.8 | 1.8 | 1.8 | 2.5 | 2.5 | 2.5 |

**Table G.4:** Upper limits on charged dilepton couplings $\mathcal{K}_{L,R}^{bd\ell\ell'}$ from high-$p_{\mathrm{T}}$ [183, 217] (top row), charged dilepton $B$-decays (mid rows) and derived ones from three-body rare $B$-decays to dineutrinos (bottom row). Numbers without ranges correspond to a limit on the modulus. The $\mu\mu$ ranges are derived from a global fit of $b \to d$ observables [18]. LFV-bounds are quoted as flavour-summed, $\sqrt{|\mathcal{K}^{\ell^+\ell'^-}|^2 + |\mathcal{K}^{\ell^-\ell'^+}|^2}$, whereas the other bounds are for a single coupling. *Table taken from Ref.* [18].

| $tc\,\ell\ell'$ | $ee$ | $\mu\mu$ | $\tau\tau$ | $e\mu$ | $e\tau$ | $\mu\tau$ |
|---|---|---|---|---|---|---|
| $\lvert\mathcal{K}_{L,R}^{tc\ell\ell'}\rvert$ | $\sim 200$ | $\sim 200$ | n.a. | 36 | 136 | 136 |
| $\lvert\mathcal{K}_{L}^{tc\ell\ell'}\rvert_{\nu\bar{\nu}}$ | $[-1.9, 0.9]$ | $[-1.9, 0.9]$ | $[-1.9, 0.9]$ | 1.8 | 1.8 | 1.8 |

**Table G.5:** Upper limits on charged dilepton couplings $\mathcal{K}_{L,R}^{tc\ell\ell'}$ from collider studies [218, 259, 260] of top plus charged dilepton processes (top row) and on charged dilepton couplings $\mathcal{K}_{L}^{tc\ell\ell'}$ derived from three-body rare $B$-decays to dineutrinos (bottom row), see Ref. [18] for details. Numbers correspond to a limit on the modulus except when a range is given. LFV-bounds are quoted as flavour-summed, $\sqrt{|\mathcal{K}^{\ell^+\ell'^-}|^2 + |\mathcal{K}^{\ell^-\ell'^+}|^2}$, whereas the other bounds are for a single coupling. *Table taken from Ref.* [18].

| $tu\,\ell\ell'$ | $ee$ | $\mu\mu$ | $\tau\tau$ | $e\mu$ | $e\tau$ | $\mu\tau$ |
|---|---|---|---|---|---|---|
| $\lvert\mathcal{K}_{L,R}^{tu\ell\ell'}\rvert$ | $\sim 200$ | $\sim 200$ | n.a. | 12 | 136 | 136 |
| $\lvert\mathcal{K}_{L}^{tu\ell\ell'}\rvert_{\nu\bar{\nu}}$ | $[-1.6, 1.8]$ | $[-1.6, 1.8]$ | $[-1.6, 1.8]$ | 2.4 | 2.4 | 2.4 |

**Table G.6:** Same as Tab. G.5 but for couplings $\mathcal{K}_{L,R}^{tu\ell\ell'}$. *Table taken from Ref.* [18].

## G.3 Extracting bounds on $c \to u$ dineutrino branching ratios

In what follows, we provide details on the computation of the limits on $x_{cu}$ collected in Eqs. (9.23) to (9.25). In doing so, we write

$$\mathcal{C}_L^{cu} = (U_{\rm PMNS})^\dagger \, \mathcal{K}_L^{sd} \, U_{\rm PMNS} + \lambda_{\rm CKM} \, (U_{\rm PMNS})^\dagger \left(\mathcal{K}_L^{ss} - \mathcal{K}_L^{dd}\right) U_{\rm PMNS} + \mathcal{O}\left(\lambda_{\rm CKM}^2\right), \tag{G.11}$$

where we have replaced the superscripts with their associated quark transition, *e.g.* $U_{12} = cu$ and $D_{12} = sd$, to ease the notation. Utilising the trace identity in Eq. (9.12), we obtain

$$\begin{aligned} x_{cu} &= \sum_{\nu=i,j} \left(|\mathcal{C}_L^{cuij}|^2 + |\mathcal{C}_R^{cuij}|^2\right) = \mathrm{tr}\left(\mathcal{C}_L^{cuij}\left(\mathcal{C}_L^{cuij}\right)^\dagger + \mathcal{C}_R^{cuij}\left(\mathcal{C}_R^{cuij}\right)^\dagger\right) \\ &= \mathrm{tr}\left(\mathcal{K}_L^{sdij}\left(\mathcal{K}_L^{sdij}\right)^\dagger + \mathcal{K}_R^{cuij}\left(\mathcal{K}_R^{cuij}\right)^\dagger\right) + \delta x_{cu} + \mathcal{O}\left(\lambda_{\rm CKM}^2\right) \\ &= \sum_{\ell=i,j} \left(|\mathcal{K}_L^{sdij}|^2 + |\mathcal{K}_R^{cuij}|^2\right) + \delta x_{cu} + \mathcal{O}\left(\lambda_{\rm CKM}^2\right), \end{aligned} \tag{G.12}$$

with the $\mathcal{O}\left(\lambda_{\rm CKM}\right)$ corrections given by

$$\begin{aligned} \delta x_{cu} &= 2\,\lambda_{\rm CKM}\,\mathrm{tr}\left(\mathrm{Re}\left(\mathcal{K}_L^{sdij}\left(\mathcal{K}_L^{ssij} - \mathcal{K}_L^{ddij}\right)^\dagger\right)\right) \\ &= 2\,\lambda_{\rm CKM} \sum_{\ell=i,j} \mathrm{Re}\left(\mathcal{K}_L^{sdij}\,\mathcal{K}_L^{ssij*} - \mathcal{K}_L^{sdij}\,\mathcal{K}_L^{ddij*}\right). \end{aligned} \tag{G.13}$$

To study the lepton flavour structure and also put bounds on the rare charm dineutrino branching ratios, it is convenient to further introduce

$$\begin{aligned} R^{\ell\ell'} &= |\mathcal{K}_L^{sd\ell\ell'}|^2 + |\mathcal{K}_R^{cu\ell\ell'}|^2, \\ R_\pm^{\ell\ell'} &= |\mathcal{K}_L^{sd\ell\ell'} \pm \mathcal{K}_R^{cu\ell\ell'}|^2, \\ \delta R^{\ell\ell'} &= 2\,\lambda_{\rm CKM}\,\mathrm{Re}\left(\mathcal{K}_L^{sd\ell\ell'}\,\mathcal{K}_L^{ss\ell\ell'*} - \mathcal{K}_L^{sd\ell\ell'}\,\mathcal{K}_L^{dd\ell\ell'*}\right). \end{aligned} \tag{G.14}$$

These quantities obey the relations $R_+^{\ell\ell'} + R_-^{\ell\ell'} = 2\,R^{\ell\ell'}$ and $R_\pm^{\ell\ell'} \leq 2\,R^{\ell\ell'}$. Furthermore, $\delta R^{\ell\ell'} < 2\,\lambda\,|\mathcal{K}_L^{sd\ell\ell'}|\left(|\mathcal{K}_L^{ss\ell\ell'}| + |\mathcal{K}_L^{dd\ell\ell'}|\right)$. We use the limits on charged lepton couplings from, *e.g.*, high-$p_{\rm T}$ data to derive bounds on $R^{\ell\ell'}$ and $\delta R^{\ell\ell'}$ given in Tab. G.7. The high-$p_{\rm T}$ limits on $\mathcal{K}_L^{sd\ell\ell'}$ and $\mathcal{K}_R^{cu\ell\ell'}$ can be fetched from Tabs. G.1 and G.2, whereas the bounds on the $ss$- and $dd$-couplings are given elsewhere [19].

Finally, we can establish the upper limits on $x_{cu}$ for the different flavour patterns,

$$x_{cu} = 3\,r^{\mu\mu} \lesssim 34 \quad (\mathrm{LU}), \tag{G.15}$$

$$x_{cu} = r^{ee} + r^{\mu\mu} + r^{\tau\tau} \lesssim 196 \quad (\mathrm{cLFC}), \tag{G.16}$$

$$x_{cu} = r^{ee} + r^{\mu\mu} + r^{\tau\tau} + 2\,(r^{e\mu} + r^{e\tau} + r^{\mu\tau}) \lesssim 716 \quad (\mathrm{general}), \tag{G.17}$$

equivalent to the bounds given in Eqs. (9.23) to (9.25).

| | $ee$ | $\mu\mu$ | $\tau\tau$ | $e\mu$ | $e\tau$ | $\mu\tau$ |
|---|---|---|---|---|---|---|
| $R^{\ell\ell'}$ | 21 | 6.0 | 77 | 6.6 | 59 | 70 |
| $\delta R^{\ell\ell'}$ | 19 | 5.4 | 69 | 5.7 | 55 | 63 |
| $r^{\ell\ell'}$ | 39 | 11 | 145 | 12 | 115 | 133 |

**Table G.7:** Bounds on $R^{\ell\ell'}$ and $\delta R^{\ell\ell'}$ from Eq. (G.14), as well as their sum, $r^{\ell\ell'} = R^{\ell\ell'} + \delta R^{\ell\ell'}$. *Table taken from Ref.* [19].

| $h_c$ | $f(c \to h_c)$ | $N(h_c)$ (a) | $N(h_c)$ (b) |
|---|---|---|---|
| $D^0$ | 0.59 | $6 \cdot 10^{11}$ | $8 \cdot 10^{10}$ |
| $D^+$ | 0.24 | $3 \cdot 10^{11}$ | $3 \cdot 10^{10}$ |
| $D_s^+$ | 0.10 | $1 \cdot 10^{11}$ | $1 \cdot 10^{10}$ |
| $\Lambda_c^+$ | 0.06 | $7 \cdot 10^{10}$ | $8 \cdot 10^{9}$ |

**Table G.8:** Charm fragmentation fractions $f(c \to h_c)$ [261] and the number of charmed hadrons $h_c$, $N(h_c) = 2\, f(c \to h_c)\, N(c\bar{c})$, expected at benchmarks with $N(c\bar{c}) = 550 \cdot 10^9$ (a, FCC-ee) and $N(c\bar{c}) = 65 \cdot 10^9$ (b, Belle II with $50\,\text{ab}^{-1}$) [85]. *Table taken from Ref.* [19].

Fragmentation fractions $f(c \to h_c)$ [261] of a charm quark to a charmed hadron $h_c$ are listed in Tab. G.8, where we also give the number of charmed hadrons $N(h_c) = 2\, f(c \to h_c)\, N(c\bar{c})$ for FCC-ee and Belle II benchmark $c\bar{c}$ numbers [85], $N(c\bar{c}) = 550 \cdot 10^9$ and $N(c\bar{c}) = 65 \cdot 10^9$, respectively.

## G.4 Updated limits on $c \to u$ dineutrino branching ratios

Here, we provide updated benchmark values for charm dineutrino modes following improved limits on $x_{cu}$, which are constructed using low energy constraints in addition to the high-$p_\text{T}$ ones [18]

$$x_{cu} \lesssim 2.6 \quad \text{(LU)}\,, \tag{G.18}$$
$$x_{cu} \lesssim 156 \quad \text{(cLFC)}\,, \tag{G.19}$$
$$x_{cu} \lesssim 655 \quad \text{(general)}\,. \tag{G.20}$$

Compared to the respective limits in Eqs. (G.15) to (G.17), we see that the inclusion of rare kaon data on $|\mathcal{K}_L^{sd\ell\ell'}|$ and $|\mathcal{K}_R^{cu\ell\ell'}|$, given in Tabs. G.1 and G.2, respectively, significantly improves the limits on $x_{cu}$. However, they are not available for all couplings, *e.g.* $\tau\tau$ and $\mu\tau$. Therefore, in our main discussion we choose to include bounds from Drell-Yan data.

The updated upper limits on dineutrino branching ratios are compiled in Tab. G.9. In Fig. G.1, we give an updated version of Fig. 9.2 which illustrates the resulting upper limits on selected charm dineutrino branching ratios assuming a specific lepton flavour structure.

| $D^0 \to F$ | $A_+$ $[10^{-8}]$ | $A_-$ $[10^{-8}]$ | $\mathcal{B}^{\max}_{\mathrm{LU}}$ $[10^{-7}]$ | $\mathcal{B}^{\max}_{\mathrm{cLFC}}$ $[10^{-6}]$ | $\mathcal{B}^{\max}$ $[10^{-6}]$ | $N^{\max}_{\mathrm{LU}}/\eta_{\mathrm{eff}}$ | $N^{\max}_{\mathrm{cLFC}}/\eta_{\mathrm{eff}}$ | $N^{\max}/\eta_{\mathrm{eff}}$ |
|---|---|---|---|---|---|---|---|---|
| $D^0 \to \pi^0$ | 0.9 | 0 | 0.5 | 2.8 | 12 | 3.5 k (30 k) | 210 k (1.8 M) | 890 k (7.6 M) |
| $D^0 \to \pi^0\pi^0$ | $0.7 \cdot 10^{-3}$ | 0.21 | 0.1 | 0.7 | 2.8 | 0.8 k (7.1 k) | 51 k (430 k) | 210 k (1.8 M) |
| $D^0 \to \pi^+\pi^-$ | $1.4 \cdot 10^{-3}$ | 0.41 | 0.2 | 1.3 | 5.4 | 1.6 k (14 k) | 98 k (830 k) | 410 k (3.5 M) |
| $D^0 \to K^+K^-$ | $4.7 \cdot 10^{-6}$ | 0.004 | 0.002 | 0.01 | 0.06 | 0.02 k (0.1 k) | 1.0 k (8.8 k) | 4.4 k (37 k) |

**Table G.9:** Updated version of Tab. G.9. Coefficients $A_\pm$ as in Eq. (9.20) for selected $D^0$-meson decays into final states $F$ for central values of input. Utilising Eq. (9.19), we provide the upper limits on branching ratios $\mathcal{B}^{\max}_{\mathrm{LU}}$, $\mathcal{B}^{\max}_{\mathrm{cLFC}}$ and $\mathcal{B}^{\max}$ corresponding to Eqs. (G.18) to (G.20), respectively. The expected number of events, see Eq. (9.22), per reconstruction efficiency $\eta_{\mathrm{eff}}$ for Belle II with $50\,\mathrm{ab}^{-1}$ (FCC-ee yields in parentheses) is updated as well and given in the last three columns.

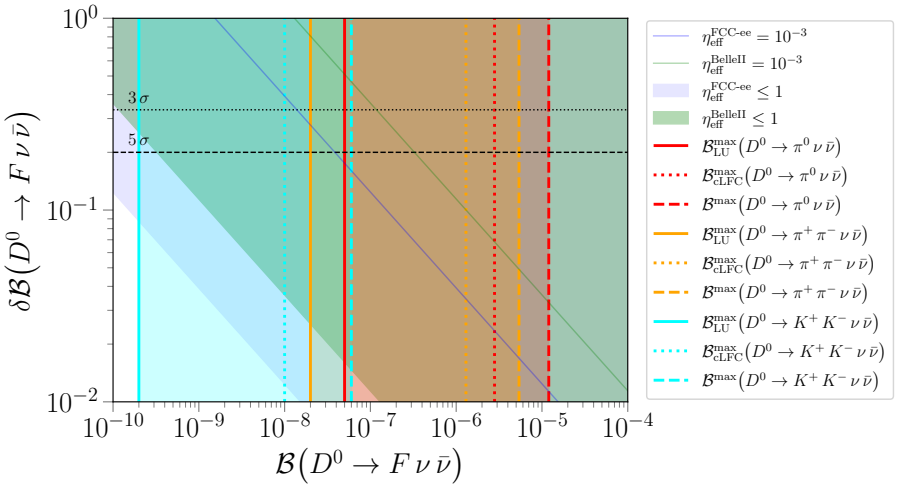


**Figure G.1:** Same as Fig. 9.2, but displaying upper limits assuming LU (solid), cLFC (dotted) and generic lepton flavour (dashed) taken from Tab. G.9.

# Abbreviations

**ACC** anomaly cancellation condition
**ADM** anomalous dimension matrix
**ATLAS** A Toroidal LHC ApparatuS

**BES** Beijing Spectrometer
**BSM** beyond the standard model

**CDF** Collider Detector at Fermilab
**CF** Cabibbo-favoured
**CKM** Cabibbo-Kobayashi-Maskawa
**cLFC** charged lepton flavour conservation
**cLFV** charged lepton flavour violation
**CMS** Compact Muon Solenoid

**DCS** doubly Cabibbo-suppressed

**EFT** effective field theory
**EWSB** electroweak symmetry breaking

**FCC** Future Circular Collider
**FCCC** flavour-changing charged current
**FCNC** flavour-changing neutral current
**FLAG** Flavour Lattice Averaging Group

**GIM** Glashow-Iliopoulos-Maiani

**HFLAV** Heavy Flavor Averaging Group
**HME** hadronic matrix element

**IR** infrared

**LEP** Large Electron–Positron Collider
**LFU** lepton flavour universality
**LFV** lepton flavour violation
**LH** left-handed
**LHC** Large Hadron Collider
**LHCb** Large Hadron Collider beauty
**LO** leading order
**LU** lepton universality

**MS** minimal subtraction

**NLO** next-to-leading order
**NNLO** next-to-next-to-leading order
**NP** new physics

**OPE** operator product expansion

**PDF** probability distribution function
**PDG** Particle Data Group
**PMNS** Pontecorvo-Maki-Nakagawa-Sakata

**QCD** quantum chromodynamics
**QED** quantum electrodynamics
**QFT** quantum field theory

**RG** renormalisation group
**RGE** renormalisation group equation
**RH** right-handed

**SCS** singly Cabibbo-suppressed
**SM** standard model
**SMEFT** standard model effective field theory
**SSB** spontaneous symmetry breaking

**UV** ultraviolet

**vev** vacuum expectation value

**WET** weak effective theory

# Bibliography


[1] S. Chatrchyan et al. [CMS]. "Observation of a New Boson at a Mass of 125 GeV with the CMS Experiment at the LHC." In: *Phys. Lett. B* 716 (2012), pp. 30–61. doi: 10.1016/j.physletb.2012.08.021. arXiv: 1207.7235 [hep-ex].

[2] G. Aad et al. [ATLAS]. "Observation of a new particle in the search for the Standard Model Higgs boson with the ATLAS detector at the LHC." In: *Phys. Lett. B* 716 (2012), pp. 1–29. doi: 10.1016/j.physletb.2012.08.020. arXiv: 1207.7214 [hep-ex].

[3] Y. Fukuda et al. [Super-Kamiokande]. "Evidence for oscillation of atmospheric neutrinos." In: *Phys. Rev. Lett.* 81 (1998), pp. 1562–1567. doi: 10.1103/PhysRevLett.81.1562. arXiv: hep-ex/9807003.

[4] Q. R. Ahmad et al. [SNO]. "Direct evidence for neutrino flavor transformation from neutral current interactions in the Sudbury Neutrino Observatory." In: *Phys. Rev. Lett.* 89 (2002), p. 011301. doi: 10.1103/PhysRevLett.89.011301. arXiv: nucl-ex/0204008.

[5] R. Aaij et al. [LHCb]. "Measurement of Form-Factor-Independent Observables in the Decay $B^0 \to K^{*0}\mu^+\mu^-$." In: *Phys. Rev. Lett.* 111 (2013), p. 191801. doi: 10.1103/PhysRevLett.111.191801. arXiv: 1308.1707 [hep-ex].

[6] R. Aaij et al. [LHCb]. "Test of lepton universality using $B^+ \to K^+\ell^+\ell^-$ decays." In: *Phys. Rev. Lett.* 113 (2014), p. 151601. doi: 10.1103/PhysRevLett.113.151601. arXiv: 1406.6482 [hep-ex].

[7] R. Aaij et al. [LHCb]. "Search for lepton-universality violation in $B^+ \to K^+\ell^+\ell^-$ decays." In: *Phys. Rev. Lett.* 122.19 (2019), p. 191801. doi: 10.1103/PhysRevLett.122.191801. arXiv: 1903.09252 [hep-ex].

[8] R. Aaij et al. [LHCb]. "Test of lepton universality in beauty-quark decays." In: *Nature Phys.* 18.3 (2022), pp. 277–282. doi: 10.1038/s41567-021-01478-8. arXiv: 2103.11769 [hep-ex].

[9] R. Aaij et al. [LHCb]. "Tests of lepton universality using $B^0 \to K^0_S\ell^+\ell^-$ and $B^+ \to K^{*+}\ell^+\ell^-$ decays." In: *Phys. Rev. Lett.* 128.19 (2022), p. 191802. doi: 10.1103/PhysRevLett.128.191802. arXiv: 2110.09501 [hep-ex].

[10] J. Ellis, M. Fairbairn, and P. Tunney. "Anomaly-Free Models for Flavour Anomalies." In: *Eur. Phys. J. C* 78.3 (2018), p. 238. doi: 10.1140/epjc/s10052-018-5725-0. arXiv: 1705.03447 [hep-ph].

[11] B. C. Allanach, J. Davighi, and S. Melville. "An Anomaly-free Atlas: charting the space of flavour-dependent gauged $U(1)$ extensions of the Standard Model." In: *JHEP* 02 (2019). [Erratum: JHEP 08, 064 (2019)], p. 082. doi: 10.1007/JHEP02(2019)082. arXiv: 1812.04602 [hep-ph].

[12] J. Aebischer, A. J. Buras, M. Cerdà-Sevilla, and F. De Fazio. "Quark-lepton connections in Z' mediated FCNC processes: gauge anomaly cancellations at work." In: *JHEP* 02 (2020), p. 183. doi: 10.1007/JHEP02(2020)183. arXiv: 1912.09308 [hep-ph].

[13] W. Altmannshofer, J. Davighi, and M. Nardecchia. "Gauging the accidental symmetries of the standard model, and implications for the flavor anomalies." In: *Phys. Rev. D* 101.1 (2020), p. 015004. doi: 10.1103/PhysRevD.101.015004. arXiv: 1909.02021 [hep-ph].

[14] J. A. Casas, M. Chakraborti, and J. Quilis. "UV completion of an axial, leptophobic, $Z'$." In: *Phys. Lett. B* 809 (2020), p. 135721. doi: 10.1016/j.physletb.2020.135721. arXiv: 1907.11207 [hep-ph].

[15] A. Crivellin, C. A. Manzari, et al. "Towards excluding a light $Z'$ explanation of $b \to s\ell^+\ell^-$." In: *PSI-PR-22-06, ZU-TH 06/22* (2022). arXiv: 2202.12900 [hep-ph].

[16] R. Bause, M. Golz, G. Hiller, and A. Tayduganov. "The new physics reach of null tests with $D \to \pi\ell\ell$ and $D_s \to K\ell\ell$ decays." In: *Eur. Phys. J. C* 80.1 (2020). [Erratum: Eur.Phys.J.C 81, 219 (2021)], p. 65. doi: 10.1140/epjc/s10052-020-7621-7. arXiv: 1909.11108 [hep-ph].

[17] R. Bause, H. Gisbert, M. Golz, and G. Hiller. "Exploiting $CP$-asymmetries in rare charm decays." In: *Phys. Rev. D* 101.11 (2020), p. 115006. doi: 10.1103/PhysRevD.101.115006. arXiv: 2004.01206 [hep-ph].

[18] R. Bause, H. Gisbert, M. Golz, and G. Hiller. "Lepton universality and lepton flavor conservation tests with dineutrino modes." In: *Eur. Phys. J. C* 82.2 (2022), p. 164. doi: 10.1140/epjc/s10052-022-10113-6. arXiv: 2007.05001 [hep-ph].

[19] R. Bause, H. Gisbert, M. Golz, and G. Hiller. "Rare charm $\boldsymbol{c \to u\,\nu\bar{\nu}}$ dineutrino null tests for $e^+e^-$ machines." In: *Phys. Rev. D* 103.1 (2021), p. 015033. doi: 10.1103/PhysRevD.103.015033. arXiv: 2010.02225 [hep-ph].

[20] R. Bause, H. Gisbert, M. Golz, and G. Hiller. "Interplay of dineutrino modes with semileptonic rare B-decays." In: *JHEP* 12 (2021), p. 061. doi: 10.1007/JHEP12(2021)061. arXiv: 2109.01675 [hep-ph].

[21] R. Bause, G. Hiller, T. Höhne, D. F. Litim, and T. Steudtner. "B-anomalies from flavorful U(1)′ extensions, safely." In: *Eur. Phys. J. C* 82.1 (2022), p. 42. doi: 10.1140/epjc/s10052-021-09957-1. arXiv: 2109.06201 [hep-ph].

[22] J. Ellis. "TikZ-Feynman: Feynman diagrams with TikZ." In: *Comput. Phys. Commun.* 210 (2017), pp. 103–123. doi: 10.1016/j.cpc.2016.08.019. arXiv: 1601.05437 [hep-ph].

[23] M. E. Peskin and D. V. Schroeder. *An Introduction to quantum field theory*. Reading, USA: Addison-Wesley, 1995.

[24] M. D. Schwartz. *Quantum Field Theory and the Standard Model*. Cambridge University Press, 2014.

[25] Y. Grossman and P. Tanedo. "Just a Taste: Lectures on Flavor Physics." In: *Theoretical Advanced Study Institute in Elementary Particle Physics: Anticipating the Next Discoveries in Particle Physics*. 2018, pp. 109–295. doi: 10.1142/9789813233348_0004. arXiv: 1711.03624 [hep-ph].

[26] A. Buras. *Gauge Theory of Weak Decays*. Cambridge University Press, 2020. doi: 10.1017/9781139524100.

[27] G. Degrassi, S. Di Vita, et al. "Higgs mass and vacuum stability in the Standard Model at NNLO." In: *JHEP* 08 (2012), p. 098. doi: 10.1007/JHEP08(2012)098. arXiv: 1205.6497 [hep-ph].

[28] D. Buttazzo, G. Degrassi, et al. "Investigating the near-criticality of the Higgs boson." In: *JHEP* 12 (2013), p. 089. doi: 10.1007/JHEP12(2013)089. arXiv: 1307.3536 [hep-ph].

[29] A. Shkerin and S. Sibiryakov. "On stability of electroweak vacuum during inflation." In: *Phys. Lett. B* 746 (2015), pp. 257–260. doi: 10.1016/j.physletb.2015.05.012. arXiv: 1503.02586 [hep-ph].

[30] J. Goldstone, A. Salam, and S. Weinberg. "Broken Symmetries." In: *Phys. Rev.* 127 (1962), pp. 965–970. doi: 10.1103/PhysRev.127.965.

[31] T. Aaltonen et al. [CDF]. "High-precision measurement of the W boson mass with the CDF II detector." In: *Science* 376.6589 (2022), pp. 170–176. doi: 10.1126/science.abk1781.

[32] P. A. Zyla et al. [Particle Data Group]. "Review of Particle Physics." In: *PTEP* 2020 (2020), p. 083C01. doi: 10.1093/ptep/ptaa104.

[33] P. A. R. Ade et al. [Planck]. "Planck 2015 results. XIII. Cosmological parameters." In: *Astron. Astrophys.* 594 (2016), A13. doi: 10.1051/0004-6361/201525830. arXiv: 1502.01589 [astro-ph.CO].

[34] W. Altmannshofer and J. Zupan. "Snowmass White Paper: Flavor Model Building." In: *2022 Snowmass Summer Study*. 2022. arXiv: 2203.07726 [hep-ph].

[35] N. Cabibbo. "Unitary Symmetry and Leptonic Decays." In: *Phys. Rev. Lett.* 10 (1963), pp. 531–533. doi: 10.1103/PhysRevLett.10.531.

[36] M. Kobayashi and T. Maskawa. "CP Violation in the Renormalizable Theory of Weak Interaction." In: *Prog. Theor. Phys.* 49 (1973), pp. 652–657. doi: 10.1143/PTP.49.652.

[37] S. L. Glashow, J. Iliopoulos, and L. Maiani. "Weak Interactions with Lepton-Hadron Symmetry." In: *Phys. Rev. D* 2 (1970), pp. 1285–1292. doi: 10.1103/PhysRevD.2.1285.

[38] S. Bilenky. *Introduction to the Physics of Massive and Mixed Neutrinos*. Vol. 947. Springer, 2018. doi: 10.1007/978-3-319-74802-3.

[39] L.-L. Chau and W.-Y. Keung. "Comments on the Parametrization of the Kobayashi-Maskawa Matrix." In: *Phys. Rev. Lett.* 53 (1984), p. 1802. doi: 10.1103/PhysRevLett.53.1802.

[40] L. Wolfenstein. "Parametrization of the Kobayashi-Maskawa Matrix." In: *Phys. Rev. Lett.* 51 (1983), p. 1945. doi: 10.1103/PhysRevLett.51.1945.

[41] S. Descotes-Genon and P. Koppenburg. "The CKM Parameters." In: *Ann. Rev. Nucl. Part. Sci.* 67 (2017), pp. 97–127. doi: 10.1146/annurev-nucl-101916-123109. arXiv: 1702.08834 [hep-ex].

[42] Y. Grossman and J. T. Ruderman. "CKM substructure." In: *JHEP* 01 (2021), p. 143. doi: 10.1007/JHEP01(2021)143. arXiv: 2007.12695 [hep-ph].

[43] Y. Grossman, A. Ismail, J. T. Ruderman, and T.-H. Tsai. "CKM substructure from the weak to the Planck scale." In: *JHEP* 06 (2022), p. 065. doi: 10.1007/JHEP06(2022)065. arXiv: 2201.10561 [hep-ph].

[44] A. J. Buras. "Weak Hamiltonian, CP violation and rare decays." In: *Les Houches Summer School in Theoretical Physics, Session 68: Probing the Standard Model of Particle Interactions*. 1998, pp. 281–539. arXiv: hep-ph/9806471.

[45] T. Appelquist and J. Carazzone. "Infrared Singularities and Massive Fields." In: *Phys. Rev. D* 11 (1975), p. 2856. doi: 10.1103/PhysRevD.11.2856.

[46] A. Grozin. "Lectures on QED and QCD." In: *3rd Dubna International Advanced School of Theoretical Physics*. 2005. arXiv: hep-ph/0508242.

[47] C. G. Bollini and J. J. Giambiagi. "Dimensional Renormalization: The Number of Dimensions as a Regularizing Parameter." In: *Nuovo Cim. B* 12 (1972), pp. 20–26. doi: 10.1007/BF02895558.

[48] G. 't Hooft and M. J. G. Veltman. "Regularization and Renormalization of Gauge Fields." In: *Nucl. Phys. B* 44 (1972), pp. 189–213. doi: 10.1016/0550-3213(72)90279-9.

[49] S. Weinberg. "New approach to the renormalization group." In: *Phys. Rev. D* 8 (1973), pp. 3497–3509. doi: 10.1103/PhysRevD.8.3497.

[50] D. F. Litim and T. Steudtner. "ARGES – Advanced Renormalisation Group Equation Simplifier." In: *Comput. Phys. Commun.* 265 (2021), p. 108021. doi: 10.1016/j.cpc.2021.108021. arXiv: 2012.12955 [hep-ph].

[51] T. Markkanen, A. Rajantie, and S. Stopyra. "Cosmological Aspects of Higgs Vacuum Metastability." In: *Front. Astron. Space Sci.* 5 (2018), p. 40. doi: 10.3389/fspas.2018.00040. arXiv: 1809.06923 [astro-ph.CO].

[52] D. J. Gross and F. Wilczek. "Ultraviolet Behavior of Nonabelian Gauge Theories." In: *Phys. Rev. Lett.* 30 (1973). Ed. by J. C. Taylor, pp. 1343–1346. doi: 10.1103/PhysRevLett.30.1343.

[53] A. Pich. "Effective field theory: Course." In: *Les Houches Summer School in Theoretical Physics, Session 68: Probing the Standard Model of Particle Interactions*. 1998, pp. 949–1049. arXiv: hep-ph/9806303.

[54] E. Fermi. "An attempt of a theory of beta radiation. 1." In: *Z. Phys.* 88 (1934), pp. 161–177. doi: 10.1007/BF01351864.

[55] A. V. Manohar. "Effective field theories." In: *Lect. Notes Phys.* 479 (1997). Ed. by H. Latal and W. Schweiger, pp. 311–362. doi: 10.1007/BFb0104294. arXiv: hep-ph/9606222.

[56] M. Neubert. "Effective field theory and heavy quark physics." In: *Theoretical Advanced Study Institute in Elementary Particle Physics: Physics in $D \geqq 4$*. 2005, pp. 149–194. doi: 10.1142/9789812773579_0004. arXiv: hep-ph/0512222.

[57] G. Buchalla, A. J. Buras, and M. E. Lautenbacher. "Weak decays beyond leading logarithms." In: *Rev. Mod. Phys.* 68 (1996), pp. 1125–1144. doi: 10.1103/RevModPhys.68.1125. arXiv: hep-ph/9512380.

[58] A. J. Buras. "Operator product expansion, renormalization group and weak decays." In: *Lect. Notes Phys.* 558 (2000). Ed. by P. Breitenlohner and D. Maison, pp. 65–85. arXiv: hep-ph/9901409.

[59] A. V. Manohar. "Introduction to Effective Field Theories." In: (2018). Ed. by S. Davidson, P. Gambino, M. Laine, M. Neubert, and C. Salomon. doi: 10.1093/oso/9780198855743.003.0002. arXiv: 1804.05863 [hep-ph].

[60] M. Neubert. "Renormalization Theory and Effective Field Theories." In: *MITP/19-002* (2019). Ed. by S. Davidson, P. Gambino, M. Laine, M. Neubert, and C. Salomon. doi: 10.1093/oso/9780198855743.003.0001. arXiv: 1901.06573 [hep-ph].

[61] B. Grzadkowski, M. Iskrzynski, M. Misiak, and J. Rosiek. "Dimension-Six Terms in the Standard Model Lagrangian." In: *JHEP* 10 (2010), p. 085. doi: 10.1007/JHEP10(2010)085. arXiv: 1008.4884 [hep-ph].

[62] S. Weinberg. "Baryon and Lepton Nonconserving Processes." In: *Phys. Rev. Lett.* 43 (1979), pp. 1566–1570. doi: 10.1103/PhysRevLett.43.1566.

[63] E. E. Jenkins, A. V. Manohar, and P. Stoffer. "Low-Energy Effective Field Theory below the Electroweak Scale: Operators and Matching." In: *JHEP* 03 (2018), p. 016. doi: 10.1007/JHEP03(2018)016. arXiv: 1709.04486 [hep-ph].

[64] A. Falkowski. "Effective field theory approach to LHC Higgs data." In: *Pramana* 87.3 (2016), p. 39. doi: 10.1007/s12043-016-1251-5. arXiv: 1505.00046 [hep-ph].

[65] V. Cirigliano, W. Dekens, J. de Vries, and E. Mereghetti. "Constraining the top-Higgs sector of the Standard Model Effective Field Theory." In: *Phys. Rev. D* 94.3 (2016), p. 034031. doi: 10.1103/PhysRevD.94.034031. arXiv: 1605.04311 [hep-ph].

[66] J. de Blas, J. C. Criado, M. Perez-Victoria, and J. Santiago. "Effective description of general extensions of the Standard Model: the complete tree-level dictionary." In: *JHEP* 03 (2018), p. 109. doi: 10.1007/JHEP03(2018)109. arXiv: 1711.10391 [hep-ph].

[67] I. Brivio and M. Trott. "The Standard Model as an Effective Field Theory." In: *Phys. Rept.* 793 (2019), pp. 1–98. doi: 10.1016/j.physrep.2018.11.002. arXiv: 1706.08945 [hep-ph].

[68] J. Ellis, C. W. Murphy, V. Sanz, and T. You. "Updated Global SMEFT Fit to Higgs, Diboson and Electroweak Data." In: *JHEP* 06 (2018), p. 146. doi: 10.1007/JHEP06(2018)146. arXiv: 1803.03252 [hep-ph].

[69] J. Aebischer, W. Altmannshofer, et al. "$B$-decay discrepancies after Moriond 2019." In: *Eur. Phys. J. C* 80.3 (2020), p. 252. doi: 10.1140/epjc/s10052-020-7817-x. arXiv: 1903.10434 [hep-ph].

[70] M. Beneke, T. Feldmann, and D. Seidel. "Systematic approach to exclusive $B \to V l^+ l^-$, $V\gamma$ decays." In: *Nucl. Phys. B* 612 (2001), pp. 25–58. doi: 10.1016/S0550-3213(01)00366-2. arXiv: hep-ph/0106067.

[71] R. Alonso, B. Grinstein, and J. Martin Camalich. "$SU(2) \times U(1)$ gauge invariance and the shape of new physics in rare $B$ decays." In: *Phys. Rev. Lett.* 113 (2014), p. 241802. doi: 10.1103/PhysRevLett.113.241802. arXiv: 1407.7044 [hep-ph].

[72] K. G. Chetyrkin, M. Misiak, and M. Munz. "Weak radiative B meson decay beyond leading logarithms." In: *Phys. Lett. B* 400 (1997). [Erratum: Phys.Lett.B 425, 414 (1998)], pp. 206–219. doi: 10.1016/S0370-2693(97)00324-9. arXiv: hep-ph/9612313.

[73] J. P. Lees et al. [BaBar]. "Evidence for an excess of $\bar{B} \to D^{(*)}\tau^-\bar{\nu}_\tau$ decays." In: *Phys. Rev. Lett.* 109 (2012), p. 101802. doi: 10.1103/PhysRevLett.109.101802. arXiv: 1205.5442 [hep-ex].

[74] J. P. Lees et al. [BaBar]. "Measurement of an Excess of $\bar{B} \to D^{(*)}\tau^-\bar{\nu}_\tau$ Decays and Implications for Charged Higgs Bosons." In: *Phys. Rev. D* 88.7 (2013), p. 072012. doi: 10.1103/PhysRevD.88.072012. arXiv: 1303.0571 [hep-ex].

[75] M. Huschle et al. [Belle]. "Measurement of the branching ratio of $\bar{B} \to D^{(*)}\tau^-\bar{\nu}_\tau$ relative to $\bar{B} \to D^{(*)}\ell^-\bar{\nu}_\ell$ decays with hadronic tagging at Belle." In: *Phys. Rev. D* 92.7 (2015), p. 072014. doi: 10.1103/PhysRevD.92.072014. arXiv: 1507.03233 [hep-ex].

[76] Y. Sato et al. [Belle]. "Measurement of the branching ratio of $\bar{B}^0 \to D^{*+}\tau^-\bar{\nu}_\tau$ relative to $\bar{B}^0 \to D^{*+}\ell^-\bar{\nu}_\ell$ decays with a semileptonic tagging method." In: *Phys. Rev. D* 94.7 (2016), p. 072007. doi: 10.1103/PhysRevD.94.072007. arXiv: 1607.07923 [hep-ex].

[77] S. Hirose et al. [Belle]. "Measurement of the $\tau$ lepton polarization and $R(D^*)$ in the decay $\bar{B} \to D^*\tau^-\bar{\nu}_\tau$." In: *Phys. Rev. Lett.* 118.21 (2017), p. 211801. doi: 10.1103/PhysRevLett.118.211801. arXiv: 1612.00529 [hep-ex].

[78] R. Aaij et al. [LHCb]. "Measurement of the ratio of branching fractions $\mathcal{B}(\bar{B}^0 \to D^{*+}\tau^-\bar{\nu}_\tau)/\mathcal{B}(\bar{B}^0 \to D^{*+}\mu^-\bar{\nu}_\mu)$." In: *Phys. Rev. Lett.* 115.11 (2015). [Erratum: Phys.Rev.Lett. 115, 159901 (2015)], p. 111803. doi: 10.1103/PhysRevLett.115.111803. arXiv: 1506.08614 [hep-ex].

[79] R. Aaij et al. [LHCb]. "Measurement of the ratio of the $B^0 \to D^{*-}\tau^+\nu_\tau$ and $B^0 \to D^{*-}\mu^+\nu_\mu$ branching fractions using three-prong $\tau$-lepton decays." In: *Phys. Rev. Lett.* 120.17 (2018), p. 171802. doi: 10.1103/PhysRevLett.120.171802. arXiv: 1708.08856 [hep-ex].

[80] S. Bifani, S. Descotes-Genon, A. Romero Vidal, and M.-H. Schune. "Review of Lepton Universality tests in $B$ decays." In: *J. Phys. G* 46.2 (2019), p. 023001. doi: 10.1088/1361-6471/aaf5de. arXiv: 1809.06229 [hep-ex].

[81] E. Graverini [ATLAS, CMS, LHCb]. "Flavour anomalies: a review." In: *J. Phys. Conf. Ser.* 1137.1 (2019). Ed. by F. Bar~ao et al., p. 012025. doi: 10.1088/1742-6596/1137/1/012025. arXiv: 1807.11373 [hep-ex].

[82] G. Hiller and F. Kruger. "More model-independent analysis of $b \to s$ processes." In: *Phys. Rev. D* 69 (2004), p. 074020. doi: 10.1103/PhysRevD.69.074020. arXiv: hep-ph/0310219.

[83] G. Hiller and M. Schmaltz. "Diagnosing lepton-nonuniversality in $b \to s\ell\ell$." In: *JHEP* 02 (2015), p. 055. doi: 10.1007/JHEP02(2015)055. arXiv: 1411.4773 [hep-ph].

[84] R. Aaij et al. [LHCb]. "Test of lepton universality with $B^0 \to K^{*0}\ell^+\ell^-$ decays." In: *JHEP* 08 (2017), p. 055. doi: 10.1007/JHEP08(2017)055. arXiv: 1705.05802 [hep-ex].

[85] W. Altmannshofer et al. [Belle-II]. "The Belle II Physics Book." In: *PTEP* 2019.12 (2019). Ed. by E. Kou and P. Urquijo. [Erratum: PTEP 2020, 029201 (2020)], p. 123C01. doi: 10.1093/ptep/ptz106. arXiv: 1808.10567 [hep-ex].

[86] A. Abdesselam et al. [Belle]. "Test of Lepton-Flavor Universality in $B \to K^*\ell^+\ell^-$ Decays at Belle." In: *Phys. Rev. Lett.* 126.16 (2021), p. 161801. doi: 10.1103/PhysRevLett.126.161801. arXiv: 1904.02440 [hep-ex].

[87] M. Bordone, G. Isidori, and A. Pattori. "On the Standard Model predictions for $R_K$ and $R_{K^*}$." In: *Eur. Phys. J. C* 76.8 (2016), p. 440. doi: 10.1140/epjc/s10052-016-4274-7. arXiv: 1605.07633 [hep-ph].

[88] B. Capdevila, S. Descotes-Genon, L. Hofer, and J. Matias. "Hadronic uncertainties in $B \to K^*\mu^+\mu^-$: a state-of-the-art analysis." In: *JHEP* 04 (2017), p. 016. doi: 10.1007/JHEP04(2017)016. arXiv: 1701.08672 [hep-ph].

[89] N. Serra, R. Silva Coutinho, and D. van Dyk. "Measuring the breaking of lepton flavor universality in $B \to K^*\ell^+\ell^-$." In: *Phys. Rev. D* 95.3 (2017), p. 035029. doi: 10.1103/PhysRevD.95.035029. arXiv: 1610.08761 [hep-ph].

[90] D. van Dyk et al. "EOS - A Software for Flavor Physics Phenomenology." In: *EOS-2021-04, TUM-HEP 1371/21, P3H-21-094, SI-HEP-2021-32* (2021). arXiv: 2111.15428 [hep-ph].

[91] D. M. Straub. "flavio: a Python package for flavour and precision phenomenology in the Standard Model and beyond." In: (2018). arXiv: 1810.08132 [hep-ph].

[92] S. Jäger and J. Martin Camalich. "Reassessing the discovery potential of the $B \to K^*\ell^+\ell^-$ decays in the large-recoil region: SM challenges and BSM opportunities." In: *Phys. Rev. D* 93.1 (2016), p. 014028. doi: 10.1103/PhysRevD.93.014028. arXiv: 1412.3183 [hep-ph].

[93] C. Hati, J. Kriewald, J. Orloff, and A. M. Teixeira. "The fate of $\mathbf{V_1}$ vector leptoquarks: the impact of future flavour data." In: *Eur. Phys. J. C* 81.12 (2021), p. 1066. doi: 10.1140/epjc/s10052-021-09824-z. arXiv: 2012.05883 [hep-ph].

[94] J. Kriewald, C. Hati, J. Orloff, and A. M. Teixeira. "Leptoquarks facing flavour tests and $b \to s\ell\ell$ after Moriond 2021." In: *55th Rencontres de Moriond on Electroweak Interactions and Unified Theories*. 2021. arXiv: 2104.00015 [hep-ph].

[95] H. Dembinski and P. O. et al. "scikit-hep/iminuit." In: (2020). doi: 10.5281/zenodo.3949207.

[96] I. Hughes and T. Hase. *Measurements and Their Uncertainties: A Practical Guide to Modern Error Analysis*. OUP Oxford, 2010.

[97] D. Becirevic, E. Kou, A. Le Yaouanc, and A. Tayduganov. "Future prospects for the determination of the Wilson coefficient $C'_{7\gamma}$." In: *JHEP* 08 (2012), p. 090. doi: 10.1007/JHEP08(2012)090. arXiv: 1206.1502 [hep-ph].

[98] W. Altmannshofer and P. Stangl. "New physics in rare B decays after Moriond 2021." In: *Eur. Phys. J. C* 81.10 (2021), p. 952. doi: 10.1140/epjc/s10052-021-09725-1. arXiv: 2103.13370 [hep-ph].

[99] R. Aaij et al. [LHCb]. "Branching Fraction Measurements of the Rare $B_s^0 \to \phi\mu^+\mu^-$ and $B_s^0 \to f_2'(1525)\mu^+\mu^-$ Decays." In: *Phys. Rev. Lett.* 127.15 (2021), p. 151801. doi: 10.1103/PhysRevLett.127.151801. arXiv: 2105.14007 [hep-ex].

[100] M. Algueró, B. Capdevila, et al. "Emerging patterns of New Physics with and without Lepton Flavour Universal contributions." In: *Eur. Phys. J. C* 79.8 (2019). [Addendum: Eur.Phys.J.C 80, 511 (2020)], p. 714. doi: 10.1140/epjc/s10052-019-7216-3. arXiv: 1903.09578 [hep-ph].

[101] M. Algueró, B. Capdevila, S. Descotes-Genon, J. Matias, and M. Novoa-Brunet. "$b \to s\ell^+\ell^-$ global fits after $R_{K_S}$ and $R_{K^{*+}}$." In: *Eur. Phys. J. C* 82.4 (2022), p. 326. doi: 10.1140/epjc/s10052-022-10231-1. arXiv: 2104.08921 [hep-ph].

[102] K. S. Babu, C. F. Kolda, and J. March-Russell. "Implications of generalized Z - Z-prime mixing." In: *Phys. Rev. D* 57 (1998), pp. 6788–6792. doi: 10.1103/PhysRevD.57.6788. arXiv: hep-ph/9710441.

[103] A. Leike. "The Phenomenology of extra neutral gauge bosons." In: *Phys. Rept.* 317 (1999), pp. 143–250. doi: 10.1016/S0370-1573(98)00133-1. arXiv: hep-ph/9805494.

[104] G. Bélanger, C. Delaunay, and S. Westhoff. "A Dark Matter Relic From Muon Anomalies." In: *Phys. Rev. D* 92 (2015), p. 055021. doi: 10.1103/PhysRevD.92.055021. arXiv: 1507.06660 [hep-ph].

[105] A. Datta, J. Kumar, J. Liao, and D. Marfatia. "New light mediators for the $R_K$ and $R_{K^*}$ puzzles." In: *Phys. Rev. D* 97.11 (2018), p. 115038. doi: 10.1103/PhysRevD.97.115038. arXiv: 1705.08423 [hep-ph].

[106] S. Di Chiara, A. Fowlie, et al. "Minimal flavor-changing $Z'$ models and muon $g-2$ after the $R_{K^*}$ measurement." In: *Nucl. Phys. B* 923 (2017), pp. 245–257. doi: 10.1016/j.nuclphysb.2017.08.003. arXiv: 1704.06200 [hep-ph].

[107] A. Datta, J. Liao, and D. Marfatia. "A light $Z'$ for the $R_K$ puzzle and nonstandard neutrino interactions." In: *Phys. Lett. B* 768 (2017), pp. 265–269. doi: 10.1016/j.physletb.2017.02.058. arXiv: 1702.01099 [hep-ph].

[108] A. D'Alise et al. "Standard model anomalies: Lepton flavour non-universality, g-2 and W-mass." In: (2022). arXiv: 2204.03686 [hep-ph].

[109] P. Langacker and M. Plumacher. "Flavor changing effects in theories with a heavy $Z'$ boson with family nonuniversal couplings." In: *Phys. Rev.* D62 (2000), p. 013006. doi: 10.1103/PhysRevD.62.013006. arXiv: hep-ph/0001204 [hep-ph].

[110] A. J. Buras, F. De Fazio, and J. Girrbach. "The Anatomy of Z' and Z with Flavour Changing Neutral Currents in the Flavour Precision Era." In: *JHEP* 02 (2013), p. 116. doi: 10.1007/JHEP02(2013)116. arXiv: 1211.1896 [hep-ph].

[111] A. Crivellin, L. Hofer, et al. "Lepton-flavour violating $B$ decays in generic $Z'$ models." In: *Phys. Rev. D* 92.5 (2015), p. 054013. doi: 10.1103/PhysRevD.92.054013. arXiv: 1504.07928 [hep-ph].

[112] C. S. Kim, X.-B. Yuan, and Y.-J. Zheng. "Constraints on a Z' boson within minimal flavor violation." In: *Phys. Rev. D* 93.9 (2016), p. 095009. doi: 10.1103/PhysRevD.93.095009. arXiv: 1602.08107 [hep-ph].

[113] B. C. Allanach, J. M. Butterworth, and T. Corbett. "Large hadron collider constraints on some simple $Z'$ models for $b \to s\mu^+\mu^-$ anomalies." In: *Eur. Phys. J. C* 81.12 (2021), p. 1126. doi: 10.1140/epjc/s10052-021-09919-7. arXiv: 2110.13518 [hep-ph].

[114] C. Promberger, S. Schatt, and F. Schwab. "Flavor Changing Neutral Current Effects and CP Violation in the Minimal 3-3-1 Model." In: *Phys. Rev. D* 75 (2007), p. 115007. doi: 10.1103/PhysRevD.75.115007. arXiv: hep-ph/0702169.

[115] A. J. Buras, F. De Fazio, J. Girrbach, and M. V. Carlucci. "The Anatomy of Quark Flavour Observables in 331 Models in the Flavour Precision Era." In: *JHEP* 02 (2013), p. 023. doi: 10.1007/JHEP02(2013)023. arXiv: 1211.1237 [hep-ph].

[116] J. J. Gil. "Parametrization of 3 × 3 unitary matrices based on polarization algebra." In: *European Physical Journal Plus* 133.5, 206 (2018), p. 206. doi: 10.1140/epjp/i2018-12032-0. arXiv: 1802.00196 [math-ph].

[117] F. Tellander. *Anomaly-free Froggatt-Nielsen extensions of the Standard Model with two Higgs doublets*. Master's thesis. 2018.

[118] J. Rathsman and F. Tellander. "Anomaly-free Model Building with Algebraic Geometry." In: *Phys. Rev. D* 100.5 (2019), p. 055032. doi: 10.1103/PhysRevD.100.055032. arXiv: 1902.08529 [hep-ph].

[119] D. B. Costa, B. A. Dobrescu, and P. J. Fox. "General Solution to the U(1) Anomaly Equations." In: *Phys. Rev. Lett.* 123.15 (2019), p. 151601. doi: 10.1103/PhysRevLett.123.151601. arXiv: 1905.13729 [hep-th].

[120] *Gröbner Bases and Applications*. London Mathematical Society Lecture Note Series. Cambridge University Press, 1998. doi: 10.1017/CBO9780511565847.

[121] U. Nierste. "Three Lectures on Meson Mixing and CKM phenomenology." In: *Helmholz International Summer School on Heavy Quark Physics*. 2009, pp. 1–38. arXiv: 0904.1869 [hep-ph].

[122] A. L. Kagan and M. D. Sokoloff. "On Indirect CP Violation and Implications for D0 - anti-D0 and B(s) - anti-B(s) mixing." In: *Phys. Rev. D* 80 (2009), p. 076008. doi: 10.1103/PhysRevD.80.076008. arXiv: 0907.3917 [hep-ph].

[123] Y. S. Amhis et al. [HFLAV]. "Averages of b-hadron, c-hadron, and $\tau$-lepton properties as of 2018." In: *Eur. Phys. J. C* 81.3 (2021), p. 226. doi: 10.1140/epjc/s10052-020-8156-7. arXiv: 1909.12524 [hep-ex].

[124] [HFLAV]. *Global Fit for $D^0$-$\overline{D}^0$ mixing (allowing for CP violation)*. https://hflav-eos.web.cern.ch/hflav-eos/charm/CKM21/results_mix_cpv.html. accessed: 16.05.2022.

[125] M. Chala, A. Lenz, A. V. Rusov, and J. Scholtz. "$\Delta A_{CP}$ within the Standard Model and beyond." In: *JHEP* 07 (2019), p. 161. doi: 10.1007/JHEP07(2019)161. arXiv: 1903.10490 [hep-ph].

[126] E. Golowich, J. Hewett, S. Pakvasa, and A. A. Petrov. "Relating $D^0$ - $\overline{D}^0$ Mixing and $D^0 \to \ell^+\ell^-$ with New Physics." In: *Phys. Rev.* D79 (2009), p. 114030. doi: 10.1103/PhysRevD.79.114030. arXiv: 0903.2830 [hep-ph].

[127] E. Golowich, J. Hewett, S. Pakvasa, and A. A. Petrov. "Implications of $D^0$ - $\overline{D}^0$ Mixing for New Physics." In: *Phys. Rev.* D76 (2007), p. 095009. doi: 10.1103/PhysRevD.76.095009. arXiv: 0705.3650 [hep-ph].

[128] L. Di Luzio, M. Kirk, A. Lenz, and T. Rauh. "$\Delta M_s$ theory precision confronts flavour anomalies." In: *JHEP* 12 (2019), p. 009. doi: 10.1007/JHEP12(2019)009. arXiv: 1909.11087 [hep-ph].

[129] S. Dwivedi, D. Kumar Ghosh, A. Falkowski, and N. Ghosh. "Associated $Z'$ production in the flavorful $U(1)$ scenario for $R_{K^{(*)}}$." In: *Eur. Phys. J. C* 80.3 (2020), p. 263. doi: 10.1140/epjc/s10052-020-7810-4. arXiv: 1908.03031 [hep-ph].

[130] A. J. Buras, D. Guadagnoli, and G. Isidori. "On $\epsilon_K$ Beyond Lowest Order in the Operator Product Expansion." In: *Phys. Lett. B* 688 (2010), pp. 309–313. doi: 10.1016/j.physletb.2010.04.017. arXiv: 1002.3612 [hep-ph].

[131] J. Brod, M. Gorbahn, and E. Stamou. "Updated Standard Model Prediction for $K \to \pi\nu\bar{\nu}$ and $\epsilon_K$." In: *PoS* BEAUTY2020 (2021), p. 056. doi: 10.22323/1.391.0056. arXiv: 2105.02868 [hep-ph].

[132] B. Holdom. "Two U(1)'s and Epsilon Charge Shifts." In: *Phys. Lett. B* 166 (1986), pp. 196–198. doi: 10.1016/0370-2693(86)91377-8.

[133] G. Hiller, D. Loose, and I. Nišandžić. "Flavorful leptoquarks at the LHC and beyond: spin 1." In: *JHEP* 06 (2021), p. 080. doi: 10.1007/JHEP06(2021)080. arXiv: 2103.12724 [hep-ph].

[134] B. C. Allanach. "$U(1)_{B_3-L_2}$ explanation of the neutral current $B-$anomalies." In: *Eur. Phys. J. C* 81.1 (2021). [Erratum: Eur.Phys.J.C 81, 321 (2021)], p. 56. doi: 10.1140/epjc/s10052-021-08855-w. arXiv: 2009.02197 [hep-ph].

[135] A. M. Sirunyan et al. [CMS]. "Search for resonant and nonresonant new phenomena in high-mass dilepton final states at $\sqrt{s} = 13$ TeV." In: *JHEP* 07 (2021), p. 208. doi: 10.1007/JHEP07(2021)208. arXiv: 2103.02708 [hep-ex].

[136] G. Aad et al. [ATLAS]. "Search for high-mass dilepton resonances using 139 fb$^{-1}$ of $pp$ collision data collected at $\sqrt{s}$ =13 TeV with the ATLAS detector." In: *Phys. Lett. B* 796 (2019), pp. 68–87. doi: 10.1016/j.physletb.2019.07.016. arXiv: 1903.06248 [hep-ex].

[137] A. D. Bond and D. F. Litim. "Theorems for Asymptotic Safety of Gauge Theories." In: *Eur. Phys. J. C* 77.6 (2017). [Erratum: Eur.Phys.J.C 77, 525 (2017)], p. 429. doi: 10.1140/epjc/s10052-017-4976-5. arXiv: 1608.00519 [hep-th].

[138] A. D. Bond and D. F. Litim. "Price of Asymptotic Safety." In: *Phys. Rev. Lett.* 122.21 (2019), p. 211601. doi: 10.1103/PhysRevLett.122.211601. arXiv: 1801.08527 [hep-th].

[139] G. Hiller, C. Hormigos-Feliu, D. F. Litim, and T. Steudtner. "Anomalous magnetic moments from asymptotic safety." In: *Phys. Rev. D* 102.7 (2020), p. 071901. doi: 10.1103/PhysRevD.102.071901. arXiv: 1910.14062 [hep-ph].

[140] G. Hiller, C. Hormigos-Feliu, D. F. Litim, and T. Steudtner. "Model Building from Asymptotic Safety with Higgs and Flavor Portals." In: *Phys. Rev. D* 102.9 (2020), p. 095023. doi: 10.1103/PhysRevD.102.095023. arXiv: 2008.08606 [hep-ph].

[141] D. F. Litim and F. Sannino. "Asymptotic safety guaranteed." In: *JHEP* 12 (2014), p. 178. doi: 10.1007/JHEP12(2014)178. arXiv: 1406.2337 [hep-th].

[142] A. D. Bond, G. Hiller, K. Kowalska, and D. F. Litim. "Directions for model building from asymptotic safety." In: *JHEP* 08 (2017), p. 004. doi: 10.1007/JHEP08(2017)004. arXiv: 1702.01727 [hep-ph].

[143] A. D. Bond and D. F. Litim. "More asymptotic safety guaranteed." In: *Phys. Rev. D* 97.8 (2018), p. 085008. doi: 10.1103/PhysRevD.97.085008. arXiv: 1707.04217 [hep-th].

[144] A. D. Bond, D. F. Litim, G. Medina Vazquez, and T. Steudtner. "UV conformal window for asymptotic safety." In: *Phys. Rev. D* 97.3 (2018), p. 036019. doi: 10.1103/PhysRevD.97.036019. arXiv: 1710.07615 [hep-th].

[145] A. D. Bond, D. F. Litim, and T. Steudtner. "Asymptotic safety with Majorana fermions and new large $N$ equivalences." In: *Phys. Rev. D* 101.4 (2020), p. 045006. doi: 10.1103/PhysRevD.101.045006. arXiv: 1911.11168 [hep-th].

[146] A. D. Bond, D. F. Litim, and G. M. Vazquez. "Conformal windows beyond asymptotic freedom." In: *Phys. Rev. D* 104.10 (2021), p. 105002. doi: 10.1103/PhysRevD.104.105002. arXiv: 2107.13020 [hep-th].

[147] S. Bißmann, G. Hiller, C. Hormigos-Feliu, and D. F. Litim. "Multi-lepton signatures of vector-like leptons with flavor." In: *Eur. Phys. J. C* 81.2 (2021), p. 101. doi: 10.1140/epjc/s10052-021-08886-3. arXiv: 2011.12964 [hep-ph].

[148] T. Feldmann, B. Müller, and D. Seidel. "$D \to \rho \ell^+ \ell^-$ decays in the QCD factorization approach." In: *JHEP* 08 (2017), p. 105. doi: 10.1007/JHEP08(2017)105. arXiv: 1705.05891 [hep-ph].

[149] H. Gisbert, M. Golz, and D. S. Mitzel. "Theoretical and experimental status of rare charm decays." In: *Mod. Phys. Lett. A* 36.04 (2021), p. 2130002. doi: 10.1142/S0217732321300020. arXiv: 2011.09478 [hep-ph].

[150] C. Greub, T. Hurth, M. Misiak, and D. Wyler. "The $c \to u\gamma$ contribution to weak radiative charm decay." In: *Phys. Lett. B* 382 (1996), pp. 415–420. doi: 10.1016/0370-2693(96)00694-6. arXiv: hep-ph/9603417.

[151] S. de Boer, B. Müller, and D. Seidel. "Higher-order Wilson coefficients for $c \to u$ transitions in the standard model." In: *JHEP* 08 (2016), p. 091. doi: 10.1007/JHEP08(2016)091. arXiv: 1606.05521 [hep-ph].

[152] C. Bobeth, M. Misiak, and J. Urban. "Photonic penguins at two loops and $m_t$ dependence of $BR[B \to X_s l^+ l^-]$." In: *Nucl. Phys. B* 574 (2000), pp. 291–330. doi: 10.1016/S0550-3213(00)00007-9. arXiv: hep-ph/9910220.

[153] S. de Boer. "Probing the standard model with rare charm decays." PhD thesis. Technischen Universität Dortmund, Dortmund U., 2017.

[154] S. de Boer and G. Hiller. "Flavor and new physics opportunities with rare charm decays into leptons." In: *Phys. Rev.* D93.7 (2016), p. 074001. doi: 10.1103/PhysRevD.93.074001. arXiv: 1510.00311 [hep-ph].

[155] M. Tanabashi et al. [Particle Data Group]. "Review of Particle Physics." In: *Phys. Rev. D* 98.3 (2018), p. 030001. doi: 10.1103/PhysRevD.98.030001.

[156] M. Beylich, G. Buchalla, and T. Feldmann. "Theory of $B \to K^{(*)} \ell^+ \ell^-$ decays at high $q^2$: OPE and quark-hadron duality." In: *Eur. Phys. J. C* 71 (2011), p. 1635. doi: 10.1140/epjc/s10052-011-1635-0. arXiv: 1101.5118 [hep-ph].

[157] A. Bharucha, D. Boito, and C. Méaux. "Disentangling QCD and new physics in $D^+ \to \pi^+ \ell^+ \ell^-$." In: *JHEP* 04 (2021), p. 158. doi: 10.1007/JHEP04(2021)158. arXiv: 2011.12856 [hep-ph].

[158] R. Aaij et al. [LHCb]. "Searches for 25 rare and forbidden decays of $D^+$ and $D_s^+$ mesons." In: *JHEP* 06 (2021), p. 044. doi: 10.1007/JHEP06(2021)044. arXiv: 2011.00217 [hep-ex].

[159] R. Aaij et al. [LHCb]. "Search for the rare decay $D^0 \to \mu^+ \mu^-$." In: *Phys. Lett. B* 725 (2013), pp. 15–24. doi: 10.1016/j.physletb.2013.06.037. arXiv: 1305.5059 [hep-ex].

[160] R. Aaij et al. [LHCb]. "Search for the lepton-flavour violating decay $D^0 \to e^\pm \mu^\mp$." In: *Phys. Lett. B* 754 (2016), pp. 167–175. doi: 10.1016/j.physletb.2016.01.029. arXiv: 1512.00322 [hep-ex].

[161] S. Fajfer and N. Košnik. "Prospects of discovering new physics in rare charm decays." In: *Eur. Phys. J.* C75.12 (2015), p. 567. doi: 10.1140/epjc/s10052-015-3801-2. arXiv: 1510.00965 [hep-ph].

[162] S. Sahoo and R. Mohanta. "New physics effects in charm meson decays involving $c \to u l^+ l^- (l_i^\mp l_j^\pm)$ transitions." In: *Eur. Phys. J. C* 77.5 (2017), p. 344. doi: 10.1140/epjc/s10052-017-4888-4. arXiv: 1705.02251 [hep-ph].

[163] A. Smolkovič, M. Tammaro, and J. Zupan. "Anomaly free Froggatt-Nielsen models of flavor." In: *JHEP* 10 (2019), p. 188. doi: 10.1007/JHEP10(2019)188. arXiv: 1907.10063 [hep-ph].

[164] S. De Boer and G. Hiller. "Null tests from angular distributions in $D \to P_1 P_2 l^+ l^-$, $l = e, \mu$ decays on and off peak." In: *Phys. Rev. D* 98.3 (2018), p. 035041. doi: 10.1103/PhysRevD.98.035041. arXiv: 1805.08516 [hep-ph].

[165] R. Aaij et al. [LHCb]. "Physics case for an LHCb Upgrade II - Opportunities in flavour physics, and beyond, in the HL-LHC era." In: *LHCB-PUB-2018-009, CERN-LHCC-2018-027* (2018). arXiv: 1808.08865 [hep-ex].

[166] S. Fajfer and N. Košnik. "Resonance catalyzed CP asymmetries in D→P$\ell^+\ell^-$." In: *Phys. Rev. D* 87.5 (2013), p. 054026. doi: 10.1103/PhysRevD.87.054026. arXiv: 1208.0759 [hep-ph].

[167] R. Aaij et al. [LHCb]. "Evidence for CP violation in time-integrated $D^0 \to h^- h^+$ decay rates." In: *Phys. Rev. Lett.* 108 (2012), p. 111602. doi: 10.1103/PhysRevLett.108.111602. arXiv: 1112.0938 [hep-ex].

[168] Y. Grossman, A. L. Kagan, and Y. Nir. "New physics and CP violation in singly Cabibbo suppressed D decays." In: *Phys. Rev. D* 75 (2007), p. 036008. doi: 10.1103/PhysRevD.75.036008. arXiv: hep-ph/0609178.

[169] R. Aaij et al. [LHCb]. "Observation of CP Violation in Charm Decays." In: *Phys. Rev. Lett.* 122.21 (2019), p. 211803. doi: 10.1103/PhysRevLett.122.211803. arXiv: 1903.08726 [hep-ex].

[170] A. Dery and Y. Nir. "Implications of the LHCb discovery of CP violation in charm decays." In: *JHEP* 12 (2019), p. 104. doi: 10.1007/JHEP12(2019)104. arXiv: 1909.11242 [hep-ph].

[171] J. Brod, A. L. Kagan, and J. Zupan. "Size of direct CP violation in singly Cabibbo-suppressed D decays." In: *Phys. Rev. D* 86 (2012), p. 014023. doi: 10.1103/PhysRevD.86.014023. arXiv: 1111.5000 [hep-ph].

[172] J. Brod, Y. Grossman, A. L. Kagan, and J. Zupan. "A Consistent Picture for Large Penguins in D -> pi+ pi-, K+ K-." In: *JHEP* 10 (2012), p. 161. doi: 10.1007/JHEP10(2012)161. arXiv: 1203.6659 [hep-ph].

[173] Y. Grossman and S. Schacht. "The emergence of the $\Delta U = 0$ rule in charm physics." In: *JHEP* 07 (2019), p. 020. doi: 10.1007/JHEP07(2019)020. arXiv: 1903.10952 [hep-ph].

[174] H.-Y. Cheng and C.-W. Chiang. "Revisiting CP violation in $D \to PP$ and $VP$ decays." In: *Phys. Rev. D* 100.9 (2019), p. 093002. doi: 10.1103/PhysRevD.100.093002. arXiv: 1909.03063 [hep-ph].

[175] H.-N. Li, C.-D. Lü, and F.-S. Yu. "Implications on the first observation of charm CPV at LHCb." In: (2019). arXiv: 1903.10638 [hep-ph].

[176] A. Khodjamirian and A. A. Petrov. "Direct CP asymmetry in $D \to \pi^-\pi^+$ and $D \to K^-K^+$ in QCD-based approach." In: *Phys. Lett. B* 774 (2017), pp. 235–242. doi: 10.1016/j.physletb.2017.09.070. arXiv: 1706.07780 [hep-ph].

[177] W. Altmannshofer, R. Primulando, C.-T. Yu, and F. Yu. "New Physics Models of Direct CP Violation in Charm Decays." In: *JHEP* 04 (2012), p. 049. doi: 10.1007/JHEP04(2012)049. arXiv: 1202.2866 [hep-ph].

[178] Y. Grossman, Z. Ligeti, and D. J. Robinson. "More Flavor SU(3) Tests for New Physics in CP Violating B Decays." In: *JHEP* 01 (2014), p. 066. doi: 10.1007/JHEP01(2014)066. arXiv: 1308.4143 [hep-ph].

[179] Y. Grossman and S. Schacht. "U-Spin Sum Rules for CP Asymmetries of Three-Body Charmed Baryon Decays." In: *Phys. Rev. D* 99.3 (2019), p. 033005. doi: 10.1103/PhysRevD.99.033005. arXiv: 1811.11188 [hep-ph].

[180] H. Mendez et al. [CLEO]. "Measurements of D Meson Decays to Two Pseudoscalar Mesons." In: *Phys. Rev. D* 81 (2010), p. 052013. doi: 10.1103/PhysRevD.81.052013. arXiv: 0906.3198 [hep-ex].

[181] Y. Grossman, A. L. Kagan, and J. Zupan. "Testing for new physics in singly Cabibbo suppressed D decays." In: *Phys. Rev. D* 85 (2012), p. 114036. doi: 10.1103/PhysRevD.85.114036. arXiv: 1204.3557 [hep-ph].

[182] G. Hiller, M. Jung, and S. Schacht. "SU(3)-flavor anatomy of nonleptonic charm decays." In: *Phys. Rev. D* 87.1 (2013), p. 014024. doi: 10.1103/PhysRevD.87.014024. arXiv: 1211.3734 [hep-ph].

[183] J. Fuentes-Martin, A. Greljo, J. Martin Camalich, and J. D. Ruiz-Alvarez. "Charm physics confronts high-$p_T$ lepton tails." In: *JHEP* 11 (2020), p. 080. doi: 10.1007/JHEP11(2020)080. arXiv: 2003.12421 [hep-ph].

[184] R. Aaij et al. [LHCb]. "Observation of the Mass Difference Between Neutral Charm-Meson Eigenstates." In: *Phys. Rev. Lett.* 127.11 (2021), p. 111801. doi: 10.1103/PhysRevLett.127.111801. arXiv: 2106.03744 [hep-ex].

[185] A. J. Paterson. "Coleman-Weinberg Symmetry Breaking in the Chiral SU($N$) X SU($N$) Linear Sigma Model." In: *Nucl. Phys. B* 190 (1981), pp. 188–204. doi: 10.1016/0550-3213(81)90489-2.

[186] D. F. Litim, M. Mojaza, and F. Sannino. "Vacuum stability of asymptotically safe gauge-Yukawa theories." In: *JHEP* 01 (2016), p. 081. doi: 10.1007/JHEP01(2016)081. arXiv: 1501.03061 [hep-th].

[187] K. Kannike. "Vacuum Stability Conditions From Copositivity Criteria." In: *Eur. Phys. J. C* 72 (2012), p. 2093. doi: 10.1140/epjc/s10052-012-2093-z. arXiv: 1205.3781 [hep-ph].

[188] B. Allanach, F. S. Queiroz, A. Strumia, and S. Sun. "$Z$ models for the LHCb and $g-2$ muon anomalies." In: *Phys. Rev. D* 93.5 (2016). [Erratum: Phys.Rev.D 95, 119902 (2017)], p. 055045. doi: 10.1103/PhysRevD.93.055045. arXiv: 1511.07447 [hep-ph].

[189] J. Kang and P. Langacker. "$Z$ ' discovery limits for supersymmetric E(6) models." In: *Phys. Rev. D* 71 (2005), p. 035014. doi: 10.1103/PhysRevD.71.035014. arXiv: hep-ph/0412190.

[190] J. P. Delahaye, M. Diemoz, et al. "Muon Colliders." In: (2019). arXiv: 1901.06150 [physics.acc-ph].

[191] H. Al Ali et al. "The Muon Smasher's Guide." In: (2021). arXiv: 2103.14043 [hep-ph].

[192] K. Long, D. Lucchesi, et al. "Muon colliders to expand frontiers of particle physics." In: *Nature Phys.* 17.3 (2021), pp. 289–292. doi: 10.1038/s41567-020-01130-x. arXiv: 2007.15684 [physics.acc-ph].

[193] F. Zimmermann. "LHC/FCC-based muon colliders." In: (2018), MOPMF065. doi: 10.18429/JACoW-IPAC2018-MOPMF065.

[194] G.-y. Huang, F. S. Queiroz, and W. Rodejohann. "Gauged $L_\mu - L_\tau$ at a muon collider." In: *Phys. Rev. D* 103.9 (2021), p. 095005. doi: 10.1103/PhysRevD.103.095005. arXiv: 2101.04956 [hep-ph].

[195] G.-y. Huang, S. Jana, F. S. Queiroz, and W. Rodejohann. "Probing the RK(*) anomaly at a muon collider." In: *Phys. Rev. D* 105.1 (2022), p. 015013. doi: 10.1103/PhysRevD.105.015013. arXiv: 2103.01617 [hep-ph].

[196] B. Abi et al. [Muon g-2]. "Measurement of the Positive Muon Anomalous Magnetic Moment to 0.46 ppm." In: *Phys. Rev. Lett.* 126.14 (2021), p. 141801. doi: 10.1103/PhysRevLett.126.141801. arXiv: 2104.03281 [hep-ex].

[197] J. P. Leveille. "The Second Order Weak Correction to (G-2) of the Muon in Arbitrary Gauge Models." In: *Nucl. Phys. B* 137 (1978), pp. 63–76. doi: 10.1016/0550-3213(78)90051-2.

[198] L. Lavoura. "General formulae for f(1) —> f(2) gamma." In: *Eur. Phys. J. C* 29 (2003), pp. 191–195. doi: 10.1140/epjc/s2003-01212-7. arXiv: hep-ph/0302221.

[199] A. Greljo, Y. Soreq, P. Stangl, A. E. Thomsen, and J. Zupan. "Muonic force behind flavor anomalies." In: *JHEP* 04 (2022), p. 151. doi: 10.1007/JHEP04(2022)151. arXiv: 2107.07518 [hep-ph].

[200] X. Wang. "Muon $(g-2)$ and Flavor Puzzles in the $U(1)_X$-gauged Leptoquark Model." In: (2021). arXiv: 2108.01279 [hep-ph].

[201] M. F. Navarro and S. F. King. "Fermiophobic Z' model for simultaneously explaining the muon anomalies RK(*) and (g-2)$\mu$." In: *Phys. Rev. D* 105.3 (2022), p. 035015. doi: 10.1103/PhysRevD.105.035015. arXiv: 2109.08729 [hep-ph].

[202] M. Ablikim et al. [BESIII]. "Future Physics Programme of BESIII." In: *Chin. Phys. C* 44.4 (2020), p. 040001. doi: 10.1088/1674-1137/44/4/040001. arXiv: 1912.05983 [hep-ex].

[203] A. Abada et al. [FCC]. "FCC Physics Opportunities: Future Circular Collider Conceptual Design Report Volume 1." In: *Eur. Phys. J. C* 79.6 (2019), p. 474. doi: 10.1140/epjc/s10052-019-6904-3.

[204] J. Brod, M. Gorbahn, and E. Stamou. "Two-Loop Electroweak Corrections for the $K \to \pi\nu\bar{\nu}$ Decays." In: *Phys. Rev. D* 83 (2011), p. 034030. doi: 10.1103/PhysRevD.83.034030. arXiv: 1009.0947 [hep-ph].

[205] G. Buchalla and A. J. Buras. "The rare decays $K \to \pi\nu\bar{\nu}$, $B \to X\nu\bar{\nu}$ and $B \to l^+l^-$: An Update." In: *Nucl. Phys. B* 548 (1999), pp. 309–327. doi: 10.1016/S0550-3213(99)00149-2. arXiv: hep-ph/9901288.

[206] M. Misiak and J. Urban. "QCD corrections to FCNC decays mediated by Z penguins and W boxes." In: *Phys. Lett. B* 451 (1999), pp. 161–169. doi: 10.1016/S0370-2693(99)00150-1. arXiv: hep-ph/9901278.

[207] A. J. Buras, J. Girrbach-Noe, C. Niehoff, and D. M. Straub. "$B \to K^{(*)}\nu\overline{\nu}$ decays in the Standard Model and beyond." In: *JHEP* 02 (2015), p. 184. doi: 10.1007/JHEP02(2015)184. arXiv: 1409.4557 [hep-ph].

[208] A. Efrati, A. Falkowski, and Y. Soreq. "Electroweak constraints on flavorful effective theories." In: *JHEP* 07 (2015), p. 018. doi: 10.1007/JHEP07(2015)018. arXiv: 1503.07872 [hep-ph].

[209] I. Brivio, S. Bruggisser, et al. "O new physics, where art thou? A global search in the top sector." In: *JHEP* 02 (2020), p. 131. doi: 10.1007/JHEP02(2020)131. arXiv: 1910.03606 [hep-ph].

[210] R. Alonso, E. E. Jenkins, A. V. Manohar, and M. Trott. "Renormalization Group Evolution of the Standard Model Dimension Six Operators III: Gauge Coupling Dependence and Phenomenology." In: *JHEP* 04 (2014), p. 159. doi: 10.1007/JHEP04(2014)159. arXiv: 1312.2014 [hep-ph].

[211] F. Feruglio, P. Paradisi, and A. Pattori. "On the Importance of Electroweak Corrections for B Anomalies." In: *JHEP* 09 (2017), p. 061. doi: 10.1007/JHEP09(2017)061. arXiv: 1705.00929 [hep-ph].

[212] M. Ablikim et al. [BESIII]. "Search for the decay $D^0 \to \pi^0\nu\bar{\nu}$." In: *Phys. Rev. D* 105.7 (2022), p. L071102. doi: 10.1103/PhysRevD.105.L071102. arXiv: 2112.14236 [hep-ex].

[213] J. Grygier et al. [Belle]. "Search for $B \to h\nu\bar{\nu}$ decays with semileptonic tagging at Belle." In: *Phys. Rev. D* 96.9 (2017). [Addendum: Phys.Rev.D 97, 099902 (2018)], p. 091101. doi: 10.1103/PhysRevD.96.091101. arXiv: 1702.03224 [hep-ex].

[214] J. P. Lees et al. [BaBar]. "Search for $B \to K^{(*)}\nu\bar{\nu}$ and invisible quarkonium decays." In: *Phys. Rev. D* 87.11 (2013), p. 112005. doi: 10.1103/PhysRevD.87.112005. arXiv: 1303.7465 [hep-ex].

[215] O. Lutz et al. [Belle]. "Search for $B \to h^{(*)}\nu\bar{\nu}$ with the full Belle $\Upsilon(4S)$ data sample." In: *Phys. Rev. D* 87.11 (2013), p. 111103. doi: 10.1103/PhysRevD.87.111103. arXiv: 1303.3719 [hep-ex].

[216] R. Barate et al. [ALEPH]. "Measurements of BR $(b \to \tau^- \bar{\nu}_\tau X)$ and BR$(b \to \tau^- \bar{\nu}_\tau D^{*\pm} X)$ and upper limits on BR$(b \to \tau^- \bar{\nu}_\tau)$ and BR$(b \to s\nu\bar{\nu})$." In: *Eur. Phys. J. C* 19 (2001), pp. 213–227. doi: 10.1007/s100520100612. arXiv: hep-ex/0010022.

[217] A. Angelescu, D. A. Faroughy, and O. Sumensari. "Lepton Flavor Violation and Dilepton Tails at the LHC." In: *Eur. Phys. J. C* 80.7 (2020), p. 641. doi: 10.1140/epjc/s10052-020-8210-5. arXiv: 2002.05684 [hep-ph].

[218] A. M. Sirunyan et al. [CMS]. "Search for new physics in top quark production with additional leptons in proton-proton collisions at $\sqrt{s} = 13$ TeV using effective field theory." In: *JHEP* 03 (2021), p. 095. doi: 10.1007/JHEP03(2021)095. arXiv: 2012.04120 [hep-ex].

[219] S. Bißmann, C. Grunwald, G. Hiller, and K. Kröninger. "Top and Beauty synergies in SMEFT-fits at present and future colliders." In: *JHEP* 06 (2021), p. 010. doi: 10.1007/JHEP06(2021)010. arXiv: 2012.10456 [hep-ph].

[220] C. C. Nishi. "Simple derivation of general Fierz-like identities." In: *Am. J. Phys.* 73 (2005), pp. 1160–1163. doi: 10.1119/1.2074087. arXiv: hep-ph/0412245.

[221] A. Deur, S. J. Brodsky, and G. F. de Teramond. "The QCD Running Coupling." In: *Nucl. Phys.* 90 (2016), p. 1. doi: 10.1016/j.ppnp.2016.04.003. arXiv: 1604.08082 [hep-ph].

[222] A. Bazavov et al. "Short-distance matrix elements for $D^0$-meson mixing for $N_f = 2 + 1$ lattice QCD." In: *Phys. Rev.* D97.3 (2018), p. 034513. doi: 10.1103/PhysRevD.97.034513. arXiv: 1706.04622 [hep-lat].

[223] S. Aoki et al. [Flavour Lattice Averaging Group]. "FLAG Review 2019: Flavour Lattice Averaging Group (FLAG)." In: *Eur. Phys. J. C* 80.2 (2020), p. 113. doi: 10.1140/epjc/s10052-019-7354-7. arXiv: 1902.08191 [hep-lat].

[224] F. Herren and M. Steinhauser. "Version 3 of RunDec and CRunDec." In: *Comput. Phys. Commun.* 224 (2018), pp. 333–345. doi: 10.1016/j.cpc.2017.11.014. arXiv: 1703.03751 [hep-ph].

[225] V. Lubicz, L. Riggio, G. Salerno, S. Simula, and C. Tarantino [ETM]. "Scalar and vector form factors of $D \to \pi(K)\ell\nu$ decays with $N_f = 2 + 1 + 1$ twisted fermions." In: *Phys. Rev. D* 96.5 (2017). [Erratum: Phys.Rev.D 99, 099902 (2019), Erratum: Phys.Rev.D 100, 079901 (2019)], p. 054514. doi: 10.1103/PhysRevD.96.054514. arXiv: 1706.03017 [hep-lat].

[226] S. Descotes-Genon, T. Hurth, J. Matias, and J. Virto. "Optimizing the basis of $B \to K^* ll$ observables in the full kinematic range." In: *JHEP* 05 (2013), p. 137. doi: 10.1007/JHEP05(2013)137. arXiv: 1303.5794 [hep-ph].

[227] R. Aaij et al. [LHCb]. "Angular analysis of the $B^0 \to K^{*0}\mu^+\mu^-$ decay using 3 fb$^{-1}$ of integrated luminosity." In: *JHEP* 02 (2016), p. 104. doi: 10.1007/JHEP02(2016)104. arXiv: 1512.04442 [hep-ex].

[228] R. Aaij et al. [LHCb]. "Measurement of $CP$-Averaged Observables in the $B^0 \to K^{*0}\mu^+\mu^-$ Decay." In: *Phys. Rev. Lett.* 125.1 (2020), p. 011802. doi: 10.1103/PhysRevLett.125.011802. arXiv: 2003.04831 [hep-ex].

[229] M. Aaboud et al. [ATLAS]. "Angular analysis of $B_d^0 \to K^*\mu^+\mu^-$ decays in $pp$ collisions at $\sqrt{s} = 8$ TeV with the ATLAS detector." In: *JHEP* 10 (2018), p. 047. doi: 10.1007/JHEP10(2018)047. arXiv: 1805.04000 [hep-ex].

[230] [CMS]. "Measurement of the $P_1$ and $P_5'$ angular parameters of the decay $B^0 \to K^{*0}\mu^+\mu^-$ in proton-proton collisions at $\sqrt{s} = 8$ TeV." In: *CMS-PAS-BPH-15-008* (2017).

[231] [CDF]. "Precise Measurements of Exclusive $b \to s\mu^+\mu^-$ Decay Amplitudes Using the Full CDF Data Set." In: *CDF-NOTE-10894* (2012).

[232] R. Aaij et al. [LHCb]. "Angular Analysis of the $B^+ \to K^{*+}\mu^+\mu^-$ Decay." In: *Phys. Rev. Lett.* 126.16 (2021), p. 161802. doi: 10.1103/PhysRevLett.126.161802. arXiv: 2012.13241 [hep-ex].

[233] R. Aaij et al. [LHCb]. "Angular analysis of charged and neutral $B \to K\mu^+\mu^-$ decays." In: *JHEP* 05 (2014), p. 082. doi: 10.1007/JHEP05(2014)082. arXiv: 1403.8045 [hep-ex].

[234] R. Aaij et al. [LHCb]. "Angular moments of the decay $\Lambda_b^0 \to \Lambda\mu^+\mu^-$ at low hadronic recoil." In: *JHEP* 09 (2018), p. 146. doi: 10.1007/JHEP09(2018)146. arXiv: 1808.00264 [hep-ex].

[235] R. Aaij et al. [LHCb]. "Angular analysis and differential branching fraction of the decay $B_s^0 \to \phi\mu^+\mu^-$." In: *JHEP* 09 (2015), p. 179. doi: 10.1007/JHEP09(2015)179. arXiv: 1506.08777 [hep-ex].

[236] R. Aaij et al. [LHCb]. "Measurements of the S-wave fraction in $B^0 \to K^+\pi^-\mu^+\mu^-$ decays and the $B^0 \to K^*(892)^0\mu^+\mu^-$ differential branching fraction." In: *JHEP* 11 (2016). [Erratum: JHEP 04, 142 (2017)], p. 047. doi: 10.1007/JHEP11(2016)047. arXiv: 1606.04731 [hep-ex].

[237] R. Aaij et al. [LHCb]. "Differential branching fractions and isospin asymmetries of $B \to K^{(*)}\mu^+\mu^-$ decays." In: *JHEP* 06 (2014), p. 133. doi: 10.1007/JHEP06(2014)133. arXiv: 1403.8044 [hep-ex].

[238] R. Aaij et al. [LHCb]. "Differential branching fraction and angular analysis of $\Lambda_b^0 \to \Lambda\mu^+\mu^-$ decays." In: *JHEP* 06 (2015). [Erratum: JHEP 09, 145 (2018)], p. 115. doi: 10.1007/JHEP06(2015)115. arXiv: 1503.07138 [hep-ex].

[239] Y. Amhis et al. [HFLAV]. "Averages of $b$-hadron, $c$-hadron, and $\tau$-lepton properties as of summer 2014." In: *FERMILAB-PUB-15-004-PPD* (2014). arXiv: 1412.7515 [hep-ex].

[240] A. Abdesselam et al. [Belle]. "Measurement of the inclusive $B \to X_{s+d}\gamma$ branching fraction, photon energy spectrum and HQE parameters." In: *38th International Conference on High Energy Physics*. 2016. arXiv: 1608.02344 [hep-ex].

[241] M. Misiak and M. Steinhauser. "Weak radiative decays of the B meson and bounds on $M_{H^\pm}$ in the Two-Higgs-Doublet Model." In: *Eur. Phys. J. C* 77.3 (2017), p. 201. doi: 10.1140/epjc/s10052-017-4776-y. arXiv: 1702.04571 [hep-ph].

[242] D. Dutta et al. [Belle]. "Search for $B_s^0 \to \gamma\gamma$ and a measurement of the branching fraction for $B_s^0 \to \phi\gamma$." In: *Phys. Rev. D* 91.1 (2015), p. 011101. doi: 10.1103/PhysRevD.91.011101. arXiv: 1411.7771 [hep-ex].

[243] R. Aaij et al. [LHCb]. "Measurement of the ratio of branching fractions $BR(B_0 \to K^{\star 0}\gamma)/BR(B_{s0} \to \phi\gamma)$ and the direct CP asymmetry in $B_0 \to K^{\star 0}\gamma$." In: *Nucl. Phys. B* 867 (2013), pp. 1–18. doi: 10.1016/j.nuclphysb.2012.09.013. arXiv: 1209.0313 [hep-ex].

[244] R. Aaij et al. [LHCb]. "Measurement of $CP$-violating and mixing-induced observables in $B_s^0 \to \phi\gamma$ decays." In: *Phys. Rev. Lett.* 123.8 (2019), p. 081802. doi: 10.1103/PhysRevLett.123.081802. arXiv: 1905.06284 [hep-ex].

[245] S. Choudhury et al. [BELLE]. "Test of lepton flavor universality and search for lepton flavor violation in $B \to K\ell\ell$ decays." In: *JHEP* 03 (2021), p. 105. doi: 10.1007/JHEP03(2021)105. arXiv: 1908.01848 [hep-ex].

[246] S. Wehle et al. [Belle]. "Lepton-Flavor-Dependent Angular Analysis of $B \to K^*\ell^+\ell^-$." In: *Phys. Rev. Lett.* 118.11 (2017), p. 111801. doi: 10.1103/PhysRevLett.118.111801. arXiv: 1612.05014 [hep-ex].

[247] R. Aaij et al. [LHCb]. "Angular analysis of the $B^0 \to K^{*0}e^+e^-$ decay in the low-$q^2$ region." In: *JHEP* 04 (2015), p. 064. doi: 10.1007/JHEP04(2015)064. arXiv: 1501.03038 [hep-ex].

[248] R. Aaij et al. [LHCb]. "Strong constraints on the $b \to s\gamma$ photon polarisation from $B^0 \to K^{*0}e^+e^-$ decays." In: *JHEP* 12 (2020), p. 081. doi: 10.1007/JHEP12(2020)081. arXiv: 2010.06011 [hep-ex].

[249] C. Bobeth, G. Hiller, and G. Piranishvili. "CP Asymmetries in bar $B \to \bar{K}^*(\to \bar{K}\pi)\bar{\ell}\ell$ and Untagged $\bar{B}_s$, $B_s \to \phi(\to K^+K^-)\bar{\ell}\ell$ Decays at NLO." In: *JHEP* 07 (2008), p. 106. doi: 10.1088/1126-6708/2008/07/106. arXiv: 0805.2525 [hep-ph].

[250] [LHCb, ATLAS, CMS]. "Combination of the ATLAS, CMS and LHCb results on the $B^0_{(s)} \to \mu^+\mu^-$ decays." In: *CERN-LHCb-CONF-2020-002* (2020).

[251] T. P. Cheng and L. F. Li. *Gauge theory of elementary particle physics*. Oxford, UK: Oxford University Press, 1984.

[252] S. Pokorski. *GAUGE FIELD THEORIES*. Cambridge University Press, 2005.

[253] S. Weinberg. *The quantum theory of fields. Vol. 2: Modern applications*. Cambridge University Press, 2013.

[254] A. Bilal. "Lectures on Anomalies." In: *LPTENS-08-05* (2008). arXiv: 0802.0634 [hep-th].

[255] H. E. Haber. "Useful relations among the generators in the defining and adjoint representations of SU(N)." In: *SciPost Phys. Lect. Notes* 21 (2021), p. 1. doi: 10.21468/SciPostPhysLectNotes.21. arXiv: 1912.13302 [math-ph].

[256] J. C. Pati and A. Salam. "Lepton Number as the Fourth Color." In: *Phys. Rev. D* 10 (1974). [Erratum: Phys.Rev.D 11, 703–703 (1975)], pp. 275–289. doi: 10.1103/PhysRevD.10.275.

[257] V. Lubicz, L. Riggio, G. Salerno, S. Simula, and C. Tarantino [ETM]. "Tensor form factor of $D \to \pi(K)\ell\nu$ and $D \to \pi(K)\ell\ell$ decays with $N_f = 2+1+1$ twisted-mass fermions." In: *Phys. Rev. D* 98.1 (2018), p. 014516. doi: 10.1103/PhysRevD.98.014516. arXiv: 1803.04807 [hep-lat].

[258] J. Koponen, C. T. H. Davies, and G. Donald [HPQCD]. "$D \to K$ and $D \to \pi$ semileptonic form factors from Lattice QCD." In: *5th International Workshop on Charm Physics*. 2012. arXiv: 1208.6242 [hep-lat].

[259] [CMS]. "Search for charged lepton flavor violation in top quark production and decay in proton-proton collisions at $\sqrt{s} = 13$ TeV." In: *CMS-PAS-TOP-19-006* (2021).

[260] [ATLAS]. "Search for charged lepton-flavour violation in top-quark decays at the LHC with the ATLAS detector." In: *ATLAS-CONF-2018-044* (2018).

[261] M. Lisovyi, A. Verbytskyi, and O. Zenaiev. "Combined analysis of charm-quark fragmentation-fraction measurements." In: *Eur. Phys. J. C* 76.7 (2016), p. 397. doi: 10.1140/epjc/s10052-016-4246-y. arXiv: 1509.01061 [hep-ex].

# Eidesstattliche Versicherung

Ich versichere hiermit an Eides statt, dass ich die vorliegende Dissertation mit dem Titel *Exploiting the phenomenology of flavourful $Z'$ models* selbstständig und ohne unzulässige fremde Hilfe erbracht habe. Ich habe keine anderen als die angegebenen Quellen und Hilfsmittel benutzt, sowie wörtliche und sinngemäße Zitate kenntlich gemacht. Die Arbeit hat in gleicher oder ähnlicher Form noch keiner Prüfungsbehörde vorgelegen.

Ort, Datum

Unterschrift

## Belehrung

Wer vorsätzlich gegen eine die Täuschung über Prüfungsleistungen betreffende Regelung einer Hochschulprüfungsordnung verstößt, handelt ordnungswidrig. Die Ordnungswidrigkeit kann mit einer Geldbuße von bis zu 50 000 € geahndet werden. Zuständige Verwaltungsbehörde für die Verfolgung und Ahndung von Ordnungswidrigkeiten ist der Kanzler/die Kanzlerin der Technischen Universität Dortmund. Im Falle eines mehrfachen oder sonstigen schwerwiegenden Täuschungsversuches kann der Prüfling zudem exmatrikuliert werden (§ 63 Abs. 5 Hochschulgesetz –HG–).

Die Abgabe einer falschen Versicherung an Eides statt wird mit Freiheitsstrafe bis zu 3 Jahren oder mit Geldstrafe bestraft.

Die Technische Universität Dortmund wird ggf. elektronische Vergleichswerkzeuge (wie z. B. die Software *turnitin*) zur Überprüfung von Ordnungswidrigkeiten in Prüfungsverfahren nutzen.

Die oben stehende Belehrung habe ich zur Kenntnis genommen.

Ort, Datum

Unterschrift